Studies on Human Centric Smart Street Lighting System in Indian Context and its Effect on Driver's Performance

Thesis submitted by

Aiswarya Dev Goswami

Doctor of Philosophy (Engineering)

Department of Electrical Engineering

Faculty Council of Engineering & Technology

Jadavpur University

Kolkata, India

2024

JADAVPUR UNIVERSITY
KOLKATA-700032, INDIA

INDEX NO: 283/21/E

1. **Title of the thesis:**

"Studies on Human Centric Smart Street Lighting System in Indian Context and its Effect on Driver's Performance"

2. **Name, Designation and Institution of the Supervisor:**

Dr. Suddhasatwa Chakraborty

Associate Professor

Department of Electrical Engineering

Jadavpur University

Kolkata, India

3. List of Journal Publications:

I. Goswami, Aiswarya Dev, Jyotipriya Roy, Atanu Naskar, and Suddhasatwa Chakraborty. "A laboratory-based study on the effect of CCT change of LED light sources on reaction time and visibility level for object recognition." Optik 264 (2022): 169353.

II. Goswami, Aiswarya Dev, Suddhasatwa Chakraborty, Budhaditya Ghosh, Jyotipriya Roy, and Atanu Naskar. "A laboratory-based study on the effect of peripheral flickering LED sources on reaction time of drivers for object recognition." Optik 273 (2023): 170428.

III. Goswami, Aiswarya Dev, and Suddhasatwa Chakraborty. "ROAD LIGHTING STANDARDS'EVOLUTION AND FUTURE DEVELOPMENT OF SMART STREET LIGHTING BASED UPON USERS'PERFORMANCE IN VIEW OF HUMAN CENTRIC LIGHTING: A REVIEW." Light & Engineering 31, no. 5.

IV. Goswami, Aiswarya Dev, Jyotipriya Roy, Suddhasatwa Chakraborty, and Badal Sarkar. "Case study of street lighting of an Indian University: present and future." Journal of Optics (2024): 1-10.

V. Goswami, Aiswarya Dev, Jyotipriya Roy, Suddhasatwa Chakraborty, and Sayanti Bag. "VALIDATION OF BEAM ANGLE SWITCHING METHOD USING A LED LUMEN MAINTENANCE TESTING DEVICE." Light & Engineering 32, no. 2.

VI. Chakraborty, Suddhasatwa, Aiswarya Dev Goswami, and Saswati Mazumdar. "Beam controlled lighting design: An approach towards optimization of road lighting design." Optik 261 (2022): 169165.

VII. Roy, Jyotipriya, Aiswarya Dev Goswami, Suddhasatwa Chakraborty, Subhajit Mandal, and Nurjahan Khatun. "A message queuing telemetry transport (MQTT) protocol-based energy-efficient smart, wireless LED street lighting solution." Journal of Optics (2024): 1-14.

VIII. Chakraborty, Suddhasatwa, Gaurav Chakraborty, Aiswarya Dev Goswami, and Jyotipriya Roy. "STUDY OF THE HARMONIC ANALYSIS OF THE HIGH-INTENSITY DISCHARGE LAMPS." Light & Engineering 31, no. 4.

4. List of Patents: NIL

5. List of Presentations in National/International Conferences/ Workshop:

I. Goswami, Aiswarya Dev, Jyotipriya Roy, Suddhasatwa Chakraborty, and Pallav Dutta. "An experimental analysis of object recognition performance under different lighting scenes for varying CCT of LED light sources." In 2023 IEEE Sustainable Smart Lighting World Conference & Expo (LS18), pp. 1-6. IEEE, 2023.

II. Goswami, Aiswarya Dev, Anirban Ghosh, Jyotipriya Roy, and Suddhasatwa Chakraborty. "Studies on Driver's Response with Peripheral Moving Targets under

Different Road Lighting Situations-A Realistic Approach." National Science Congress on Illumination: Luminescence 2023 2 (1), 72-83.

III. Goswami, Aiswarya Dev, Jyotipriya Roy, and Suddhasatwa Chakraborty. "Study on Implementation of PWM Dimming in Beam Angle Switched LED Street Light to Achieve Energy Efficient Standard Lighting." In 2023 IEEE 3rd Applied Signal Processing Conference (ASPCON), pp. 33-37. IEEE, 2023.

IV. Goswami, Aiswarya Dev, Jyotipriya Roy, Sounak Dey, Suddhasatwa Chakraborty. “Development of A Low-Cost Novel CCT Meter using Machine Learning Regression Techniques to Estimate Real-time CCTs”. In 2024 IEEE Kolkata Section Flagship Conference (CALCON). In Press.

V. Roy, Jyotipriya, Aiswarya Dev Goswami, and Suddhasatwa Chakraborty. "Implementation of Beam Angle Switching in Smart LED Street Lighting System Using MQTT Protocol." In 2023 IEEE 3rd Applied Signal Processing Conference (ASPCON), pp. 38-43. IEEE, 2023.

VI. Roy, Jyotipriya, Aiswarya Dev Goswami, Suddhasatwa Chakraborty. “A Machine Learning Based Laboratory Simulated Experiment for Determining the Effect of Varying Correlated Color Temperature of LED Sources on Close Proximity Task Performances”. In 2024 IEEE Kolkata Section Flagship Conference (CALCON). In Press.

"Statement of Originality"

I, **Aiswarya Dev Goswami**, registered on **23rd July, 2021** do hereby declare that this thesis entitled **"Studies on Human Centric Smart Street Lighting System in Indian Context and its Effect on Driver's Performance"** contains literature survey and original research work done by the undersigned candidate as part of Doctoral studies. All information in this thesis have been obtained and presented in accordance with existing academic rules and ethical conduct. I declare that, as required by these rules and conduct, I have fully cited and referred all materials and results that are not original to this work. I also declare that I have checked this thesis as per the "Policy on Anti Plagiarism, Jadavpur University, 2019", and the level of similarity as checked by iThenticate software is **3%**.

Aiswarya Dev Goswami

Signature of Candidate:

Date : 29/1/2025

Certified by Supervisor:

(Signature with date, seal)

1. Siddhartha Chakrabarty

Associate Professor
Electrical Engg. Dept.
Jadavpur University
Kolkata - 700 032

29/01/25

CERTIFICATE FROM THE SUPERVISOR/S

This is to certify that the thesis entitled "**Studies on Human Centric Smart Street Lighting System in Indian Context and its Effect on Driver's Performance**" submitted by Shri **Aiswarya Dev Goswami**, who got his name registered on **23rd July, 2021** for the award of Ph. D. (Engg.) degree of Jadavpur University is absolutely based upon his own work under the supervision of **Dr. Suddhasatwa Chakraborty** and that neither his thesis nor any part of the thesis has been submitted for any degree/diploma or any other academic award anywhere before.

Signature of the Supervisor and date with Office Seal

29/01/25

Associate Professor
Electrical Engg. Dept.
Jadavpur University
Kolkata - 700 032

Acknowledgement

I would like to express my heartfelt gratitude to Jadavpur University for providing me the opportunity to complete this work.

First and foremost, I extend my sincere thanks to my supervisor and the In-charge of Illumination Engineering Laboratory of the Electrical Engineering Department, Dr. Suddhasatwa Chakraborty, for his invaluable guidance, insightful suggestions, and continuous encouragement throughout my Ph.D. journey. His deep knowledge and unwavering support have been instrumental in shaping this research over the past four years.

I am also deeply thankful to Former-Research Scholar Dr. Basudeb Das of the Electrical Engineering Department for his expert guidance and contributions in the field of tunable CCT generation using color mixing theory.

My sincere appreciation goes to Dr. Saswati Mazumdar, former HOD and Professor (Retired) of Electrical Engineering Department, for sharing her profound insights and experiences in experimental design and encouragement, which have greatly enriched my research and will continue to inspire me in the future.

I extend my gratitude to my esteemed teachers, Head of Electrical Engineering Department and Prof. Biswanath Roy, and Dr. Sangeeta Sahana of the Illumination Engineering Section, for their valuable advice and support. I am equally grateful to Dr. Parthasarathi Satvaya of the School of Illumination Science Engineering and Design (SISED) for providing essential instruments and insights for my research.

I extend my heartfelt gratitude and respect to Mr. Jyotipriya Roy, research scholar of the Illumination Engineering Section, Electrical Engineering Department, for his invaluable support in experimental design and assistance in conducting experiments. His helps in knowledge discovery have been instrumental in advancing my thesis work and will continue to inspire me in the future.

Special thanks to Mr. Asit Kumar Sur, Former Visiting Demonstrator of the Illumination Engineering Section, for his unwavering assistance for control circuit design, and to the staff members of the Illumination Engineering Laboratory — Mr. Samir Mandi, Mr. Pradip Pal and Mr. Santosh Sahoo—for their cooperation.

I am indebted to my friends and colleagues— Dr. Moutusi Bag, Dr. Shibabrata Mukherjee, and Mr. Sounak Dey, Mr. Pallav Dutta and Mr. Atanu Naskar—for their support and for creating a stimulating environment in the laboratory.

My deepest thanks go to my wife, Ms. Arpita Chatterjee, for her unwavering support, patience, and sacrifices throughout this journey. Her encouragement at every step has been invaluable.

Specially, I would like to express my gratitude and thanks to my father Mr. Partha Goswami, former assistant school teacher (English) of Chhotakurpa (Ratanpur) High School, for his unhesitating support and encouragement towards my Ph.D. journey.

Lastly, I am profoundly grateful to my parents, in-laws, and family members for their moral and emotional support, which has been a cornerstone in the completion of this thesis.

Aishwarya Dev Goswami

30/1/25

Abstract

Standardized and appropriate road lighting is crucial for industrialization, economic progress, individual safety and security, work efficiency, and human well-being in a growing nation like India. Aside from that, the development of power LEDs and their application in street lighting luminaires has revolutionized the design schemes of street lighting due to their controllability, low power consumption, and longer lifespan in terms of a variety of lighting parameters, including efficacy, color rendering index (CRI), luminance, correlated color temperature (CCT), and dynamic nature. They not only replaced age old light sources like incandescent lamps, high intensity discharge lamps, fluorescent lamps etc., but also opened a vast plethora of research domains, where optimization of lights and lighting designs can be done by examining the visual and non-visual effects of various lighting parameters on human observers. Detection of intrinsic photosensitive retinal ganglion cell (ipRGC) in human eye and extensive study on circadian rhythm already established that light has profound effect on human physiology and psychology. Since then, efforts are made to optimize the indoor or outdoor light keeping the human needs in mind and these types of lighting designs are named as 'Human Centric Lighting'. Human centric lighting can help users since it considers factors that can improve their mood, productivity, health, etc. Additionally, it has been established that LED lighting is more energy-efficient than traditional lighting options and they have a longer lifespan, use much less electricity, have a smaller carbon impact, and have lower energy costs.

That is why, the primary focus of this thesis is to develop a smart energy efficient human centric street lighting in Indian context by analyzing visual and non-visual effects of various lighting parameters on object detection of human observers. It investigates the effect of LED lighting systems on object detection capabilities, focusing on varying correlated color temperatures (CCTs) and flickering frequencies of LED light sources. This research is driven by the growing demand for street lighting systems that are both energy-efficient and user-friendly, aiming to improve safety while reducing environmental impact and financial expenses. The research is grounded in multiple laboratory and field studies, as well as innovative experimental designs that examine the interaction between lighting parameters and human visual and non-visual performances under various environmental conditions. This thesis builds on a series of interconnected studies carried out over several years.

The first study explored the understanding of human performance under different lighting conditions. It assessed how varying CCT levels influence drivers' reaction times and visibility levels. Conducted in a controlled laboratory setting, the experiment revealed that increasing ambient lighting from peripheral sources reduced reaction times. Importantly, this study established a correlation between CCT, reaction times, and visibility levels. The findings suggested that peripheral lighting sources could significantly enhance object detection, thus providing a basis for optimizing street lighting designs to improve driver safety and comfort. The study revealed that a 4000K CCT of main source offered the best object recognition results when peripheral lights were turned off. Further experimentation identified optimal CCT levels of 5000K for the main source and 6000K for peripheral sources, reaffirming the central role of CCT in designing effective street lighting schemes. Additionally, another behavioral study is also done with the same

experimental setup, which supported the previous results. Building on the results of the previous studies, subsequent research addressed the effect of peripheral flickering LED light sources on static human observers' ability to recognize objects. This laboratory-based experiment tested the influence of different flicker frequencies of peripheral sources and CCTs of main LED source on human visual and non-visual performances. The findings were profound, which is increment of the CCT of the main light source reduced reaction times, while the flicker of peripheral LED lights increased reaction times. These insights highlighted the negative impact of flickering on human visual performance, particularly when peripheral lights were involved, suggesting the need for stable lighting conditions to enhance safety.

The next phase of research tackled emerging dimming concepts, like Beam Angle Switching (BAS) and Pulse Width Modulation (PWM), aimed at energy saving. Impact of BAS technique on human performance including drivers' performance is also reviewed. Furthermore, validation of BAS method is also carried out in laboratory by checking whether the lumen output is depreciated or not when the LED is subjected to frequent switching and it is found that BAS technique does not alter the lumen output and does not have any effect on LED body (heat sink) temperature. Besides, a precise case study for arterial roads of Jadavpur University, employing BAS enabled street lights in place of existing ones, is conducted. Study found that the upgraded street lighting system can reduce 55.52% of electrical energy consumption saving roughly 53.14 tons of CO2 emissions per year compared to the old installed street lighting. After that, another study is also done to amalgamate PWM dimming and BAS technique to achieve further energy saving. Besides, experimentation is also done to find the effect of variation of switching frequencies of PWM signal on LEDs' CCT and it is seen that switching frequencies have least effect on CCT.

Third phase of this research is aimed to optimize LED street light depending upon the decoded temporal brain processes of the human observer, realized using Electroencephalograph (EEG) and Galvanic Skin Response (GSR) during object detection task under specially designed experimental lighting scenes, where the CCT of main and peripheral sources are varied. Effects of peripheral and main source CCTs on various frequency bands of EEG signals, event related potentials (ERP) and GSR are measured. Besides, reaction time and behavioral studies also done to corelate all the findings of the experimentation. It is found that CCT range of 4500K to 5000K for both the main and peripheral light sources is optimal for accurate object recognition. Furthermore, a score factor for lighting scenes is also proposed for evaluation of human centrism and it can be used as a future metric. Finally depending upon all the previous findings, a smart energy efficient CCT tunable human centric smart luminaire system is developed. Furthermore, another low-cost device, which can be used for monitoring of CCT, is developed to measure the real-time CCT values of the developed light source using RGB sensor and regression models.

In conclusion, this thesis presents a comprehensive exploration of the interaction between smart lighting technologies and human visual and non-visual performances. It provides actionable insights for designing energy-efficient, human-centric street lighting systems that enhance safety and visibility while reducing energy consumption. The research findings suggest that careful manipulation of CCT, flicker, and usage of PWM dimming and beam angle switching can significantly improve object detection and overall user satisfaction and reduce energy

consumption, making it a valuable contribution to the field of smart street lighting and road safety. These insights pave the way for future innovations in lighting design, with the potential for widespread application in urban planning and traffic safety management.

Table of Contents

List of Figures

List of Tables

List of Abbreviations

.edf	European Data Format File
.ies	Illuminating Engineering Society File
.txt	Text File
3D	Three Dimensional
AC	Alternating Current
AF	Age Factor
ALT	Accelerated Life Testing
ANSI	American National Standards Institute
ART	Average Reaction Time
ARWVL	Average Relative Weighted Visibility Level
AUC	Area Under the Curve
AutoCAD	Automatic Computer-Aided Design
BAS	Beam Angle Switching
BEM dipfit	Boundary Element Method Dipole Fit
CAGR	Compound Annual Growth Rate
CCR	Constant Current Reduction
CCT	Co-related Color Temperature
CESC	Calcutta Electric Supply Corporation
CFL	Compact Fluorescent Lamp
CIE	Commission internationale de l´éclairage
CMH	Ceramic Metal Halide
CNN	Convolutional Neural Network
COB	Chip on Board
CRI	Color Rendering Index
CS	Circadian Stimulus
DC	Direct Current
DIALux	DIAL Lighting Design
EDA	Electro-Dermal Activity
EEG	Electro-encephalogram
EEGLAB	EEG Laboratory
EMI	Electro-Magnetic Interference
EN	European Standards
ERP	Event Related Potential
ETD	Electro Technical Division
FIR	Finite Impulse Response
FWHM	Full Width at Half Maximum
FY	Financial Year

GaN	Gallium Nitride
GHz	Giga-Hertz
GPR	Gaussian Process Regression
GPS	Global Positioning System
GSR	Galvanic Skin Response
GUI	Graphical User Interface
GWh	Giga-Watt Hour
HCL	Human Centric Lighting
HPMV	High Pressure Mercury Vapor Lamp
HPSV	High Pressure Sodium Vapor Lamp
ICA	Independent Component Analysis
IDE	Integrated Development Environment
IEEE	Institute of Electrical and Electronics Engineers
IESNA	Illuminating Engineering Society of North America
InGaN	Indium Gallium Nitride
IoT	Internet of Things
ipRGC	intrinsic photosensitive Retinal Ganglion Cell
IS	Indian Standards
KHz	Kilo-Hertz
KNN	K-Nearest Neighbors Regression
KΩ	Kilo-Ohm
LCD	Liquid Crystal Display
LED	Light Emitting Diode
LF/HF	Low Frequency to High Frequency
LoRa	Long Range
LPSV	Low Pressure Sodium Vapor Lamp
LPWAN	Low Power Wide Area Network
MATLAB	Matrix Laboratory
MCPCB	Metal core printed circuit board
MH	Metal Halide Lamp
microSD	Micro Secure Digital
ML	Machine Learning
MNI	Montreal Neurological Institute coordinate
MOSFET	Metal-Oxide-Semiconductor Field-Effect Transistor
MS	Measuring Sphere
MSE	Mean Squared Error
OLED	Organic Light Emitting Diode
PBT	Polybutylene Terephthalate
PWM	Pulse Width Modulation

RBF	Radial Basis Function
RGB	Red-Green-Blue
RGBA	Red-Green-Blue-Amber
RGB-CAW	Red-Green-Blue-Cyan-Amber-White
RGBW	Red-Green-Blue-White
RMS	Root Mean Squared
RMSE	Root Mean Squared Error
RNN	Recurrent Neural Network
RT	Reaction Time
RTMCD	Reaction Time Measuring Compact Device
RTMD v2.0	Reaction Time Measuring Device Version 2.0
S/P	Scotopic/Photopic
SCN	Suprachiasmatic Nucleus
SCR	Skin Conductance Responses
SD	Standard Deviation
SLNP	Street Lighting National Program
SMD	Surface Mount Device
SMPS	Switched-Mode Power Supply
SPD	Spectral Power Distribution
STV	Small Target Visibility
SVL	Sodium Vapor Lamps
SVR	Support Vector Machine Regression
TAOS	Texas Advanced Optoelectronic Solutions
THD	Total Harmonic Distortion
TLA	Temporal Light Artefacts
TLM	Temporal Light Modulation
TPU	Tensor Processing Units
TTL	Transistor-Transistor Logic
UISD	User Interface cum Storage Device
UK	United Kingdom
US	United States
VL	Visibility Level
VR	Virtual Reality
WGB	White-Green-Blue

List of Symbols

T_c	CCT
$\hat{y}_i$	Predicted values of dependent variable using regression model
(x,y)	Chromaticity Co-ordinates of the light source
$A(x_a,y_a)$	Chromaticity Co-ordinates of LED A
$a(\alpha, L_b)$	Parameter depends on size of target and background luminance
$B(x_b,y_b)$	Chromaticity Co-ordinates of LED B
$C(x_c,y_c)$	Chromaticity Co-ordinates of LED C
D	Duty Cycle
D_b	Applied Duty cycle to source B for three-point color mixing
d_{bc}	Linear distances between point B and point C for three-point color mixing
d_{bm}	Linear distances between point B and point M for three-point color mixing
D_c	Applied Duty cycle to source C
D_m	Applied Duty cycle to point M for three-point color mixing
E_{aT}	Instantaneous Illuminance value of source A to achieve Target CCT
E_{avg}	Average Illuminance of Grid
E_b	Instantaneous Illuminance value of B light source
E_{bM}	Maximum Illuminance value of B light source
E_{bT}	Instantaneous Illuminance value of source B to achieve Target CCT
E_c	Instantaneous Illuminance value of C light source
E_{cM}	Maximum Illuminance value of C light source
E_{cT}	Instantaneous Illuminance value of source C to achieve Target CCT
E_m	Instantaneous Illuminance value of co-ordinates within the chromaticity diagram representing the color mixture of light sources B and C required to produce the desired correlated color temperature (CCT)
E_{min}	Minimum Illuminance on Grid

E_{mM}	Maximum Illuminance value of co-ordinates within the chromaticity diagram representing the color mixture of light sources B and C required to produce the desired correlated color temperature (CCT)
E_r	Required Illuminance
F_{cp}	Contrast polarity factor
F_y	Failure Fraction at Rated Life of LED
k	Factor for the probability of perception (k = 2.6 for 100% probability)
$L^{1/2}$	Luminance function
L_b	Background luminance
L_b	Luminance values of B light source
L_c	Luminance values of C light source
L_t	Target luminance
L_x	LED Life Span
$M(x_m,y_m)$	Coordinates within the chromaticity diagram representing the color mixture of light sources B and C required to produce the desired correlated color temperature (CCT)
n	Empirical Formulation for CCT Calculation using Mc-Cammy's Formula
N	Number of observations in population for SD calculation
n	Number of observations in MSE calculation
$r(D_a, D_m)$	Ratio of Applied Duty cycles of light source A and point M for three component color mixing
$r(D_c, D_b)$	Ratio of Applied Duty cycles of light source C and B for three component color mixing
$r(E_{aM}, E_{mM})$	Ratio of Maximum Illuminance values of light source A and point M for three component color mixing
$r(E_{cM}, E_{bM})$	Ratio of Maximum Illuminance values of light source C and B for three component color mixing
$r(W_{c2}, W_{c1})$	Ratio of weighted co-efficients of light source C and B for three component color mixing
$r(W_{c4}, W_{c3})$	Ratio of weighted co-efficients of light source A and point B for three component color mixing
$r(y_a, y_m)$	Ratio of Y co-ordinates of chromaticity co-ordinates of light source A and point M for three component color mixing
$r(y_c, y_b)$	Ratio of Y co-ordinates of chromaticity co-ordinates of light source C and B for three component color mixing

SD	Standard deviation of the population
t	Observation time
T	Time period of the given signal
$T(x_t,y_t)$	Chromaticity Co-ordinates of Target CCT point
U_o	Overall Uniformity
v	A smoothness parameter balancing flexibility and regularity for Gaussian Process Regression with Matérn Kernel
W_{c1}	Weighted co-efficient of light source B for three component color mixing
W_{c2}	Weighted co-efficient of light source C for three component color mixing
X	Switching Frequency
X_i	i^{th} observation in the population for SD calculation
Y_{10}	SD of CCT for 10 Watt LED
Y_{10}^*	SD of CRI for 10 Watt LED
Y_{20}	SD of CCT for 20 Watt LED
Y_{20}^*	SD of CRI for 20 Watt LED
y_i	Measured values of the dependent variable
α	Target size
ΔL_{actual}	Luminance difference between the target and the background in the Laboratory conditions
$\Delta L_{threshold}$	Luminance difference between target of certain angular size and its background for minimum visibility
μ	Mean of the population
τ	on-time of the given signal
$\Phi^{1/2}$	Luminance flux function
$\bar{y}_i$	Mean of the population measured values of the dependent variable

Chapter 1: Introduction

1.1. Introduction

Climate change, carbon emission reduction, and independence from fossil fuels have been major global challenges in recent decades. Enormous research efforts are also being made to create human friendly rather human oriented systems or machines to nurture human emotion, mood and to reduce human workload. Numerous initiatives to address and implement these issues have begun to yield positive results, with the percentage of energy generated from renewable sources increasing dramatically. Graphical representation for renewable energy generation is given in Fig. 1.1.

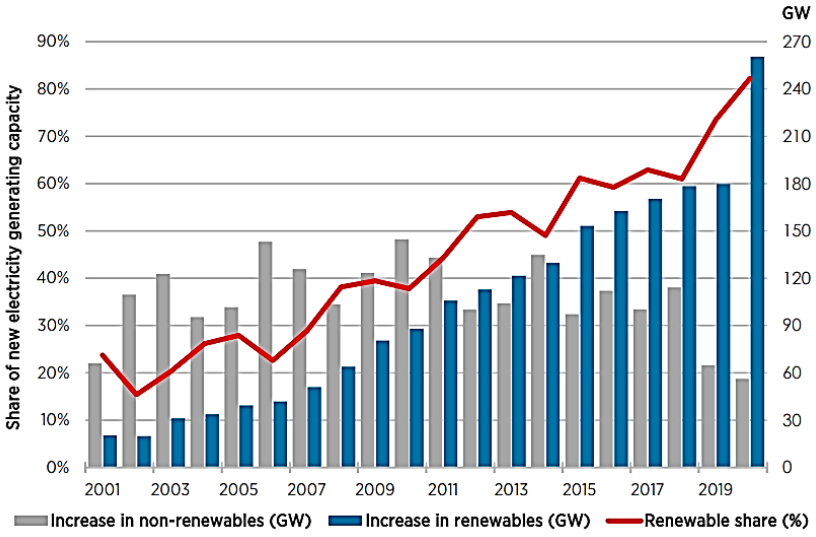

Fig.1.1: Proportion of Renewable Energy in Yearly Power Capacity Growth

One of the major public convenience systems in India, which consumes a huge chunk of electrical energy is street lighting. Approximately 78 million street lights provide illumination across Indian roads as of FY2019 [1]. Statistics reveal that 1% to 3% of our produced electrical energy (about 8,478 GWh of electricity in FY13) is needed to illuminate our streets for a particular municipality in India, where the maintenance cost of them can reach up-to 10-15% of the municipal budget. It is proven that, using effective lighting designs can cut energy use by 25-60% in India [2-3].

Generally, the lamps utilized in these luminaires are from prehistoric times. The majority of them are fluorescent lamps, sodium vapor lamps (SVL), incandescent lamps, metal halide lamps, or CFLs. Besides, one of the major problems in India is that, the street luminaires are majorly seen to be operational at day time or when there is little to no traffic at night, leading to significant energy wastage. Furthermore, another problem arises in this context, where night-time road accidents contribute to substantial global casualties, with injuries from such incidents ranking as the ninth most significant cause of disability till the year 2000 [4]. India, unfortunately, holds the top position in road accident fatalities among 199 countries, accounting for 11% of global road accident deaths. From 2005 to 2019, the number of deaths due to road accidents in India surged by a staggering 59.116%, with 151,113 fatalities reported in 2019 alone [5]. A 2014 study in Tamil Nadu revealed that visual factors were responsible for 47% of accidents, with lighting and visibility playing a crucial role in driver and pedestrian safety [6]. This underscores the need for improved lighting infrastructure on Indian roads, particularly highways, to reduce accidents caused by poor visibility. In contrast of this, India's Street Lighting National Program (SLNP) has made strides by installing 13 million energy-efficient LED streetlights across 2,70,000 km till now, contributing to reduced power consumption [1].

For the sake of historical facts, it is known that, during the 16th and first half of 17th centuries, metropolitan areas such as Paris and London were lighted by oil lanterns set on poles at specific intervals. In the late 17th century, a new style of oil lamp replaced the older ones. They're called *Réverbère*. Later, gas-powered street lights were introduced. It remained for a century. In the late 18th century, Arc lamps replaced gas lamps in nations such as the US and UK. This was the first street light powered by electricity [7]. Along with the heavy usage of street lights, standards for street lighting designs, operations and maintenance are evolved all around the world, depending upon the road categories, weather, traffic density, human perception etc. In October 1820, the police commissioners of the city of Edinburgh developed a well-recognized standard (Specifications of cast iron pillars, lanterns, and lamps for burning gas) for Edinburgh's Street lighting. That was the first recognized standard or code for street lighting in Britain and as well as in world [7]. Current road lighting standards, like CIE115:2010, EN13201–1:2014, EN13201–2:2015, IESNA/ANSI RP-8:2014, BS5489–1:2013 etc., are made based upon two distinctive purposes. The first one is to ensure that all road users, including drivers and pedestrians, can move safely, detect hazards and avoid them safely and the latter is to enhance the street's appearance both on day and night. India also published a street lighting standard (IS:1944 (parts I and II)-1970) for public lighting. It recognizes two sorts of lighting suggestions (illuminance-based): one for drivers and one for pedestrians. The Indian code of practice for street lighting design provides a creative approach to designing, installing, and maintaining specified lighting. But there exist several scopes of developments in Indian as well as in other street lighting standards because they do not include smart lighting schemes or designs and human oriented approach. Furthermore, in these standards, quantification of illuminance-based basis is not clear and it demands to be changed to luminance-based basis because it gives a better measure than illuminance of how well can an object be seen [8].

Coming back to the story of lights. From 16th century, light sources have evolved from oil lanterns and gas lamps to LEDs. There are several types of lamps, which came and go in between them, including high-pressure sodium (HPSV), low-pressure sodium (LPSV), and high-pressure mercury vapor (HPMV). But now a days LEDs have flooded the lighting industry and market, because of its higher spectral power density (SPD) output, a shorter start-up time, and infinite control options compared to HPSV and LPSV. Besides, LED lighting is more energy-efficient compared to older lighting choices. Furthermore, invention of power LEDs revolutionize the street lights, which have a longer lifespan, are very easier to control, consume less electricity, have a reduced carbon footprint, and cost less to operate [9]. Primarily, with the adoption of LEDs in street illumination, a new era of road lighting design emerges, which is called smart street lighting. It reduces manual intervention, curbs excess electrical energy consumption by scheduling the on time of LEDs, introduces controllability of various lighting parameters like illuminance, CCT, beam angle etc. Secondarily, the introduction of mesopic photometry significantly altered road lighting standards. Although nighttime road conditions should align with mesopic photometry, where rods and cones simultaneously contribute to visual perception for drivers and pedestrians, traditional road lighting relied solely on photopic photometry, which only considers cone responses. Mesopic vision, however, involves a weighted combination of both photopic (cone) and scotopic (rod) responses, for which the CIE mesopic system was developed [10]. Last but not least, the emergence of the third photoreceptor of the human eye, which is ipRGC (intrinsic photosensitive retinal ganglion cell), and comprehensive studies on circadian rhythm have long demonstrated that light has significant impacts on human physiology and psychology [11]. Moreover, the integration of precise global positioning system (GPS), smart cameras, sensors, lighting measurement tools, and ambulant eye tracking devices provides valuable data from road illumination scenes. Recent developments mark a new age in lighting design. In the lighting research zone, a new word was introduced: human-centric lighting, where little to no exploration is done in street lighting domain specifically in Indian context. Human-centric lighting considers light and illumination as components influencing visual, biological, and behavioral responses in humans. It integrates the visual and non-visual impacts of light on humans [12].

With these views, lighting designs must consider various energy consumption reduction techniques, where dimming of LED lights, when needed, opens a new avenue. There exist several dimming techniques like constant voltage dimming, PWM (Pulse Width Modulation) dimming, beam angle switching (BAS) etc. Taking all these points in mind, there arises a strong need for a smart human centric street lighting solution. That is why, this thesis tries to investigate various visual and non-visual effects of lighting parameters upon human object detection, to study amalgamation of various dimming techniques with a confirmative case study, to design a smart human centric street lighting solution through optimization using the experimental results.

1.2. Some Definitions

To understand the context of smart human centric street lighting and optimization of various lighting parameters and human centric parameters fully, some definitions regarding these topics must be discussed in the purview of this part. The portion of this chapter is grossly divided into four sub-portions.

1.2.1. The first sub-portion talks about *human visual system*, which determines how human sight reacts in different lighting condition like day or night. Human visual system heavily depends upon human eye and interpretation of human brain towards the output of eye. They act together to form a simulation of the external world in-front of human eye. By not going under the hood of physical construction of the system, vision can be grossly classified into three sensitivity states. They are *photopic vision*, *mesopic vision* and *scotopic vision*. These states are triggered by *eye adaptation*. Human visual systems can withstand a huge range of luminance values from 0.000001 cd/m2 on night to 100,000 cd/m2 on a sunny sea shore. To subsist this range, human visual system unconsciously and continuously shifts its sensitivity towards external light falling on the eye via a special process, which is called *adaptation.* This process depends upon three unique physical processes, which are *change in pupil size*, *neural adaptation* and *photochemical adaptation.*

Photopic vision happens at luminance values higher than roughly 3 cd/m2, where response of visual system is dominated by *cone photoreceptors* and observer get fine resolution of details and color vision. But in contrary of the above state, *scotopic vision* happens at luminance values less than 0.001 cd/m2, where eye response is dominated by *rod photoreceptors* and the observer get only shades of grey and color is not perceived. Moreover, *mesopic vision* states are happened at intermediate luminance values between photopic and scotopic vision states (between 0.001 cd/m2 to 3 cd/m2). In this state, both the cone and rod photoreceptors are active [13]. In road lighting scenarios, the visual system works at the boundary of the photopic and mesopic states [14]. For information, there exists 6-7 million cone and 75-150 million rod photoreceptors distributed across the surface of the retina of human eye. If the relative spectral sensitivity curve for both the cone and rod photoreceptors are examined, then it can be seen that cone or photopic curve peaks at 555 nm and rod or scotopic curve peaks at 510 nm. That means at night time our eye's sensitivity shifts towards shorter wavelength or bluish region. Relative spectral sensitivity curve for both the cone and rod photoreceptors are given in Fig. 1.2.

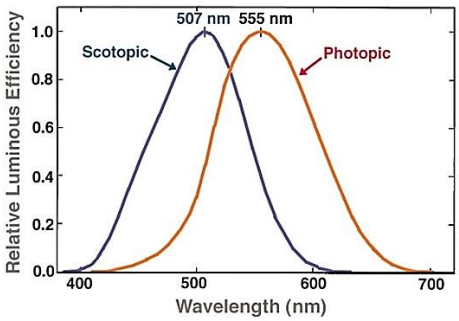

Fig. 1.2: Relative Spectral Sensitivity Curve for Photopic and Scotopic Vision

1.2.2. The second sub-portion describes various lighting parameters used in the experimentations, described in this thesis, to optimize the LED street lights human centrically. They are stated in a simplified manner to ease the reading process. *Light emitting diode* or LED is a type of solid-state lighting and is used in street light *luminaire*

for its controllability, reduced energy consumption and long life with better *efficacy*. A *luminaire* refers to a complete and functional lighting system, comprising the lamp, housing, power circuitry for operation, and control elements to direct and enclose the lamp housing. *Luminous energy* is the radiant energy perceived visually, traveling as electromagnetic waves, and is measured in lumen-seconds (lm-s). *Luminous flux* represents the rate of flow of luminous energy over time, measured in lumens (lm). *Luminous intensity* indicates the density of luminous flux in a specific direction per unit solid angle, expressed in candelas (cd). *Luminance* refers to the luminous flux per unit of projected area per unit solid angle emanating from a particular point in a specific direction, measured in candelas per square meter (cd/m^2). Illuminance is defined as the luminous flux incident on a small surface per unit area, measured in lux. *Luminous efficacy* is the ratio of total luminous flux emitted by a light source to the power input, measured in lumens per watt (lm/W) [15]. The *correlated color temperature* (CCT) of a light source indicates the temperature of a Planckian radiator whose perceived color most closely resembles that of the light source under the same brightness and viewing conditions, measured in Kelvin (K). The *color rendering index* (CRI) evaluates the ability of a light source to accurately reproduce the colors of objects compared to a reference or standard light source. It reflects the illuminant's effect on the color appearance of objects, whether through conscious or subconscious comparison.

1.2.3. The third sub-portion describes three human centric parameters used in the experiments to examine the visual and non-visual impacts of lighting parameters from an LED light source on a stationary human observer. These three parameters are chosen depending upon previous experimentations done by other researchers [17 – 20]. These three parameters strongly evaluate the human perception and ability to detect an object under various lighting conditions. They are *reaction time* (RT), *visibility level* (VL) and *small target visibility* (STV). *Reaction time* or *response time* is typically the time between a presentation of stimuli (visual or auditory) and a discrete response, which is created by the stimuli, given using a response key [21]. That means it is the necessary time required to identify the stimuli, to decide a particular action and to initiate the action by using particular muscles [22]. Dr. Ing W Adrian described the *STV method* or *VL calculation* method and the effect of before said parameters in his paper and gave the formulas for calculation of VL. *Quantified visibility parameter* or VL is a complex unit less metric, which mainly follows Ricco's law and Weber's law, and depends upon luminance difference between object and background, exposure time or reaction time, age of the observer, nature of contrast (positive or negative), glare [23]. IESNA-RP-8–00 described the very method of *STV calculation* easily and gave us the formulas we needed [24]. Moreover, two other methods are also undertaken in the experiments, which are behavioral study and electroencephalogram or EEG based study to measure the human perception and human brain's temporal procedures under lighting scenes. From behavioral studies, scores are assigned for experimented lighting conditions to find the best suited scene for proper object detection. From EEG based study relative logarithmic spectral power vs frequency and event related potential (ERP) plots are plotted and various features are extracted from that.

1.2.4. The last sub-portion talks about two specific dimming techniques named as pulse width modulation (PWM) and beam angle switching (BAS) methods. PWM dimming technique can be referred as vanguard in the field of dimming. In this method light output of a LED can be changed by feeding the LED with a pulsed dc current with variable duty cycle. Besides, in PWM method junction temperature of a LED does not increase fanatically unlike other dimming method and for that reason lifetime of the LED increases [25-31]. On other hand several studies on BAS method and the visual and non-visual effect of lighting parameters on human reaction times clearly indicates that the BAS enabled LED street lights provide extra illuminance on street. The BAS method enabled LED street light has three lighting conditions. The “FULL GLOW”, “PRO” and “COUNTER” states of the light beam are the three lighting conditions. The "FULL GLOW" state means that all of the LED clusters are turned on to provide the maximum amount of light from the specific luminaire. When the luminaire's single LED array is turned on in the direction of traffic under “PRO” control, light output is reduced to about one-third of its "FULL GLOW" state, lowering energy usage. The “COUNTER” state is identical to the "PRO" state, but it directs the light beam in a direction, where it opposes the flow of traffic [32]. Graphical representation of BAS is given in Fig. 1.3.

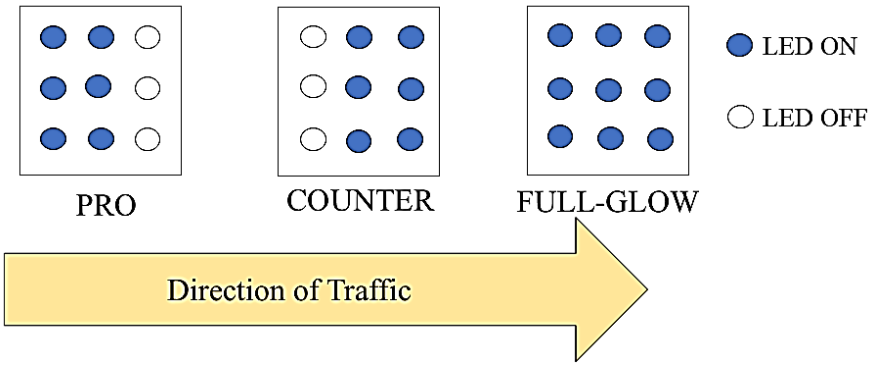

Fig. 1.3: Beam Angle Switching Method

1.3. Background of the Work

Street lighting is a dedicated lighting application that focusses on object identification and human interactions in dynamic environments. It is essentially a public lighting system that remains operational for extended periods. Roads are used throughout the day by various types of users including drivers and pedestrians in diverse conditions. While the primary purpose of human is often object detection, the specific requirements vary depending on traffic composition during different times of the day. Object identification is the most important, complex and brain’s temporal process intensive job for a human driver as well as for pedestrians in a road. It is a necessary step and task for night time driving and accident avoidance [33-34]. Indian city roads, in particular, are characterized by mixed traffic. On major roads, pedestrians and bicycles are commonly seen, while small lanes may still accommodate motorized vehicles. A field study cum experimentation is conducted to assess visual performance at mesopic illumination levels in a driving context. Subjects drove a vehicle on a lighted street while performing a decision-making task involving off-axis target detection, using two types of lighting (ceramic metal halide (CMH)

and high-pressure sodium vapor (HPSV) lamps).The results showed that response times improved with increased unified luminance, but the study used outdated light sources and equipment, suggesting that modern LEDs and advanced technology could yield more accurate insights [20]. Reaction time under HPSV and MH lamps are measured and compared by He et. al. The experiment resulted that a higher S/P ratio (a ratio between the scotopic lumens the lamp produces and the photopic lumens) gave benefit to the drivers at a luminance level under approximately 1.0 cd/m2 [35]. Moreover, researches showed that VL plays an important role for object identification for drivers. Recent study showed that VL $\geq$ 7.0 ensured proper target detection [36]. This diverse research and their promising results force the need to examine both the visual and non-visual effects of various lighting parameters (like CCT) of LED, positioned at on-axis vision as well as at off-axis vision or peripheral vision, on object detection by static human observers as there is little to no work is done.

Furthermore, street lights in municipal area consumes a huge chunk of generated electrical energy. That's why, street lights are one of the primary sources of pollution, which contribute considerably in green-house gas and nuclear dust emission affecting road ecology badly. Electrical energy expenses, along with environmental issues, drive municipalities across the world to create systems to measure, analyze, and minimize energy usage in order to cut expenditure and maintenance costs.

Various researches show that implementation of dimming techniques like PWM dimming and newly innovated BAS method in smart street lighting systems can lower energy consumption further and increase the life span of the system [37-39, 32]. These findings kickstarts the research to amalgamate and optimize these dimming techniques in a system for further energy reduction.

Although, some research on object identification or visibility model includes various human factors like age or reaction time, the progress does not totally include direct effect of main and peripheral light sources' CCT on human brain temporal processes. That is why, the lighting scheme design for road does not evolve totally human centrically. Besides, the effect of CCT on human brain is also not quantified enough to convert the effect to an empirical parameter, which can be calculated for designing a lighting scheme on demand. That is why, it is the need of hour to re-define human centrism and smartness of LED light sources. For this reason, this thesis focuses on *electroencephalography* (EEG) and *galvanic skin response* (GSR) measurement of human under various lighting conditions, where the lighting parameters of LED, like CCT of main and peripheral light sources, are varied and EEG and GSR signals are acquired using proper reliable devices. Furthermore, an effort was made to quantify those effects to find a new parameter for lighting design of street lights. For information, *electroencephalography* or EEG is a method, where electrical activities, generally measured in microvolts, in various parts of human brain are recorded using some precisely positioned electrode over the scalp, which can also tell about the cognitive processing or load of the task given to the human participants [40]. In other hand, *galvanic skin response* or GSR, a form of an electrodermal activity, measures sweat gland activity, which reflects changes in skin conductance linked to the excitation of the sympathetic nervous system. Higher levels of electrodermal activity are associated with increased arousal, often indicative of heightened stress, fear, anxiety, or surprise [41].

All these points discussed above in this section forms the background of this research work or thesis, which offers an in-depth investigation into how smart lighting technologies influence both visual and non-visual aspects of human performance. By focusing on street lighting systems, it

provides valuable guidance for creating energy-efficient, human-centered lighting solutions that prioritize safety and visibility, while simultaneously minimizing energy consumption. The research emphasizes the importance of factors such as correlated color temperature (CCT), flicker, pulse-width modulation (PWM) dimming, and BAS method. These elements, when carefully optimized, can greatly enhance object detection, improve user satisfaction, and contribute to energy conservation. This work represents a significant advancement in the field of human centric smart street lighting and road safety, offering practical insights for urban planners and traffic safety professionals. The findings have the potential to drive future innovations in lighting design, with broad applications for improving urban infrastructure and public safety in cities worldwide.

1.4. Organization of the Thesis

Given the street lighting scenario of India as well as world, there exist a constant search for a smart human centric LED street lighting solution. The main focal point of this thesis is to define and design that. Besides, this thesis also tries to find out the visual and non-visual effects of various lighting parameters like CCT on objects recognition task by human observers to optimize the developed street light. Furthermore, it also tries to amalgamate two specific dimming techniques which will further reduce the energy consumption and reduce the carbon emission. Finally, this thesis proposes using electroencephalography (EEG) to evaluate human cognitive reaction for object identification tasks under various road lighting scenes.

Chapter 2 describes the what and why of human centric lighting in context of street lighting design. Besides, it gives a profound understandings and definition of human centric lighting. The chapter also talks about the advantages and disadvantages of it. Last portion talks about the experimental approaches and implementation of it in street lights.

Chapter 3 deals with the description of some laboratory developed instruments for experimentations. It describes, why these types of instruments are needed and how it is developed. First, it discussed about active shutter glass, then reaction time measuring device and last but not the least galvanic skin response measuring device.

Chapter 4 describes about the visual and non-visual effects of various lighting parameters of LED on object detection by human observer. The first half talks about the experimentation, which involves variation of CCT of on-axis or main source and off-axis or peripheral sources. The second half talks about the experimentation, which involves variation of CCT of on-axis or main source and variation of flickering frequencies of off-axis or peripheral sources. It also talks about temporal light modulations.

Chapter 5 is a heavy-duty chapter containing a novel approach. It actually finds the effect of CCT variations of on-axis or main source and off-axis or peripheral sources on human brain temporal processing and cognitive loads. It introduces electroencephalography or EEG and galvanic skin response or GSR for measurement of brain processing and mental and physical arousals.

Chapter 6 narrates the energy consumption reduction possibilities for LED street lights. It talks about two distinctive dimming techniques named as PWM dimming and BAS method. It tries to amalgamate these two techniques and attempts to study its effect.

Finally in Chapter 7, the thesis developed a smart CCT tunable human centric street light. It describes the understandings taken from the previous experiments and how it is implemented in the developed street lights. It talks about the three-point color mixing theory and its application in this context. It also talks about the developmental process.

Last but not the least, chapter 8 summarizes the current work and outlines the future scope of diligence.

1.5. Originality of the Thesis

Original contributions are given below in points-

- **1.5.1.** Defining the scope of research on smart human centric street lighting in India context by jotting down various experiments and doing extensive literature review.
- **1.5.2.** Defining a statistical coherency between on-axis and off-axis simultaneous CCT variation of LED light sources and object recognition capability of static human observer using reaction time measurements and behavioral study in a controlled environment.
- **1.5.3.** Defining a statistical coherency between on-axis simultaneous CCT variation and off-axis flickering frequency variation of LED light sources and object recognition capability of static human observer using reaction time measurements and behavioral study in a controlled environment.
- **1.5.4.** Development of three novel measuring devices in laboratory to measure various human centric parameters.
- **1.5.5.** Development of a machine learning based R-G-B measuring device.
- **1.5.6.** Defining proper switching frequency for PWM dimming technique to maintain CCT value.
- **1.5.7.** Validating BAS method using a laboratory developed wireless continuous luminous flux measuring device.
- **1.5.8.** Defining the energy saving capacity of BAS method in an Indian University campus using a precise case study.
- **1.5.9.** Developing and designing EEG and GSR techniques to measure the cognitive processing when object detection tasks is given to the human observer under certain lighting condition.
- **1.5.10.** Development of a smart CCT tunable BAS enabled human centric LED street light luminaire.

Chapter 2: Human Centric Lighting

2.1. Introduction

Lakhs and crores of people in India as well as all over the world spend a huge time every day in road. Crucial things like transportation of goods, economy, mobility, healthcare etc. are very much dependent on the proper roadway connectivity. Electric street lighting is provided to the street to make sure that they can identify any obstacles or other moving objects like pedestrians quickly during night-time. That means, the scope of street lighting has an enormous impact on economic growth of a country beyond the cost of designing and erecting street lights, which implies a proper street lighting and development of street lighting condition and technology can further affect the whole system positively. Introduction of intrinsic photosensitive retinal ganglion cell (ipRGC), a specialized photoreceptors in the human retina, by Dr. David Berson and his colleagues at Brown University in 2002, opens a new plethora of lighting research to increase the chance of moving or static object detection on the roads by drivers. Unlike two major retinal photoreceptors (rods and cones), who are largely accountable for image formation, ipRGCs detect ambient light, notably in the blue spectrum, at around 480 nm. This sensitivity enables ipRGCs to hold a major role in non-visual processes such as circadian rhythm regulation, pupil response, and mood management. They do this by delivering signals directly to the brain's suprachiasmatic nucleus (SCN), where it is responsible for maintaining human being's internal clock, as well as other regions related with alertness and sleep control [42-43]. This ipRGCs function as slow-reacting light sensors, meaning that the variables influencing the state of the SCN include the intensity and spectrum of light reaching the human retina, along with the timing and duration of exposure [44]. This means, optimization of street lighting, if possible, according to the responses of non-image-forming visual process can benefit rapid object detection and obstacle avoidance. This chapter describes about this correlation between light and human being explored till date to better understand this thesis.

2.2. Definitions and Understandings

To understand the experimental works done in this thesis related to human centric lighting, some definitions must be discussed. Light can affect human efficiency and performance in three ways. The first way is through visual system of human being, second one is by affecting circadian rhythm of human body and last but not the least by mood and motivation. Fig 2.1 depicts a skeleton for understanding the elements, which impact development along each path and their interconnections [44].

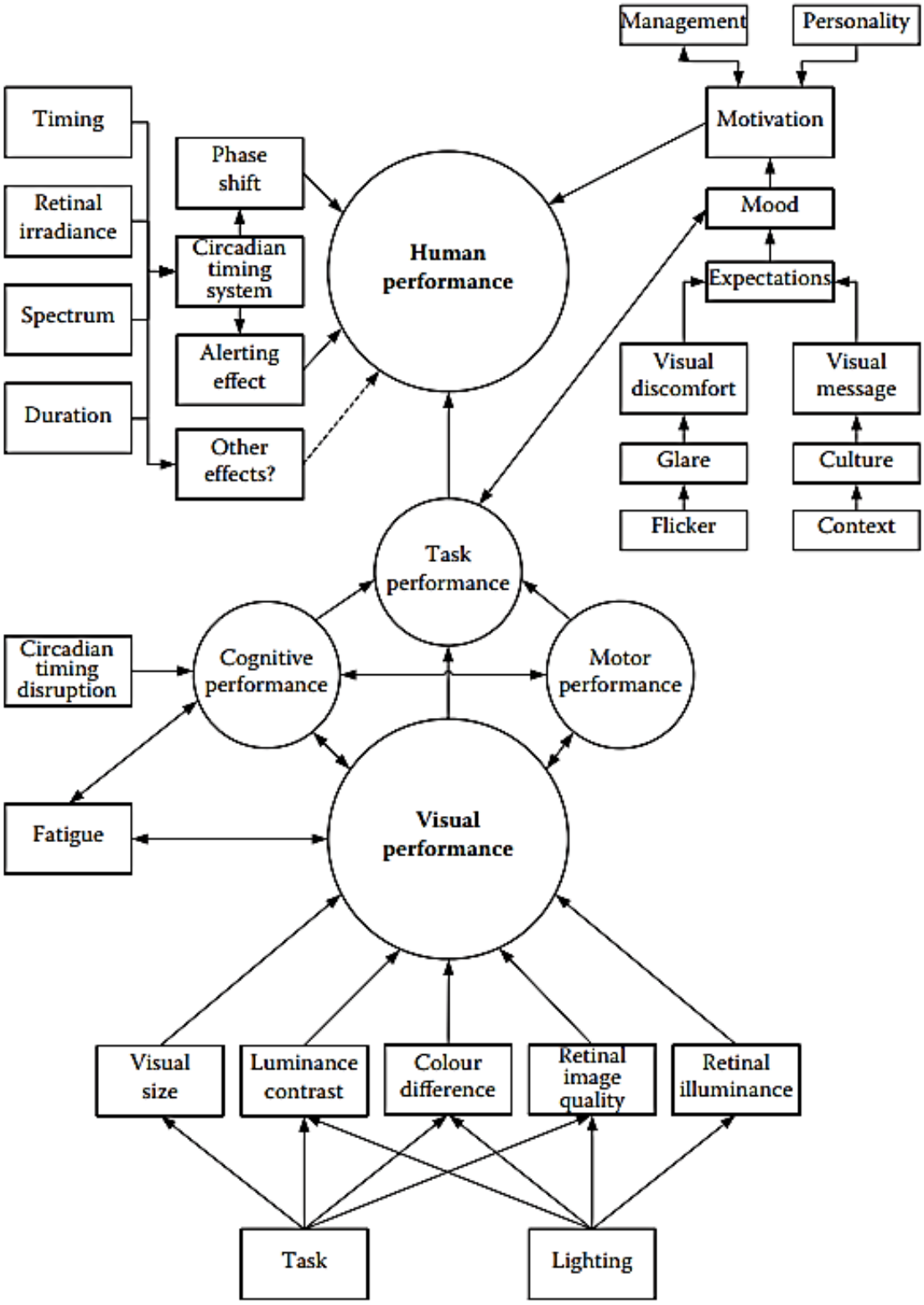

Fig. 2.1: A skeleton outlining the three pathways through which lighting conditions can impact human performance. The arrows in the diagram represent the direction of these effects.

The most evident impact of lighting on humans occurs via the visual system, which serves as an image-capturing and processing mechanism. The eye's optics focus an image of the external environment onto the retina, where preliminary image processing happens. Different aspects of this retinal image are conveyed to the brain's visual cortex through specialized pathways or channels. The visual system is also spatially divided: the retina's central area, the fovea, is responsible for capturing fine details, while the periphery acts as a detection system, guiding the fovea's direction within the visual field. In bright conditions, such as daylight, the entire retina is active, whereas in low-light situations, like a dark night, the fovea becomes inactive, and only the peripheral retina functions and the image losses its color and texture. Any object presented in front of human eye can be categorized by five parameters and they are *visual size*, *luminance contrast*, *color difference*, *retinal image quality* and *retinal illuminance*. They validate up to which extent stimulus is detectable and identifiable. *Visual size* for detecting a stimulus is the solid angle, subtended by the stimulus at human eye. It is the ration of areal extent of stimulus and the square of the distance from the viewers' perspective. The *luminance contrast* of a stimulus represents its brightness relative to the surrounding background. Higher luminance contrast makes the stimulus easier to detect. *Luminance* measures the quantity of light emitted from the stimulus, without considering the spectral power distribution of the emitted light. However, the specific combination of wavelengths in the light significantly influences stimulus identification. A stimulus can be detected and identified in spite of zero luminance contrast due to the differences from the background color. This is called *color difference*. *Retinal image quality* totally depends upon the spatial frequency distribution of the stimulus. A sharp image produces better retinal image quality, where the stimulus must have high spatial frequency distribution and vice-versa. The level of illuminance on the retina or *retinal illuminance* influences the visual system's adaptation state, thereby affecting its overall performance and capabilities. The net amount of light, which enters into eye and fall upon retina, is primarily fixed by the luminance in the field of view. Visual tasks consist of three main parts: visual, cognitive, and motor. First one involves gathering information needed for the task through vision. Second one is the elucidation of sensory input to decide on the necessary actions. Finally, the third one is the procedure of interacting with the stimuli to gather information or to execute the chosen actions. The best suited and deterministic parameter to see whether the visual system is working efficiently or not is *reaction time*.

Another way by which light plays its importance, is by manipulating the non-visual system of human being. One side of this system, which have proven effects on human performance, is *circadian rhythm* or *biological clock*. The most important evidence of this rhythm is sleep-wake cycle of human being, which is governed by various manipulations between hormones inside human body over a 24-hour period. Melatonin and cortisol hormones have profound effect to that. Suprachiasmatic nucleus or SCN, which is directly linked to ipRGCs of human retina, controls this rhythm in human body. There exists two ways to improve the task performance of a human being by using light through this system. They are: *phase shifting effect*, where the phase of the circadian cycle can be enhanced or slowed up by exposing human being to bright light at certain times [45] and *suppression of melatonin hormone* at night to increase the alertness level [46]. Interestingly, it falls under the purview of this thesis to find if lighting parameters like CCT can affect the phase shifting. Research shows that exposure to high light levels shortly after waking

can increase cortisol levels, though the effects on cortisol for the rest of the day remain uncertain [47]. In one study, participants exposed to 5000 lux between noon and 4 PM showed no changes in cortisol levels but did experience increased alertness [48]. Similarly, another study found that early afternoon exposure to daylight exceeding 2000 lux boosted alertness [49]. These findings suggest that both physiological and psychological factors contribute to levels of alertness. There exist many aspects of this system, which needs further study. A small try to add some exploration to this vast knowledge pool is done by this thesis.

The last route by which light can alter the work performance of a human being is through altering mood and motivation of that particular human being. The visual system creates a visual sensation about the world in the field of view of human observer and that visual sensation about the world can trigger emotional responses and can alter the mood and motivation for doing a specific task. Lighting can impact mood and motivation by creating visual discomfort, especially when it hinders visual performance or causes distractions, like glare or flicker. However, lighting also conveys messages about its designers, users, and environment. People interpret these messages based on context, culture, and expectations, sometimes finding meaning in the design that can outweigh any physical discomfort it may cause [44]. Another experimentation is also done in this thesis to identify the non-visual effect of flickering of peripheral sources on stimulus identification task.

All these recent developments push the whole idea of lighting design into a new era. A new term surfaced in research zone that – the *human centric lighting* (HCL) concept. HCL revolves around a holistic approach to light and illumination, considering them as factors influencing visual, biological, and behavioral responses in humans. It integrates both the visual and non-visual effects of light on individuals. It is a way of illumination, which promotes and revolves around human mood, well-being, and health. It can also be called as human factors in illumination. Light is the primary stimulus for human biological clock. As discussed before in this chapter, HCL incorporates several aspects or factors in it. Some of them are circadian rhythm, mood, visual acuity, perception, energy saving and sustainability, productivity, and performance. The guess is that some new aspects will also join the mentioned list in near future. Although HCL or dynamic lighting or circadian lighting are marketing term. Variation in spectrum or illuminance or both over a 24-hour day are the common feature of these luminaires. It can be predicted easily that HCL with daylighting and smart LED systems will become the future aspects of lighting technology in upcoming years [11-12].

2.3. Advantages and Disadvantages of HCL

HCL combines the visual and non-visual responses of human being to improve human well-being, and its performance. It can be divided into three aspects:

1. Visual benefits: good visibility, visual comfort, and safety.
2. Biological benefits: alertness, concentration, deep and stable sleep wake cycle, cognitive Performance.
3. Emotional benefits: improved mood, relaxation, and impulse control [50]

In contrary of these advantages, the main disadvantage, which it can face, is incorporation of vast human perception towards a specific lighting scene. It may lead to ambiguous street lighting design. This means that a specific lighting scene may be best for a particular driver for its object

identification task but the same lighting scene may create hindrance towards another driver, because perception about the lighting plays a major role in this context.

2.4. Experimental Approaches for Human Centric Lighting

For proper identification of the correlation of the above-mentioned pathways and to explore the visual and non-visual effect of a specific lighting scene on stimulus identification some experimentations are done in this thesis. These experiments follow some specific set of approaches to quantify the acceptability of a specific lighting condition based upon visual and non-visual effects. Over the past 50 years, numerous studies have investigated human work performance under various lighting conditions. These approaches are generally evaluated using two key quality parameters: face validity and generality. Table 2.1 illustrates how these studies can be interpreted from the perspectives of face validity and generality.

Table 2.1: The evaluation criterion for human factors in lighting

Type of approaches	Face Validity	Generality
Real Task Studies	High	Very Low
Laboratory Simulation based studies	Moderate	Low
Scientific technique for development of models	Low	Very High

Evaluating a lighting installation from the perspective of human acceptance is crucial. This assessment can be approached in three ways: (i) subjective judgment through measurements of human centric parameters (RT, VL, STV) with statistical data analysis, (ii) behavioral studies coupled with statistical analysis using questionnaire, and (iii) an innovative approach combining physiological studies like electroencephalography (EEG) and galvanic skin response (GSR) with behavioral studies.

Subjective judgment, commonly used in prior research, involves collecting feedback on lighting installations and analyzing the data statistically [51]. However, this method often faces issues like bias in subjective responses and the generality of questionnaire designs, which can limit accuracy. Behavioral studies address this by having subjects perform tasks, such as object detection, to gauge response under specific lighting, though biases and experimental design challenges still persist [18-19, 51-53].

On the other hand, the new method integrates physiological studies like EEG and GSR with behavioral studies to assess lighting effectiveness based on neural responses and electro dermal activity (EDA) to real-world stimuli. While EEG captures detailed neural data, potential interference from unrelated stimuli suggests that combining EEG with behavioral data may yield the most reliable and unbiased results. In this thesis laboratory-based studies are chosen to explore the visual and non-visual effects of LED street lighting.

Chapter 3: Developed Instruments for Lighting Experiments

3.1 Background

Human-centric lighting embodies a comprehensive approach to understanding light and lighting as light has influences on human visual, biological, and behavioral responses. This concept is expansive, acknowledging the wide variety of effects of light on human being, both visual and non-visual. Some reactions occur instantly, like pupil dilation or glare perception, while others, such as mood changes, may develop over hours. Additionally, certain negative health effects may take years to become apparent. Additionally, responses to light can span physiological, perceptual, psychological, and behavioral domains. Optimally, HCL is designed to evoke a targeted set of visual, biological, and behavioral outcomes that are considered beneficial for the intended users. In essence, this has always been the hallmark of effective lighting. However, as understanding deepens regarding light's influence on non-image-forming responses, the illumination researchers and industry are encountering a broader spectrum of considerations, explorations, experimentations and responsibilities. Fundamentally, HCL represents a vision for lighting solutions that promote positive human responses [12]. In the future, lighting will need to shift from fixed or standardized designs to adaptable systems that can align with diverse lifestyles and accommodate the circadian rhythms of various age groups, keeping the findings of experimentations done in the field of human centric lighting in mind. Lighting tailored to individual needs is anticipated to become prevalent over the next century, fostering a more productive, safe, and healthy living environment. Advancements in information technology, particularly through the Internet of Things (IoT) and advancement in embedded systems, hold promise for automated lighting control that benefits not only human lives but also the broader ecosystem [54]. This whole scenario of visual and non-visual effect of lighting on human being indicates that there exists a huge possibility of new explorations and experimentations in this domain. Implementation of these findings in lighting designs including indoor and outdoor is the second most priority in the list after the quest for new knowledge. Being the main agenda of this thesis, based upon these findings, street lighting, should be optimized and controlled.

To explore the visual and non-visual effect of LED, researchers from all over the world are extensively doing experiments on human participants. It has already been found that light has direct biological effects on people, influencing pupil size, immediately suppressing melatonin, and impacting levels of alertness, body temperature, and heart rate. It also holds a role in regulating the timing of circadian rhythms [55-63]. It is universally a truth that this type of

specialized experiments needs specialized equipment to measure any valuable data. Along with the classical devices like luxmeter, luminance meter or colorimeter, maximum experiments demand some new devices which can measure a parameter of researchers' need or interests. After careful review, considerations and reciprocations, some characteristics of these devices can be set and they are –

A. The device should be portable and easy to handle, allowing it to be used in various locations of interest for lighting experiments.
B. The device should be robust and durable to ensure it lasts throughout the entire experimentation period.
C. The cost of the device should be low.
D. The device can be quickly and easily remade if the previous one malfunctions.
E. If the device is wearable, it should not interfere with tasks assigned to human participants. This means it must be lightweight, fit properly, and avoid causing any psychological discomfort.
F. Lastly, the device must be energy-efficient, ideally powered by a battery or a 5-9 volts DC adapter.

As discussed in this chapter and Chapter 2, first the visual and non-visual effects of various lighting parameters of a LED on human being are needed to explored. This thesis focuses on the effects created by outdoor lighting, specially by street lighting on human drivers and pedestrians. Specialized experiments are conducted in the Laboratory of Illumination Engineering, part of the Electrical Engineering Department at Jadavpur University in Kolkata, India, to evaluate these effects. Because of the before-mentioned specialized experiment's nature, some unique devices are developed in this same laboratory to measure various physiological or human centric parameters as well as lighting parameters.

3.2 Developed Instruments

To perform some specialized experimentations, which are described later in this thesis, some devices have been developed in the laboratory. These devices can be broadly divided into two sections. One is human centric parameter measuring devices, which are described in the first three sub-headings and the other one is lighting parameter measuring devices, which are described in the last two sub-headings. They are as follows.

3.2.1 ***Special Active Shutter Glass*** – This is a modified active 3D shutter glass, available in the market. It uses a technique that displays stereoscopic 3D images by rapidly alternating between the left-eye image and the right-eye image, blocking opposite eye during each presentation. This swift alternation prevents interruptions, allowing the images to fuse into a cohesive 3D perception. The lenses of this type of glasses are made of LCD (liquid crystal display), where by applying a small voltage, the lenses can be made opaque. This blocking action of the glass lenses is used for the special device. Here, the internal control circuitry of a standard active 3D shutter glass is removed and substituted with a custom laboratory-built control circuit. This setup allows the lenses to turn transparent for 0.7 seconds when

a push button is pressed, after which they return to their default dark state. This low-cost handy device is very light weight and properly fits on human eye. It is operated by a 9 Volts battery. The hardware of the control circuit consists of a 555 timer and a MC14069 hex inverter. Detailed pictorial depictions of the control circuit and the device are given in Fig. 3.1 (a) & (b). The primary purpose of this special active shutter glass is to regulate the exposure time for human participants, who participated in an object detection task under certain lighting condition. Studies indicate that a minimum exposure duration of 13-100 milliseconds is required for the average person to recognize objects [64]. The active shutter glass, however, provides a 700-millisecond exposure, which exceeds this threshold, allowing ample time for object recognition and identification. Furthermore, this device is integrated with a microcontroller-based Arduino controlled reaction time measuring device, and activation is achieved through a manually operated push button. This mechanism transitions the lenses from an opaque to a transparent state and back to opaque after 700 milliseconds, allowing clear visibility of grid points positioned at approximately a 2° eccentricity angle for the duration of exposure.

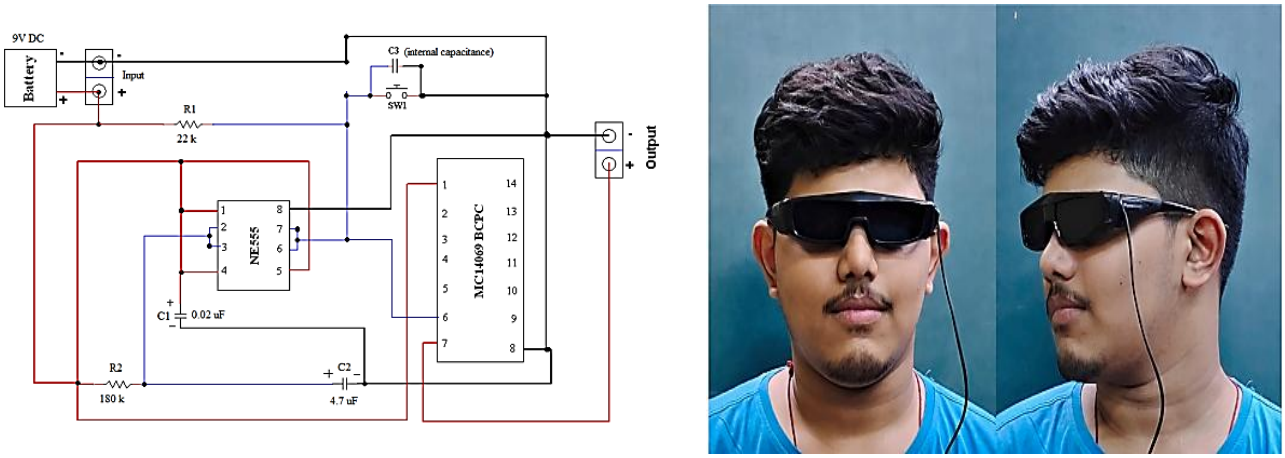

Fig. 3.1(a)&(b): Control Circuit and Actual Photo of a Special Active Shutter Glass

3.2.2 ***Reaction Time Measuring Device*** – It is a compact, microcontroller-based timing device, controlled by an Arduino UnoR3. It is developed to measure the reaction time (RT) of human participants during experimentation. The recorded reaction time is displayed on an attached 16x2 LCD screen on the back side of the plastic box, to avoid direct glare from display towards the subjects' eye. All components, including the Arduino circuit, LCD display, and wiring, are enclosed in a portable plastic casing. This device operates on a 9V battery and can record time stamps in milliseconds. The timer starts upon activation by a researcher, while the participant independently stops it. All actions are controlled via push buttons. The microcontroller is programmed in such a way that, when the researcher presses the button, a highly precise millisecond-level stopwatch is activated. Simultaneously, the shutter glass becomes transparent for 700 milliseconds, allowing the observer to view the scene ahead. After this period, the glass returns to an opaque state. During the transparent phase, the observer can attempt to recognize objects placed in the field of view. Once

observer identifies an object and presses their button, the stopwatch stops, and the recorded reaction time is displayed on the attached LCD screen. Proper pictorial representation is given in Fig. 3.2 (a). Previously, special active shutter glass and reaction time measuring device worked like two separated devices, where they are used in conjugation and named as reaction time measuring compact device (RTMCD), but later another device was developed where these devices are merged, where the circuit for active shutter glass is eliminated and control of the glass is handed over to the Arduino Uno microcontroller, to form a better rugged device and named as reaction time measuring device v2.0 (RTMD v2.0). A pictorial representation is given in Fig. 3.2 (b). Used Arduino IDE codes for these devices are given in Annexture 1.

Fig. 3.2 (a)&(b): RTMCD and RTMD v2.0

3.2.3 ***Galvanic Skin Response Measurement Device*** – It is an Arduino Uno-based device, which was developed in the laboratory to measure electrodermal activity (EDA), also known as galvanic skin response (GSR), during object recognition tasks involving static participants. The device utilizes a Seed Studio Grove GSR sensor, which operates at 3.3 or 5 volts and offers adjustable sensitivity. Previous research suggests that low-cost GSR sensors like this can provide sufficient accuracy for such experiments, acting as a less expensive replacement for high-priced commercial devices [65]. During the experiment, participants wear two nickel electrodes embedded in finger bands, placed on adjacent fingers, to capture GSR signals throughout the task. These electrodes are connected to the sensor, which measures the electrical resistance between them and converts it into an analog signal. The recorded data is saved onto a microSD card as a '.txt' file for later analysis. Additionally, a 5mm blue LED is embedded in the device to indicate successful and error-free data recording on the microSD card. All the circuitry of this device is embedded in a single hard plastic box to make it robust. This device is powered by a 9 volts DC adapter. Pictures are given in Fig. 3.3 (a) & (b).

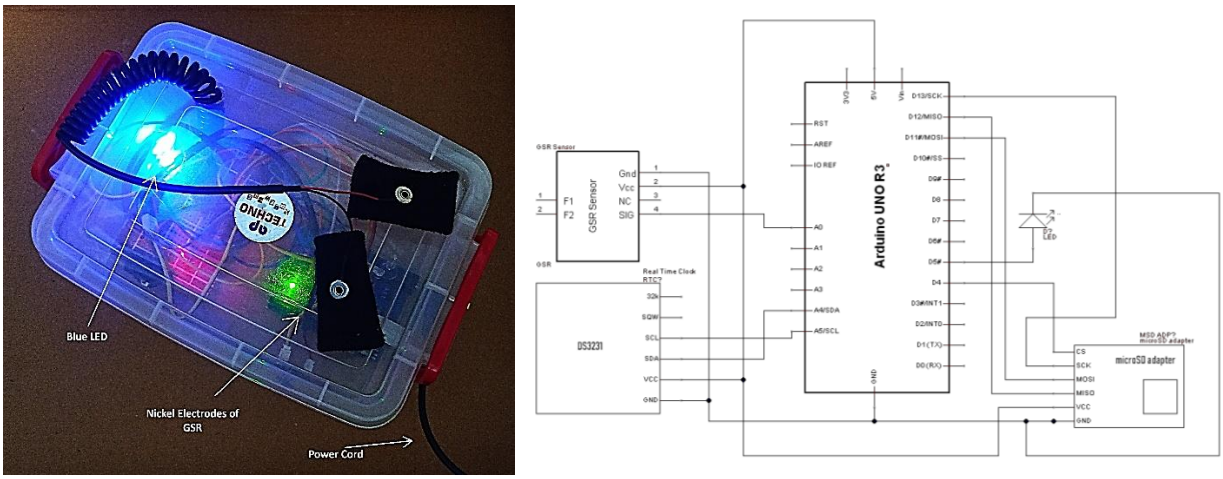

Fig. 3.3 (a)&(b): Actual Photo and Control Circuit of GSR Measuring Device

3.2.4 ***R-G-B Meter*** – This low-cost measuring device is designed to capture CIE 1931-compliant RGB values for various CCT settings selected by the user through an application. It is built using a compact cardboard box, with a TCS3200 color sensor from TAOS and a 128x32 OLED display mounted on its top surface. The device operates with an ESP32-WROOM-DA microcontroller module, which receives RGB readings from the color sensor and displays them on the OLED screen. The microcontroller is powered by a 5V 2A DC adapter. To minimize fluctuations in the RGB measurements, the microcontroller calculates the average of 100 consecutive readings and presents the averaged result on the display. To ensure optimal sensor performance, both the internal and external surfaces of the device are painted with a deep black color to eliminate the influence of stray or reflected light. Additionally, a small hollow cylinder of 1 inch made of black paper is positioned over the sensor to ensure it only receives direct light from the CCT-adjustable light source. It can be implemented with the street lights to produce feedback about the CCT values produced by the lights with respect to the input CCT values given by the users. Pictorial representation is given in Fig. 3.4.

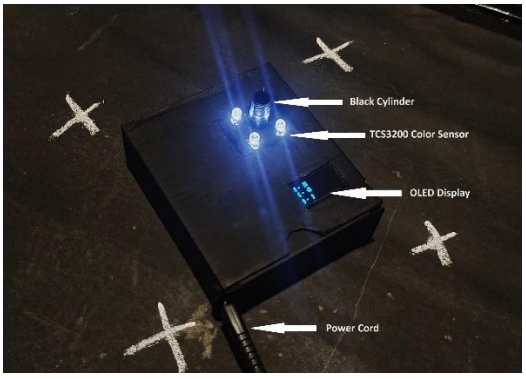

Fig. 3.4: R-G-B Meter

3.2.5 ***Lumen Maintenance Testing Device*** - The developed prototype system consists of two main parts: the *Measuring Sphere (MS)* and the *User Interface and Storage Device (UISD)*. These two parts communicate wirelessly through a low-power wide-area network (LPWAN) using a LoRa 02 module. Each component has its own microcontroller, both implemented using Arduino Uno Rev3 boards. The MS, made of steel, incorporates two sensors: a BH1750 FVI illuminance sensor, positioned at the bottom of the sphere, and a DHT11 temperature and humidity sensor, which is attached to the base of the LED bulb during testing. The control circuit of the MS, containing the microcontroller and the LoRa 02 module, is mounted on the outer wall of the sphere. All sensors and circuitry are secured using heat-resistant tape and housed within a transparent protective box. The test LED light is placed in the center of the sphere, held by a thin steel rod attached to the upper dome's interior. To scatter light through multiple reflections, the inner surface of the sphere is coated with a mixture of barium sulfate and magnesium oxide, exhibiting an 82% reflectance. This diffusion eliminates spatial information, ensuring uniform light distribution, which allows accurate measurement of total luminous irradiance or power emitted by the LED. The outer surface of the sphere is painted plain white. For temperature regulation and power supply, the MS device features three air circulation holes, which can be sealed once connections are completed to maintain proper isolation. Users can control the LED operation, either setting it to turn on and off at specific intervals or keeping it continuously on. Both AC and DC power sources can be used. A detailed photo and schematic block diagram of the MS device is provided in Fig. 3.5 (a) & (b). The UISD's control circuit also uses an Arduino Uno Rev3 microcontroller and includes a low-budget, precise real-time clock module (DS3231) for timestamping data. Additionally, it features a microSD adapter with a microSD card for data storage and a LoRa 02 module for communication with the MS device. A detailed photo and schematic block diagram of the UISD device is provided in Fig. 3.6 (a) & (b).

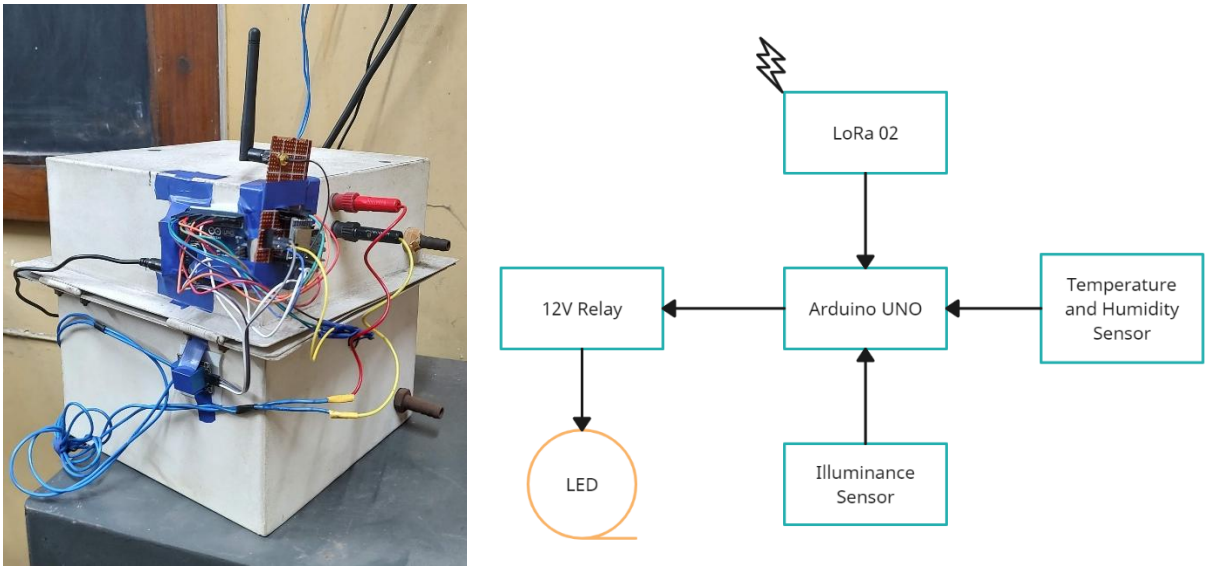

Fig. 3.5 (a)&(b): Actual Photo and Block Diagram of Measuring Sphere

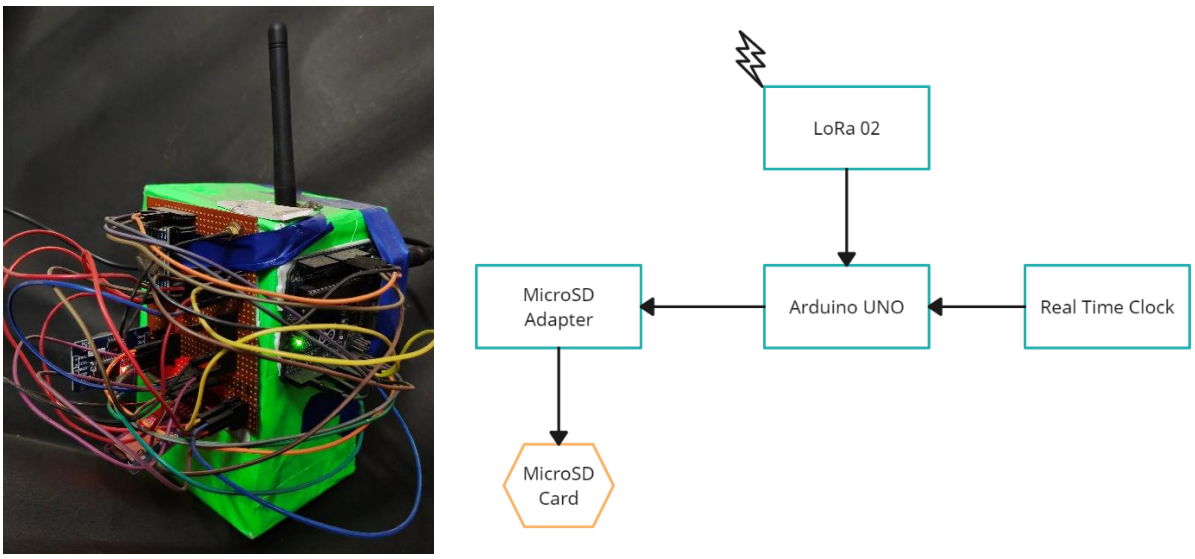

Fig. 3.6 (a)&(b): Actual Photo and Block Diagram of User Interface and Storage Device

Chapter 4: Effect of Lighting Parameter and Temporal Light Modulation on Object Detection by Human Observers

4.1 Introduction

Road traffic accidents are a global health crisis, responsible for the deaths of over a million individuals and tens of millions of injuries each year, particularly during night-time when visibility is compromised. Astonishingly, road traffic injuries rank as the ninth leading source of disability globally as of 2000, according to World Health Organization data [4]. In India, which leads the list of 199 countries in terms of road accident fatalities, road accidents account for 11% of all crash-related deaths worldwide. Between 2005 and 2019, the number of road traffic fatalities in India increased dramatically by 59.1%, reaching 151,113 deaths in 2019 [5]. This alarming rise underscores the urgent need for enhanced road safety measures, especially in terms of lighting infrastructure on Indian roadways. Research consistently highlights that night-time driving poses unique risks due to limited visibility, as visual factors play a significant role in accident occurrence, previously discussed in chapter 2. A case study conducted in Tamil Nadu in 2014 found that visual factors were responsible for 47% of road accidents, with lighting and visibility playing the most critical roles [66]. Properly designed road lighting, therefore, is vital in ensuring driver and pedestrian safety by providing clear, comfortable, and accurate visibility during night hours. Such design not only decreases accident rates due to improved visibility but also provides benefits to economic, social, and safety development. These include improved law enforcement capabilities, traffic flow management, increased safety for users, and extended commercial activity by making public spaces more accessible at night [24].

In the context of lighting design and standards for street lighting, a range of country-specific guidelines exist globally. In India, standards such as IS-1944 part I and II, IS-1944 part – III, IV, V, VI and VII and IS-9583.1981 set the parameters for road lighting design [67]. Internationally, standards like CIE 140-2000 and IESNA-RP-8-00 offer rigorous benchmarks for optimal road lighting design, emphasizing metrics that correlate directly with driver visibility. Historically, older standards prioritized illuminance levels at road pavements as the primary design criterion. However, recent studies show that luminance values from road surfaces correlate more effectively with drivers' visibility and object recognition capabilities, leading most modern standards to adopt luminance-based criteria for lighting design [24, 68-69]. One key metric, introduced for evaluating night-time visibility on roads, is Small Target Visibility (STV), developed by Dr. Ing W. Adrian. STV quantifies the difference between an object luminance and its background luminance, providing a robust measure of visibility for drivers. Since its

introduction, STV has been adopted by numerous road lighting standards as a critical design parameter [23-24]. Additionally, research indicates that both chromatic and achromatic stimuli can influence luminance sensitivity, which can be evaluated through reaction time [21, 70].

In parallel, effective identification of oncoming or roadside objects is a crucial visual task for drivers, influencing their decision-making processes and potentially preventing fatal collisions. Any failure in object identification or decision-making accuracy can lead to catastrophic accidents. Studies indicate that low- and middle-income countries includes over 90% of road accidents, where accident-related deaths are anticipated to become the third-largest contributor to the global disease burden by 2020 [71]. It has been estimated that proper street lighting could reduce nighttime fatalities by 65% and injuries by 30% [72]. In an experimental study, it is seen that these night fatalities were reduced through adequate street lighting, highlighting the crucial role that effective lighting plays in mitigating road safety risks [73]. Rockwell's research showed that enhanced street lighting results in early object detection, controlled speed, and more responsive braking [74], while a multi-year study on Philadelphia roadways demonstrated a significant drop in night-time accidents following street lighting modernization [75]. With the adoption of improved street lighting standards, nighttime crashes could decrease by up to 36% [76]. A recent review consolidates these findings, reinforcing the link between traffic injuries and lighting, and further confirming that quality lighting systems can substantially reduce accident rates, as already discussed in the first phase of this section [77]. Furthermore, beyond visibility, other factors like bad weather, poor road conditions, and substandard lighting design exacerbate road risks. One of the major factors is temporal light modulations (TLM) [78]. It corresponds to any quantifiable fluctuations or variations in light intensity or spectral distribution that occur over time. These modulations may occur at various frequencies. In other hand TLM can cause various visual and non-visual discomfort to the human observers including starting form visibility to serious health hazards like epilepsy. Temporal light artefacts (TLA) are the effects of TLM on human being. Temporal Light Artefacts (TLA) such as glare or flicker or phantom array effect are particularly detrimental, leading to visual discomfort, reduced performance in visual tasks, and potential health concerns for drivers with conditions like photosensitive epilepsy [79-83]. TLAs such as flicker, which occurs within a frequency range of a few Hz to 80 Hz, can be a significant source of irritation [84]. These artefacts arise from fluctuations in voltage or product characteristics and are commonly found in road and vehicle lighting systems, particularly when peripheral flickering sources are present, impacting the driver's line of sight. CIE describes TLA as an undesirable change in visual perception for an observer in certain surroundings, which a light stimulus whose brightness or spectral distribution swings over time might cause [85]. In road lighting scenarios, flickering lights, often from street lights or car headlights, tend to be located in the driver's peripheral field. Studies show that flicker in the peripheral view increases reaction times and affects object recognition. It was also observed that when bright and dark bands appear periodically in the driver's peripheral vision for 20 seconds at frequencies ranging from 4 Hz to 11 Hz, a flicker effect can occur [86]. De Lang further demonstrated that the perception of flicker depends on the shape of the light fluctuation waveform [87]. There is very limited documentation on the effects of this type of hazard (peripheral flicker) on drivers, and standards or guidelines addressing limits on peripheral flickering are also largely absent.

To mitigate these knowledge gaps in Indian context two experiments are done in a controlled environment at the Illumination section laboratory of Electrical engineering department of Jadavpur University. The first experiment explores the effects of varying correlated color temperatures (CCTs) on human participants' reaction times and visibility levels for object recognition tasks. The experiment utilized a CCT-tunable LED as the primary light source, with two peripheral LEDs also capable of CCT adjustment. Reaction times were measured under different CCT combinations of the primary and peripheral sources to investigate the effects of CCT on visibility and object recognition. Findings suggest that CCT is indeed an influential parameter, affecting visibility level (VL) and significantly impacting reaction time, thus underscoring its relevance in visibility calculations and nighttime lighting design.

In the other study, an experimental setup, incorporating a main LED light source with variable CCT and two peripheral flickering LED sources, measured reaction times of the human participants across 12 combinations of CCT levels and flickering frequencies. Results indicate that higher CCT levels decrease reaction time, while flickering sources cause reaction time to increase, especially when flickering frequency intensifies. This study underscores the relationship between CCT and driver response under flickering conditions, finding that both flicker frequency and CCT affect reaction time. This study reveals that, at times, the presence of a target or obstacles in the observers' line of sight may vary with changes in the main source's color appearance, particularly when flicker is present as an irritating glare. Under such lighting conditions, vision can be significantly impacted, resulting in longer reaction times for observers. These findings show the necessity of taking both luminance and chromaticity in road lighting design, especially in scenarios where flickering sources may be present. As CCT increases, reaction time decreases; however, flickering sources consistently lengthen reaction times, suggesting that reducing flicker and optimizing CCT could improve driver safety.

This paper focuses on two main parameters: reaction time and CCT. Reaction time, or response time, is defined as the interval between the presentation of a stimulus (visual or auditory) and a clear response triggered by that stimulus, measured through a reaction key [21]. This reflects the time required to recognize the stimulus, decide on an action, and initiate that action using specific muscle groups [22]. Reaction time (RT) relates to a person's ability for rapid decision-making [88]. Correlated color temperature (CCT) is defined as "the temperature of a Planckian radiator whose perceived color most closely matches that of a given stimulus at the same brightness and under specified viewing conditions" [89]. The chromaticity coordinate of the closest black-body radiation for a particular light source is determined by the CIE 1960 (u, v) diagram. Chromaticity, independently of luminance, empirically defines a color's quality, composed of colorfulness and hue—often referred to as saturation, chroma, intensity, or excitation purity [90]. The chromaticity of Planckian radiators at various temperatures is depicted along the Planckian locus, a continuous curve representing the chromaticity-temperature relationship of these radiators. Therefore, a Planckian radiator's chromaticity directly correlates with its temperature, allowing either to be determined if the other is known [91]. This phenomenon prompted researchers to investigate the impact of chromaticity and flicker on drivers, selecting CCT as a closer representation of chromaticity, with unit of Kelvin (K). Mc-Cammy demonstrated that CCT (T) can be expressed as a function of chromaticity coordinates.

$$T = -437n^3 + 3601n^2 - 6861n + 5524.31$$

Where, $n = \frac{(x - 0.3320)}{(y - 0.1858)}$ and (x, y) is the chromaticity co-ordinate of the light sources [92].

Ultimately, these findings advocate for the inclusion of CCT and flicker mitigation in road lighting standards, calling for a re-evaluation of current guidelines to prioritize driver-centric lighting solutions. By optimizing lighting conditions, road safety can be significantly enhanced, reducing the risk of nighttime accidents and fostering safer driving environments worldwide.

4.2 Human Vision and Street Lighting

As earlier described in the chapter 2, lighting impacts humans primarily through the visual system, an image-capturing and processing mechanism. The eye projects images onto the retina, where the initial image processing occurs mainly via two photo receptors namely rods and cones, with different aspects of the image sent to the brain's visual cortex through specialized channels. The retina's central area, the fovea, handles fine detail detection, while the peripheral retina aids in detecting movement and adjusting focus. In bright light, the entire retina functions, but in low light, only the peripheral vision remains active, with color and detail fading. Factors like visual size, luminance contrast, color difference, retinal image quality, and retinal illuminance influence the detectability and identification of objects. These parameters are crucial for visual performance, with reaction time serving as a key measure of efficiency [13]. The major type of lighting, which affects human vision under mesopic condition, is street lighting. During night-time, a human driver's vision falls under mesopic region. Mesopic vision states occur at intermediate luminance values between photopic and scotopic vision levels (between 0.001 and 3 cd/m2). In this stage, both the rod and cone photoreceptors of human eye are activated [44]. Ensuring the driver's visual satisfaction and comfort is essential on the road, particularly for nighttime driving when object detection becomes a primary concern. Road lighting installations play a critical role in supporting the driver's vision and ability to detect objects. The light distribution and spectrum from these installations significantly impact the driver's performance, safety, and comfort during night driving [32]. Numerous studies have examined how effective the light sources are at making mostly achromatic objects on the road visible. However, no clear conclusions have been reached, indicating that any effects on on-axis object detection are likely minimal [93-95]. However, recent studies on the influence of light spectrum on the detection of off-axis objects indicate that the light spectrum plays a crucial role in the effectiveness of road lighting. In particular, He et al. conducted a laboratory experiment comparing HPS and MH light sources. Their findings revealed a significant increase in reaction time as photopic luminance decreases from photopic to mesopic conditions, impacting both on-axis and off-axis target identification [35]. These effects drive this thesis to find the effect of varying correlated color temperatures (CCTs) on human participants' reaction times and visibility levels for object recognition tasks.

4.3 Temporal Light Modulation (TLM)

As described by Commission Internationale de l'Eclairage, 'Temporal light modulation (TLM) is a fluctuation in the luminous quantity or spectral distribution of the output of a lighting system over time' [96]. Device and system designs, including drivers and control gear, as well as electrical supply variations, lead to changes in lighting modulation (TLM). In the past, lighting products of the same type had similar TLM characteristics; for example, AC-powered incandescent lamps

displayed a sinusoidal wave pattern for its TLM with a frequency that was twice that of the main power supply, while fluorescent lights with electronic ballasts operated at 20–40 kHz with minimal modulation. Back then, knowing the lighting technology was enough to infer TLM properties, but with LEDs, direct measurement is now required due to their rapid current response and varied designs [82, 97]. Many LED systems also use PWM for intensity controlling, resulting in 100% modulation at frequencies over 300 Hz. TLM can negatively impact visual, behavioral, and health aspects, causing flicker, stroboscopic, and phantom array effects, collectively called temporal light artefacts (TLA) [97]. The definition of flicker is 'perception of visual unsteadiness induced by a light stimulus the luminance or spectral distribution of which fluctuates with time, for a static observer in a static environment' [98]. This phenomenon is observed in light sources exhibiting temporal light modulation (TLM) at frequencies below 60-80 Hz. The Talbot-Plateau law posits that the human visual system perceives flickering signals as continuous when they exceed a specific frequency, termed the critical fusion frequency (CFF). Under photopic eye adaption conditions, the CFF typically ranges around 60 Hz for most individuals [99]. Although, temporary visual effects of TLM at rates up to 200 Hz is also reported [100-101]. Furthermore, the stroboscopic effect is defined as 'change in motion perception induced by a light stimulus the luminance or spectral distribution of which fluctuates with time, for a static observer in a non-static environment' [102]. With stroboscopic effects, TLM can be hazardous by causing false motion perceptions, especially around moving machinery with fluctuating frequencies between 80 Hz to 2 kHz [99]. On the other hand, phantom array effect is defined as a 'change in perceived shape or spatial positions of objects, induced by a light stimulus the luminance or spectral distribution of which fluctuates with time, for a non-static observer in a static environment' [102]. The source exhibits this kind of effect, which causes excessive visual stress [103], at a frequency range starting from 3 kHz to ending at 11 kHz. Periodic TLM is a consequence of the electronic design of the light source or its control system. It depends upon four parameters. First is the frequency for which the cycles of TLM are repeating, second is the depth in light output variation or modulation depth, third one is the waveform's shape due to the electronics associated with the source or control systems and the last one is the duty cycle, where the duty cycle represents the fraction of a cycle where the light output is not zero. It is commonly expressed as a ratio or percentage of the total cycle time, particularly for rectangular waveforms [102]. With the development of LEDs, effects of TLA on human observers, be it static or moving, have become the major concerns of the researchers, because a wide range of TLM can be exhibited by LED systems depending upon the design of its drivers and control circuit and specially on dimmable drivers' design due its pulse width modulation (PWM) characteristics [104]. The late 1990s witnessed a surge in research interest concerning the effects of light source TLM, coinciding with the widespread adoption of high-frequency fluorescent lighting equipped with electronic ballasts operating at 40 kHz. These electronic ballasts replaced the traditional magnetic ballasts, which operated at lower frequencies (120 Hz in North America, 100 Hz elsewhere). Studies revealed that this transition, primarily motivated by energy efficiency goals, led to significant improvements in visual performance, more stable saccadic eye movements, and enhanced performance in clerical tasks [80-81, 105-106]. For these reasons, this thesis experimented on an experimental set-up to find the visual and non-visual effects of peripheral flickering sources, one of the major TLAs experienced in Indian roads, on static human observers' object detection task under varying CCT of main or on-axis source.

4.4 Effects of Variations of CCT of LED Light Sources on Reaction Time and Visibility Level for On-axis Object Recognition

To investigate driver responses across different CCTs (Correlated Color Temperatures), this study examines how reaction time (RT) and visibility level (VL) change with variations in CCT. Utilizing an LED as the primary source and two identical LEDs as peripheral sources, the study was conducted in a controlled laboratory environment. The study also evaluates the impact of these peripheral sources on RT and VL. Findings indicate a decrease in average reaction time as the ambient lighting level increases due to the contribution of peripheral sources. Notably, the study reveals significant correlations between reaction time and CCT, and between visibility level and CCT, which will be further discussed in later parts of this chapter.

4.4.1 Experimental Setup Development

Though the study examines the characteristics of roadway lighting, the experiment itself was conducted indoors at the Illumination Engineering Laboratory in the Electrical Engineering Department of Jadavpur University to explore any strong correlation between CCT and VL. The lab is painted in dark black to minimize light reflection and prevent stray light, ensuring an uninterrupted, reliable result that can serve as a reference for future real-road experiments. The setup includes three main components: light sources, objects, and reaction time measuring instruments. Building the total experimental setup, including these components is also described in this section.

4.4.1.1 Light Sources

The experiment uses three smart LED lights from Halonix, each rated at 12 watts, 220–240V AC input, 50Hz, with a B22 base and a luminous flux of 820 lumens. These RGBW LEDs offer dimmable intensity (0–100%), CCT control (2500K–6500K), color-changing capability, and can be controlled via a 2.4 GHz Wi-Fi based Android app. They operate in temperatures from -10°C to +50°C. One LED serves as the main light source (S), mounted at a height of 2m, while the other two act as peripheral sources (P), mounted at 1.5m, all on miniature street light poles. Pictorial representation of light source is given in Fig. 4.1.

Fig. 4.1: LED bulb used as Main and Peripheral Sources

Pictorial representations of mounted main and peripheral sources are given in Fig. 4.2 (a) and (b).

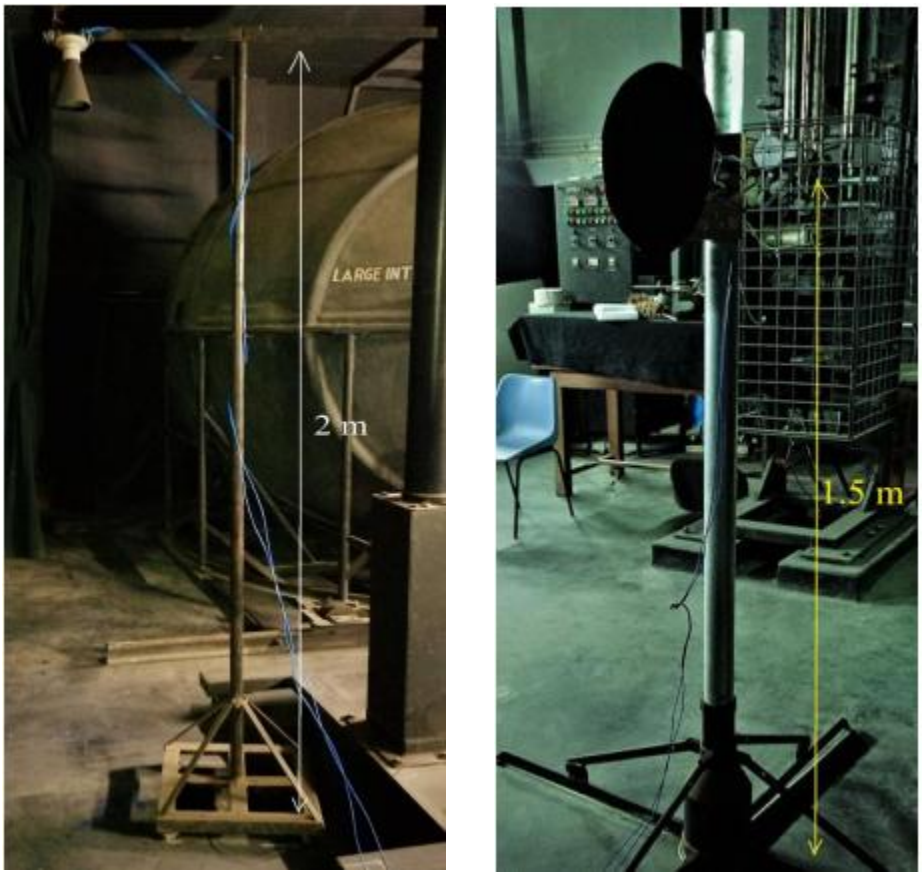

Fig. 4.2 (a) & (b): Main source (S) and Peripheral source (P) are mounted on 2m and 1.5m street light pole respectively.

The spectral compositions or SPD of the main light source (S) at four different CCT levels, 3000K, 4000K, 5000K, and 6000K, were measured using a Konica Minolta CL-70F colorimeter and are shown in Fig-4.3 (a), (b), (c), and (d), respectively.

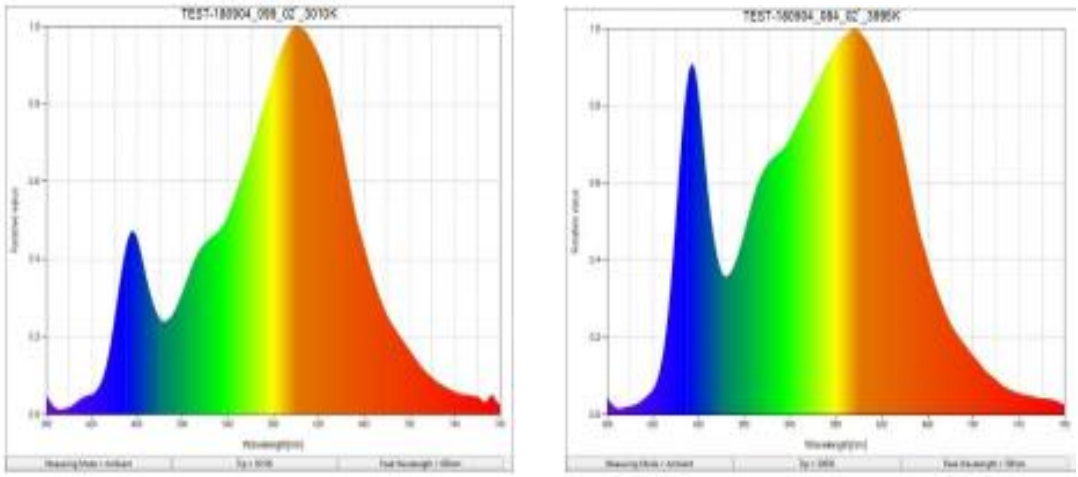

Fig. 4.3 (a) & (b): SPDs of Main Source at 3000 K & 4000 K

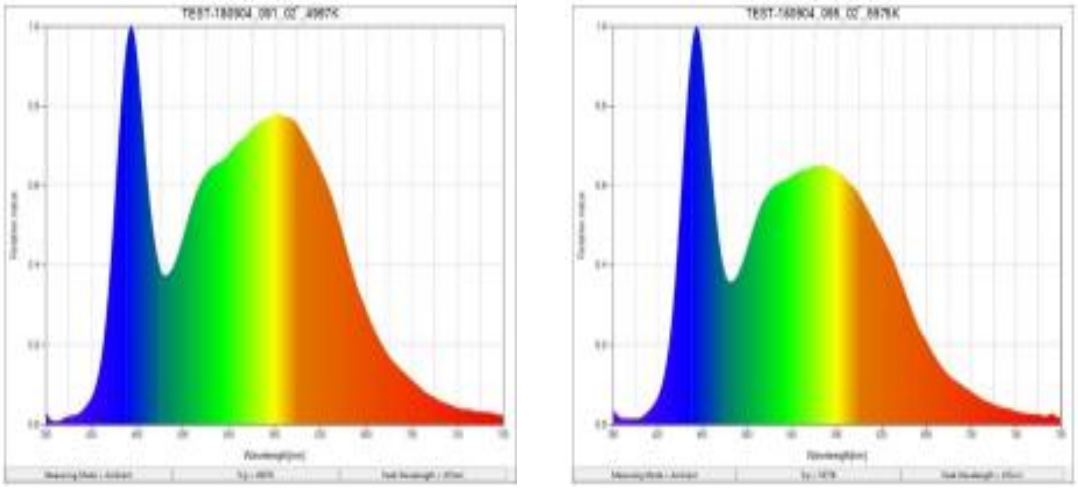

Fig. 4.3 (c) & (d): SPDs of Main Source at 5000 K & 6000 K

4.4.1.2 Stimuli or Colored Objects

To measure Reaction Time (RT) for object recognition and behavioral responses of the human participants, twelve standard objects of specific shapes and colors were created. The objects, made from cardboard, are in three shapes: cuboid, cylindrical, and prismatic. Each object is covered in one of four standard colors: yellow, green, violet, or black. They are constructed with specific dimensions, and their individual reflectance has been measured to meet standard value, which is in between 20% to 50% [107]. Detailed specifications of the objects are provided in Table 4.1, and a sample photo is shown in Fig. 4.4 below.

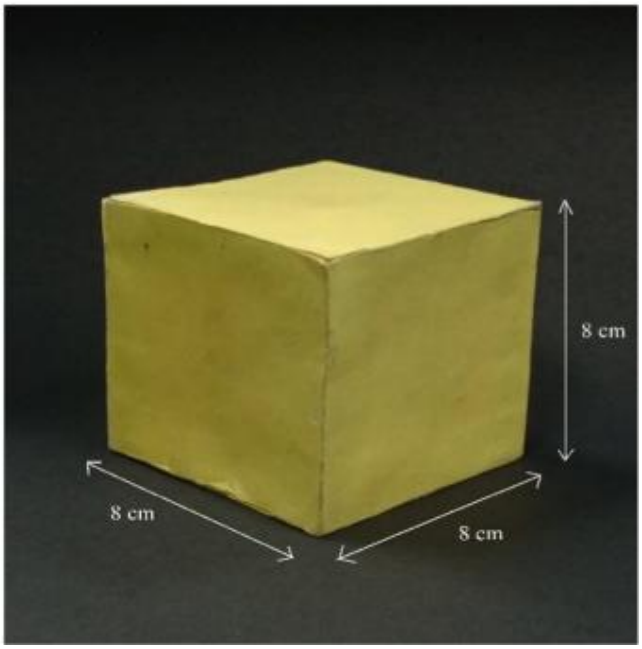

Fig. 4.4: Used Sample Target object

Table 4.1 : Details of the objects used for experimentation

Sl No.	Object Shape	Object Colour	Object Reflectance (%)	Object Dimension		Picture of Object
1	Cuboid	Yellow	19.2	length (cm)	8	
2		Green	16.6	Width (cm)	8	
3		Violet	17			
4		Black	15.6	Height (cm)	8	
5	Cylindrical	Yellow	19.1	Diameter (cm)	8	
6		Green	24			
7		Violet	18.6	Height (cm)	9	
8		Black	19.5			
9	Prismatic	Yellow	13.9	length of the Base (cm)	10	
10		Green	15	Width of the Base (cm)	10	
11		Violet	13.2			
12		Black	14.8	Height cm)	8	

4.4.1.3 Reaction Time Measuring Compact Device

A microcontroller-based timer device was developed to measure Reaction Time (RT) in human subjects. This device includes a 16x2 LCD display for showing recorded times, and all other components, including the active shutter glass circuit, Arduino, display, and wiring, are housed in a portable box. Powered by a 9V battery, the device can timestamp in milliseconds. A researcher initiates the start time, while the subject stops it, all using push buttons. Further details of the device's operation are covered in the experimental procedures**.** Active shutter glass is a specialized spectacle, often used in 3D cinemas and VR glasses, includes LCD lenses that remain opaque under normal conditions, blocking visual input. A modified electronic circuit within the frame allows a 9V battery-powered push button to switch the lenses from opaque to transparent. Designed to control human exposure time, the spectacle's active shutter

provides 700 milliseconds of visibility, ample time for object recognition (normally 100 milliseconds for an average human being). Linked to an Arduino microcontroller, the push button activates the lens to turn transparent for 700 milliseconds before automatically returning to opaque, allowing observers to view grid points at a 2° solid angle. These two devices are used in conjugation to form the reaction time measuring compact device (RTMCD). Pictorial representations of these two devices are given in Fig. 4.5 (a) and (b).

Fig. 4.5 (a): Reaction Time Measuring Compact Device (RTMCD) with Top and Back Side View

Fig. 4.5 (b): Special active shutter glass

4.4.1.4 Other Experimental Setups

In addition to the three main components, the experimental setup is carefully arranged. Three steel miniature street light poles are used to mount the smart LED lights, where the main source is positioned 2m above the floor, while the two peripheral sources are set 1.5m high, located bilaterally to the observer's visual on-axis. A detailed grid is designed based on CIE 140-2000, with six evenly spaced points across five rows and three columns, each separated by 0.5m [108]. The main source aligns in such a way, so that its nadir falls on point ‘E1’. For informational purpose, nadir point is one of the drawn grid points with the maximum illuminance value. The observer’s position lies along an extended line, 15m from grid point ‘E3’ in column 3. To prevent direct light from reaching the observer’s eyes, the sides of the light sources are covered with pitch-black paper, acting as baffles to block direct glare or stray light. Although glare or veiling luminance is considered in VL calculations, results show that the greatest glare comes from higher intensity at wider angles in distant street lighting [109].

Detailed picture of grid is given in Fig. 4.6 (a) and the side view of the total experimentation setup is given in Fig. 4.6 (b).

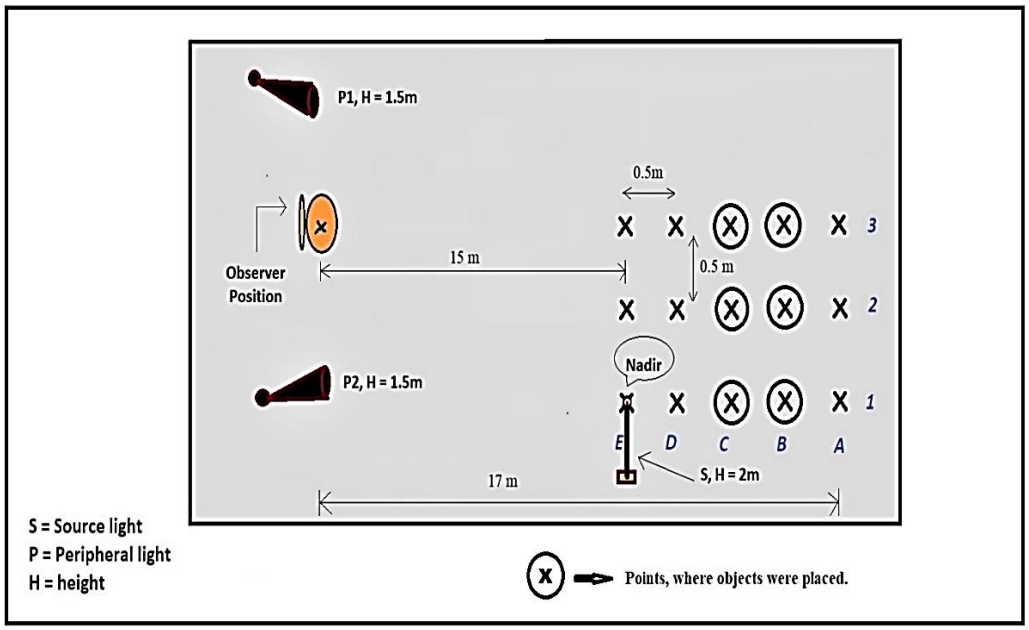

Fig. 4.6 (a): Detailed Top View of the Experimental setup

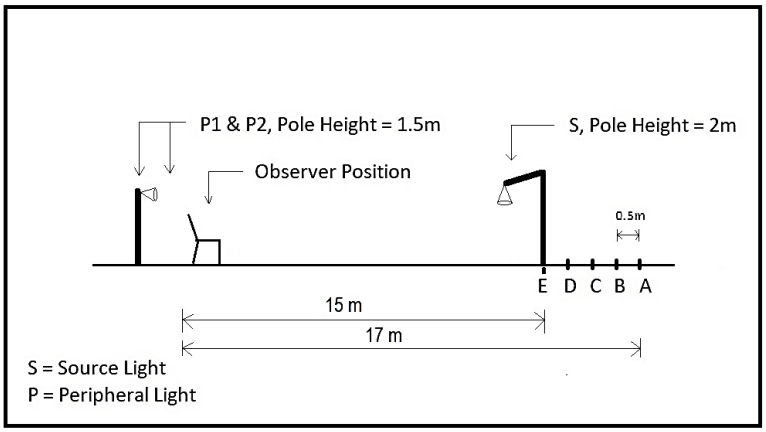

Fig. 4.6 (b): Detailed Side View of the Experimental setup

4.4.2 Human Participants

Ten healthy physiologically and neurologically intact participants (five males, and five females, mean age 22.5 yrs., S.D., ± 1.5) were recruited for this study. All the participants reported normal or corrected to normal vision. They were provided with detailed understanding of the entire experimental procedure and signed informed consent before participating in the experiment. The protocol was cleared by Institutional Ethics Committee.

4.4.3 Experimental Procedure

The experimentation is conducted in two distinct parts. In the first part, only the main or on-axis light source is used, while in the second phase, both the main and peripheral light sources are utilized. For the first phase, the study tests four CCT levels (3000 K, 4000 K, 5000 K, and 6000 K) of the main source, achieving 95% accuracy for setting the CCT values. The objects are placed at six fixed grid points for each CCT level, with random positioning among these points, which remain unknown to the observer. These six points, located behind the main light source, create positive contrast to make the object appear brighter than the background. A Konica-Minolta CL-70F colorimeter and an Android app are utilized to control and modify CCT levels. The observer, wearing active shutter glasses, is provided a push button to push, when it identifies any object in the frontal vicinity. Another push button is given to a researcher to start the timer and to make the special active shutter glass transparent. Once the object is positioned, the reaction time is recorded using the reaction time measurement compact device. Target and background luminance values are measured from the observer's position using a Konica-Minolta LS-100 luminance meter, set at 2° field of view, for calculation of VL values for each object placement. In the second phase, the setup is the same, but two peripheral light sources are added on either side of the observer's eyes. These peripheral sources are tested at three CCT levels (3000 K, 4500 K, and 5000 K) with 95% accuracy of setting for each main source CCT level. Each observer therefore records four (4 levels of CCT of main source) runs in the first phase with 24 readings (4 lighting scenes x 6 grid points) and twelve (4 levels of CCT of main source × 3 levels of CCT of peripheral sources) runs in the second phase with 72 readings (12 lighting scenes x 6 grid points). Distances between the objects, observer, and luminance meter, for VL calculations, are measured with a Fluke 406E laser distance meter. Since this is a laboratory-based study, assuming road-like conditions is unnecessary, so no classification for road type is applied. In each of the readings, participants respond to four specific questions for each object position, provided in a questionnaire. Marks are assigned based on agreement or disagreement with the actual shape, size, and other subjective answers, using a Likert scale. Researchers utilize the Likert scale, which is a unidimensional measure, to gather respondents' attitudes and opinions. This psychometric scale is frequently used by researchers to comprehend the opinions and thoughts of the participants. After calculating the total marks for one object position, the process is repeated for the remaining five positions, and the scores are averaged to rate each lighting scene. Fig. 4.7 shows a detailed view of the questionnaire. Once scenes are rated, comparative analysis identifies the best and worst lighting scenes. The four questionnaire questions are divided into two categories: a "subjective" category, covering the first and last questions, based on subjects' personal impressions, and an "objective" category, covering the second and third questions, which focus on the shape and color of objects and rely on subjects' perception of them. The marks, to be given, are categorized into three levels for objective category, where the first level or 'match' will carry 2 marks, second level or 'mismatch' will carry -2 marks and the third level or 'nor recognized' will carry 0 marks.

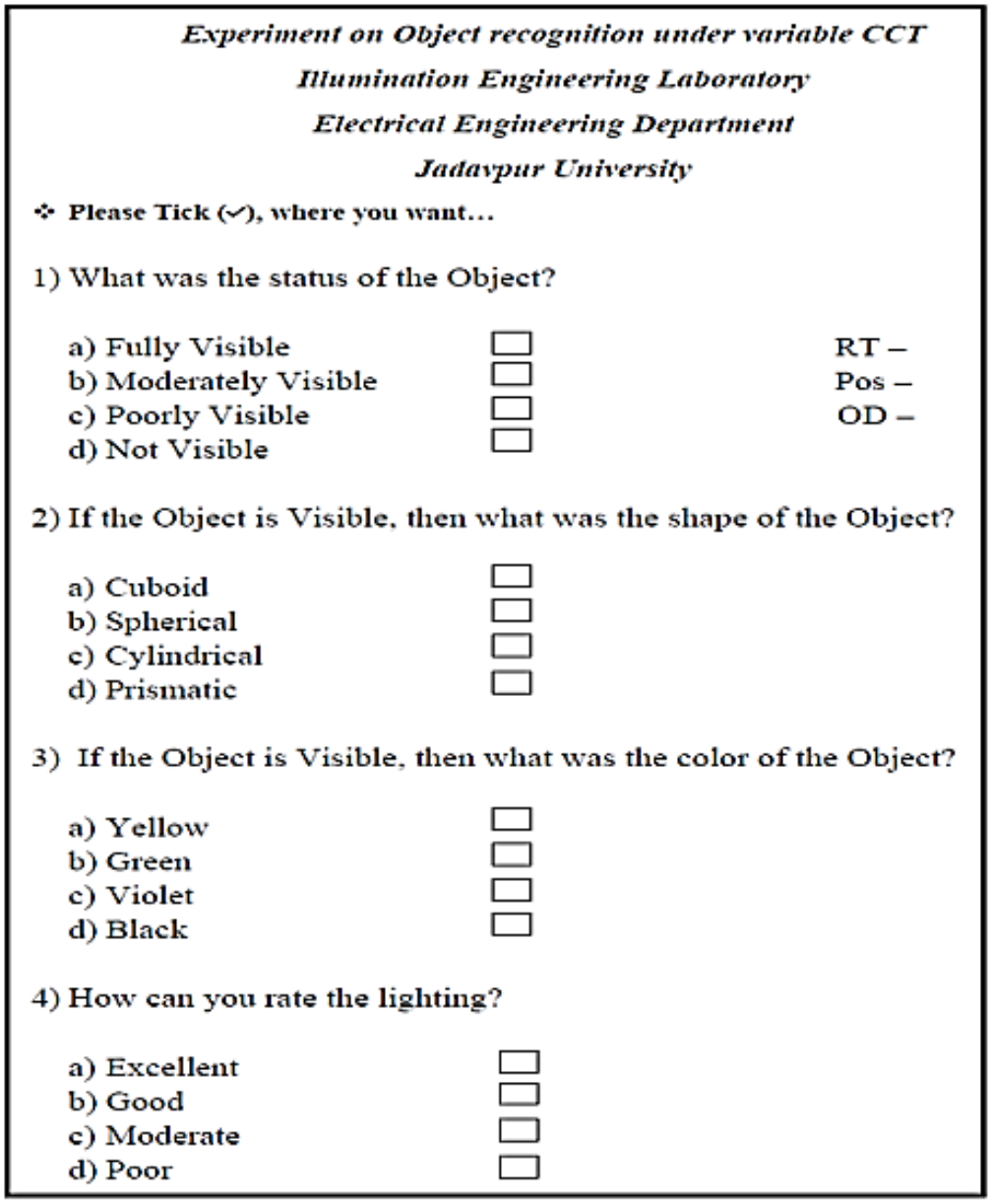

Fig. 4.7: Questionnaire set asked to the observer as feedback about individual experimental run.

Furthermore, for subjective type questions (the first and last one), it carries 3 marks for option (a), 2 marks for option (b), 1 mark for option (c) and 0 marks for option (d). Additionally, between two consecutive runs of two lighting scenes, all observers are given 15 to 20 minutes of exposure to normal lighting to help reset their focus from the previous lighting condition and prepare for the next trial. Actual pictorial representations of total experimental scenario are given in Fig. 4.8 (a) and (b).

Fig. 4.8 (a) and (b): Experiments and Measurements are going on

4.4.4 Calculations and Results

The reaction time (RT) is initially measured using the developed dedicated instrument and then analyzed and averaged in relation to different CCT levels. The average reaction times of the subjects for the trials under four different levels of CCTs when only source (S) light being ON and overall uniformity of the selected six grid points are given in the Table 4.2. The average

reaction times of the subjects for the trials under four different levels of CCTs of main source (S) and three different levels of CCTs of peripheral sources (P) and overall uniformity of the selected six grid points are given in the Table 4.3. The study demonstrates that reaction time (RT) is shorter when the main and peripheral sources have higher CCTs. Specifically, for a main source CCT of 6000 K, with CCT range of peripheral sources starting from 3000 K to ending at 6000 K, the average RT is 0.1944 seconds. In contrast, with a main source CCT of 3000 K and the same peripheral CCT variation, the average RT increases to 0.2816 seconds. A java script, described in Annexture 1, is also written to calculate the VL and STV values easily and quick. The visibility level (VL) of the target at each grid point is calculated using factors such as target luminance, background luminance, reaction time, observer age, and the angular size of objects. The study includes twelve sets of six VL values for twelve combinations of main and peripheral source CCTs. From data on illuminance, reaction time, and luminance, several metrics are computed, including Overall Uniformity (U_O), average reaction time (ART), average relative weighted visibility level (ARWVL), and small target visibility (STV), with results summarized in Table 4.4. It is evident that the highest average STV of 37.98, occurs at a main source CCT of 5000 K, with peripheral CCTs between 3000 K and 6000 K. Conversely, the lowest STV, with an average value of 31.45, is observed at a main source CCT of 6000 K under the same peripheral CCT variation. Notably, the best VL values are achieved with a main source CCT of 4000 K, while the poorest VL values are found at a main source CCT of 6000 K, again with peripheral variation of CCTs from 3000 K to 6000 K. Graphs in Fig. 4.9 (a), (b) and (c) illustrate the variations in ART, STV, and VL across different CCT levels for both main and peripheral sources. The study also reveals that peripheral light sources raise the overall adaptation light level of the observers' eyes, leading to increased values for both reaction time (RT) and small target visibility (STV). It was also observed that the lowest average RT occurs at a peripheral CCT of 6000 K, regardless of variation of the main source CCT. Reaction time reaches its minimum when both the peripheral and main sources are set to 6000 K. Additionally, STV values increase with a peripheral CCT of 6000 K and higher main source CCTs (5000 K and 6000 K). The highest STV, reaching 45.986, is observed with a peripheral CCT of 4500 K paired with a main source CCT of 4000 K.

Additionally, all lighting scenes are evaluated, using the answers given by the participants after each reading to the questionnaire for behavioral study, in two parts: the first part measures the combined effect of subjective and objective factors, while the second assesses only the objective factors. Calculations are done to evaluate the average scores of the lighting scenes. The results indicate that a main source CCT of 4000K provides the optimal lighting for object recognition and observer comfort, while 6000K ranks the lowest when peripheral sources are absent. With peripheral sources present, a 5000K main source gives the best lighting environment, while 3000K is rated the poorest when peripheral effects are averaged. Specifically, peripheral sources at 6000K yield the highest lighting quality, while 3000K is rated the lowest when averaging the effect of the main source. In terms of individual scenes, a 6000K CCT for both main and peripheral sources produce the best results, whereas a 6000K main source combined with a 3000K peripheral source yields the worst outcome. Graphs in Fig. 4.10 (a), (b), (c), and (d) illustrate variations in scores across sections, showing trends with CCT changes in main and peripheral sources. Table 4.5 presents the average sectional scores for scenes created by the main source alone, while Table 4.6 shows scores for combinations of main and peripheral sources. Furthermore, T-tests were conducted assuming unequal

variances, with P-values indicating that CCT changes significantly affect total and objective average scores of lighting scenarios. For scenes without peripheral sources, two-tailed P-values for total and objective averages are 0.0131 and 0.0130, respectively. When peripheral CCTs vary, the P-values for total and objective scores are 0.041 and 0.043, with similar P-values across other main source CCT levels. Thus, the null hypothesis, stating no relationship between CCT and lighting scores, is rejected, confirming that CCT influences the scores of lighting scenarios.

Table 4.2: Overall Uniformity and subject's Average Reaction Time under different levels of Source CCTs.

CCT	Overall Uniformity (U0)	Average RT (Seconds)
3000 K	0.17621	0.4567
4000 K	0.18477	0.4328
5000 K	0.17334	0.4298
6000 K	0.17236	0.469

Table 4.3: Overall Uniformity and subject's Average Reaction Time under different levels of Source and peripheral source CCTs

CCT (Source)	CCT (Peripheral)	Overall Uniformity (U0)	Average RT (Seconds)
3000 K	3000 K	0.476	0.3433
	4500 K	0.554	0.24
	6000 K	0.554	0.2616
4000 K	3000 K	0.453	0.266666667
	4500 K	0.5	0.29
	6000 K	0.51	0.225
5000 K	3000 K	0.422	0.2216
	4500 K	0.5	0.2466
	6000 K	0.486	0.2
6000 K	3000 K	0.48	0.2116
	4500 K	0.48	0.1883
	6000 K	0.48	0.1833

Table 4.4: Table of Overall Uniformity (U_O), average reaction time (ART), average relative weighted visibility level (ARWVL) and small target visibility (STV)

CCT (Source)	CCT (Peripheral)	Overall Uniformity (U_0)	Average RT (Second)	ARWVL	STV
3000 K	3000 K	0.476	0.343333333	0.000415027	33.81924027
	4500 K	0.554	0.24	0.000164115	37.84851701
	6000 K	0.554	0.261666667	0.000109402	39.60972938
4000 K	3000 K	0.435	0.266666667	0.000149506	38.25340625
	4500 K	0.5	0.29	2.51985E-05	45.98624868
	6000 K	0.51	0.225	0.004447658	23.51868634
5000 K	3000 K	0.422	0.221666667	0.000999852	30.00064194
	4500 K	0.5	0.246666667	4.37995E-05	43.58530448
	6000 K	0.486	0.2	9.20043E-05	40.36191731
6000 K	3000 K	0.48	0.211666667	0.000518447	32.85295348
	4500 K	0.48	0.188333333	0.001880307	27.2577131
	6000 K	0.48	0.183333333	0.000376155	34.24632911

Table 4.5: CCT of Source (S) and Total Average and Objective Average.

CCT	Total Avg.	Obj. Avg.
3000 K	7.783	3.05
4000 K	7.983	3.233
5000 K	7.967	3.15
6000 K	7.65	3

Table 4.6: CCT of Main (S) and Peripheral sources (P) and Total Average and Objective Average.

CCT (Source)	CCT (Peripheral)	Total Avg.	Objective Avg.
3000 K	3000 K	8.417	3.633
	4500 K	8.633	3.667
	6000 K	8.55	3.7
4000 K	3000 K	8.8	3.8
	4500 K	8.675	3.8
	6000 K	8.575	3.7
5000 K	3000 K	8.8125	3.75
	4500 K	9.0125	3.95
	6000 K	8.625	3.65
6000 K	3000 K	8.325	3.5
	4500 K	8.525	3.5
	6000 K	9.15	4

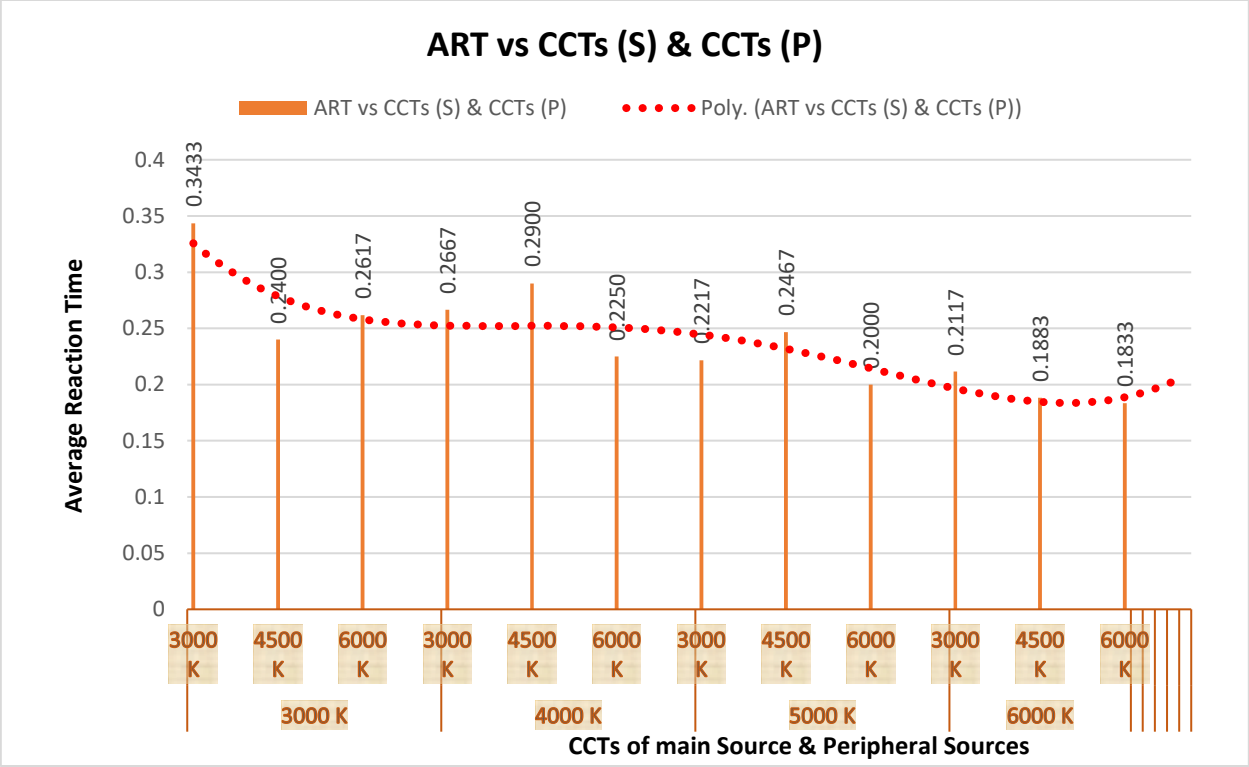

Fig. 4.9 (a): Average Reaction Time vs. CCTs of Main and Peripheral Sources

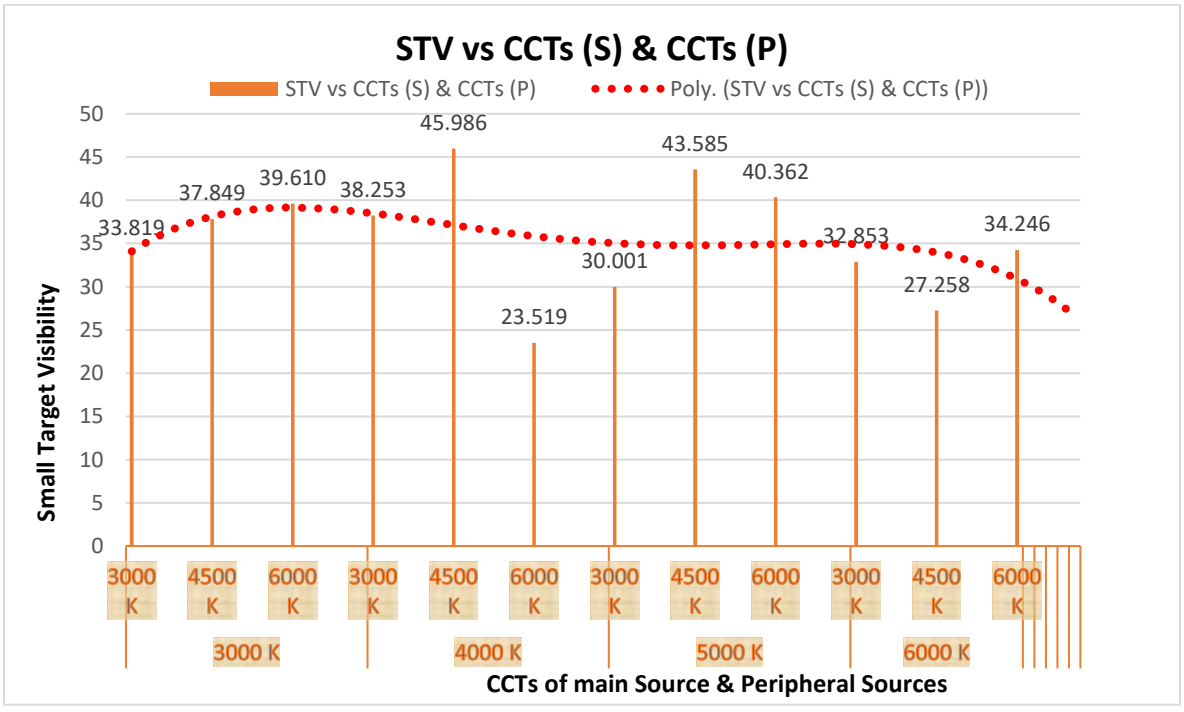

Fig. 4.9 (b): Small Target Visibility vs. CCTs of Main and Peripheral Sources

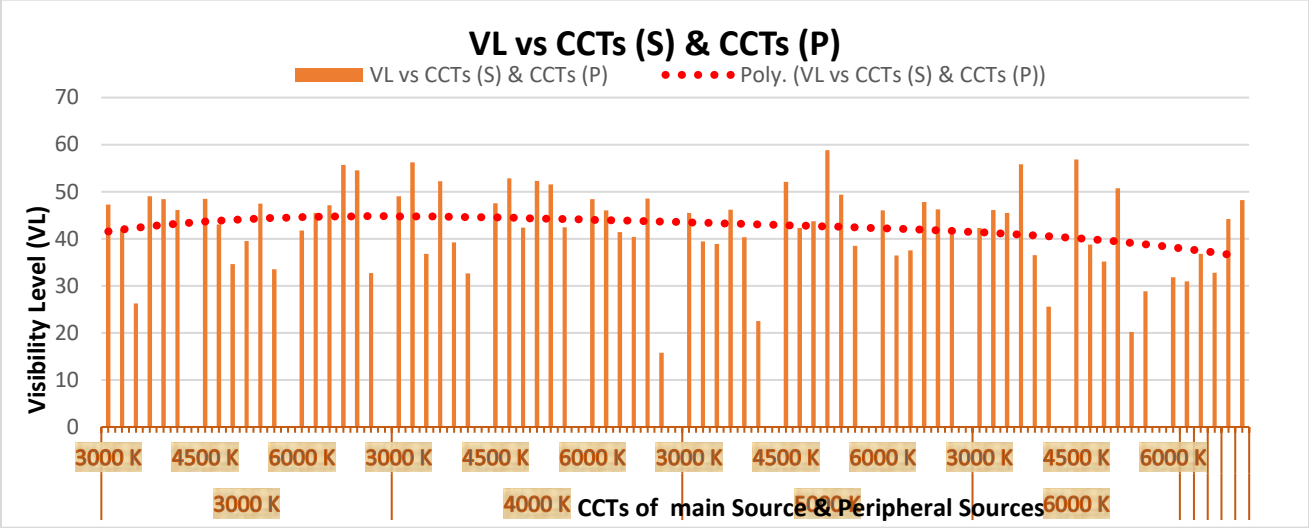

Fig. 4.9 (c): Visibility vs. CCTs of Main and Peripheral Sources

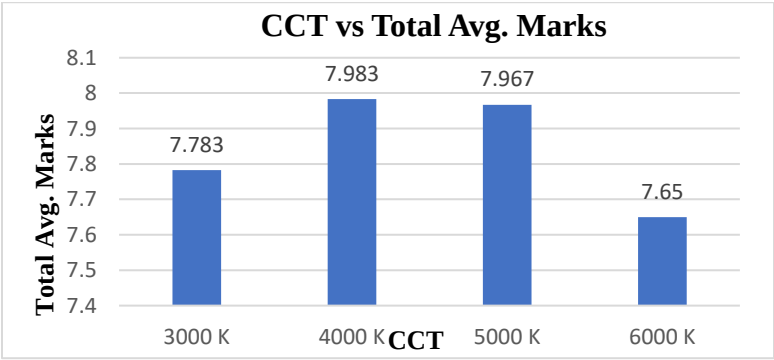

Fig. 4.10 (a): Graph between CCT and Total Average Marks when Peripheral Sources are off

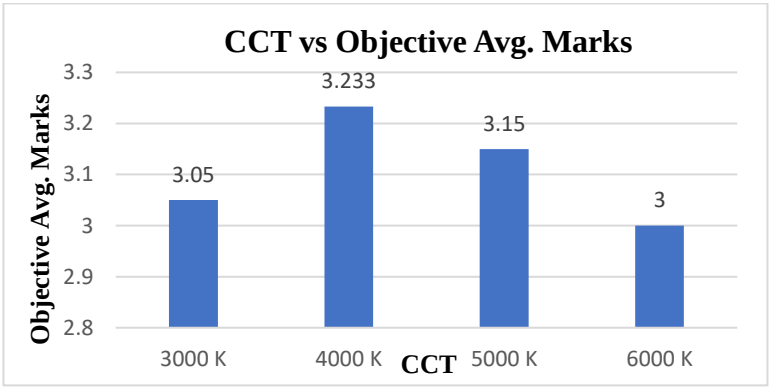

Fig. 4.10 (b): Graph between CCT and Objective Average Marks when peripheral sources are off.

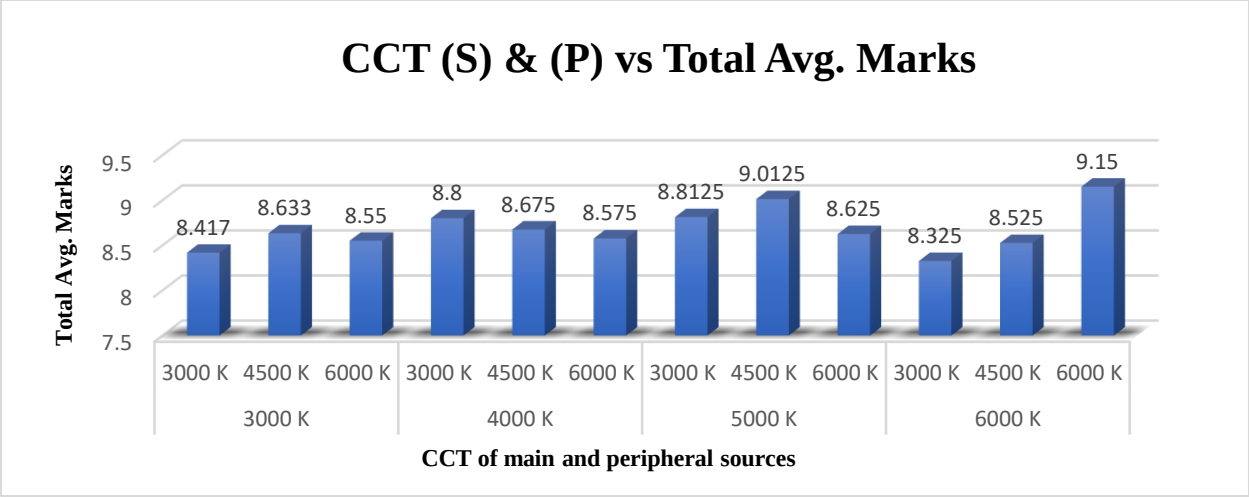

Fig. 4.10 (c): Graph between CCT & Total Average Marks with combination of Main & Peripheral source.

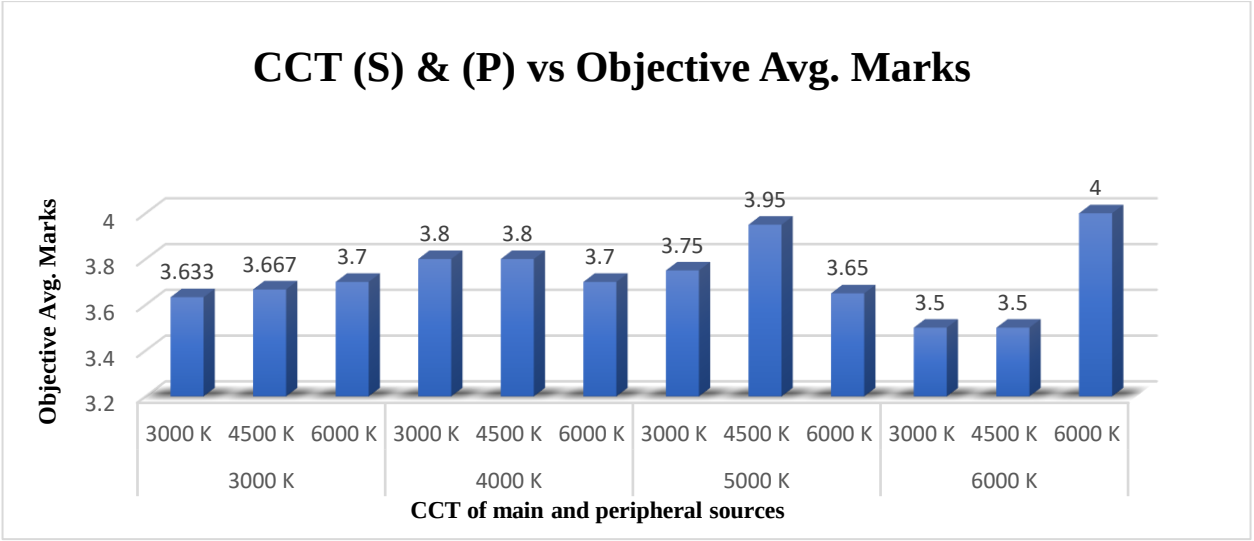

Fig. 4.10 (d): Graph between CCT & Objective Avg. Marks with combination of Main & Peripheral source.

If the graph represented in Fig. 4.9 (a), (b) and (c) is analyzed, then it can be stated that with the increment of CCT of main or on-axis and peripheral sources average reaction time (ART) decreases to a certain limit after that it again increases, small target visibility (STV) also shows near similar trend of reduction and visibility level (VL) also decreases. Furthermore, analysis of the graphs of Fig. 4.10 (c) and (d) revealed that total and objective average marks are higher for 4000K CCT of main source.

4.4.4.1 Visibility Level Calculation

The quantified visibility parameter, or VL, is a complex, dimensionless metric primarily guided by Ricco's law and Weber's law. It depends on factors such as the luminance difference between an object and its background, exposure or reaction time (RT), the observer's age,

contrast type (positive or negative), and glare [23]. The IESNA-RP-8–00 standard outlines a straightforward method for calculating STV and provides necessary formulas [24]. Notably, the STV method has been shown to deliver optimal results compared to other visibility models, which is why it was chosen for this study [110]. Additionally, since dark highway environments increase the likelihood of hazardous conditions, it was observed that raising drivers' eye light adaptation levels can reduce glare effects from oncoming headlights or distant street lights [24]. For this reason, the study also incorporates peripheral light sources to assess the impact of increased human eye adaptation levels. Furthermore, this research explores the human eye's ability to detect objects and perceive object details across various correlated color temperature (CCT) levels, aiming to correlate visual acuity with CCTs [69]. The visibility level of the specified objects in the study is calculated by

$$VL = \frac{\Delta L_{actual}}{\Delta L_{threshold}}$$

where, ΔL_{actual} is the luminance difference between the target and the background in the Laboratory conditions.
$\Delta L_{threshold}$ is the luminance difference between target of certain angular size and its background for minimum visibility.
Now, $\Delta L_{actual} = L_t - L_b$ Where, L_t is target luminance and L_b is background luminance.

To calculate $\Delta L_{threshold}$, it is essential to determine whether the object exhibits positive or negative contrast. Positive contrast occurs when the target's luminance is higher than that of the background, whereas negative contrast happens when the background luminance surpasses the target's luminance. Research has shown that objects with negative contrast are consistently more visible at the same ΔL_{actual} compared to those with positive contrast [111]. These findings reveal that the threshold difference is highly dependent on the background luminance (L_b) and the angular size of the target object [112]. Based on these factors and the collected data, Adrian introduced the contrast polarity factor (F_{cp}). Additionally, he incorporated an age factor (AF) to account for age-related adjustments in the eye. Detailed steps of calculations are given in Annexture 2.

$$\Delta L_{threshold} = k * \left(\frac{\Phi^{\frac{1}{2}}}{\alpha} + L^{\frac{1}{2}}\right) * F_{cp} * \frac{(a(\alpha, L_b)+t)}{t} * AF$$

Where, $\Phi^{1/2}$: Luminance flux function.
$L^{1/2}$: Luminance function.
α: Target size (given in Fig. 4.11).
F_{cp}: Contrast polarity factor.
$a(\alpha, L_b)$: Parameter depends on size of target and background luminance.
t: Observation time.
AF: Age factor.
k : Factor for the probability of perception (k = 2.6 for 100% probability) [23,109,113].

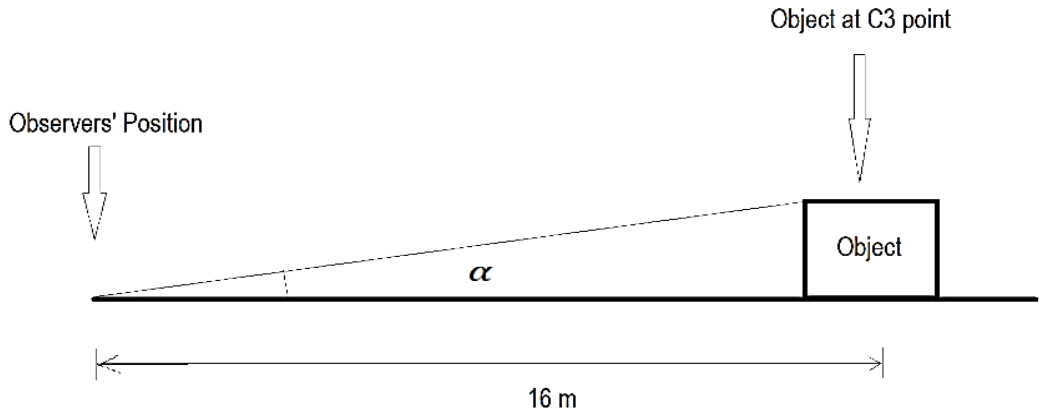

Fig. 4.11: Depiction of angular size of the object

4.4.5 Conclusions

The study demonstrates that increasing the CCT of both primary and peripheral light sources enhances eye adaptation and sensitivity. Higher CCT levels are shown to significantly reduce drivers' average reaction times and improve the STV values in the lighting environment. These findings indicate that road lighting designs should prioritize higher CCT values for street lights to optimize driver response. Additionally, using the behavioral responses of the human participants, the study suggests that at 4000K, in the absence of peripheral lighting, optimal object recognition and observer comfort are achieved. When peripheral sources are present, the best object recognition shifts to a higher CCT level of 5000K for the primary source. These insights should be considered in road lighting design, particularly in the Indian context. Future studies are necessary to explore how CCT and other lighting parameters affect drivers' and pedestrians' cognitive and temporal processes. Such research could contribute to developing lighting standards tailored to the Indian environment, enhancing human performance and safety. However, as this research was conducted in a controlled laboratory setting, further investigation on real roads is essential to confirm that higher CCT street lighting can indeed improve drivers' cognitive responses and obstacle detection.

4.5 Effects of Variations of CCT of On-axis LED Light Source and of Flickering Frequency of Peripheral Sources on Reaction Time and Visibility Level for On-axis Object Recognition

It is well-established that peripheral light sources significantly impact human visual task performance in various lighting environments, especially for tasks requiring direct on-axis vision. The color temperature of both main and peripheral light sources also significantly affects drivers' performance in real road settings. Thus, it's important to study how peripheral glaring LED sources influence task performance. This experimentation presents a laboratory experiment designed to assess the effects of various frequencies of peripheral flickering LED sources, combined with

different levels of CCTs of the main or on-axis LED source, on the reaction times of static human observers in recognizing test objects. It also aims to find correlations between observers' reaction times, the chromaticity of the main source, and flickering frequency. Correlated color temperature (CCT) serves as a valuable lighting parameter for this experiment, as it can be directly linked to chromaticity, a key characteristic of light sources. The experiment reveals that reaction time decreases as the CCT of the main source increases, regardless of flickering frequency changes. Additionally, introducing flicker and altering flicker frequency significantly impact reaction times, with peripheral glare sources' flickering increasing reaction time for object recognition. Further behavioral studies with participants in the same setup reinforce the reaction time findings.

4.5.1 Experimental Setup Development

This experiment was conducted in the laboratory of the Illumination Engineering division in the Electrical Engineering Department at Jadavpur University, even though the study focused on road lighting characteristics and conditions. The aim was to explore the general correlation between the CCT of the main light source, the flickering frequency of peripheral sources, and observers' reaction times for object recognition. To minimize internal light reflection, the lab's walls, ceiling, floor, and furnishings were painted dark, and steps were taken to block any stray external light. These measures ensured a clear, reliable outcome, intended as a benchmark for future field experiments on real roads. Based on the prevailing lighting scenarios, the experiment was divided into two distinct phases: one without peripheral flickering glare and one with a peripheral flickering glare source. The trials with flickering glare were further divided into four sub-trials based on different flicker frequencies as 3Hz, 5Hz, 8Hz and 10 Hz. The reason behind the choice of these values is that they are commonly seen in Indian roads. For each flickering glare condition and the no-glare condition, the CCT of the main light source was varied. Behavioral data was collected using a questionnaire and reaction time data is recorded using reaction time measuring compact device, operated by each participant during their trials. The experiment relied on three key elements: light sources, objects, and devices for measuring reaction times. Other setups are also done to do this experimentation.

4.5.1.1 Light Sources

This experimental setup used three LED lights: one as the main source and two as peripheral sources. The main source is a Halonix made smart LED light controlled by an Android app (for adjusting CCT), with a power rating of 12 watts, a B22 base, and a luminous flux output of 820 lumens. The two peripheral LED sources are 12 volts and 9 watts, custom-built in the lab by mounting 12-volt phosphor-coated LED chips onto heat sinks with two diffusers. They have a fixed CCT of 5500 K, with chromaticity coordinates of x = 0.3324, y = 0.3486 when fully lit. Flickering for the peripheral sources is managed by an Arduino Uno microcontroller-controlled controller circuit enclosed in a transparent plastic box, which generates the desired flicker frequency through pulse width modulation of a square wave. The code responsible for this operation is given in Annexture 1. The flickering controller device includes two 12-volt LED drivers to convert 240 volts AC to 12 volts DC. Fig. 4.1 and Fig. 4.12 (a), (b), and (c) below shows detailed images of the light sources, the chromaticity diagram of the peripheral sources, and the flickering controller device.

4.5.1.2 Stimuli or Object

To measure Reaction Time (RT) for object recognition and behavioral responses of the human participants, a cuboid shaped and yellow colored object were created. It is constructed with specific dimensions, and their individual reflectance has been measured to meet standard value. According to some sources, the ideal reflectance for an object should range from 20% to 50% [107]. In this study, a target object with an average reflectance of 36.5% across all CCT levels is used. A Metravi 1310 digital light meter is employed to measure the reflectance. It is shown in Fig. 4.4.

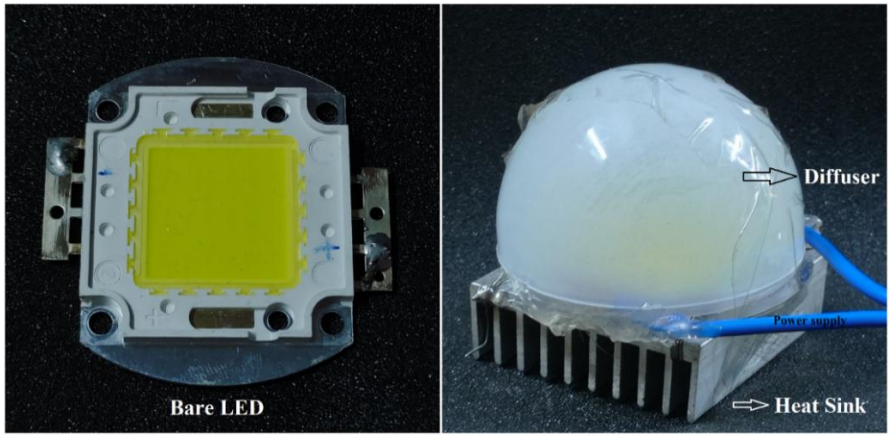

Fig. 4.12 (a): Bare and Covered Peripheral Light source with Heat Sink

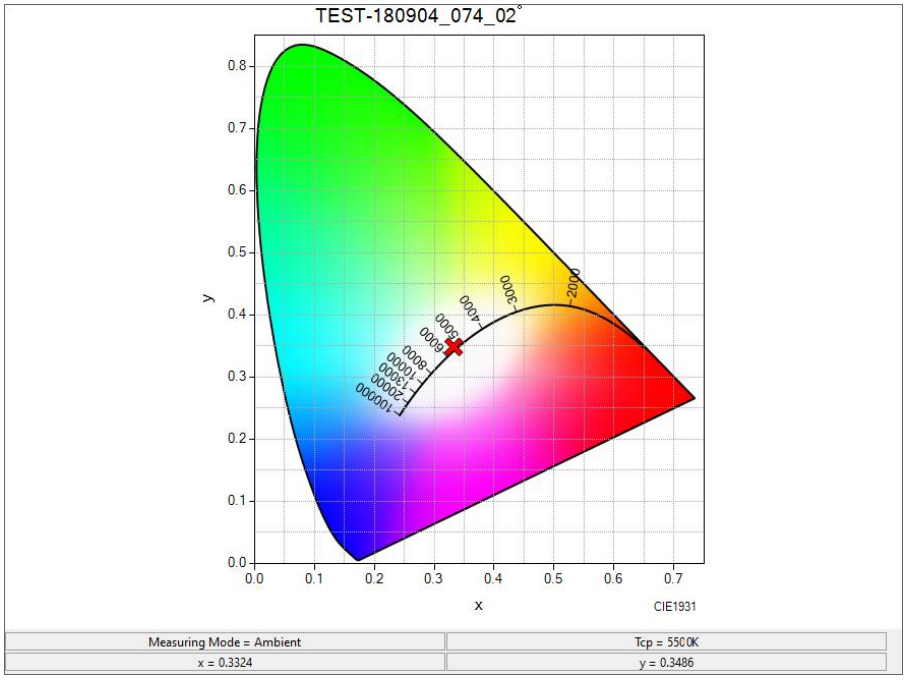

Fig. 4.12 (b): Chromaticity Diagram of Peripheral Light Sources

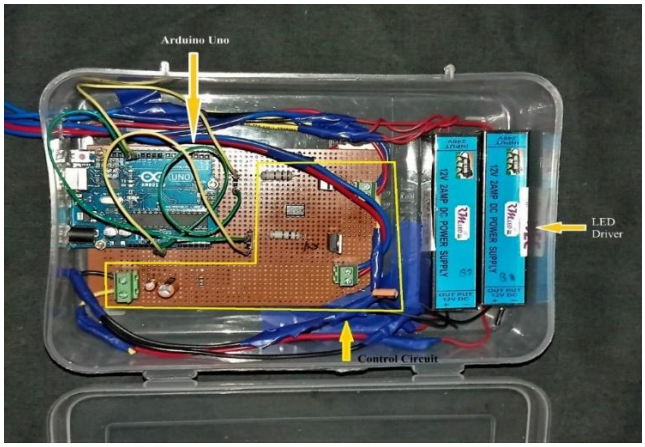

Fig. 4.12 (c): Flickering Source controller

4.5.1.3 Reaction Time Measuring Compact Device

A microcontroller-based timer device was developed to measure Reaction Time (RT) in human subjects. This device features a 16x2 LCD display to show recorded times, with all components, including the active shutter glass circuit, Arduino, display, and wiring, enclosed in a portable box. Powered by a 9V battery, it can timestamp in milliseconds. The researcher starts the timer, while the subject stops it, both using push buttons. Further operational details are provided in the experimental procedures. The active shutter glass, a specialized type of eyewear commonly used in 3D cinemas and VR headsets, includes LCD lenses that normally stay opaque to block visual input. A modified electronic circuit within the frame allows the lenses to switch from opaque to transparent with a 9V battery-powered push button. This setup controls the subject's exposure time, with the active shutter providing 700 milliseconds of visibility, sufficient for object recognition, which typically requires around 100 milliseconds. Connected to an Arduino microcontroller, the push button makes the lenses transparent for 700 milliseconds before automatically reverting to opaque, allowing observers to view grid points at a 2° solid angle. These two devices work together to form the Reaction Time Measuring Compact Device (RTMCD). Fig. 4.5 (a) and (b) provide images of these devices.

4.5.1.4 Other Experimental Setup

In addition to these three elements, the experiment location was also set up carefully. The main smart LED source and two auxiliary flickering sources were mounted on three steel light poles. The primary source was positioned 2 meters above the ground, while the two auxiliary sources, each acting as glare sources, were positioned 1.5 meters above ground near the observers, aimed at their eyes at a 15º angle to the horizontal axis parallel to the ‘A’ column of the grid. Following CIE 140–2000, a grid with 25 evenly spaced points was created, arranged in 5 rows and 5 columns, with each grid point spaced 0.5 meters apart [108]. The main light source or pole was aligned so that its nadir point fell on grid point "E1." The observer was positioned along the extended line that connects all points in column 3, at a distance of 15 meters from grid point "E3." Fig. 4.13 (a) and (b) provides a detailed illustration of the experimental setup, highlighted for clarity.

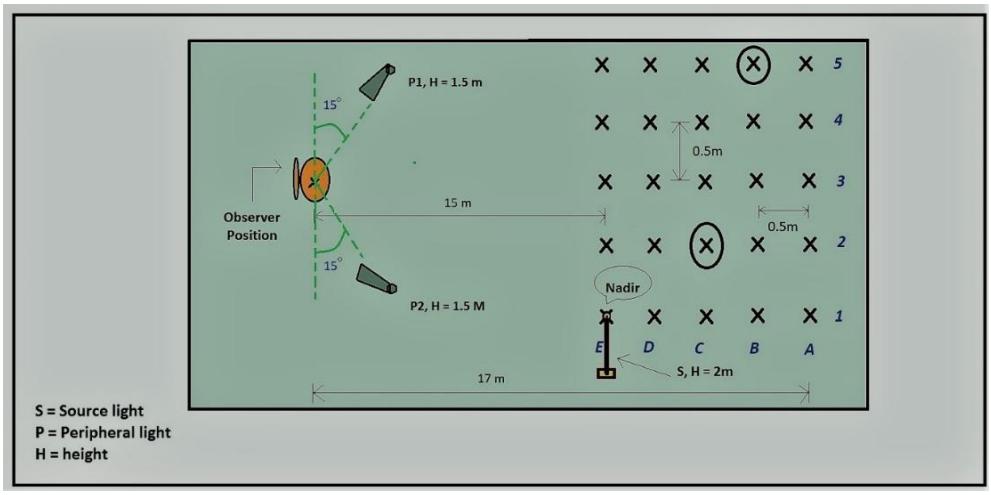

Fig. 4.13 (a): Top view of the experimental setup

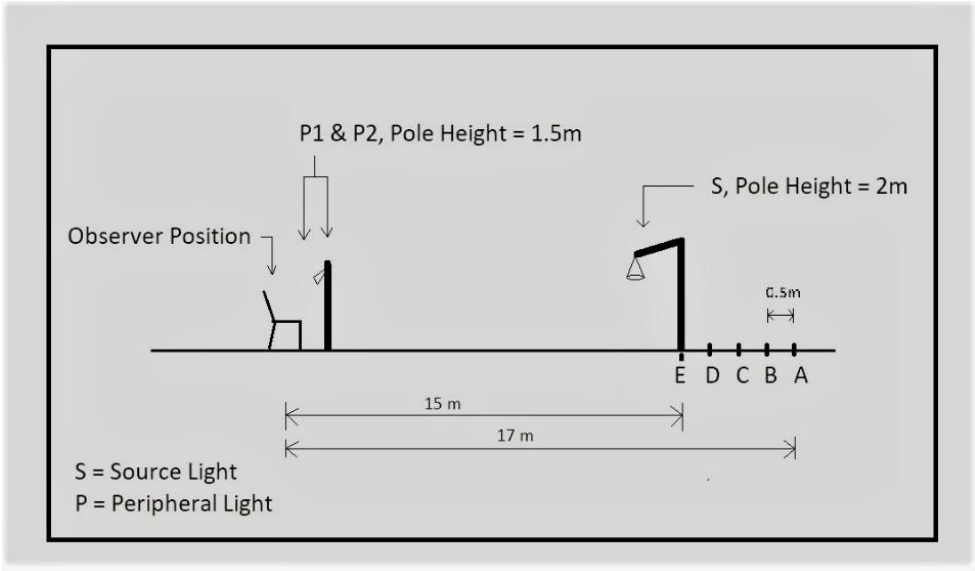

Fig. 4.13 (b): Side View of the Experimental Set-Up

4.5.2 Human Participants

The participants in this study included five healthy individuals (four men and one woman) with an average age of 22.5 years (SD 5%), all in good physiological and neurological health. Each reported normal or corrected-to-normal vision. Before the trial, they were given a comprehensive explanation of the procedure and provided informed consent. The study protocol was approved by the institutional ethics committee. Figure 4.14 (a) shows illustrative image of the experiment, while Figure 4.14 (b) provides a sample image of a participant with special active shutter glass.

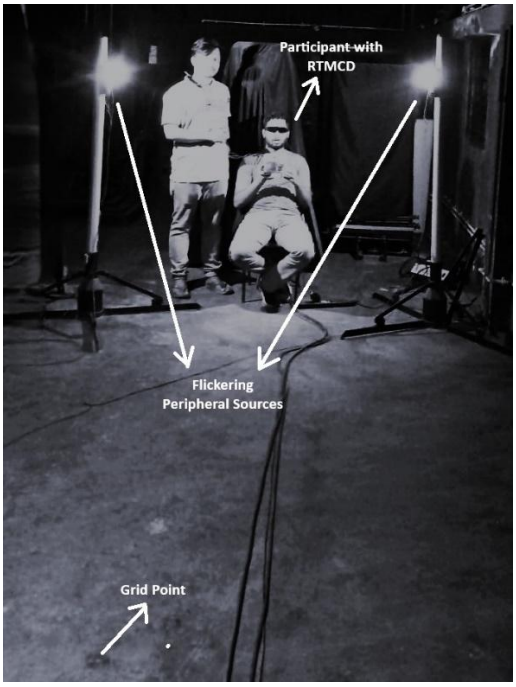

Fig. 4.14 (a): Experiment is going on

Fig. 4.14 (b): Participant with Special Active Shutter Glass

4.5.3 Experimental Procedure

This study was conducted in two main steps. In the first step, the yellow target object was placed at specific grid points, positioned at C2 and B5 grid points, unknown to the observers. The object was placed repeatedly at each point three times under three different CCT levels for the main light source (3000 K, 4500 K, and 6000 K, with SD ±5%), while no peripheral flickering sources were present, resulting in a total of 6 measurements per participant (3 CCT levels x 2 object positions). When the main source was set to 3000 K, its chromaticity coordinates were x = 0.4328 and y = 0.3966; for 4500 K, they were x = 0.3608 and y = 0.3636; and for 6000 K, the coordinates were x = 0.3219 and y = 0.3433. Fig. 4.15 provides detailed chromaticity diagrams for the main source. The object was placed in front of the observers, positioned behind the main source to create positive contrast (making the object appear brighter against its background). The CCT levels were controlled and fixed using a specific Android

application and were verified with a Konica-Minolta CL-70 F colorimeter. Observers were given a designated push button, and the object was placed randomly in front of them, with reaction time (RT) measured using the RT measuring compact device. In the second step of the experiment, the procedures remained the same, but two peripheral flickering sources were added. The flickering frequency was adjusted from 3 Hz to 10 Hz, including intervals at 5 Hz and 8 Hz, for each CCT level of the main source. Reaction times were recorded again, resulting in a total of 24 measurements per participant (3 CCT levels x 4 flickering frequencies x 2 object positions). Fluke 406E laser distance meter is used to measure and fix distances between setup elements. Due to the laboratory environment, any road-like assumptions for the flooring were unnecessary and not categorized. Additionally, a behavioral study was conducted using a predefined Likert scale with the five participants. The Likert scale, a unidimensional measure commonly used by researchers, was employed to capture participants' attitudes and opinions. A detailed questionnaire was administered to participants after each lighting scene, and they recorded their preferences. Picture of the questionnaire is given in Fig. 4.7. The behavioral data were then aggregated by averaging the scores given to each question for each lighting scene, resulting in a summative score on a scale of 10 for each scene. These scores were then averaged across all participants, yielding the final scores used to evaluate the lighting scenes.

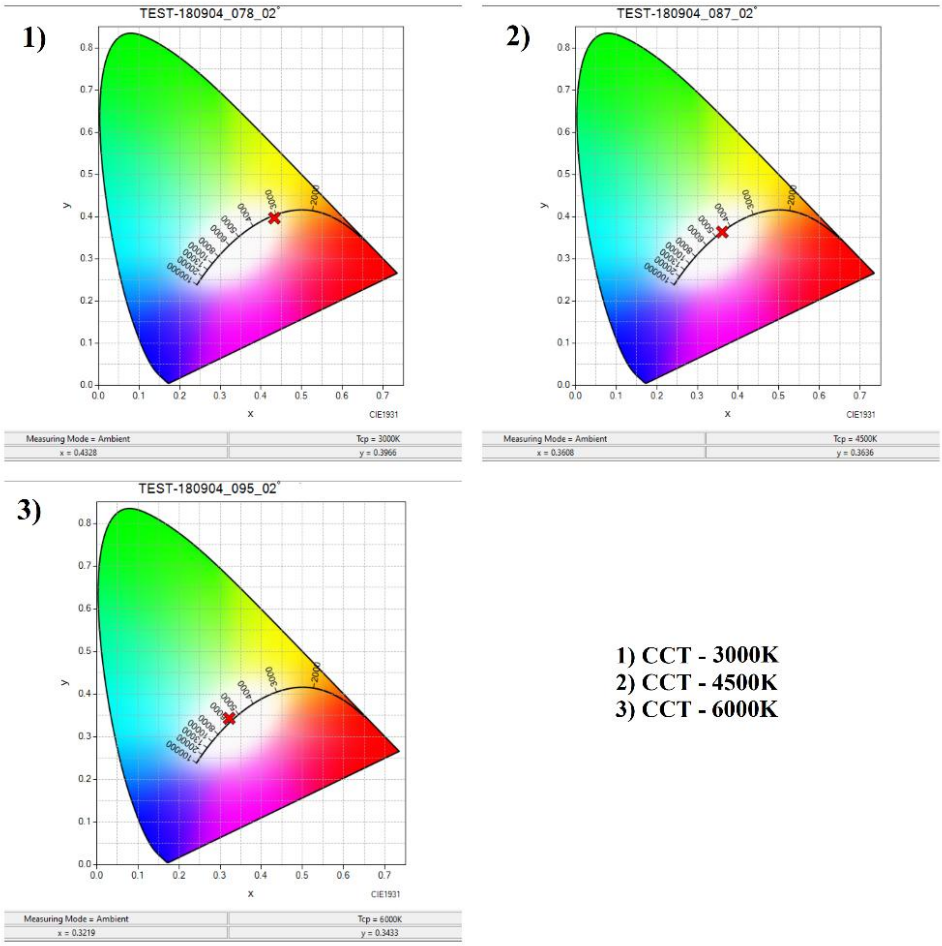

Fig. 4.15: Chromaticity Diagram of Main Source's three CCT level

4.5.4 Calculations and Results

The average reaction time for the five participants was calculated and analyzed in relation to CCT levels and flickering frequencies. Reaction times were plotted against the CCT values of the main source while keeping flickering frequency constant, resulting in five distinct graphs. After gathering behavioral data from questionnaires, each lighting scene received a summative score out of 10, derived by averaging each participant's responses for the scene. These scores were further averaged across all participants to yield final evaluation scores for each lighting scene. The graphs created for flickering frequencies of 8 Hz, 10 Hz, and no flickering show a clear trend: reaction time decreases as the CCT of the main source increases, with the longest reaction times at 3000 K and the shortest at 6000 K. At 3 Hz, however, the reaction time peaks at 4500 K and is lowest at 6000 K. Meanwhile, at 5 Hz, reaction times are longest at 3000 K and shortest at 4500 K. The difference between intermediate and maximum reaction times at 3 Hz, as well as between intermediate and minimum reaction times at 5 Hz, is minimal. Overall, the results indicate that reaction time decreases as the main source CCT increases, regardless of changes in flickering frequency. Additionally, when reaction times were plotted against flickering frequency while keeping the main source CCT constant, three more graphs were generated. Data from the behavioral study show that lighting conditions with flickering frequencies of 8 Hz and 10 Hz, at all CCTs of the main light source, created the least favorable conditions. In contrast, lighting scenes with a 3 Hz flickering frequency at main source CCTs of 3000 K and 6000 K, and a 5 Hz frequency at 4500 K, scored reasonably well, following the scenes with no flickering. This clearly suggests that peripheral flickering generally increases observer reaction times compared to scenes without peripheral flickering. A detailed table of the measured data is presented in Table 4.7. The graphs showing the relationship between reaction times and main source CCTs are provided in Fig. 4.16 (a), (b), (c), (d), and (e), while those between reaction times and flickering frequencies are shown in Fig. 4.17 (a), (b), and (c). Fig. 4.18 (a), (b), and (c) illustrate the average scores given to each lighting scene against flickering frequency at three levels of the main source's CCT. Fig. 4.19 provides an additional graph to explore the relationship between reaction times, CCTs, and flickering frequencies combined.

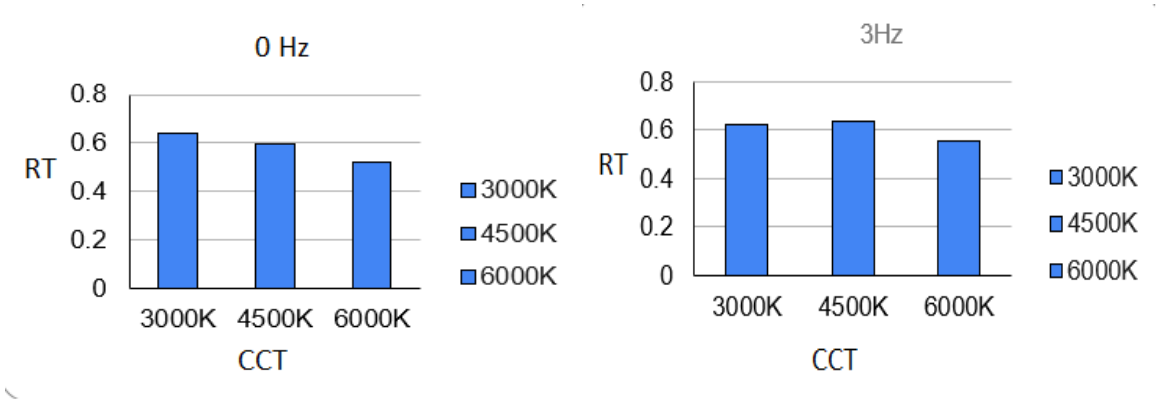

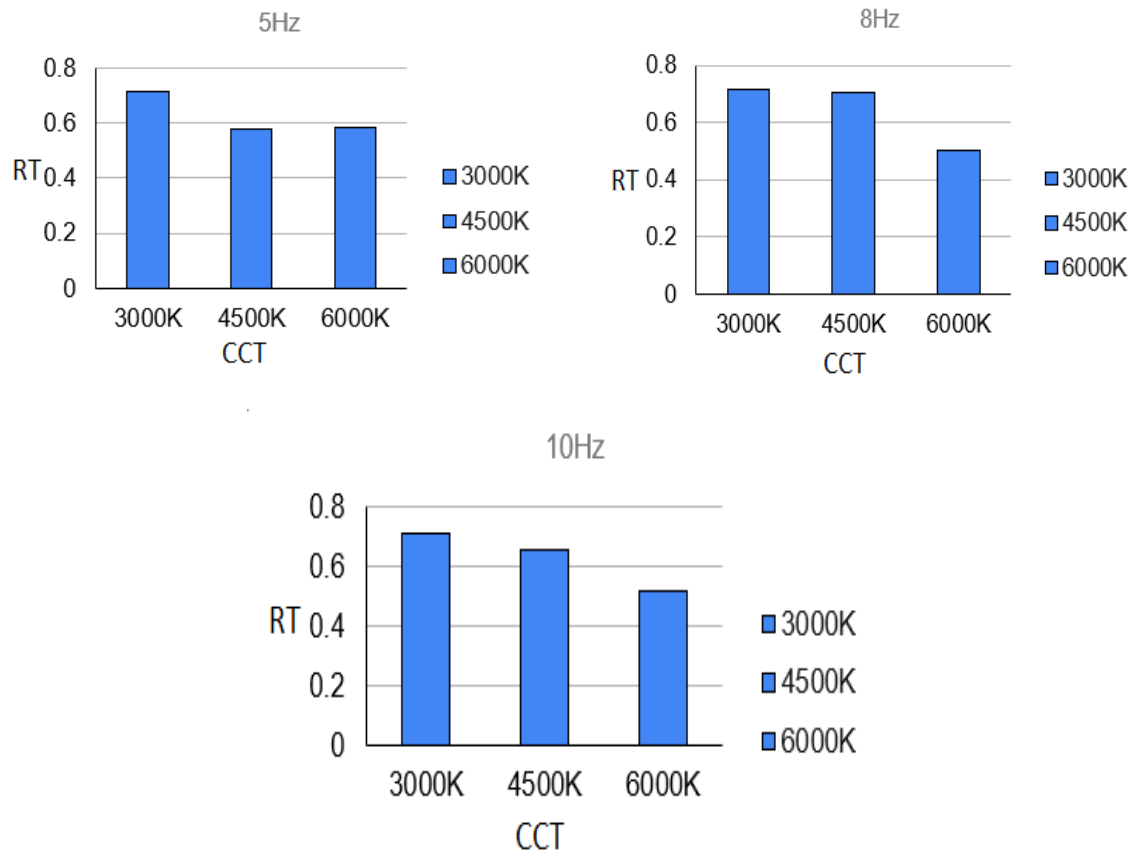

Fig. 4.16 (a), (b), (c), (d), (e): Reaction Time (RT) vs. CCT at different flickering frequencies

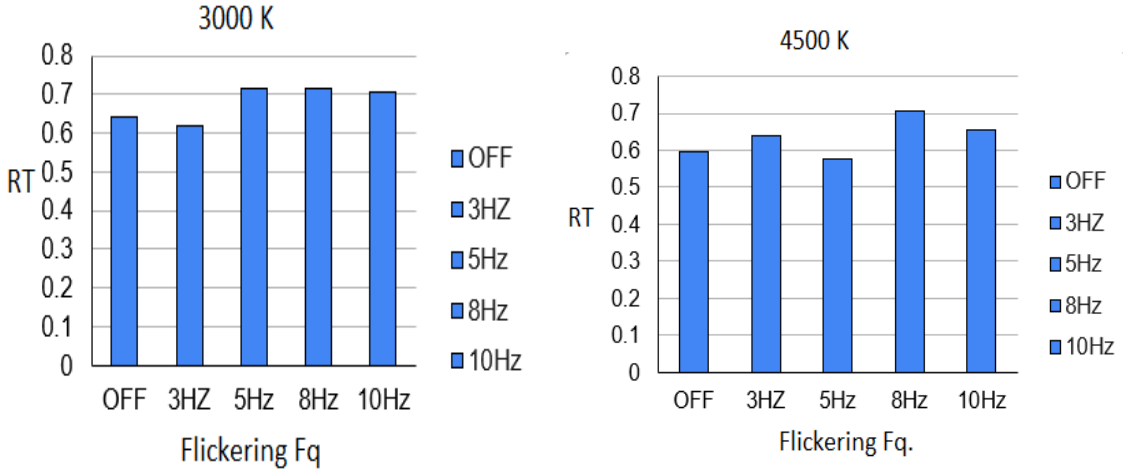

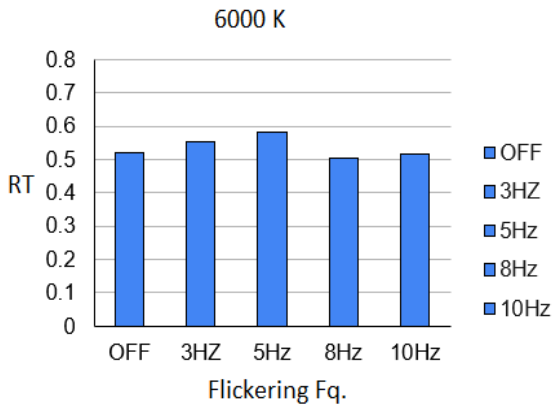

Fig. 4.17 (a), (b), (c): Reaction Time (RT) vs. Flickering frequencies at different level of CCT

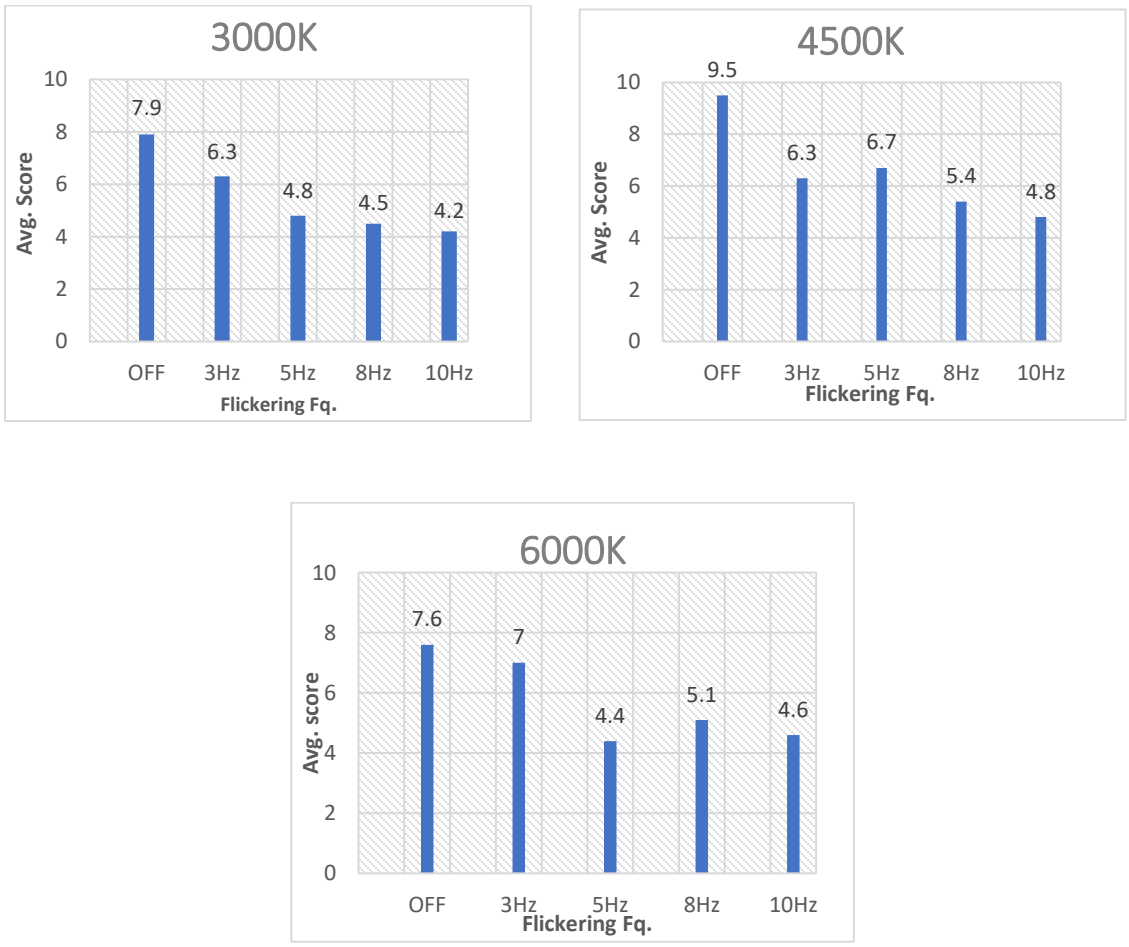

Fig. 4.18 (a), (b), (c): Average score of lighting scene vs. Flickering frequencies at different level of CCT

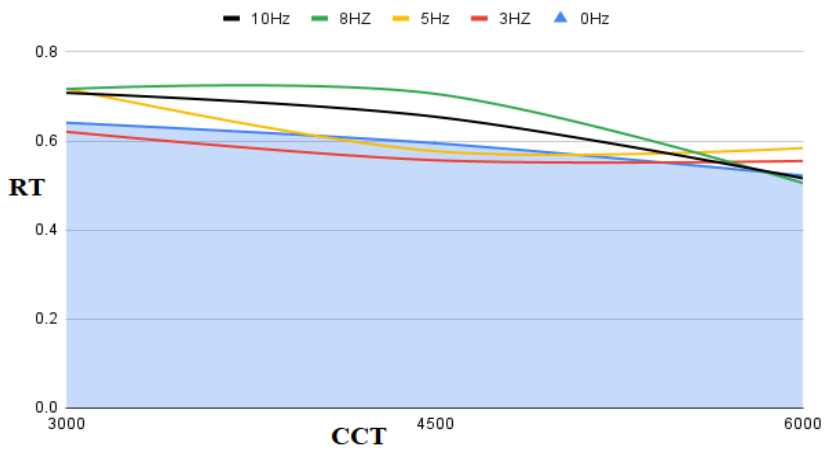

Fig. 4.19: Relation between RT, CCT and Flickering frequencies

Table 4.7: Measured Reaction Time in different level of CCT and Flickering Frequencies

CCT	Flickering Frequencies				
	OFF	3 Hz	5 Hz	8 Hz	10 Hz
3000 K	0.641 s	0.6207 s	0.7176 s	0.7165 s	0.708 s
4500 K	0.595 s	0.639 s	0.577 s	0.706 s	0.6545 s
6000K	0.522 s	0.555 s	0.584 s	0.505 s	0.516 s

4.5.5 Conclusion

The study on reaction times highlights that peripheral flickering significantly impacts an observer's reaction time when detecting objects, as it tends to increase the time required for object recognition. In addition, the behavioral study conducted with participants under the same experimental setup yielded consistent similar results, aligning with the findings from the reaction time measurements for object detection. Observers' reaction times decreased as the CCT of the main light source increased, regardless of changes in flickering frequency. Participants also reported that peripheral flickering was disruptive and acted as an irritating peripheral glare source. Previous studies have demonstrated that higher CCTs for both primary and peripheral light sources notably improve drivers' reaction times and enhance the visibility of small targets (STV) under these lighting conditions. Depending upon these findings, it can be inferred that road lighting designs should minimize sources that may cause peripheral flickering. After a lighting scheme has been installed, it is essential to assess the lighting conditions to identify any potential flickering. If flickering is detected, the waveform should be examined, and corrective measures should be taken as necessary. Moreover, when the use of glaring or flickering peripheral sources is unavoidable, setting the flickering frequency at around 3 Hz is recommended if the ambient CCTs of light sources are 3000 K or 6000 K. If the ambient CCT is around 4500 K, a flickering frequency of approximately 5 Hz would be

ideal. Finally, incorporating high CCT light sources into the lighting scheme could be beneficial for improving visibility and reducing reaction times.

4.6 Work Flow Diagrams

In this section three work flow diagrams are given. The first one describes how reaction time is measured for the previous experiments, given in Fig. 4.20. Second and third diagrams states the experimental steps of the previous two studies and given in Fig. 4.21 and Fig. 4.22.

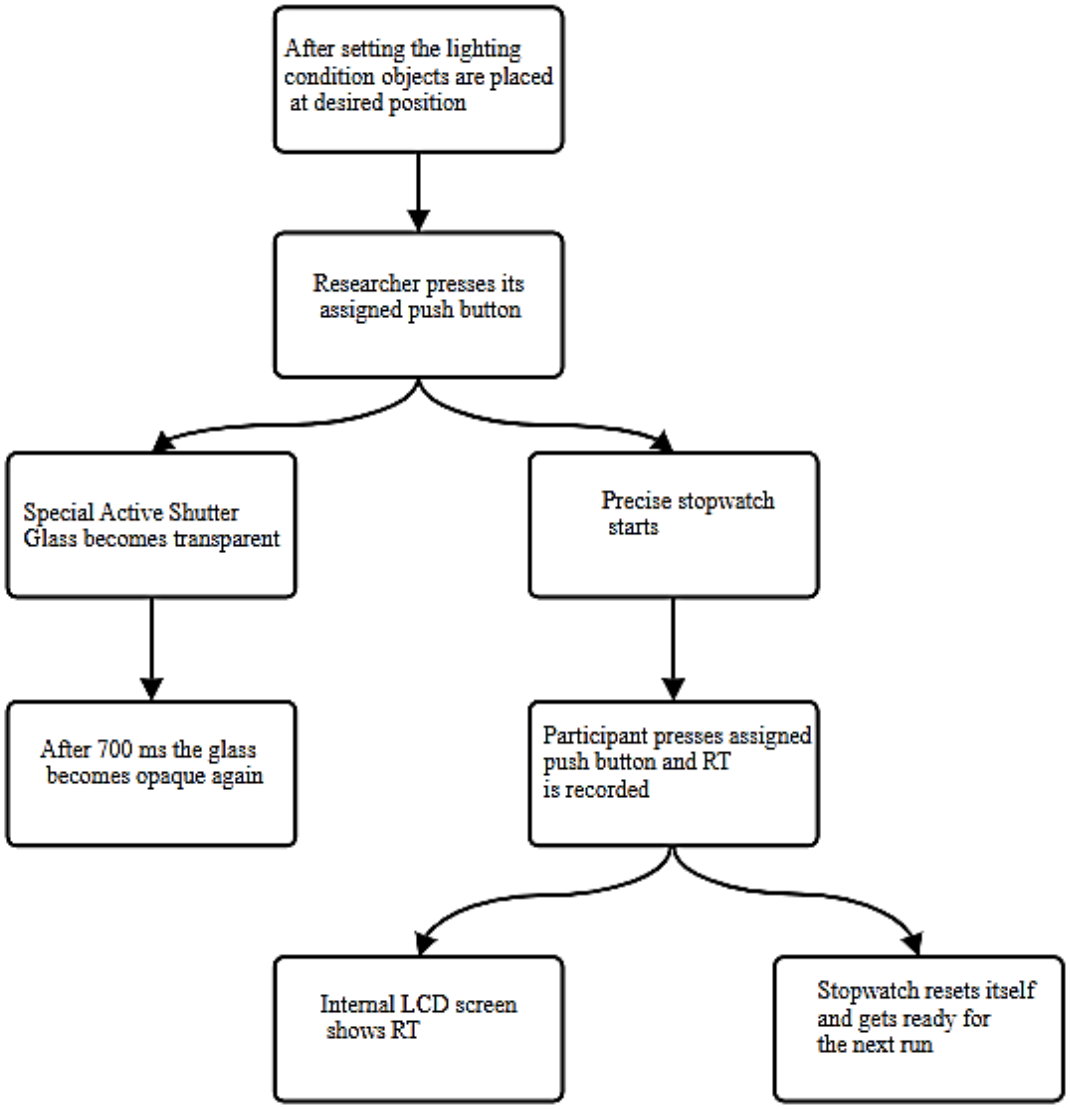

Fig. 4.20: Work Flow Diagram to Measure RT

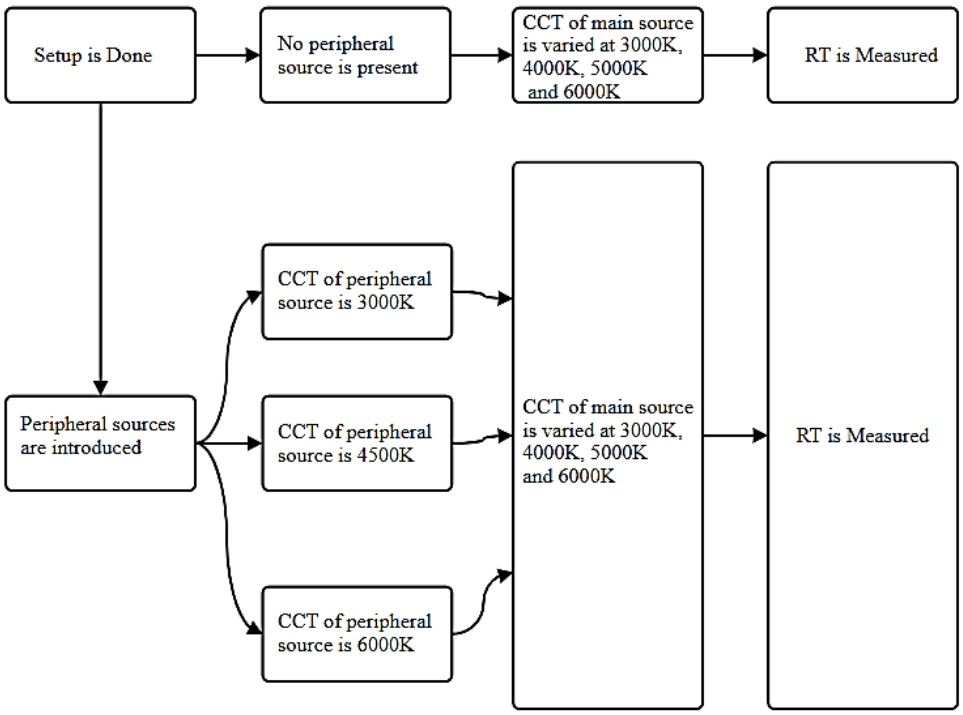

Fig. 4.21: Work Flow Diagram of First Experiment

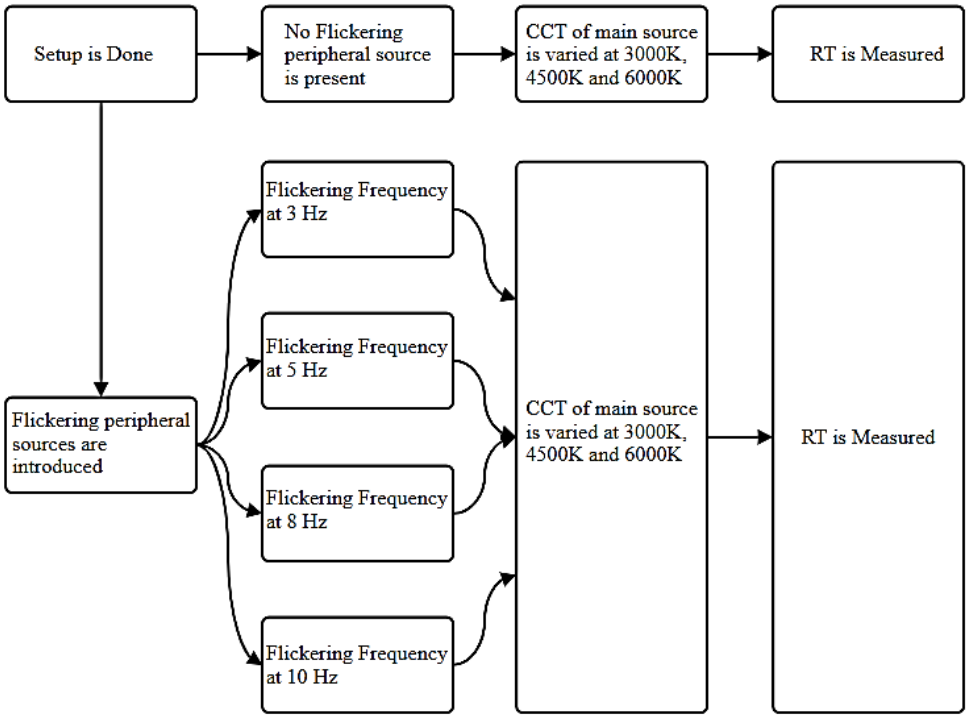

Fig. 4.22: Work Flow Diagram of Second Experiment

Chapter 5: Effect of Lighting Parameter on Object Detection by Human Observers: An EEG and GSR based Novel Approach

5.1 Introduction

Street lighting serves as a specialized application focused on facilitating object recognition and supporting human interactions within dynamic public environments. Primarily functioning as a public lighting system with extended operational hours, street lighting accommodates a wide range of users, drivers and pedestrians, under diverse conditions throughout the day. While its core purpose centers on object detection, specific requirements vary according to the traffic composition at different times. For both drivers and pedestrians, object identification is a critical and cognitively demanding task, especially for nighttime navigation and accident prevention [33-34]. In Indian cities, where roads frequently feature mixed traffic, including pedestrians and bicycles on major roads and motorized vehicles in narrow lanes, this need is particularly pronounced. Lighting impacts human efficiency and presentation via three key mechanisms: the visual system, circadian rhythms, and mood and motivation. Visual system provides an image-based representation of the world, shaping perceptual experience and enabling object detection, which relies on parameters like visual size, luminance contrast, color difference, retinal image quality, and retinal illuminance. Additionally, lighting influences the non-visual system, which affects the circadian rhythm or biological clock, a process managed by the suprachiasmatic nucleus (SCN) related to the retina's ipRGC cells. This system regulates the sleep-wake cycle and other functions through hormonal interactions, with melatonin and cortisol playing significant roles. Lighting further influences mood and motivation, as visual stimuli and the environment surrounding it can induce emotional responses that affect task engagement. Visual discomfort, such as glare or flicker, can impair performance, while thoughtfully designed lighting may communicate symbolic meanings based on context, culture, and social expectations, sometimes outweighing minor physical discomforts. The visual system, as an image-capturing and processing mechanism, projects the external world onto the retina, where initial image processing occurs. Objects are identified by parameters including visual size, contrast, color difference, image quality, and brightness, which together determine the detectability and recognizability of stimuli

[44]. Some studies on object identification and visibility models incorporate human factors such as age and reaction time [23], but they do not fully address the direct impact of CCT from primary and peripheral light sources on the brain's temporal processing. As a result, road lighting designs are not yet fully human-centered. Additionally, the effect of CCT on brain function remains insufficiently quantified, making it difficult to translate this impact into a measurable parameter for on-demand lighting design. This highlights the need to redefine human-centric approaches and the "smartness" of LED lighting. To address this gap, this thesis explores electroencephalography (EEG) and galvanic skin response (GSR) measurements of individuals under varying LED lighting conditions, specifically altering the CCT of main and peripheral sources. EEG and GSR data were gathered using reliable instruments to attempt quantifying these effects and develop a new parameter for street lighting design. Where EEG measures electrical activity in different brain regions, typically in microvolts, via electrodes precisely placed on the scalp, providing insights into cognitive load and processing involved in specific tasks [40]. GSR, a type of electrodermal activity, assesses sweat gland activity that reflects skin conductance changes tied to sympathetic nervous system arousal. Elevated electrodermal activity correlates with heightened arousal, often signaling stress, anxiety, or surprise [41]. These insights indicate that both physiological and psychological elements contribute to overall alertness levels, underscoring the need for further exploration. This thesis aims to contribute new insights to this expanding field of knowledge by finding the visual and non-image forming effects of variation of certain lighting parameter, here CCT, of LED on object recognition task by human observers.

5.2 Background

Object identification on roads is a critical, complex, and cognitively demanding task for both drivers and pedestrians. It is essential for nighttime driving and accident prevention [114-115]. Failure to correctly identify objects and make precise decisions can lead to fatal accidents. Road accidents cause over a million deaths and numerous injuries worldwide, with India accounting for 11% of global fatalities, ranking highest among 199 countries [4-5]. In a 2014 study in Tamil Nadu, visual factors were linked to 47% of accidents, highlighting the role of lighting and visibility for both drivers and pedestrians [66]. Object detection under night-time conditions is challenging due to fluctuating luminance levels on road surfaces, varying shapes, sizes, colors, and movement directions of objects (e.g., on-axis or peripheral) and driver fatigue [77]. Research suggests that adequate street lighting could reduce nighttime fatalities by 65% and injuries by 30% [72,76]. Effective street lighting provides sufficient illuminance and luminance, helping drivers maintain stability and accuracy for object detection. The degree of object recognition, under various lighting sources and scenes, is evaluated through human-centered parameters like reaction time (RT), visibility level (VL), and small target visibility (STV). Studies have shown that variations in correlated color temperature (CCT) in white LED sources can impact both visual and non-visual cognition in road users. In the past three decades, street lighting design has shifted from illuminance-based to luminance-based approaches, as luminance is central to human vision [70]. In 1989, W. Adrian introduced a formula for calculating VL, demonstrating that luminance, age, and glare significantly impact object identification [23]. This model has since been included in various road lighting standards [24]. An alternative, the visibility index (VI), based on luminance and contrast, was developed but gained limited use due to complex calculations [110]. Researchers have validated the VL model [113]. Studies on the visual and behavioral effects of CCT variations of LEDs on VL and RT of human observers for object identification task indicate that as CCT

increases, RT decreases, and VL improves [116]. Other research found that RT decreases with higher CCT in main LED sources, despite flickering peripheral lights. However, an increase in flicker frequency in peripheral lights can increase RT [117]. Although some object identification and visibility models consider human factors like age and RT, they do not fully address the direct effect of CCT from main and peripheral light sources on temporal brain processes of human observers. As a result, road lighting schemes lack a fully human-centered approach. Additionally, the influence of CCT on brain function has not been sufficiently quantified to provide an empirical parameter for on-demand lighting design, underscoring the need to redefine human-centered LED lighting approaches. This study investigates electroencephalography (EEG) and galvanic skin response (GSR) measurements under varied lighting conditions, focusing on CCT adjustments in primary or on-axis and peripheral LED light sources. Reliable devices were used to capture EEG and GSR data, with an aim to quantify these effects and propose a new parameter for street lighting design. A behavioral and RT data comparison was also conducted to support the experimental claims. EEG records electrical brain activity in microvolts across different regions via electrodes on the scalp, capturing both cognitive processing and artifacts from facial and bodily movements, which are treated as noise during cognitive analyses [40]. A lab-based study found significant ERP differences under high-pressure sodium vapor (HPSV) versus metal halide (MH) lighting, with MH lighting enhancing object identification efficiency [118]. In real-road EEG studies, MH lighting was superior to HPSV for cognitive performance [119]. In another study, simulated EEG analysis of urban drivers showed that warmer CCT of light sources positively influenced driving-related cognitive processing [120]. GSR, an electrodermal activity measurement, assesses sweat gland activity linked to sympathetic nervous system arousal. Elevated electrodermal activity, often associated with stress, fear, anxiety, or surprise, is measured through skin conductance responses (SCR) or the phasic part of GSR [41]. In this study, GSR data complemented EEG findings to detect mental strain in participants' responses [121]. Many studies have utilized GSR or the phasic part as a secondary measure to assess participants' stress levels through skin conductance analysis [122-123]. In fact, one study differentiated cognitive load and stress using GSR data analysis [124]. As the background suggests, to study the image-forming and non-image-forming effects of CCT variations of Main or on-axis and peripheral LED sources on object identification task by human observers, an experimental setup was created in the Illumination Engineering Lab of Electrical Engineering Department of Jadavpur University. The setup included three wirelessly controlled, low-power LEDs in a simulated dark environment, with one LED serving as the main source and the other two as peripheral sources. Twelve lighting scenarios were created by adjusting CCT levels of the main and peripheral sources. EEG, GSR, and RT data were measured for two specific object positions with high positive contrast. Results indicated that CCT variations in primary and peripheral sources strongly affected brain activity, GSR signals, RT, and behavior. The study found that a CCT range of 4500K to 5000K for both main and peripheral sources is optimal for accurate object recognition. Excessively high or low CCT, producing a bluish or reddish hue, delayed object recognition and increased RT. Additionally, the low-to-high frequency power ratio in the logarithmic spectral power plot of EEG recordings may serve as a metrical for assessing the human-centered quality of a particular lighting scene. Through extensive research, scientists have identified different types of brain waves, which are primarily classified into five categories according to their frequencies. As brain activity intensifies, the frequency of these waves also rises. Listed in ascending order of frequency, the categories include Delta, Theta, Alpha, Beta, and Gamma waves. Table 5.1 below provides a simplified overview of the significance of each brain wave type.

Table 5.1: Details about Brain Waves

Brain Wave	Frequency range	Important Features
Delta	0.5-8 Hz	***Key Feature:*** *Cure, sleep very well.* This wave has the lowest frequency of all. It denotes minimal brain activity. Delta is most prominent when someone is in deep sleep or in a state where he has no external awareness for example meditation. Delta is also associated with empathy and intuition.
Theta	3-8 Hz	***Key Feature:*** *Deep relaxation, meditation, Improved Memory* Theta signals dominate when we dream in light sleep many times it is called having a dream consciously. Also, during meditation Theta signals are produced. It is also associated with stress relief and memory relocation.
Alpha	8-12 Hz	***Key feature:*** *Creativity, Relaxation, Visualization* Alpha signals are associated with overall body and mental coordination, calmness, alertness. It is said that this signal denotes the best condition for reflex and problem solving and visualization when we are learning or doing something creative.
Beta	12-38 Hz (Beta 1: 12-15 Hz, Beta 2: 15-22 Hz, Beta 3: 22-38 Hz)	***Key feature:*** *Being aware, Concentration.* Denotes a state of high consciousness and alertness and focus towards a cognitive task in decision making or judgement or producing new ideas. It is beneficial for productivity for the tasks that require a higher level of brain engagement and concentration.
Gamma	38-42 Hz	Fastest of brain waves, highly prominent when expanded consciousness and spiritual emergence, altruism.

5.3 A Laboratory Based Investigation into the Impact of CCT Variations of LED on Human Object Recognition: A Novel Approach Using EEG and GSR

Research has demonstrated that CCT of light sources have notable influences on human drivers' ability to identify objects. EEG-based studies are highly effective for identifying neural responses to real-life stimuli. However, other factors can also affect neural responses. Thus, EEG alone cannot serve as a fully effective standalone approach; combining it with behavioral studies enhances the accuracy and objectivity of the findings. Consequently, behavioral and physiological studies are essential to measure the effects of various CCT levels in street lighting. For this reason, a laboratory study was conducted to study the behavioral effect of different CCT levels in main and peripheral LED lighting on object recognition by stationary human observers within simulated lighting environments. The study aimed to gain insight into possible brain processes and emotional responses during object recognition tasks using electroencephalography (EEG) and galvanic skin response (GSR). The effects of CCT levels from both peripheral and main on-axis sources on EEG frequency bands, event-related potentials (ERPs), and GSR were analyzed. Additionally, reaction time and behavioral data were collected to correlate these findings. Results indicate that a CCT

range of 4500K to 5000K for both primary and peripheral light sources is ideal for accurate object recognition. Furthermore, a scoring factor for lighting scenes was proposed to assess human-centered design, which could serve as a future metric.

5.3.1 Experimental Setup Development

This experimental study was planned and orchestrated to examine the impact of different CCT levels in main and peripheral LED light sources on the brain's temporal processing, GSR signals, reaction time in object detection, and the behavioral responses of stationary human observers. The complete experimental setup consists of four primary components: EEG, GSR, reaction time, and behavioral experiment setups. Excluding these four sections, other experimental setups are also described in this section.

5.3.1.1 EEG Setup

In this object detection study involving stationary human participants, a 14-channel portable EEG headset is employed to capture time-dependent brain signals specifically related to object detection events. The study utilizes the Emotiv Epoc X wireless EEG device, which is positioned on participants' heads following the international 10-20 electrode placement system. In this system, '10' and '20' designate the intervals between neighboring electrodes. These distances are determined as 10% or 20% of the overall skull length, measured either along the anterior-posterior or lateral axis [125]. Fig. 5.1 (a) illustrates the 10-20 system layout. Once the EEG headset is secured on the participant's head, data recording begins through a dedicated laptop, where a specific key is assigned for marking event occurrences. The setup protocol requires participants to keep their eyes open for one minute, then closed for one minute, and subsequently engage in the object detection task. This task is supported by a lab-developed special active shutter glass, designed to block peripheral stimuli in normal conditions, otherwise the brain may engage with peripheral stimulus, and is connected and synchronized with the reaction time measuring device. An illustrative image is shown in Fig. 5.1 (b).

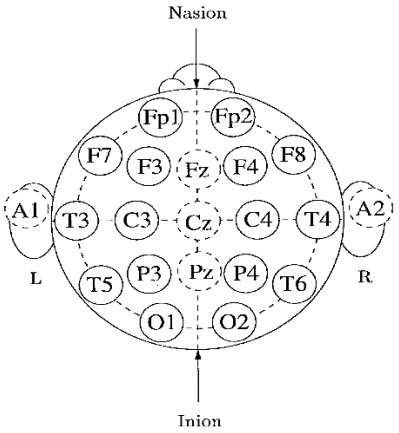

Fig. 5.1 (a): 10-20 Co-ordinate system

Fig. 5.1 (b): Special Active Shutter Glass

5.3.1.2 GSR Setup

To measure electrodermal activity (EDA) or galvanic skin response (GSR) of stationary participants during object recognition tasks, a laboratory-developed device based on an Arduino Uno microcontroller was created. This device employs a Seed Studio Grove GSR sensor with an operating voltage of 3.3 or 5V and adjustable sensitivity. Previous research has shown that such low-cost GSR sensors can provide sufficient accuracy for recording GSR signals in this type of experimental setup, offering a cost-effective alternative to expensive branded equipment [65]. During the object detection experiment, participants wear two nickel electrodes embedded in finger bands on adjacent fingers, allowing for continuous GSR signal recording. These electrodes connect to the GSR sensor, which measures the resistance between them and converts it into an analog signal. The data is recorded onto a microSD card as a .txt file for later analysis. A 5mm blue LED inside the device serves as an indicator, confirming flawless data recording onto the microSD card. An illustrative image is shown in Fig. 5.2. Responsible code for GSR device is given in Annexture 1.

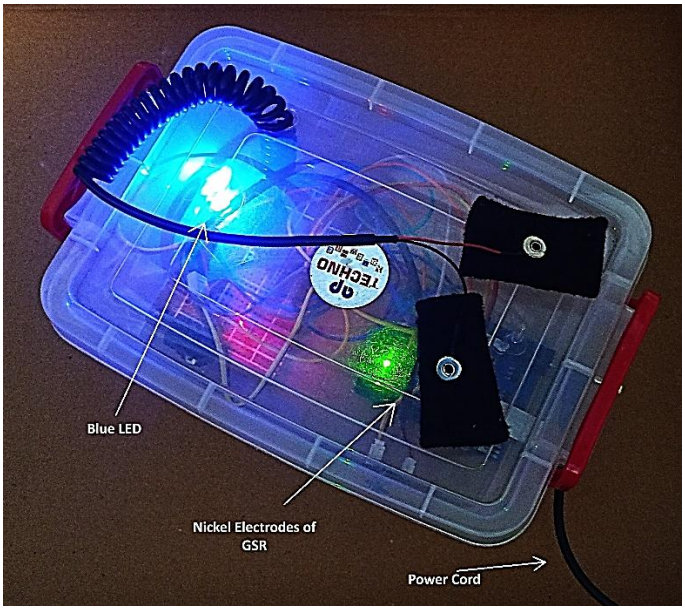

Fig. 5.2: GSR Device

5.3.1.3 Reaction Time Measuring Setup

Previously, in other experiment a rudimentary version of reaction time measuring device is used. It was replaced by a new, more compact and rugged reaction time measuring device, where the control circuit for special active shutter glass is eliminated and the glass is directly attached with the Arduino Uno microcontroller, with OLED screen. To measure participants' reaction times, a specialized device called the Reaction Time Measuring Compact Device (RTMCD) v2.0 was developed. This lab-built device uses an Arduino-based (Uno Rev3) microcontroller synchronized with programmed active shutter glasses. The glasses are typically opaque or dark, used to block the wearer’s view. Both the participant and the researcher are provided with separate push buttons. When the researcher presses their button,

a timer with millisecond precision starts, and the glasses become transparent for 700 milliseconds before turning opaque again. During this brief transparent window, the participant has an opportunity to recognize objects. Once an object is identified, the participant presses their designated push button, stopping the timer, and the reaction time is shown on an OLED screen, as shown in Fig. 5.3.

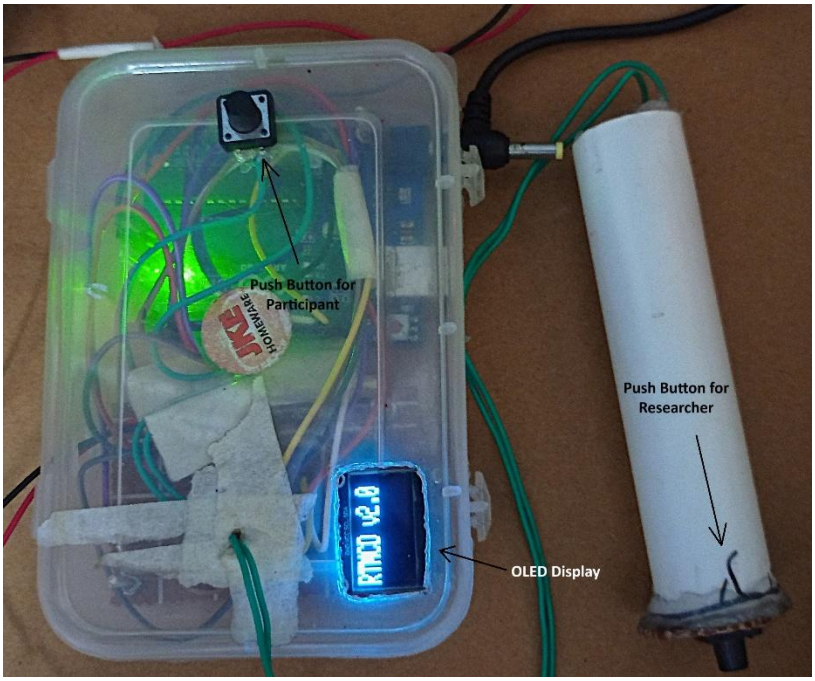

Fig. 5.3: RTMD v2.0

5.3.1.4 Behavioral Study Setup

To evaluate the behavioral responses of participants in the object recognition experiment under varying CCT levels of main and peripheral light sources, a questionnaire with four questions was provided. These questions are grouped into two primary parts: subjective and objective questions. Responses to the subjective questions are based on the participants' feelings about the lighting scene presented, while answers to the objective questions depend on the perceived color, shape, and general appearance of the objects. Each answer is recorded and marks are given to the answer for each participant under each lighting scene and object position, following the Likert scale method [126]. After recording all scores, average scores are calculated for each lighting scene.

5.3.1.5 Other Experimental Setup

In addition to the four main setups, the experiment required a carefully controlled lighting and environmental setup. The experimentation was carried out in a specially designed black laboratory to minimize light reflection, maximize absorption, and significantly reduce glare and flicker impacting the participants' eyes. To achieve this effect, additionally the floor was also covered with black jute. Three smart, CCT-tunable 12-watt LED bulbs were mounted on three

miniature steel street light poles to simulate scaled-down road lighting scenarios. One pole contained the main light source, positioned at a height of 2 meters, while the two peripheral sources mounted on other two poles, each 1.5 meters high, provided peripheral lighting. These LED bulbs, which emit 820 lumens and have a B22 base, were controlled through an Android app. The main light source was positioned directly in front of the subjects, with a marked nadir point directly beneath it representing the point of maximum illuminance. Using the nadir as a reference, a grid of eight equidistant points (0.75 meters apart) was laid out following the CIE 140-2000 standard [108]. This grid was organized into two columns with four rows labeled A1 to A4 in one column and B1 to B4 in the other, with B1 as the nadir point. Iso-lux diagrams are drawn for better understanding of the overall uniformity (U_o) and are given in Fig. 5.4 (a) and 5.4 (b), where the first figure depicts the Iso-lux diagram when there are no peripheral sources and the second figure depicts the Iso-lux diagram when there are peripheral sources present in the lighting scenes. The subjects were placed 15 meters from the nadir, with their eye level set at 1.15 meters above the ground, measured using a Fluke 406E laser distance meter. Additionally, the peripheral light sources were placed behind and to the sides of the subjects, 5 meters apart, and focused on the grid. Each LED source was fitted with a black conical baffle to prevent glare. Objects of various shapes, colors, and reflective properties were used for the object identification task. The main LED source was also covered with a small baffle to reduce glare. Both main and peripheral sources were arranged to achieve uniformity levels of 0.166 and 0.17 along columns A and B respectively and 0.34 across the grid, aligning with "Group-B" road lighting standards in India [68]. Details of the used objects for object identification task are given in Table 5.2. For the object identification, contrasts at each grid point were measured using a Konica Minolta LS-100 luminance meter, and grid points A2 and A3, having the highest positive contrast values, were chosen for object placement. The experiment tested four CCT levels (3000K, 4000K, 5000K, 6000K) for the main source and three CCT levels (3000K, 4500K, 6000K) for peripheral sources, creating 12 unique lighting conditions (4 main CCT levels × 3 peripheral CCT levels). Fig. 5.4 (c) and Fig. 5.4 (d) provide a visual overview of the setup.

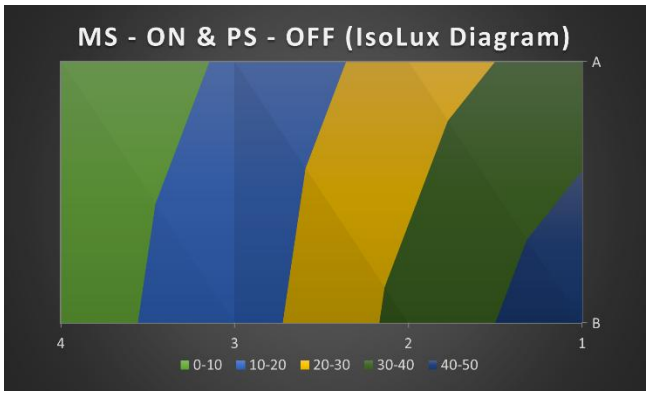

Fig. 5.4 (a): Iso-lux diagram (Peripheral Sources-off)

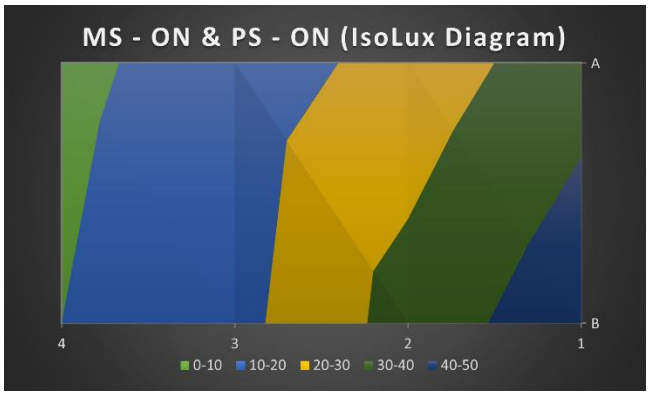

Fig. 5.4 (b): Iso-lux diagram (Peripheral Sources-on)

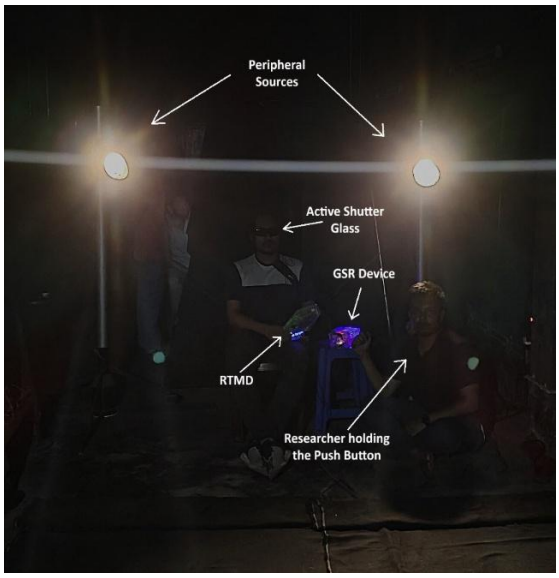

Fig. 5.4 (c): Set-up of Peripheral Source and Observer

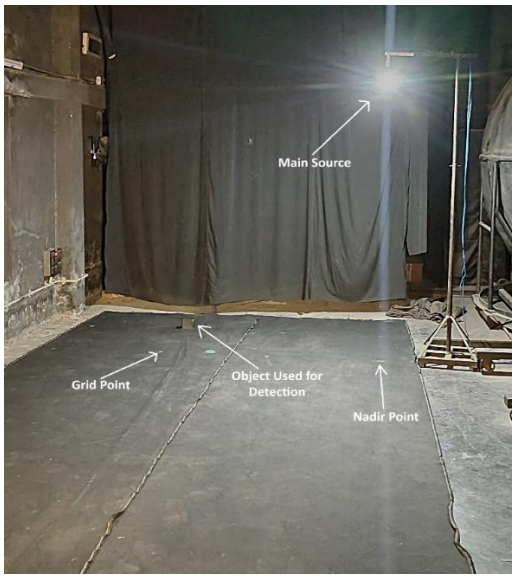

Fig. 5.4 (d): Set-up of Main Source and Object

Table 5.2: Details of Presented Objects

Sl No.	Object Shape	Object Colour	Reflectance (%)	Object Dimension		Picture of Object
1	Cuboid	Yellow	24.2	length (cm)	8	
2		Green	16.6	Width (cm)	8	
3		Violet	17			
4		Black	11.6	Height (cm)	8	
5	Cylindrical	Yellow	24.8	Diameter (cm)	8	
6		Green	17.2			
7		Violet	18.6	Height (cm)	9	
8		Black	10.5			
9	Prismatic	Yellow	23.9	Base Length (cm)	10	
10		Green	15	Base Width (cm)	10	
11		Violet	17.4			
12		Black	10.8	Height cm)	8	

5.3.2 Participants

The study included ten healthy participants, consisting of six male and four female university students, all of East Indian origin, with an average age of 22.1 years (SD = 5%). Study inclusion criteria included right-handedness and normal or corrected-to-normal vision. They were told to get sufficient sleep and avoid specific light exposure for at least one week prior to the experiment. Before the experiment, participants were thoroughly told about the questionnaire and experimental procedure, and written consent was obtained from each. The laboratory's indoor temperature was maintained at a constant 20°C during the experiment. Participants were also asked to wash their hair with shampoo to reduce dandruff, which would lower the resistance between the EEG electrodes and the scalp, allowing for optimal EEG recording. Ethical approval for this procedure was obtained from the University ethics committee. Fig. 5.5 provides a visual representation of an observer wearing the EEG headgear and special active shutter glass.

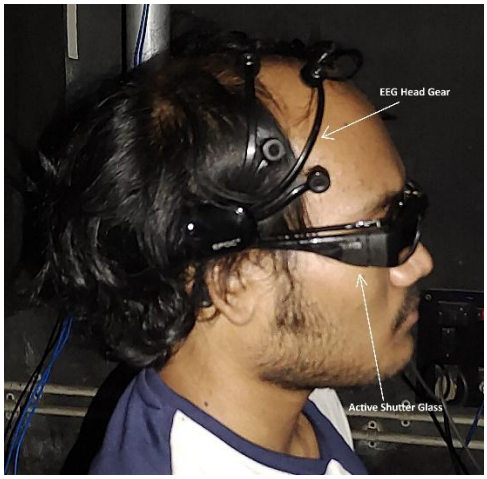

Fig. 5.5: An Observer with EEG Head Set and Special Active Shutter Glass

5.3.3 Experimental Procedure

To set up the experimental bed, luminance values were first measured at each grid point using a luminance meter, where the grid points are marked on the basis of nadir point's position. Once luminance values were collected, contrast values were calculated, and grid points A2 and A3, which showed the highest positive consecutive contrast values, were selected to enhance visibility for participants. Selected objects were then randomly placed at these points, unknown to the subjects, for an object detection task. The experiment recorded four types of data: EEG, GSR, reaction time (RT), and behavioral data, as described previously. Smart LEDs were adjusted to the desired CCT values to create specific lighting scenes using an Android app. Subjects were suited with a 14-channel EEG headset, with saline solution applied to the electrodes to maintain low inter-electrode impedance (< 20 KΩ). They also wore active shutter glasses and GSR electrodes. EEG signals were recorded wirelessly on a laptop using Emotiv Pro software. Subjects were told to keep their eyes open for one minute and then close them for another minute, with events automatically marked at the start and end of each phase in the laptop. GSR recording started simultaneously with EEG. Participants held the RTMD device

and were instructed to press a button on it when they identified an object in the lower frontal vicinity. Each time the special active shutter glasses turned transparent or an object detection task was initiated, an event was marked as a stimulus onset on the assigned laptop. After setting up the devices and darkening the active shutter glasses, a random object was placed at either A2 or A3, and subjects were notified to prepare. When they indicated readiness, a researcher behind the subject pressed a button on the RTMD device, turning the shutter glasses transparent, while another researcher marked the event in the EEG recording in assigned laptop. Participants then had 700 milliseconds to view the lower frontal area and pressed the RTMD button when they identified the object. Reaction time (RT) was recorded and displayed on an OLED screen. After each detection, subjects answered a questionnaire, from which the behavioral data are gathered. Another object was then placed on the remaining selected grid points, and the process was repeated. Thus, each subject identified two objects randomly placed at the two selected grid points under each lighting scene, while EEG, GSR, RT, and behavioral data were continuously recorded. The procedure was repeated for all ten subjects under twelve different lighting scenes. EEG data were saved in European Data Format (.edf), GSR data in text files (.txt), and all other data in Excel sheets. Illustrative images are shown in Figure 5.6 (a) and (b).

```
-------------------------------------
2024-4-30 19:27:0  --  gsr_average = 560,
2024-4-30 19:27:1  --  gsr_average = 560,
2024-4-30 19:27:1  --  gsr_average = 560,
2024-4-30 19:27:2  --  gsr_average = 560,
-------------------------------------
2024-4-30 19:41:23  --  gsr_average = 213,
2024-4-30 19:41:23  --  gsr_average = 213,
2024-4-30 19:41:24  --  gsr_average = 212,
2024-4-30 19:41:24  --  gsr_average = 213,
2024-4-30 19:41:25  --  gsr_average = 213,
2024-4-30 19:41:25  --  gsr_average = 213,
2024-4-30 19:41:26  --  gsr_average = 213,
2024-4-30 19:41:27  --  gsr_average = 215,
2024-4-30 19:41:27  --  gsr_average = 214,
2024-4-30 19:41:28  --  gsr_average = 214,
2024-4-30 19:41:28  --  gsr_average = 214,
2024-4-30 19:41:29  --  gsr_average = 215,
2024-4-30 19:41:30  --  gsr_average = 215,
```

Fig. 5.6 (a): Recorded GSR Data

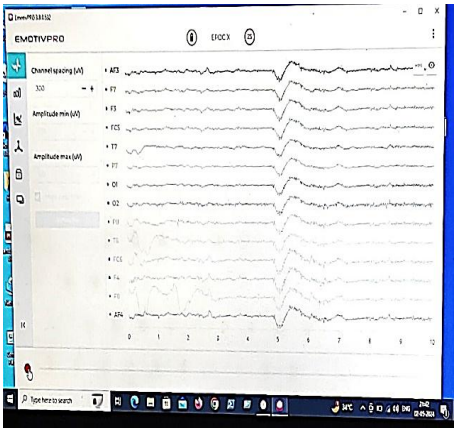

Fig. 5.6 (b): EEG Recording is being Taken

5.3.4 Analysis and Results

This experiment investigates the effect of varying the CCT of main and peripheral smart LED sources on both visual and non-visual responses of a stationary human subject in a simulated lab setting. Measurements were taken and evaluations are done based upon EEG, GSR, reaction time (RT), and behavioral assessments. Following the setup, the experimental procedure was conducted, and the mentioned data were collected with precise instruments. The analysis of this data is then conducted using multiple methods, organized into four sections, with each section dedicated to analyzing a specific data type. These are –

5.3.4.1 Reaction Time Data Analysis

As described, reaction time (RT) for object identification by a static observer is measured using a reaction time measuring compact device (RTMCD v2.0). Each of the twelve lighting

conditions was used for two object identification tasks, performed by ten subjects. To simplify, the RTs for both tasks under the same lighting scene are averaged for each subject, and these averaged RTs are then averaged across all 10 subjects for that particular lighting scene. Next, with the main source CCT held constant, the RTs for three different CCT levels of the peripheral sources are averaged, and these RTs are plotted against the main source CCTs, shown in Fig. 5.7 (a). A similar graph, shown in Fig. 5.7 (b), plots peripheral source CCT against averaged RTs, where peripheral CCTs are held constant and RTs are averaged across four levels of main source CCTs. The results from these graphs show that RT is lowest at a 5000K CCT for the main source when averaging the effects of the peripheral sources. Similarly, RT is lowest at 6000K for the peripheral sources when averaging the main source's effect. Conversely, RT reaches its highest value at 3000K for the main source with the peripheral effects averaged, and at 4500K for the peripheral sources with the main source effects averaged. Table 5.3 and Table 5.4 describe the average values of reaction times for main source, where the effects of peripheral sources are averaged and for peripheral sources, where the effect of main source is averaged.

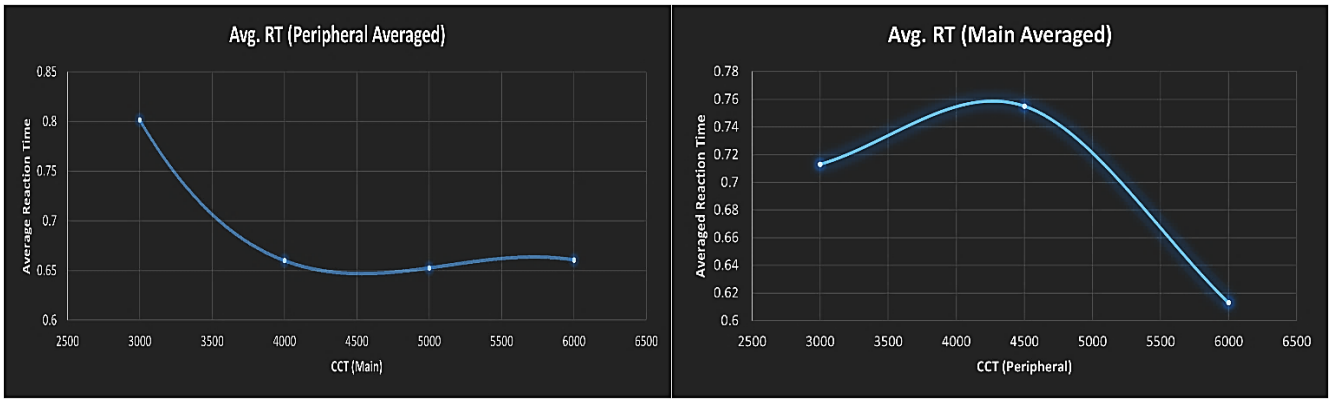

Fig. 5.7 (a) & (b): Average RT vs CCT of Main Source and Average RT vs CCT of Peripheral Sources

Table 5.3: The average values of reaction times for main source, where the effects of peripheral sources are averaged

Main CCT	Peripheral CCT	Avg. Scores of each lighting scene	Avg. Scores when Peripheral is averaged
3000	3000	0.739	0.801334
	4500	0.856	
	6000	0.809	
4000	3000	0.82	0.66
	4500	0.595	
	6000	0.565	
5000	3000	0.693	0.652667
	4500	0.67	
	6000	0.595	
6000	3000	0.6	0.660667
	4500	0.899	
	6000	0.483	

Table 5.4: The average values of reaction times for peripheral sources, where the effects of main source is averaged

Peripheral CCT	Main CCT	Avg. Scores of each lighting scene	Avg. Scores when Main is averaged
3000	3000	0.739	0.713
	4000	0.82	
	5000	0.693	
	6000	0.6	
4500	3000	0.856	0.755
	4000	0.595	
	5000	0.67	
	6000	0.899	
6000	3000	0.809	0.613
	4000	0.565	
	5000	0.595	
	6000	0.483	

5.3.4.2 Behavioral Data Analysis

After each object detection task under a specific lighting scene and object position, a questionnaire with four questions is given to the observer. These questions fall into two main categories: subjective and objective, each with distinct evaluation criteria as previously discussed. Subjective questions use a Likert scale, scoring from '0' to '3', with '2' and '1' as intermediate values. Objective questions are scored based on three conditions: a "match" earns '2' points, "not-recognized" receives '0' points, and a "mismatch" receives '-2' points. This no-score or negative score system penalizes lighting scenes with poorer visibility conditions. After tallying the scores, a final score is assigned to each object position within a lighting scene. As in the RT analysis, scores for the two object positions are averaged for each subject under each lighting scene. These averaged scores are further averaged across all 10 subjects, producing a score for each lighting scene. Then, with the main source CCT held constant, scores for three different peripheral CCT levels are averaged and plotted against main source CCTs, as shown in Fig. 5.8 (a). A similar graph is created by holding the peripheral source CCT constant and averaging the scores across four different main source CCTs, as shown in Fig. 5.8 (b). These graphs show that the highest average score occurs at 5000K CCT for the main source with peripheral source effects averaged, and at 6000K for the peripheral sources with main source effects averaged. Conversely, the lowest average score appears at 3000K CCT for the main source with averaged peripheral effects, and at 4500K CCT for the peripheral sources with main source effects averaged. Table 5.5 and Table 5.6 describe the average values of assigned scores for main source, where the effects of peripheral sources are averaged and for peripheral sources, where the effect of main source is averaged.

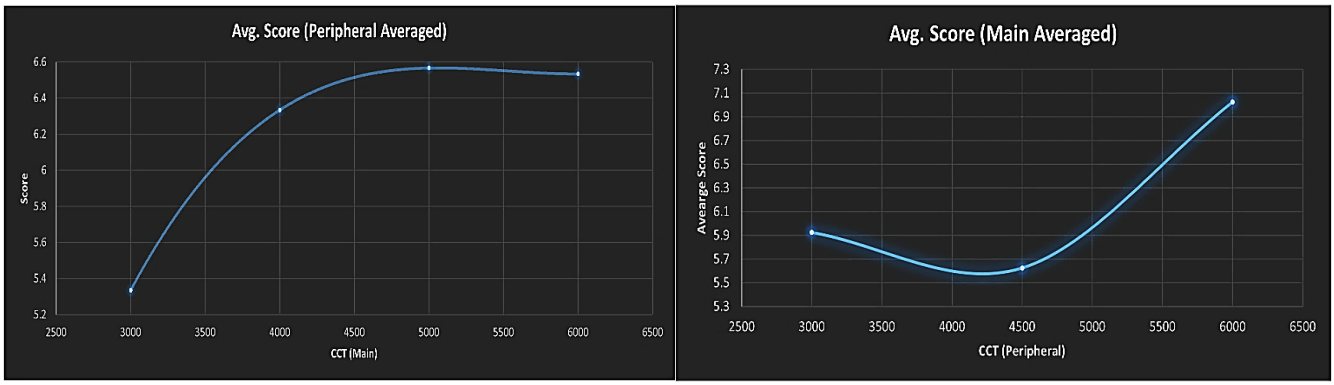

Fig. 5.8 (a) & (b): Average Score vs CCT of Main Source and Average Score vs CCT of Peripheral Sources

Table 5.5: The average values of assigned scores for main source, where the effects of peripheral sources are averaged

Main CCT	Peripheral CCT	Avg. Scores of each lighting scene	Avg. Scores when Peripheral is averaged
3000	3000	5.9	5.334
	4500	3.9	
	6000	6.2	
4000	3000	5.2	6.334
	4500	6.2	
	6000	7.6	
5000	3000	6.3	6.567
	4500	6.6	
	6000	6.8	
6000	3000	6.3	6.534
	4500	5.8	
	6000	7.5	

Table 5.6: The average values of assigned scores for peripheral sources, where the effects of main source is averaged

Peripheral CCT	Main CCT	Avg. Scores of each lighting scene	Avg. Scores when Main is averaged
3000	3000	5.9	5.925
	4000	5.2	
	5000	6.3	
	6000	6.3	
4500	3000	3.9	5.625
	4000	6.2	
	5000	6.6	
	6000	5.8	
6000	3000	6.2	7.025
	4000	7.6	
	5000	6.8	
	6000	7.5	

5.3.4.3 GSR Data Analysis

As previously detailed, a custom device was developed in the lab to measure the galvanic skin response (GSR) of stationary subjects under varying CCT levels of main and peripheral LED light sources during object identification tasks. This device uses an Arduino Uno microcontroller with a Seed Studio Grove GSR sensor and a microSD card to record electrodermal activity from participants. After collecting GSR data from 10 subjects under each lighting scene, these readings are averaged, and then re-referenced by subtracting the overall average from each data point. The re-referenced data is plotted against recording time, and the slope of the trendline is calculated for each of the 12 lighting scenes. For analysis, the slopes corresponding to three different CCT levels of the peripheral sources (while holding the main source CCT constant) are root mean squared (RMS) and plotted against the main source CCTs, as shown in Fig. 5.9 (a). Similarly, another graph is created by holding the peripheral source CCT constant and plotting the RMS slopes for four main source CCT levels, shown in Fig. 5.9 (b). The RMS approach, rather than a simple average, is used to manage the presence of negative trendline slopes across scenes. These graphs indicate that anxiety, excitement, stress levels, and physiological arousal are lowest at 5000K CCT for the main source when averaging the effects of peripheral sources, and at 6000K CCT for the peripheral sources when averaging main source effects. Conversely, these responses are highest at 3000K CCT for the main source with averaged peripheral effects, and at 3000K and 4500K CCT for the peripheral sources with averaged main source effects. For reference, the slope of a GSR trendline represents the rate of skin conductance change, correlating with physiological arousal levels. A steeper slope indicates a faster rise in conductance, signaling increased emotional or sympathetic nervous system activity, often linked to heightened states such as stress, excitement, or anxiety. A gentler slope reflects a slower change in conductance, suggesting reduced arousal or a more relaxed state [127]. Table 5.7 and Table 5.8 describe the average values of RMS (root mean square) slopes for main source, where the effects of peripheral sources are averaged and for peripheral sources, where the effect of main source is averaged.

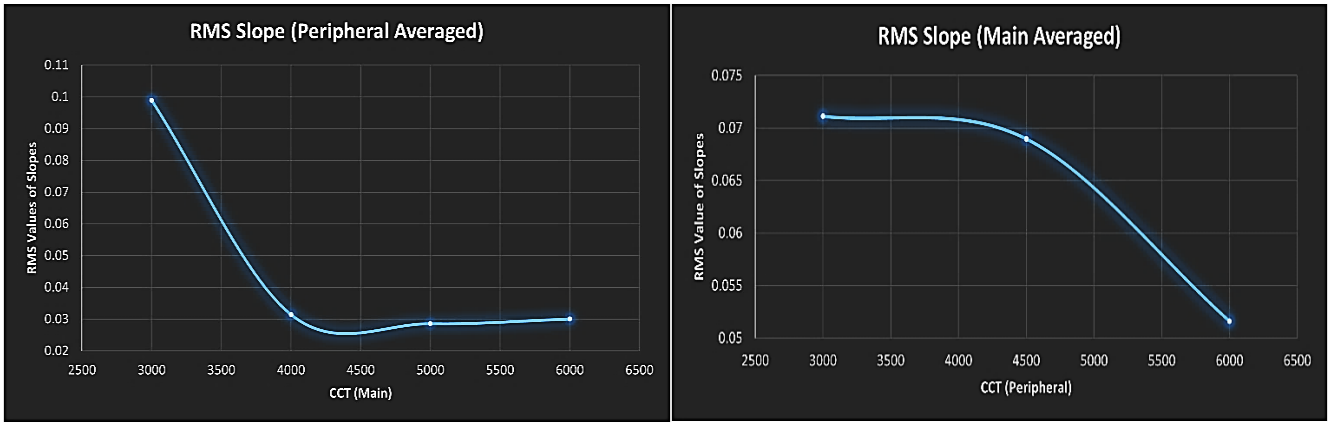

Fig. 5.9 (a) & (b): RMS Slope vs CCT of Main Source and RMS Slope vs CCT of Peripheral Sources

Table 5.7: The average values of RMS (root mean square) slopes for main source, where the effects of peripheral sources are averaged

Main Source CCT	RMS Slope
3000	0.098895298
4000	0.03140743
5000	0.028515551
6000	0.029995833

Table 5.8: The average values of RMS (root mean square) slopes for peripheral sources, where the effect of main source is averaged

Peripheral CCT	RMS Slope
3000	0.071126648
4500	0.068982848
6000	0.051594186

5.3.4.3 EEG Data Analysis

As previously mentioned, an Emotiv Epoc X EEG recording device was used in this study to monitor the temporal brain activity of stationary human observers during object identification tasks under varying CCTs of main and peripheral light sources. This device, equipped with 14 channels, wirelessly records data via a dedicated laptop with Emotiv Pro software installed. It employs an MNI coordinate file for the BEM dipfit model, a validated 10-20 montage for channel locations, with a 2D head model for channel visualization shown in Fig. 5.10.

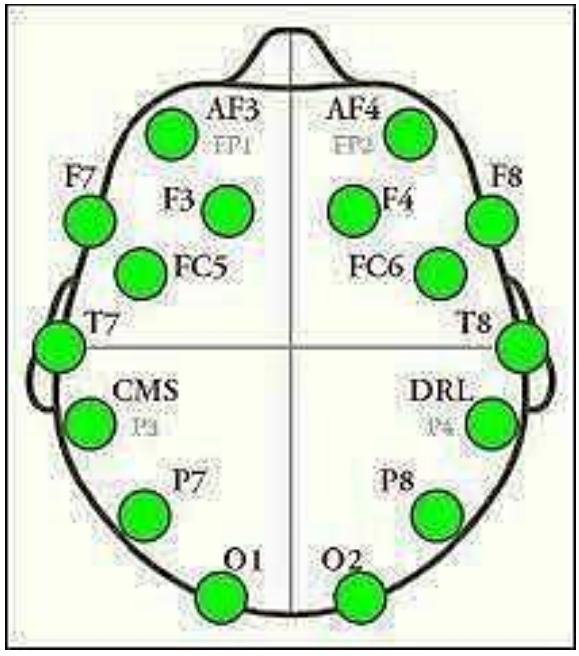

Fig. 5.10: A 2D Head Model for Channel Visualization

The recorded EEG data is analyzed using EEGLAB, a widely-used, open-source MATLAB toolbox for EEG data processing and analysis. EEGLAB provides both a graphical user interface (GUI) and command-line functionalities, allowing researchers to import, visualize, and analyze EEG signals through operations like data filtering, artifact removal, and independent component analysis (ICA). ICA helps separate brain signals from artifacts such as eye movements and muscle activity, enhancing data quality and enabling identification of independent neural components and brain networks, making EEGLAB a good choice for neuroscience and cognitive analysis [128-129]. The recorded data are preprocessed using this toolbox. First, the data is filtered with a basic bandpass FIR filter ranging from 0.5 Hz to 60 Hz, then the baseline and any DC offset of the data is removed. The data is then re-referenced using a computation of average reference. Event epochs are extracted, spanning from 2 seconds before to 2 seconds after stimulus onset. The study includes three types of epoch data for each of the 10 subjects: eyes closed, eyes open, and object identification conditions across 12 lighting scenes. Two EEGLAB studies are created for each condition: one with the main source constant and peripheral sources averaged, and the other with peripheral sources constant and main sources averaged. Independent component analysis is conducted for each of the 12 lighting conditions in these mentioned studies. Moreover, another two studies are created for eyes closed condition and eyes opened condition. From these analyses, event-related potentials (ERPs), relative logarithmic spectral powers, and ERP scalp maps are derived for each study. ERP data is plotted over time from -500 ms before to 1000 ms after stimulus onset, and relative spectral power is plotted against frequency from 0.5 Hz to 60 Hz. Plots of ERPs, spectral powers, and ERP scalp maps for the eyes closed and open conditions are shown in Figs. 5.11 (a), 5.11 (b), 5.11 (c), Fig. 5.12 (a), 5.12 (b), and 5.12 (c). Various features were then extracted using MATLAB codes (given in Annexture 1), including the area under the curve (AUC), baseline shift (slow drift or variation in the signal's baseline level), half peak width (the duration between the points on the signal where the amplitude is half of its maximum peak value), mean amplitude, peak amplitude and peak latency (time interval between the stimulus onset and the occurrence of the maximum peak amplitude) from the ERP plots. From the spectral power plots, features like low-to-high frequency power ratio, relative power of Alpha (8-13 Hz), Beta (13-30 Hz), Delta (0.5-4 Hz), Theta (4-8 Hz), and Gamma (30+ Hz) waves, spectral centroids (frequency at which the center of mass of the spectrum is located, indicating where most of the signal's power is concentrated), and mean power were extracted. The graphs for conditions with a constant main source are presented in Fig. 5.13 (a) through 5.13 (j), and those with a constant peripheral source are in Fig. 5.14 (a) through 5.14 (j). Scalp maps with the main source held constant are shown in Fig. 5.15, and those with the peripheral source constant in Fig. 5.16. For context, EEG signals fall into five frequency bands: delta, theta, alpha, beta, and gamma. Delta waves (0.5 - 4 Hz) dominate during deep sleep, theta waves (4 - 8 Hz) are seen in certain sleep stages and calm focus states, alpha waves (8 - 13 Hz) appear during relaxation, beta waves (13 - 30 Hz) are associated with normal waking consciousness and mental activity, and gamma waves (above 30 Hz) reflect heightened response to visual stimuli [130].

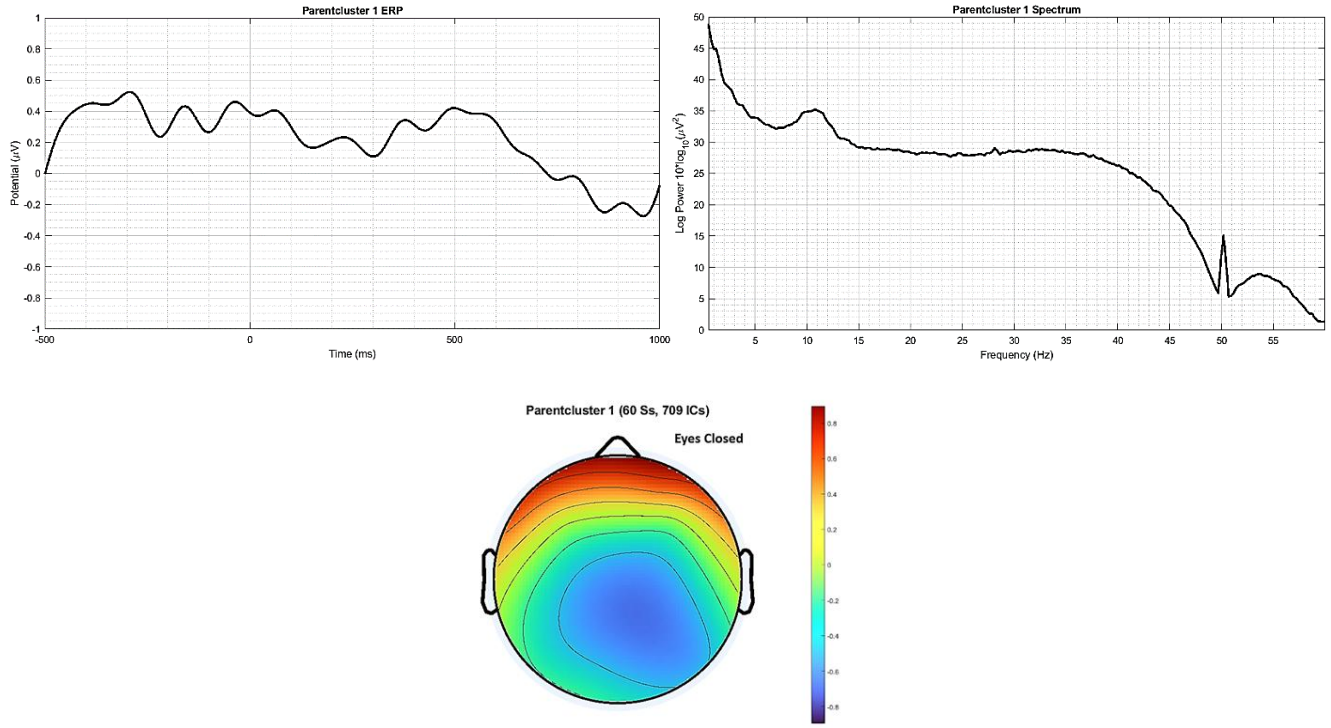

Fig. 5.11 (a), (b) & (c): ERP Plot, Relative Log power spectral Plot and Scalp map at Eyes Closed Condition

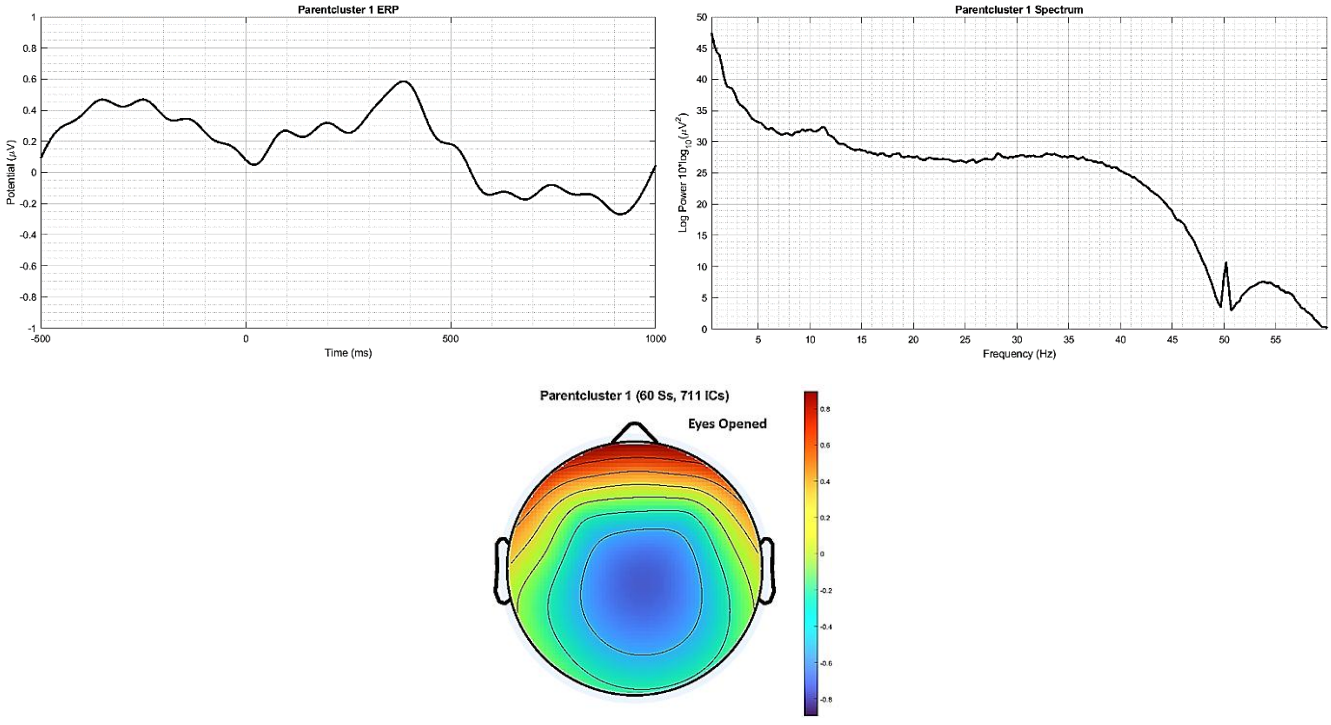

Fig. 5.12 (a), (b) & (c): ERP Plot, Relative Log power spectral Plot and Scalp map at Eyes Opened Condition

These graphs and plots suggest that in the second ERP plot (eyes open condition), the P300 wave is more pronounced, indicating greater cognitive processing compared to the eyes closed condition. This is expected, as the P300 wave, a positive deflection around 300-400 milliseconds post-stimulus, is associated with attention and cognitive processing. Additionally, early components like N100 and P200 (negative and positive deflections around 100-200 milliseconds) reflect sensory processing and show slight differences in amplitude and latency between the two ERP plots. In the relative log spectral power plots, the alpha band shows higher power, and the beta band is slightly lower in the eyes closed condition compared to eyes open, which aligns with the study design. A spike at 50 Hz appears in both plots, likely due to power line interference. Furthermore, the scalp maps reveal that in the eyes closed condition, the occipital region is more negatively charged, while the frontal and temporal regions are more positively charged compared to eyes open. In contrast, the parietal region is more negatively charged in the eyes open condition.

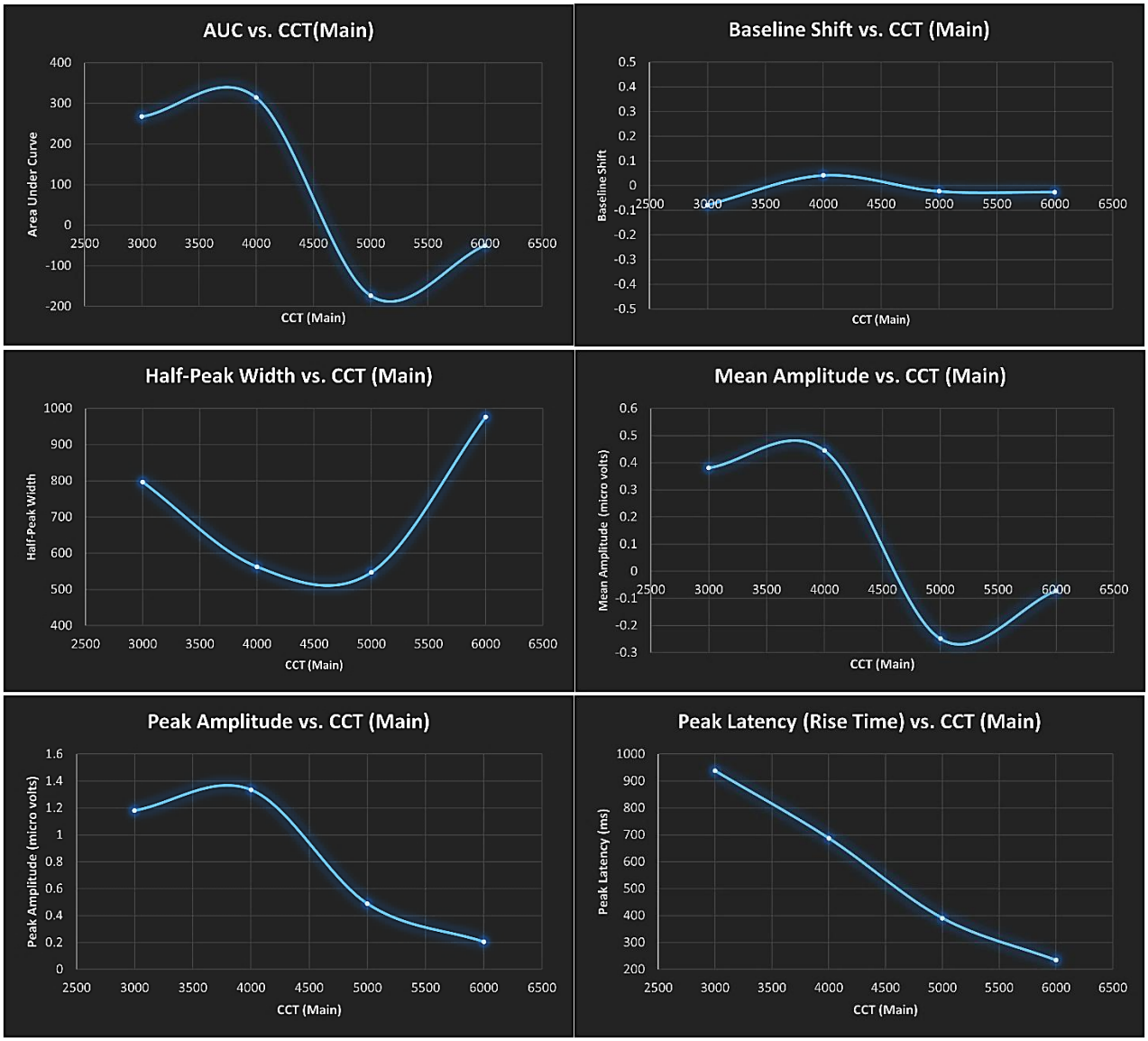

Fig. 5.13 (a), (b), (c), (d), (e), (f): AUC, Baseline Shift, Half-peak Width, Mean Amplitude, Peak Amplitude and Peak Latency vs CCT of Main source plots, where Effect of Peripheral Sources are Averaged

The area under the curve (AUC) in an ERP plot reflects the brain's overall response to a stimulus, capturing both the magnitude and duration of neural activity. A larger AUC suggests more prolonged or intensive neural engagement, whereas a smaller AUC may indicate quicker or reduced involvement in cognitive processing. As seen in Fig. 5.13 (a), the AUC is smallest (absolute value) at 6000K CCT and close to this at 5000K CCT for the main source with averaged peripheral source effects, suggesting less neural engagement or quicker cognitive resolution. A baseline shift in an ERP plot, meanwhile, shows changes in electrical potential before the stimulus, hinting at possible recording drift, which may result from electrode impedance, muscle artifacts, or slow-wave brain activity. Ideally, the baseline should be stable and near zero for clear interpretation (it provides a reference) of ERP components. In Fig. 5.13 (b), the baseline shift across all four CCT levels of the main source is close to zero, indicating good data quality. The half peak width (full-width at half maximum or FWHM) in an ERP plot represents the duration of neural response at half of the peak amplitude, with a wider width suggesting extended neural processing and a narrower width indicating faster response. Fig. 5.13 (c) shows that the half peak width is lowest at 5000K CCT of the main source with averaged peripheral sources, indicating faster response. Mean amplitude reflects the average strength of neural responses over a specific period and is used to assess overall brain response. It is useful in analyzing brain activity because it smooths out any short-lived peaks or noise and gives a better sense of the overall brain response to a stimulus. Fig. 5.13 (d) indicates the lowest mean amplitude at 5000K CCT and second lowest at 6000K CCT of the main source with averaged peripheral sources. Peak amplitude, which reflects brief, high-intensity responses (e.g., the P300 component), is lowest at 6000K CCT and second lowest at 5000K CCT for the main source, as seen in Fig. 5.13 (e). Lastly, peak latency, the time to reach maximum amplitude after stimulus onset, reflects neural processing speed, with shorter latencies showing quicker cognitive responses. Longer latencies can suggest delays in cognitive processing due to task complexity or neurological conditions. Fig. 5.13 (f) shows the lowest peak latency at 6000K CCT and close to this at 5000K CCT of the main source, with averaged peripheral source effects.

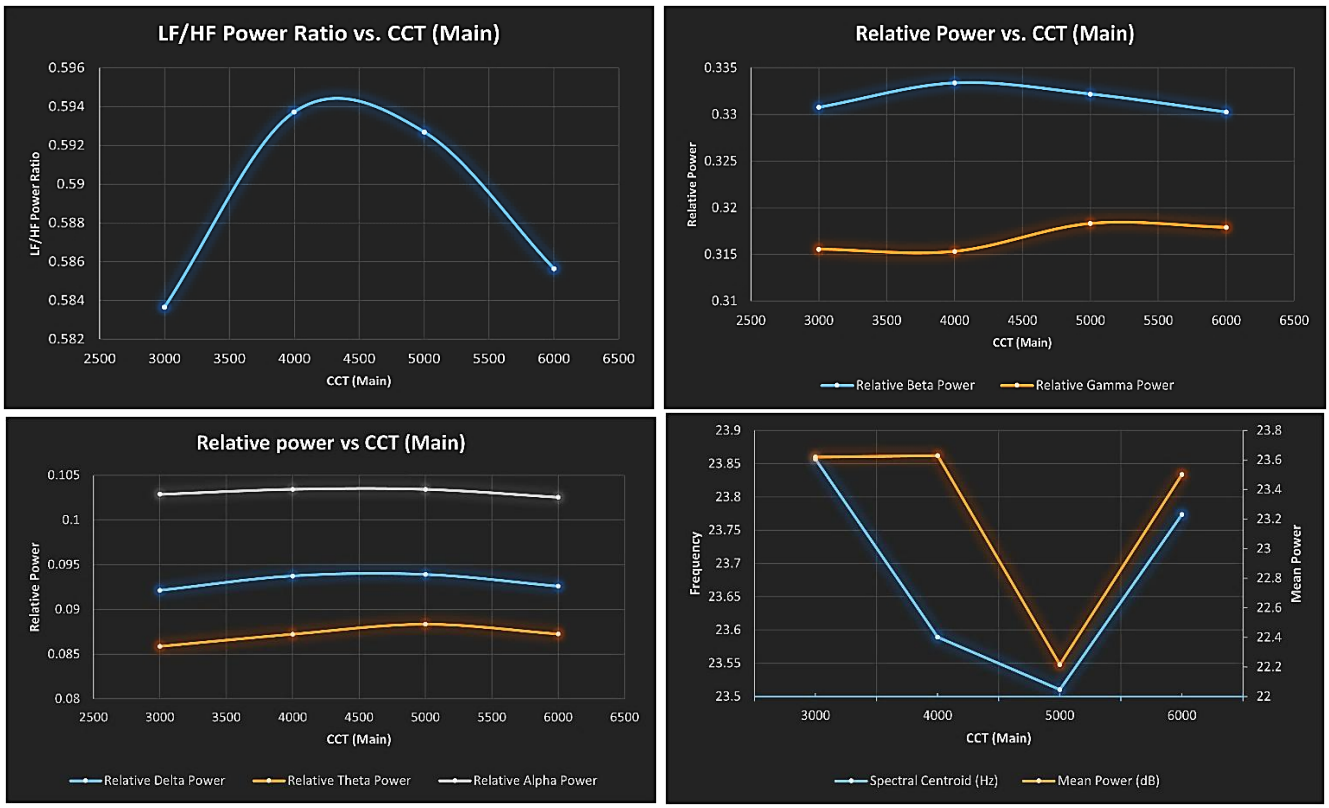

Fig. 5.13 (g), (h), (i), (j): Low Frequency to High Frequency Power Ratio, Relative Power (dB) of Beta, Gamma, Delta, Theta and Alpha Frequency Band, Spectral Centroid and Mean Power (dB) vs CCT of Main source Plots, where the Effect of Peripheral Sources are Averaged.

The low-frequency to high-frequency power ratio in EEG reflects the balance between slower and faster brain wave activity. A higher ratio indicates a dominance of low-frequency waves, which are typically associated with relaxation or drowsiness, whereas a lower ratio suggests increased cognitive activity or stress. Fig. 5.13 (g) shows that the low-to-high frequency power ratio is highest at 4000K CCT and closely followed by 5000K CCT of the main source. In Fig. 5.13 (h) and Fig. 5.13 (i), we observe that the relative power of the alpha and gamma bands is highest, with the beta band showing the second-highest power at 5000K CCT for the main source, when the effects of peripheral sources are averaged. Additionally, the spectral centroid represents the "center of mass" for frequency distribution, pointing to where most of the signal's power is concentrated. A lower spectral centroid implies dominance of lower frequencies, linked to relaxed states or sleep, while a higher centroid is associated with active thinking or alertness. Fig. 5.13 (j) shows that the spectral centroid is lowest for the 5000K CCT of the main source, with averaged peripheral source effects. Finally, mean power reflects the average power across all frequencies, with higher values indicating overall heightened brain activity and lower values suggesting a more relaxed state. In the same plot, we see that at 5000K CCT of the main source, where peripheral source effects are averaged, mean power is at its lowest.

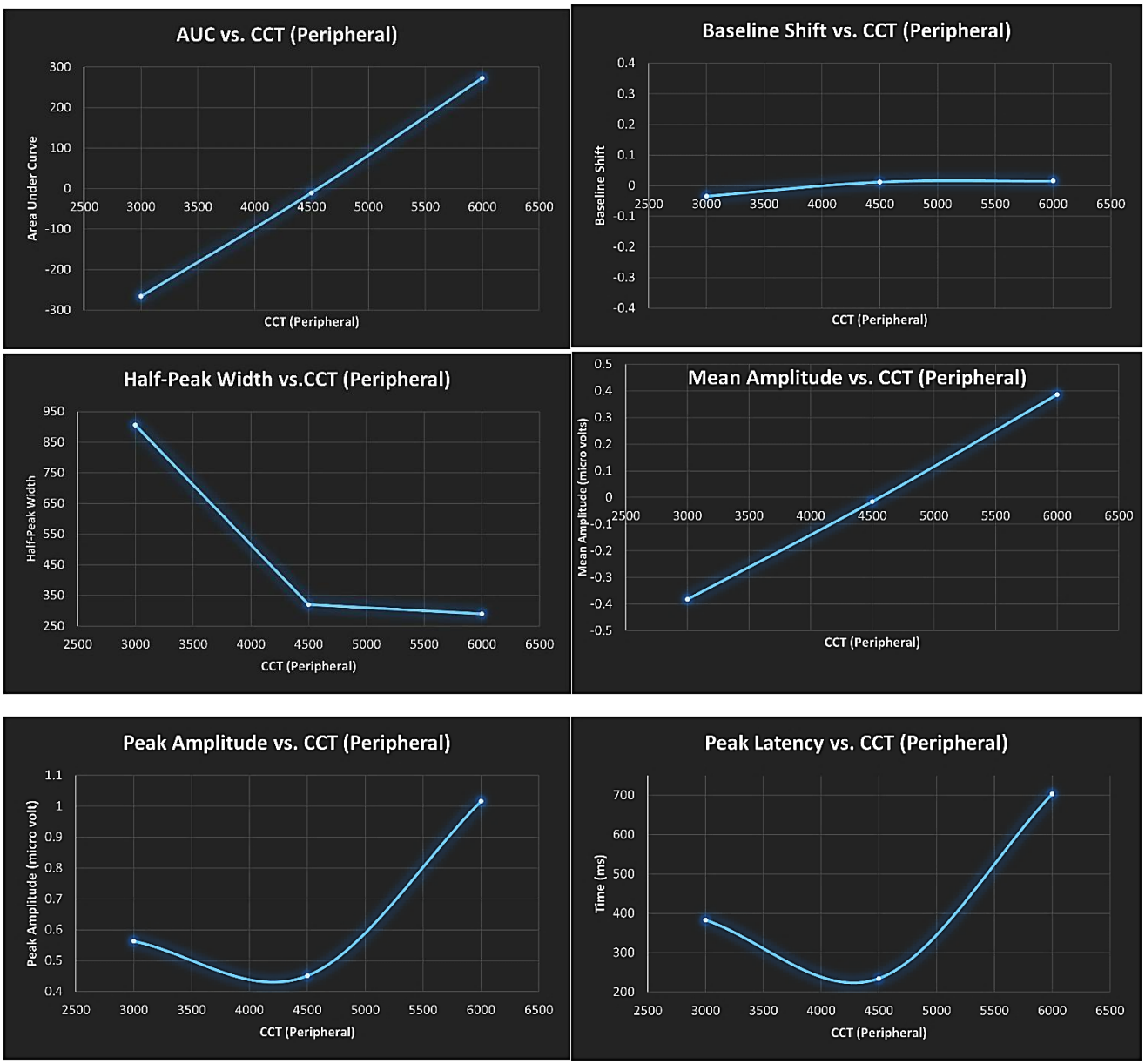

Fig. 5.14 (a), (b), (c), (d), (e), (f): AUC, Baseline Shift, Half-peak Width, Mean Amplitude, Peak Amplitude and Peak Latency vs CCT of Peripheral source plots, where Effect of Main Source is Averaged

In Fig. 5.14 (a), the smallest AUC value occurs at 4500K CCT, with the second smallest at 6000K CCT of the peripheral sources, when the main source effect is averaged. Fig. 5.14 (b) shows that baseline shifts for all three CCT levels of the peripheral sources are close to zero, indicating high data quality. Additionally, Fig. 5.14 (c) reveals that the half-peak width is lowest at 6000K CCT for the peripheral sources with the main source effect averaged. Fig. 5.14 (d) indicates that the mean amplitude reaches its lowest (absolute) value at 4500K CCT of the peripheral sources under averaged main source conditions. In Fig. 5.14 (e) and Fig. 5.14 (f), the lowest peak amplitude and

peak latency are observed at 4500K CCT, while the highest values occur at 6000K CCT of the peripheral sources, with the main source effect averaged.

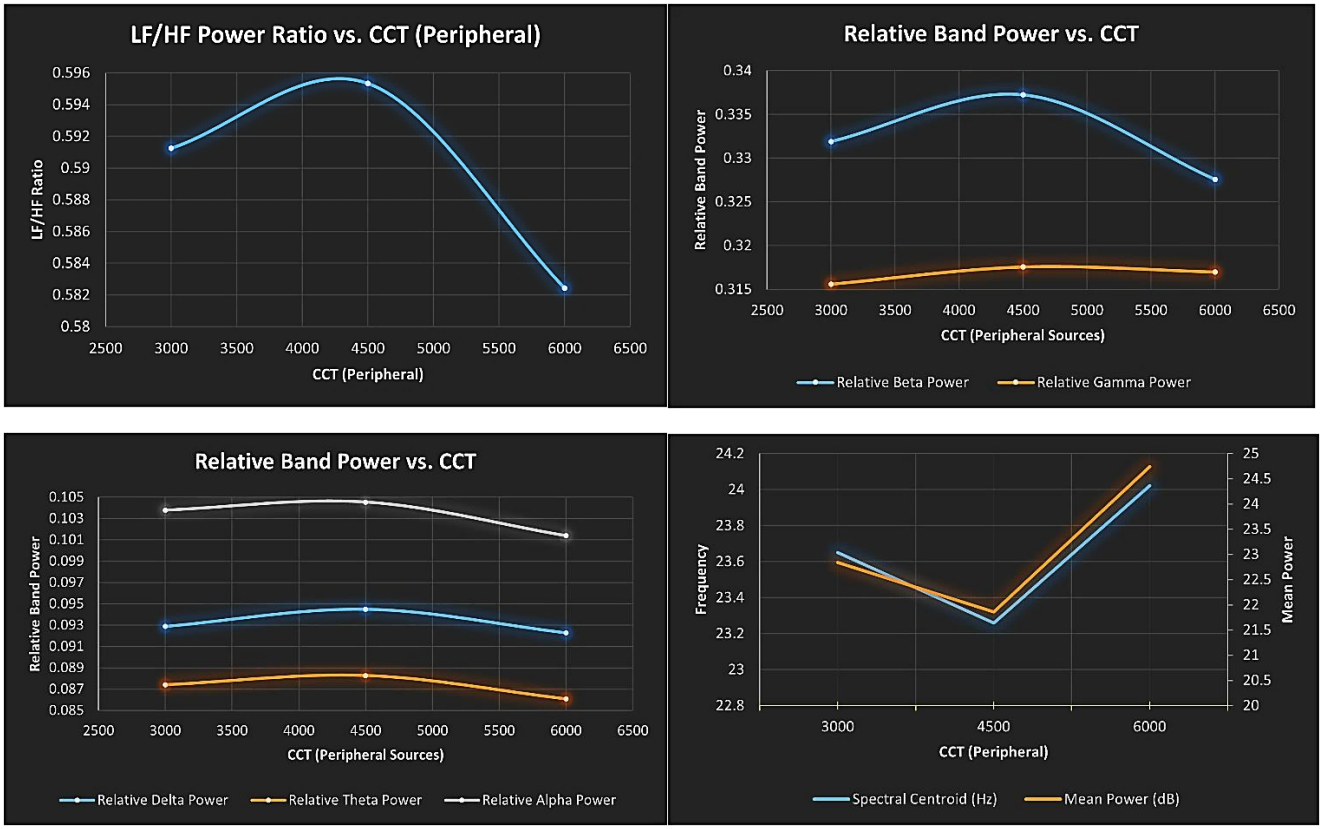

Fig. 5.14 (g), (h), (i), (j): Low Frequency to High Frequency Power Ratio, Relative Power (dB) of Beta, Gamma, Delta, Theta and Alpha Frequency Band, Spectral Centroid and Mean Power (dB) vs CCT of Peripheral source Plots, where the Effect of Main Source is Averaged.

The plots in Fig. 5.14 (g) and 5.14 (j) show that the low-frequency to high-frequency power ratio is highest, the frequency representing the spectral centroid is lowest, and the mean power of the relative logarithmic spectral power plot is lowest at 4500K CCT of the peripheral sources. Additionally, Fig. 5.14 (h) and 5.14 (i) indicate that the relative power of the beta, gamma, and alpha frequency bands is lowest at 6000K CCT and highest at 4500K CCT of the peripheral sources, with the effect of the main source averaged. Table 5.9 and Table 5.10 describe the values of various features, extracted from ERP plot and relative log power spectral plot, for main source, where the effects of peripheral sources are averaged. Table 5.11 and Table 5.12 describe the values of various features, extracted from ERP plot and relative log power spectral plot, for peripheral sources, where the effect of main source is averaged.

Table 5.9: Values of various features, extracted from ERP plot, for main source, where the effects of peripheral sources are averaged

Lighting Scene (main)	Peak Amplitude	Peak Latency (samples)	AUC	Half-Peak Width (samples)	Baseline Shift	Mean Amplitude
3000	1.180307	937.5	267.3765	796.875	-0.07912	0.38109377
4000	1.33495	687.5	314.3431	562.5	0.041633	0.44484408
5000	0.488977	390.625	-173.709	546.875	-0.02341	-0.2484663
6000	0.205805	234.375	-50.1299	976.5625	-0.02635	-0.0714065

Table 5.10: Values of various features, extracted from relative log power spectral plot, for main source, where the effects of peripheral sources are averaged

CCT of Lighting Scene (K)	Relative Delta Power	Relative Theta Power	Relative Alpha Power	Relative Beta Power	Relative Gamma Power	Spectral Centroid (Hz)	LF/HF Power Ratio	Mean Power (dB)
3000	0.092123	0.085885	0.102871	0.330769	0.31556	23.85675	0.583654	23.6202
4000	0.09374	0.087234	0.103437	0.333388	0.315318	23.58899	0.593726	23.63073
5000	0.093899	0.088336	0.103429	0.332199	0.318317	23.51051	0.592693	22.21616
6000	0.092582	0.087256	0.102554	0.330264	0.317898	23.77345	0.58564	23.50143

Table 5.11: Values of various features, extracted from ERP plot, for peripheral sources, where the effect of main source is averaged

Lighting Scene (Peripheral)	Peak Amplitude	Peak Latency (samples)	AUC	Half-Peak Width (samples)	Baseline Shift	Mean Amplitude
3000	0.56293964	382.8125	-266.265	906.25	-0.03409	-0.381519183
4500	0.45112041	234.375	-10.3358	320.3125	0.012257	-0.015661563
6000	1.0171077	703.125	272.6611	289.0625	0.015017	0.385424284

Table 5.12: Values of various features, extracted from relative log power spectral plot, for peripheral sources, where the effect of main source is averaged

CCT of Lighting Scene (K)	Relative Delta Power	Relative Theta Power	Relative Alpha Power	Relative Beta Power	Relative Gamma Power	Spectral Centroid (Hz)	LF/HF Power Ratio	Mean Power (dB)
3000	0.0928705	0.08740011	0.1037797	0.3319048	0.3155998	23.649465	0.5912581	22.843734
4500	0.0944978	0.08826572	0.1045327	0.3372334	0.3175545	23.2588	0.5953482	21.856721
6000	0.09226424	0.08607593	0.1013891	0.327574	0.3169798	24.022856	0.5824286	24.737333

5.3.5 Discussion

This experimentation explored the visual, non-visual, and behavioral effects of varying correlated color temperature (CCT) of main and peripheral LED light sources on the object recognition abilities of static human observers. Various analysis methods are applied, including reaction time (RT) analysis, behavioral studies, galvanic skin response (GSR), and most importantly, temporal processing analysis of the brain using EEG recordings. As previously noted, no prior studies have examined the correlations between these types of analyses under varying CCT conditions, which makes establishing these connections the main agenda of this research. Additionally, the study proposes a metric to assess how lighting environments can be optimized for human-centric purposes. The analysis of RT, behavioral, and GSR data reveals that optimal results occur with a 5000K CCT for the main light source, with lower performance at lower CCTs (such as 3000K), where impact of peripheral lighting is generally averaged. However, at a main source CCT of 6000K with averaged effect of peripheral sources, these parameters decline again. Interestingly, when the peripheral source is set at 6000K CCT and the main source effect is averaged, these metrics reach their best values, while lower CCTs (around 3000K) again show degraded outcomes. This indicates that increasing CCT alone does not necessarily enhance human-centered outcomes, a conclusion also supported by the nonlinear patterns in the data. However, it appears that CCT values around 5000K are beneficial for object recognition tasks. In the EEG analysis, optimal values for measures like area under the curve (AUC), half-peak width, mean amplitude, peak amplitude, and latency are observed at 5000K CCT for the main source and degrade for CCT values below or above 5000K, with averaged effects from peripheral sources. Similar optimal outcomes are seen for the power ratio of low to high frequencies, relative power of various EEG frequency bands, spectral centroid, and mean power of the logarithmic spectral power curves, all supporting 5000K CCT for the main source whilst the effect of peripheral sources is averaged. This finding aligns closely with the RT, behavioral, and GSR results. When the main source's effect is averaged, the optimal CCT for the peripheral source falls around 4500K, where only the ERP plot’s half-peak width indicating 6000K CCT of peripheral sources as optimal. These findings suggest that a CCT range of 4500K to 5000K for both main and peripheral sources is optimal for accurate object recognition, though reaction time, behavioral, and GSR results also indicate that 6000K CCT is beneficial for the peripheral source, with 5000K showing similar results. However, rapid CCT changes are impractical in high-traffic environments, reinforcing the 4500K to 5000K range as ideal. Additionally, comparisons of spectral power distributions across CCTs, such as 3000K, 4000K, 5000K, and 6000K based upon the outcome of the study, reveal that excess blue or red components in LED sources can impair object recognition. Moreover, the low-to-high frequency power ratio in the EEG's relative logarithmic spectral power can serve as an effective metric to find the degree of human centrism of a lighting scene, as the low frequency to high frequency power ratio (LF/HF) ratio’s trend across varying CCTs aligns well with other studies on object detection capabilities. This LF/HF metric could therefore support future human-centric lighting designs.

5.3.6 Conclusion

With the arrival of groundbreaking innovations in illumination engineering, significant advancements have transformed road lighting design. The primary focus has shifted from

traditional illuminance-based metrics to luminance-based ones, enabling lighting systems that better suit human needs. This shift reflects the broader trend toward human-centered lighting design, with substantial research into optimizing street lighting for both safety and comfort. Studies on human-centric lighting and street lighting optimization have paved the way for new technological advancements and theoretical frameworks. Building on this foundation, the current study explores the visual, non-visual, and behavioral impacts of varying correlated color temperatures (CCTs) in main and peripheral LED light sources, specifically focusing on how these variations influence static human observers' object recognition capabilities. To achieve this, two specialized devices were developed in the Illumination Engineering Laboratory at Jadavpur University: a reaction time measuring compact device (RTMCD) and a galvanic skin response (GSR) measuring device. Additionally, behavioral studies complemented these measures. Most importantly, electroencephalography (EEG) was used to record participants' brain activity, offering insight into the brain's temporal processing of object recognition tasks under different CCT conditions. This study made a concentrated effort to correlate findings from RT, GSR, behavioral studies, and EEG data. Experimental results indicate that a CCT range of 4500K to 5000K for both main and peripheral LED light sources is optimal for accurate object recognition. Findings also show that excess blue or red-light content in LEDs may hinder object recognition, slowing reaction times. Furthermore, the low-to-high frequency power ratio in the EEG's relative logarithmic spectral power plot emerged as a promising metric for assessing how "human-centric" a lighting setup is. Together, these tools demonstrate the value of EEG and GSR-based approaches for evaluating human performance in different lighting conditions. While this study provides foundational insights, it highlights the need for broader research involving a wider range of CCTs for both main and peripheral sources, along with a larger participant sample, to draw more generalized conclusions. By establishing these methods, this research offers a novel approach and serves as a stepping stone toward more comprehensive studies in human-centered lighting design.

Chapter 6: LED Dimming: An Approach towards Energy Conservation and Sustainability

6.1 Introduction

Daylight is one of the most efficient and preferred sources of lighting but is not consistently available throughout the day, so the world depends heavily on artificial lighting, typically powered by electricity. Producing electricity is costly and often involves complete or incomplete coal or petroleum burning, which increases the amount of carbon dioxide in climate and expedites climate change and global warming. To address this, governments and local official bodies are working to create low-emission power systems and reduce electricity demand. Lighting (indoor and outdoor) alone accounts for about 19% of global electricity consumption, where public lighting, majorly street lighting accounts for 2.3% of worldwide power usage [131-132]. Among various types of lighting in indoor and outdoor lighting, street lighting is typically one of the largest electricity or energy consumer, account for up to 40% electricity consumption in municipalities [133]. Street lighting is also a major energy-consuming public service in India, with around 78 million street lights illuminating roads as of FY2019 [1]. Data shows that street lighting uses 1-3% of India's electricity production (about 8,478 GWh in FY13) for a single municipality, where maintenance can account for 10-15% of municipal budgets. Studies indicate that efficient lighting designs could reduce this energy use by 25-60% [2-3]. Most street lights still use outdated technology, including fluorescent, metal halide, sodium vapor, incandescent, or CFL lamps. Additionally, street lights often remain on during the day or in low-traffic night hours, leading to considerable energy wastage. With Nakamura's invention of high luminance GaN based LED in 1993, light emitting diodes' compatibility, controllability, durability, and performance have increased dramatically every day. LEDs have become widespread in the lighting industry due to their high spectral power density, quick start-up, and versatile control options compared to other street lighting solutions like HPSV and LPSV, indicative picture of LED market growth is given in Fig. 6.1. LEDs are more energy-efficient, longer-lasting, easier to control, consume less power, have a lower carbon footprint, and are cheaper to operate [9]. With LEDs in street lighting, a new era of smart street lighting has begun. This system reduces manual control, minimizes energy consumption by scheduling LED operation times, and allows for control over lighting parameters like brightness, color temperature, and beam angle. One such energy reduction techniques for LEDs is dimming, where the light output, brightness and electrical energy

consumption can be controlled and varied. There exist two types of dimming techniques for constant current LED drivers. One is analog dimming or constant current reduction (CCR) and the other is digital dimming or pulse width modulation (PWM) [134].

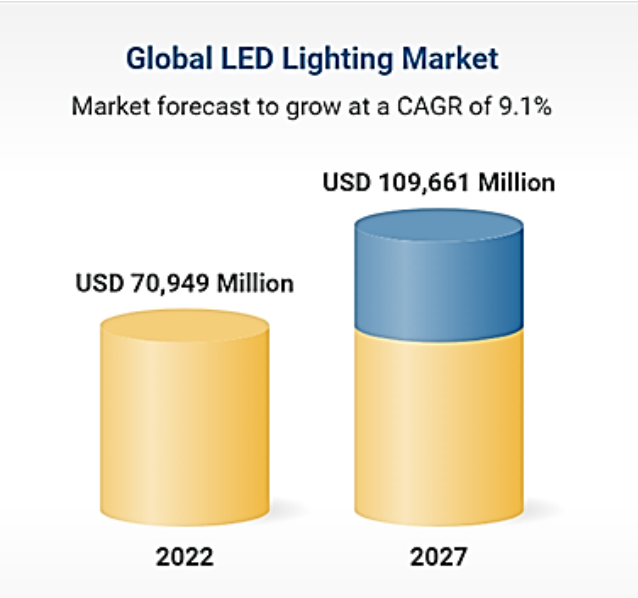

Fig. 6.1: World LED Market Growth in USD

Research has shown that PWM dimming is one of the most effective methods for LED dimming. This technique adjusts the LED's light output by supplying it with a pulsed DC current with a variable duty cycle. Furthermore, in CCR type dimming current, which is continuously flowing, is reduced to decrease light output of the light source. Additionally, PWM dimming, commonly used, prevents excessive increases in the LED's junction temperature, which helps to extend the LED's lifespan [25-31]. Besides, another energy reduction technique for LED street lighting was first introduced by Suddhasatwa Chakraborty et. al. and is named as Beam Angle Switching (BAS) method. In this method, lens of a particular LED strip inside the street LED luminaire are fixed in such a way that by using proper control gear, direction of outgoing beam can be altered in a pre-fixed path by turning the LED strips on or off inside the luminaire [32]. In this chapter, two experimentations are done to find out the effectiveness and validity of BAS method and to analyze whether PWM dimming and BAS method can be amalgamated. Besides, another case study is also done in streets of Jadavpur University, to check the energy saving potential of BAS method in real scenario.

6.2 Dimming Methods

As discussed in the introduction part that controlling or reducing the amount of light coming out from a light source is called dimming. Dimming can reduce huge amount of electrical energy consumption by LED light sources. For constant current drivers, there exist two types of dimming technique, which are analog dimming or CCR dimming and PWM dimming or digital dimming. Besides, a new technique has emerged for energy reduction, which is called BAS method. Descriptions about them are given below –

6.2.1 CCR Dimming

Constant Current Reduction (CCR), also known as analog dimming, controls LED brightness by reducing the steady current supplied to the LED, resulting in a smooth and flicker-free dimming experience. Unlike PWM, which switches the LED on and off rapidly, CCR reduces the current directly, making it ideal for settings that need minimal electromagnetic interference and simpler circuit design, as it does not involve high-speed switching. CCR is effective for installations with long wire runs, as it avoids the EMI and voltage-drop issues associated with PWM. However, the primary drawback of CCR is its potential to affect the LED's color temperature and efficiency at lower currents, as LEDs may shift in color when not operating at full power. This makes CCR less suited for applications requiring precise color stability across dimming levels. Despite these limitations, CCR is often used in environments with strict EMI requirements or where high switching frequencies would cause signal distortion or performance issues, like in medical, industrial, or high-motion environments [26,134]. For the before-said reason, use of this particular method is rejected for street lighting implementation as this kind of lights must maintain a constant spectral power distribution, which can affect object recognition on street and efficiency and moods of the drivers, at any cost. A picture is given in Fig. 6.2, where an example of a LED is given with approximately 25% of rated light output using CCR method.

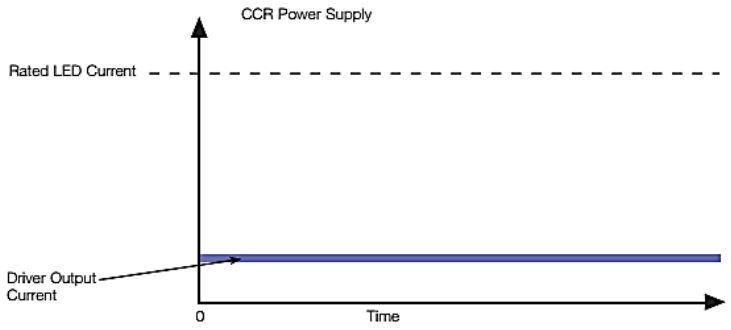

Fig. 6.2: CCR Dimming Method with 25% LED Brightness

6.2.2 PWM Dimming

Pulse-width modulation (PWM) dimming is a highly effective process for controlling LED brightness by switching the LED on and off at a high frequency. This creates a series of pulses, where the brightness level depends on the "duty cycle" (D) or the ratio of on-time to time period within each cycle. For example, at a 50% duty cycle, the LED is on half the time (50% of the time), producing about half its maximum brightness. PWM maintains a constant, generally rated, current level during each on period, which prevents shifts in the LED's color and efficiency, unlike other dimming techniques where brightness is achieved by lowering the current. PWM's rapid switching efficiently keeps the LED operation at peak, ensuring stable color temperature and brightness, crucial in applications that require color accuracy, such as displays, street lights or color-mixing systems. However, due to its high switching frequency, PWM can introduce electromagnetic interference (EMI) in sensitive environments, such as medical or industrial settings. Additionally, achieving flicker-free low brightness with PWM

requires a high frequency, typically over 200 Hz, to avoid visible flicker and stroboscopic effects. A graphical representation of PWM dimming is given in Fig. 6.3, where the duty cycle is set to 25% with 25% light output of LED [26,31,134].

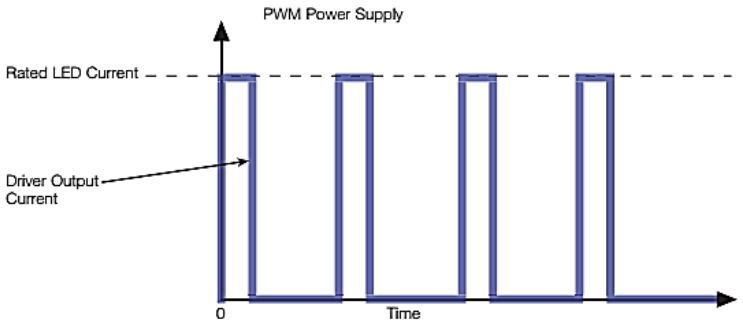

Fig. 6.3: PWM Dimming Method with 25% LED brightness

Here, Duty Cycle, D = $\frac{\tau}{T}$ = 0.25

Where, τ = on-time of the given signal

T = Time period of the given signal

6.2.3 BAS Method

The *Beam Angle Switching* (BAS) technique provides an alternative to traditional dimming for LED street lighting by enabling control over the beam angle to achieve various luminance levels from a single luminaire. First introduced by Dr. Suddhasatwa Chakraborty and colleagues, BAS adjusts the direction of light output by configuring LED strip lenses within the luminaire. This is achieved through a control system that turns specific LED strips on or off to direct the beam along a preset path, effectively reducing energy consumption. BAS operates in three lighting modes: "FULL GLOW," "PRO," and "COUNTER." In the "FULL GLOW" mode, all LED clusters are illuminated, providing maximum brightness. The "PRO" mode activates a single LED array directed along the flow of traffic, producing approximately one-third of the full brightness, thus conserving energy. Conversely, the "COUNTER" mode also uses a single array but directs the light against the flow of traffic. These adjustable lighting states allow the same luminaire to deliver varying brightness levels, optimizing energy use based on lighting needs [32]. A pictorial description of BAS method is given in Fig. 6.4.

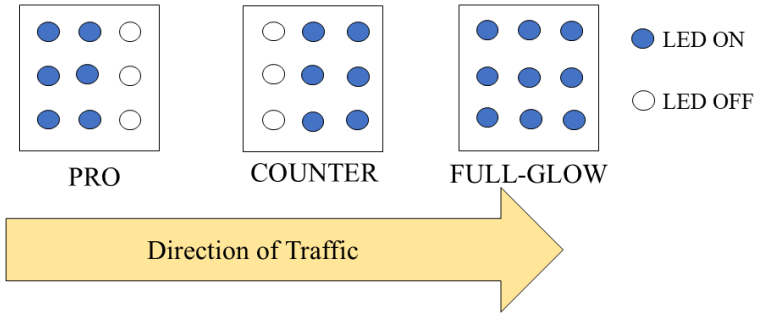

Fig. 6.4: BAS Method (each rectangle represents a single street light luminaire)

6.3 Validation of BAS Method Using a Novel Device

In 1993, Nakamura's invention of high-luminance GaN (Gallium Nitride)-based LEDs marked a turning point for LEDs, enhancing their compatibility, controllability, durability, and performance at a rapid pace. As semiconductor and packaging technology progressed, LED lifespan, light efficiency, and other photometric qualities also significantly improved [135]. Traditional sources of illumination like incandescent, high-intensity discharge, and fluorescent lamps are being replaced by LED lighting, which has higher energy efficiency, superior controllability, and longer lifespan. LEDs outperform older light sources in photometric parameters like CCT, CRI, illuminance at work plane, and luminous efficacy. This shift has made it essential to find effective ways to evaluate all of its characteristics. In India, LEDs have started replacing outdated lighting in government buildings, factories, streets, and homes. Despite these efforts, old lighting still consumes about 40% of urban electricity due to widespread use [136-138]. Street lighting in particular requires an urgent update to support road safety, as proper lighting can reduce night-time crime by 20% and nocturnal traffic accidents by 19% [4-5]. To meet these goals, the government is accelerating LED retrofitting for economic and transportation benefits. For this to be effective, maintaining consistent LED light output is essential. One reliable method is measuring the lumen maintenance factor using accelerated life testing (ALT)[139-141], as outlined in Indian standard IS:16102 (Part II): 2017. This approach calculates two main factors: LED lifespan (L_x) and the failure fraction at rated life (F_y). Here, L_x denotes the time period for which an LED lamp maintains a specified luminance level during standardized testing, while F_y represents the percentage of the same type of LED lamps failing at rated lifespan. Lumen maintenance is another key factor, showing the ratio of LED light output at a particular time to its initial luminance under specific conditions [142]. With these considerations in mind, a low-cost prototype device with remote communication capability (based on a low-powered wide-area network, or LoRa) was developed at the Illumination Engineering Laboratory of Jadavpur University. This system includes built-in memory to store photometric data and other measurements taken by sensors installed within a small, precisely crafted integrating sphere with internal temperature control. Additionally, a case study was conducted to verify the system's flawless operation. Through this case study, a dimming technique called beam angle switching, developed by Dr. Suddhasatwa Chakraborty in the same laboratory [32], was validated using a timed switching method designed for Indian road lighting. The study found that implementing this method does not significantly decrease LED light output, nor does it cause drastic changes in junction temperature.

6.3.1 LED Life Test

As previously mentioned, the ALT method is a primary approach for estimating an LED's operational lifetime, and it is endorsed by the Indian standard IS:16102 (Part II): 2017 [142]. The prerequisites for this assessment are outlined in another standard, ANSI/IES LM-80–08, which provides guidelines for assessing lumen maintenance of LED light sources. This standard specifies that the test must be conducted at three junction temperatures namely 55 °C, 85 °C, and a third temperature chosen by the manufactures, where it requires data collection over a minimum of 6,000 hours with recording intervals of at least 1,000 hours. The test LED must be operated at constant current and rated voltage, with all photometric data recorded at room temperature. Key metrics include lumen maintenance, chromaticity,

catastrophic failures, and data reporting procedures [143]. As a follow-up to LM-80–08, the TM-21–11 standard was developed, allowing LM-80 data to be extrapolated beyond the test duration. This is essential for estimating L70 data (the point at which brightness falls to 70% of its initial value) over timelines of 25,000 to 35,000 hours, as recommended by the EPA ENERGY STAR® Luminaire Guide. Many customers seek ENERGY STAR or DESIGNLIGHTS CONSORTIUM certification for their light sources, so TM-21–11 is referenced in both guides for qualification [144]. Researchers worldwide have conducted experiments to improve LED testing methods. One study aimed to create a low-cost testing device with remote connectivity through the internet for data acquisition, specifically for street lighting applications [145]. Another study developed a way to record data continuously while the testing device operates, avoiding the need to stop the device for data collection as in conventional methods. This was achieved by using a highly durable optical fiber to transfer light emitted from the test LED from high temperature test chamber to room temperature, enabling real-time monitoring of optical properties without risking the used sensors from overheating [146]. Another study distinguishes LED life and LED system life and described a proper on-off method to determine LED system life, which is more important as the LED package comes with other systems incorporated with alongside LED light source [146]. Considering all these insights, our device was designed with two distinct components that interact via an LPWAN-based LoRa communication module. The measurement unit, which is a small integrating sphere, is equipped to accommodate both the mounting of an entire LED system and individual LED packages, allowing for versatile testing configurations. Additionally, a case study was conducted using this device to validate a specific LED dimming technique known as beam angle switching. This study provided an opportunity to confirm the functionality and effectiveness of the dimming method within real-world testing conditions.

6.3.2 System Description

The developed prototype system comprises two distinct parts. One part is designated as the Measuring Sphere (MS), and the other as the User Interface cum Storage Device (UISD). This system components bi-directionally communicate between them using a low-power wide-area network (LPWAN) or LoRa 02 module. Each part is equipped with its own microcontroller, which is implemented using an Arduino Uno Rev3. Additionally, two primary sensors are integrated within the sphere. The first sensor is an illuminance sensor, the BH1750 FVI, mounted at the base of the sphere, and the second is a temperature and humidity sensor, the DHT11, which should be attached to the base of the LED bulb during testing. The control circuit of the MS, containing the microcontroller and the LoRa 02 module, is installed on the external wall of the sphere. All sensors and the control circuit are safeguarded with heat-resistant tape and enclosed in a transparent box. The test LED light is positioned at the center of the sphere, supported by a thin steel rod positioned at the center of the upper dome within the sphere. The inside of the MS device is coated with a white mixture of barium sulfate and magnesium oxide, offering 82% reflectance. This coating diffuses the light from the LED through multiple scattering reflections, ensuring uniform light distribution across all points within the sphere, which eliminates spatial information from the light output, thereby providing an accurate measurement of total luminous irradiance or power emitted from the source. The exterior of the sphere is painted white with plain white paint. The MS device includes three dedicated openings for hot air circulation, internal temperature control, and

power supply, which can be sealed post-connection for proper isolation. Based on findings from one study [32], the system allows for switching the LED light on and off, with customizable on/off durations set by the device user. Alternatively, the LED can be set to a continuous on mode. Power can be supplied in either AC or DC. A pictorial representation of the MS device is shown in Fig. 6.5 (a). The control circuit of the UISD includes the same Arduino Uno Rev3 microcontroller, a low-cost, highly accurate real-time clock module (DS3231) for timestamping the data, a microSD adapter for data storage, and the LPWAN-based LoRa 02 communication module for interaction with the MS device. It has been observed that the devices communicate seamlessly over a distance of 500 meters with no time lag. The UISD device is illustrated in Fig. 6.5 (b). For a comprehensive understanding of the system, block diagrams and flow charts have been developed for both the MS and UISD. These are provided in Fig. 6.6 (a) and (b) and Fig. 6.7 (a) and (b), respectively. Both the used codes is given in Annexture 1.

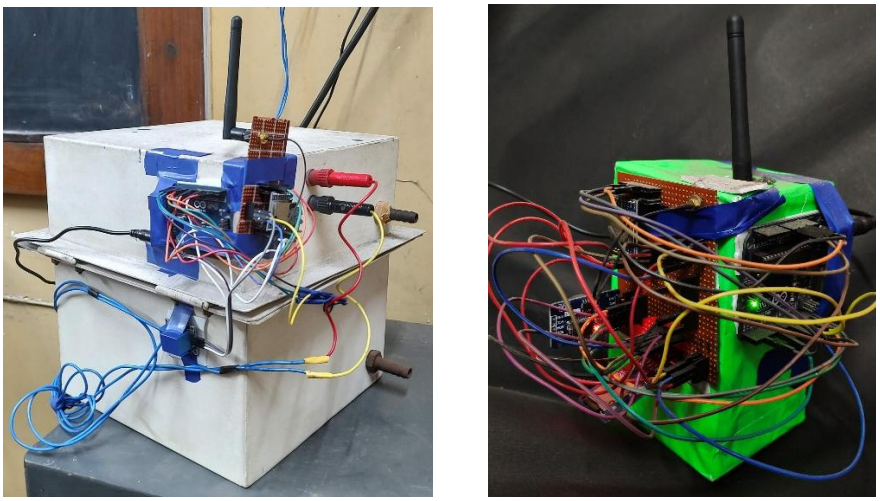

Fig. 6.5 (a) & (b): Measuring Sphere (MS) & User Interface cum Storage Device (UISD)

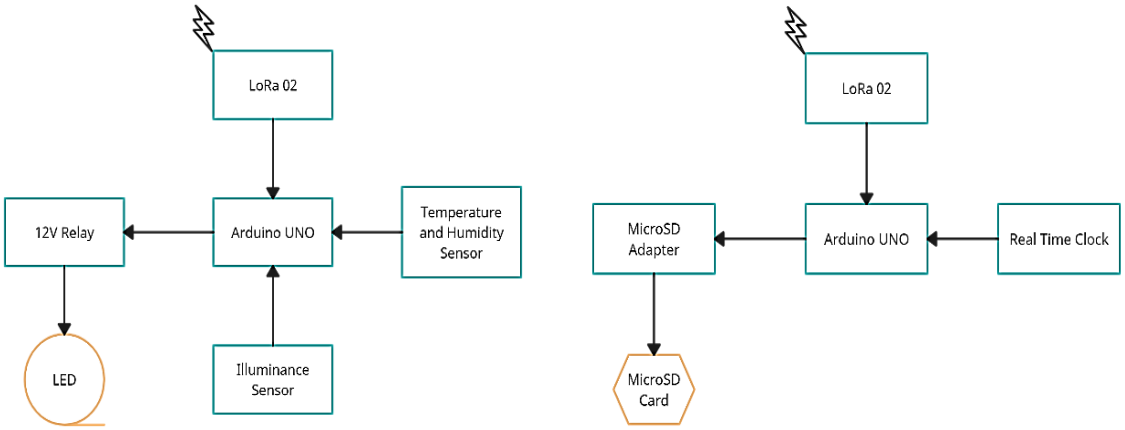

Fig. 6.6 (a) & (b): Block Diagram of MS and UISD

6.3.3 Hardware Implementation

As discussed in the previous section, this device consists of two main components: the MS, which measures all photometric and ambient data, and the UISD, which tags this data with accurate date and time stamps and stores it on a microSD card. The MS device is designed to operate with both 240V, 50Hz AC, and 110V DC power supplies. The microcontroller and sensors within it operate on 5V TTL logic and are powered by a 9V, 2A DC adapter, with sensors directly connected to the microcontroller. However, the LPWAN-based LoRa02 module operates on 3.3V TTL logic, which is converted from the microcontroller's 5V TTL logic using logic level shifters. The UISD also uses the same type of logic level shifters for the LoRa02 module, while other devices, namely microSD card adapter and real time clock module, connected to the microcontroller operate with 5V TTL logic, similar to the MS device. The UISD's power supply requirements are identical to those of the MS device.

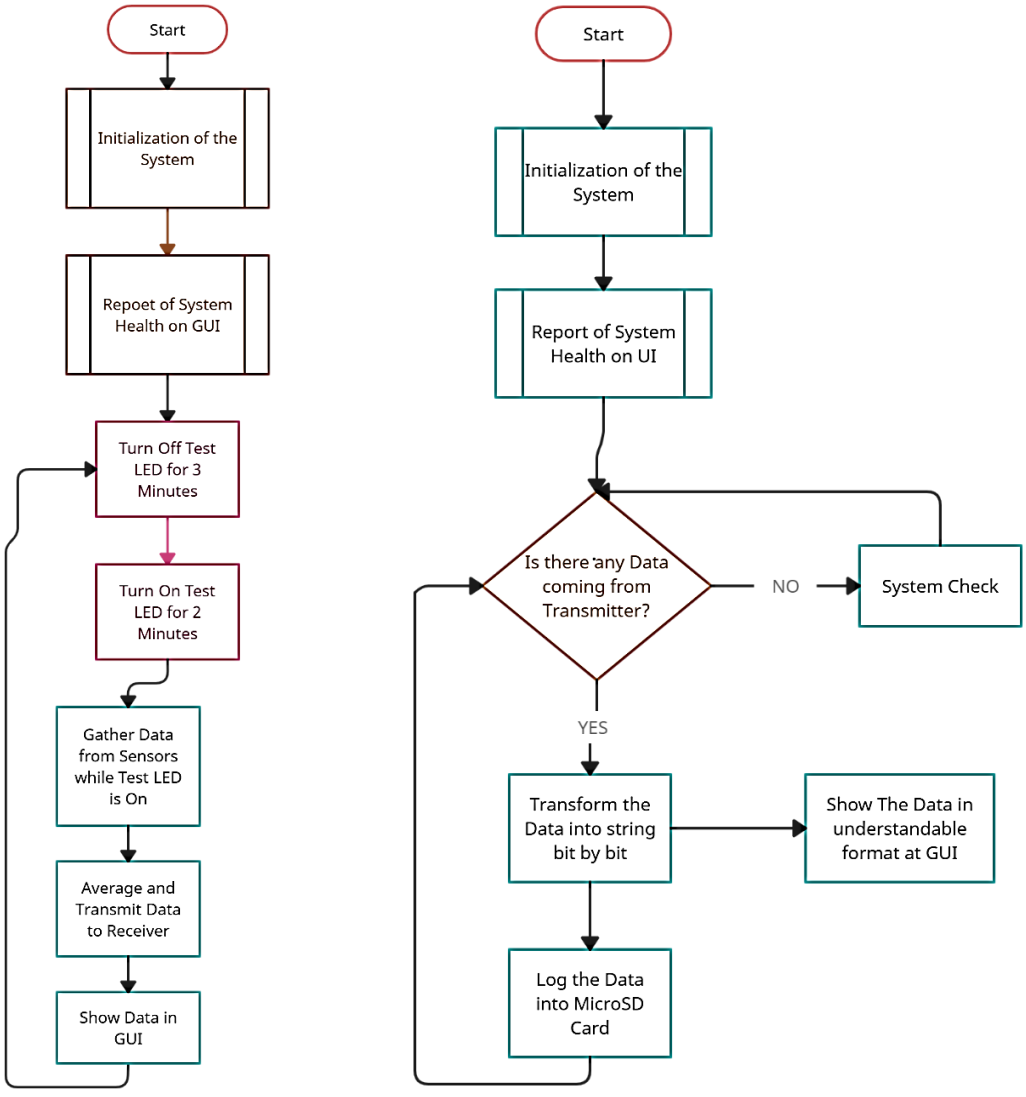

Fig. 6.7 (a) & (b): Flow Chart of MS and UISD

6.3.4 Validation of BAS Method

As discussed previously, a small-scale case study was performed to assess the effect of a novel dimming technique, termed beam angle switching (BAS), on the light output of an LED strip, as well as to evaluate the functionality of the newly developed system. In the BAS method, the beam of the luminaire is adjusted to deliver three distinct lighting modes. Specifically, this dimming technique uses LED luminaires that contain three separate LED arrays, each equipped with lenses mounted on individual LED chips to create three dedicated beam angles for three arrays. The luminaires are designed to allow each beam to be turned on or off through an appropriate lighting control system. The luminaire beam control operates in three stages based on street traffic density and other road factors: "FULL GLOW" beam control, "PRO" beam control, and "COUNTER" beam control. Under the "FULL GLOW" setting, all LED arrays light up, producing maximum output. The "PRO" mode activates a single LED array directed toward the traffic flow, reducing light intensity to around one-third of the "FULL GLOW" output and saving energy accordingly. Similarly, the "COUNTER" mode directs the beam opposite to traffic, following the same dimming pattern as "PRO." This "shadow and light" pattern is repeated for the entire road under "PRO" control, while "light and shadow" is repeated under "COUNTER" control, both initiated when traffic density is low. The LED arrays in the luminaire are switched on and off with specific manners at varying intervals, depending on the road's traffic density. In this case study, a scaled-down LED cluster was utilized, with lenses designed to provide a fixed beam angle of 90°, to assess whether the light output of the specialized LED cluster changed due to frequent switching. This LED cluster contains 12 LED chips and operates at approximately 30 watts. Fig. 6.8 (a) shows an image of this specially designed LED cluster. After configuring the LED array, specific details for switching timing were programmed into the MS part of the system, so that the LED would turn on for 2 minutes and off for 3 minutes. The LED cluster was installed in the MS part, and the system was activated. This experiment was conducted during college hours (12 PM to 8 PM) over three consecutive months, excluding Sundays, resulting in a total operating time of (8×6×4×3) hours or 576 hours. The MS part precisely measured lighting and peripheral (temperature and humidity) data using the installed illuminance sensor and temperature and humidity sensor, which then transmitted the data wirelessly via LoRa to the UISD part, where it was stored in a text file. Fig. 6.8 (b) provides a sample of the recorded text data. Since the system measures luminous irradiance in a controlled sphere environment, minor variations in light output are reflected in the recorded data, validated by the study. Due to the large volume of data, the results for three consecutive days were averaged and plotted graphically in Fig. 6.9 (a), where the Y-axis represents the averaged illuminance values and the X-axis shows the middle date of each three-day period. Additionally, another two graphs are presented in Fig. 6.9 (b) and (c), where measured and averaged junction temperature is plotted against the middle date of consecutive three days, and measured and averaged humidity is plotted against measured and averaged illuminance values, respectively.

DATE	Time	Illuminance	Humd.	Temp(C)	Temp(F)
21-12-2022	20:04:30	219348.94	34.80	33.10*C	91.58*F
21-12-2022	20:09:30	230852.44	35.30	32.90*C	91.22*F
21-12-2022	20:14:31	224732.28	35.10	33.00*C	91.40*F
21-12-2022	20:19:31	216301.17	34.90	33.00*C	91.40*F
21-12-2022	20:24:32	230284.19	34.90	33.00*C	91.40*F

Fig. 6.8 (a) & (b): Used Test LED Cluster and Text Pattern Recorded in the UISD Device

Fig. 6.10 provides further graphical representations. In Fig. 6.10 (a), the Y-axis shows averaged hourly illuminance for a single day, while the X-axis displays the hours of the middle date for each three 30-day period. Fig. 6.10 (b) and 6.10 (c) are plotted between measured and averaged junction temperature values of 1 h for 1 day and hours of the middle date of each three equal 30 days span, and measured and averaged values of humidity of 1 h for 1 day is plotted against measured and averaged illuminance values of 1 h for 1 day for each three equal 30 days span. These figures give a clear view of daily parameter fluctuations, while Fig. 6.9 provides an overall understanding of changes in illuminance, junction temperature, and humidity over the three months. From the graphs in Fig. 6.9 (a) and Fig. 6.10 (a), it is apparent that the averaged illuminance of the LED cluster, installed in the MS part, does not significantly fluctuate with frequent switching. Furthermore, Fig. 6.9 (b) and 6.10 (b) indicate that the averaged junction temperature of the LED cluster increases with time but remains within safe limits. The study also confirms that junction temperature increments slightly impact illuminance output. Besides, this experiment also discovered that the ambient averaged humidity of the sphere does not affect the averaged illuminance output of the specially designed LED array, and it can be seen that averaged illuminance values slightly increases with increment in humidity values, which is good for a humid country like India. These findings suggest that specialized LED arrays (each LED chip fitted with lenses to create specific beam angles) can tolerate frequent switching, a core principle of the BAS dimming technique. This case study also validates the functionality of the newly developed LED lumen maintenance testing device. It is evident that users can input switching time details, allowing the microcontroller to control the LED cluster accurately and measure illuminance,

temperature, and humidity. As previously mentioned, all these measurements are wirelessly transmitted to the UISD part via LPWAN, using the LoRa 02 module. The UISD part stores each measurement with a unique timestamp on a microSD card. It can be concluded that the system's procedures and functionality meet expectations successfully.

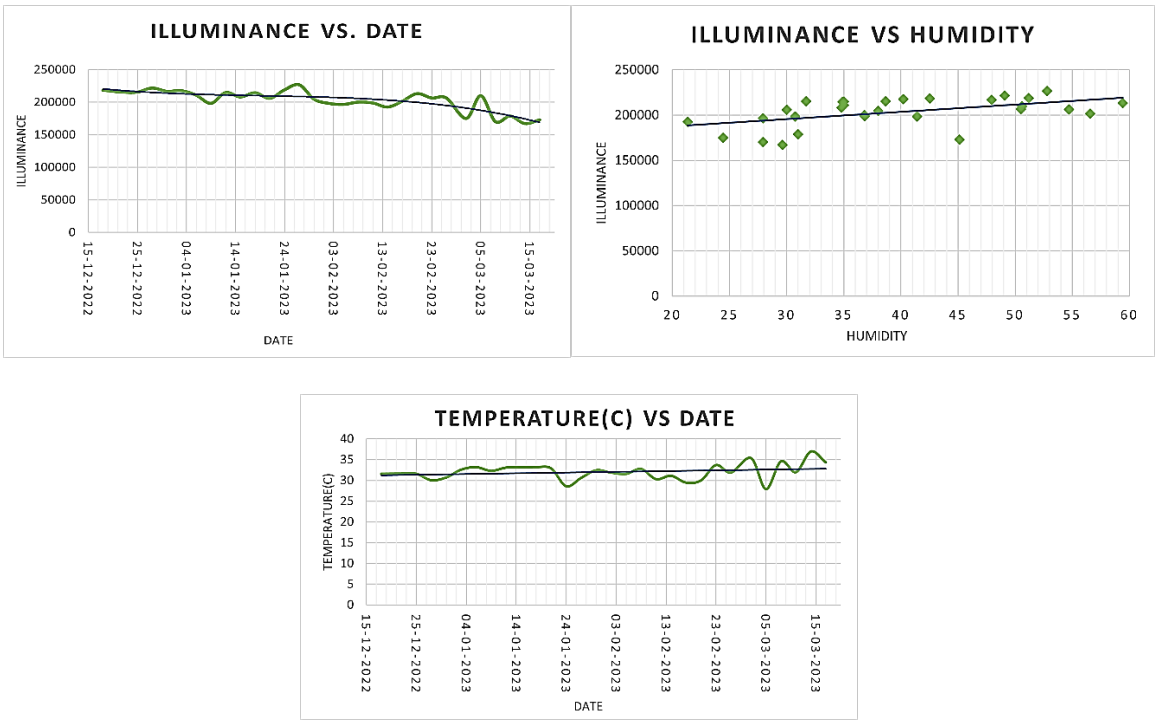

Fig. 6.9 (a), (b) & (c): Graphical Representation of Averaged Illuminance Values and Middle Date of Consecutive Three Days Taken, Measured and Averaged Junction Temperature and Middle Date of Consecutive Three Days Taken, and Measured and Averaged Humidity is Plotted against Measured and Averaged Illuminance Values for Consecutive Three Days

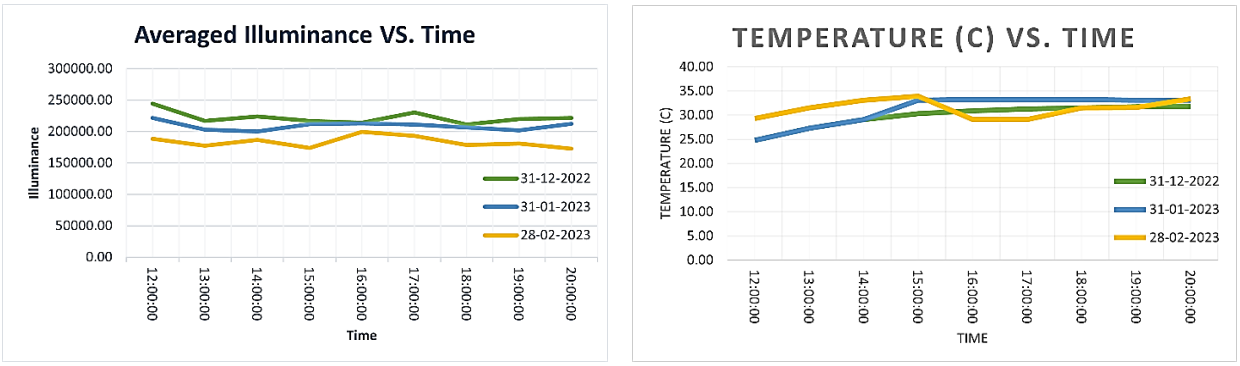

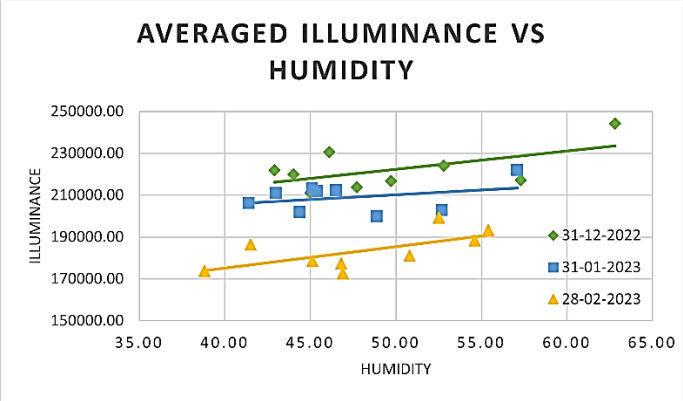

Fig. 6.10 (a), (b) & (c): Graph between Measured and Averaged Illuminance Values of 1 h for 1 day and hours of the Middle Dates of each three Equal 30 Days Span, Graph between Measured and Averaged Junction Temperature Values of 1 h for 1 ay and hours of the Middle Date of each three Equal 30 Days Span, and Graph between Measured and Averaged Illuminance Values of 1 h for 1 day and Averaged Values of Humidity of 1 h for 1 day

6.3.5 Discussion

This newly developed LED testing device prototype performs effectively in the aforementioned case study. Through a comparative analysis with other market-available testing devices, it is evident that this system and its development methodology are superior to existing options. Additionally, the entire system is significantly more cost-effective than other LED testing devices. Another key advantage is its low power consumption, excluding the power used for the LED itself. The real-time measured power for this new LED testing device is precisely 21.16 W, with the RTC (real-time clock) module consuming around 14 W and the microSD card with adapter consuming about 5 W. Furthermore, the system offers scalability, allowing for easy optimization of its size, based on test object specifications, due to the simplicity of its components. Only the sphere's size needs adjustment for larger systems, while other components, such as microcontrollers, the LoRa 02 module, and sensors for illuminance, temperature, humidity, and storage, remain the same across all configurations. Additionally, this developed system aligns closely with important standards like IES LM-80-2015 and IES-TM-21-11, with previous section detailing correlations between the system and these standards.

6.3.6 Conclusion

The literature review suggests that LEDs have an exceptionally long lifespan (around 50,000 to 60,000 hours, or approximately 6.5 years), making it challenging to test and predict their lifecycle. Properly testing LEDs would require leaving them on for 6.5 years, but the accelerated lifecycle testing method allows prediction within about 10,000 hours by continuously switching the light source over roughly 1.2 years. This is why the newly developed system is crucial, as it enables such tests. Additionally, this system is highly advanced compared to other LED testing devices due to its compact, cost-effective design,

scalability, and wireless communication, allowing remote and safe testing. There is significant potential for further enhancement, such as creating a user-friendly graphical interface to allow immediate input. Improving the system's capabilities to predict faults, plot graphs, and provide real-time values of parameters like current and power consumption of the test LED would also be beneficial. A case study validates both the system and a new dimming method known as the BAS (Beam Angle Switching) method, demonstrating the system's robustness and simplicity. The study also confirms that the rapid and random switching of the specially designed LED cluster does not impact its light output. Furthermore, it shows that the LED's junction temperature remains within optimal limits, and ambient humidity does not affect the illuminance of the LED array. This dimming method could be implemented easily in Indian street lighting, with significant benefits in terms of electrical power savings. In conclusion, the newly developed LED life testing device performs well and could serve as a prototype for future development into a more rugged and robust device.

6.4 Case Study of Street Lighting of an Indian University: Present and Future of BAS Method

In a developing country like India, it is essential that streets are well-lit to promote economic growth through efficient transportation, ensure the safety of drivers and pedestrians, and enhance road ecology. However, street lighting consumes approximately 40% of cities' total electrical energy [136-138], contributing significantly to pollution and greenhouse gas emissions. This has led municipalities to develop systems for monitoring and minimizing energy use to reduce costs [147]. Compared to older lighting technologies like incandescent, mercury vapor, sodium vapor, and compact fluorescent lamps, LED street lights have a longer lifespan, consume less energy, and reduce carbon emissions and energy costs [9]. LEDs also perform well in terms of luminous efficacy, illuminance, CCT, and CRI [148-149]. Their controllability allows for precise adjustments in light output and CCT, which studies suggest improves human performance at a CCT of 4500 K [116-117,150]. However, while pulse width modulation (PWM) dimming can reduce LED output, it may affect LED lifespan and efficiency due to high-frequency switching and potential shifts in the white point [151]. As an alternative, Suddhasatwa et al. propose the beam angle switching (BAS) method, which adjusts the beam angle to control luminance levels and reduce energy use [32]. This section presents a case study on street lighting at Jadavpur University, focusing on energy consumption and smart control, and examines the effectiveness of BAS for energy reduction. The study involves an inspection of the existing lighting setup, simulations in AutoCAD and Dialux, and a comparison of BAS with the current system and a full LED retrofit scenario. Findings indicate that BAS can cut energy consumption to one-third of current levels, reducing costs associated with LED street lighting maintenance.

6.4.1 Description of the Existing Street Lighting System of University

Jadavpur University, a renowned public institution, is located in Kolkata, West Bengal, India, known as the "City of Joy." Founded in 1905 as the Bengal Technical Institute, it was renamed Jadavpur University in 1955 [32]. Street lighting on this educational campus has evolved over time, reaching its current state through extensive modernization efforts. The university operates two campuses in Kolkata, at Jadavpur and Salt Lake. This paper focuses on a case study of the street lights in the Jadavpur campus. However, the current lighting scheme is not energy-

efficient. It relies on outdated sources like metal halide lamps, sodium vapor lamps, and CFLs, which consume substantial energy and have shorter lifespans compared to LEDs. Statistics reveal that 52% of Jadavpur campus lights are mercury vapor lamps, 40% are LEDs, and 4% are sodium vapor lamps and fluorescent tubes. Additionally, 64% of the lights come from one company (C1), while the rest are from another (C2), as illustrated in Fig. 6.11 (a) and (b). Total number of street lights in Jadavpur campus is 136.

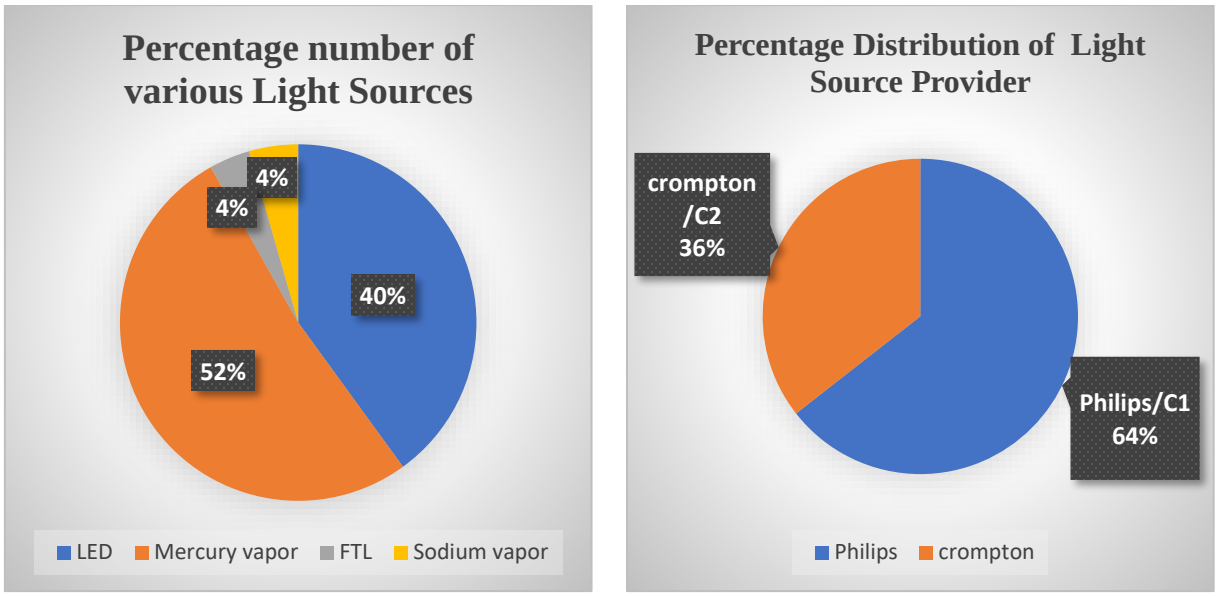

Fig. 6.11 (a) & (b): Percentage Distribution of Lamps and Light Source Providers

All light fixtures are mounted on steel poles, where the average height is 6.12 m, with an average pole span of 21.82 m, ranging from 9 m to 50 m. These distances are measured with a laser distance meter (Fluke 406E). Four poles have dual brackets, one pole has three, and one has four brackets for holding luminaires. LED lights include 45 W, 70 W, and 160 W lamps; mercury vapor lamps are available in 250 W and 150 W; sodium vapor lamps come in 250 W and 400 W; and fluorescent tubes are 40 W. Sample lighting, both during the day and night, is shown in Fig. 6.12 (a) and (b). All of the wattage data are measured using a clamp meter. The average illuminance on streets is 46.38 lx, and illuminance uniformities are recorded for each light type using a lux meter, as shown in Fig. 6.12 (c). Classifying campus roads by the Indian road lighting standard IS:1944 (Parts I and II)-1970 places them in Groups B2 and C. According to these standards, Groups B2 and C require a minimum overall illuminance uniformity of 0.3, calculated as the ratio of minimum to average illuminance, which indicates evenness of light distribution. Table 6.1 presents the measured and recommended illuminance uniformity values for various types of campus street lights. These measurements show that uniformity on campus exceeds the standard recommendations, indicating excessive lighting and leading to unnecessary energy consumption. This analysis shows that the campus lighting scheme requires a complete transition to LEDs. Implementing the BAS method with smart controls can further reduce energy use and maintenance costs. A pictorial representation of the campus map with the street light's position and categorization is given in the Fig. 6.13. It is clearly seen from the map that, some places in the campus need sufficient lighting, where there is none and some

places have extra lighting. That's why it can be concluded that the future street lighting scheme of the campus must distribute the light evenly in the campus.

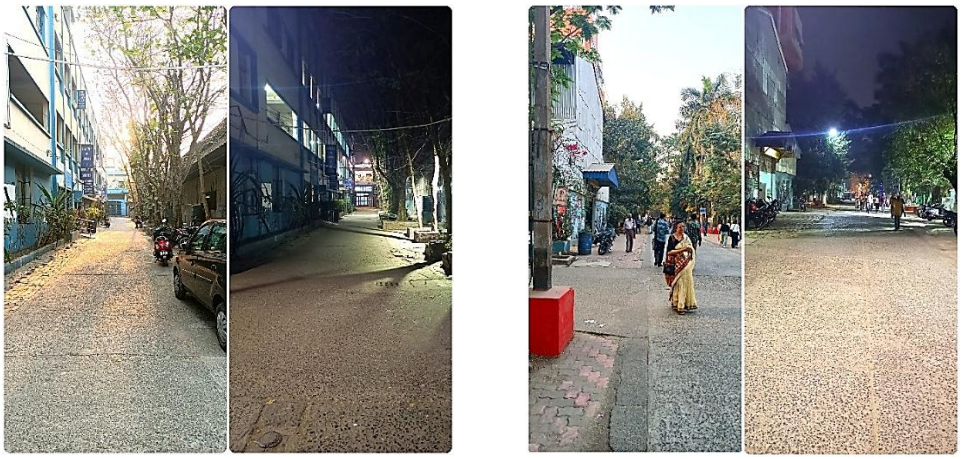

Fig. 6.12 (a) & (b): Two Scenes of Same Campus Road at Day and Night

Fig. 6.12 (c): Illuminance Meter and Grid Points with Measured lux Values

Table 6.1: Corresponding Illuminance Uniformity values of street lights of campus road and recommended values of Indian Standard

Type of Light Sources	**Measured Illuminance Uniformity**	**Recommended Illuminance Uniformity**
LED Lamp	0.84	0.3
Sodium Vapor Lamp	0.75	0.3
Mercury Vapor Lamp	0.8	0.3
FTL	0.77	0.3

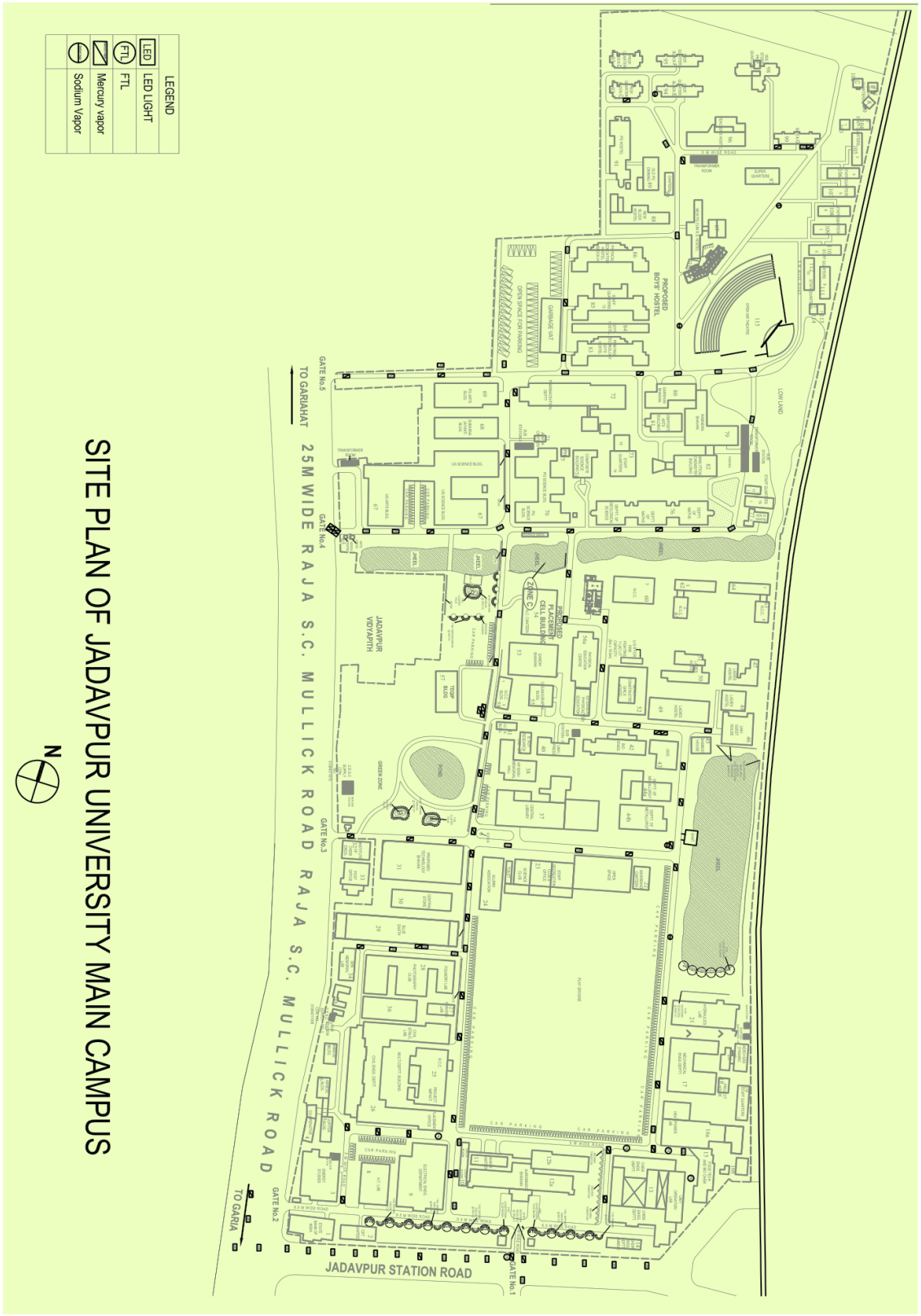

Fig. 6.13: Pictorial representation of the campus map with the street light's position and categorization

6.4.2 Description of Future Upgradable Smart Street Lighting System

According to the statistical analysis of measured data from Jadavpur University's Jadavpur campus, it is observed that 40% of the total lighting fixtures installed on street poles of campus road are LEDs. Studies indicate that LEDs demonstrate far superior luminous efficacy compared to other light sources present on campus, such as mercury vapor lamps, sodium vapor lamps, and fluorescent tube lights. These findings suggest that LEDs can achieve equivalent lighting levels while consuming less electrical energy than the other mentioned sources. Moreover, LEDs possess a longer lifespan, which can be substantiated using the LM-18 [152] and TM-21 [153] standards from IESNA. In addition to these benefits, LEDs offer advantages in other lighting parameters, including better CRI and adaptable CCT, attributed to their enhanced controllability. This controllability feature allows for the integration of smart functionalities such as automated operations, wireless communication, and BAS method of dimming into the campus street lighting scheme. Despite these advantages, it is noted that the LEDs currently installed on campus roads lack smart capabilities, suggesting a significant potential for upgrading the existing lights to incorporate smart features. Retrofitting other light sources with smart LED lights would enable substantial energy savings for the campus. Furthermore, one commonly employed feature that adds "smartness" to LED systems is the dimming function, which allows for reduced energy consumption when there is minimal or no traffic on campus roads. This dimming is usually achieved through single pulse-width modulation (PWM), a method that adjusts the current in LED drivers, by changing the duty cycle (D), using the pulse-width modulation technique to dim the LEDs. As part of the dimming process, PWM switches the LED current between 0 and the rated current at high frequency, creating a ratio of on-time to total time period of one cycle that regulates the LED's intensity. However, the PWM method also presents some disadvantages. The primary drawback of PWM dimming is its susceptibility to generating electromagnetic interference, which can negatively impact the efficiency and life-span of the LEDs. Specifically, PWM dimming can decrease the lifespan of LEDs because the high-frequency switching of the LED chip (typically between 500 Hz and several kHz) generates substantial electromagnetic interference. This interference may impair the driver's efficiency, as the repeated switching can overheat components such as capacitors and MOSFETs. If not carefully managed, PWM dimming can also affect the LED's white point, where the white point of an illuminant is the chromaticity of a white object under this specific, defined by chromaticity coordinates like the x, y coordinates on the CIE 1931 chromaticity diagram. Such shifts in the white point can degrade the LED's light quality, potentially hindering object detection under that specific light source, which can be detrimental to both drivers and pedestrians [154]. To address these limitations, a novel technique known as Beam Angle Switching (BAS) was developed at the Illumination Engineering Laboratory in the Department of Electrical Engineering at Jadavpur University [32]. This technique controls the beam angle of LED lights based on factors such as vehicular density, the primary traffic direction, and the time of day, allowing for various levels of illuminance from the same LED luminaire. The beam is designed to operate in three distinct illumination modes: "FULL GLOW," "PRO," and "COUNTER." In the FULL GLOW setting, all LED arrays are activated to provide maximum brightness from the luminaire. The PRO mode, on the other hand, engages only one LED array in the direction of traffic, reducing the light output to roughly a third of the FULL GLOW condition, which conserves energy. The COUNTER mode is similar to the PRO mode but directs the light beam opposite to the primary

traffic flow. The PRO control results in a “Shadow and Light” illumination pattern on the roadway, whereas the COUNTER control creates a “Light and Shadow” effect. According to Suddhasatwa Chakraborty et al., the FULL GLOW setting is suitable during peak traffic hours, PRO mode is ideal for moderate traffic, and COUNTER mode can be used during low traffic periods [32]. Fig. 6.4 provides graphical representations of the FULL GLOW, PRO, and COUNTER conditions for these luminaires. To test these modes, a 155 W street light designed with smart BAS capabilities (set to FULL GLOW mode) was developed in the laboratory, adhering to all applicable standards. This luminaire was mounted on a LISUN LSG 1890-B High Precision Rotation Luminaire Goniophotometer for generating the '.ies' file, which was subsequently used in DiaLux simulations for assessing photometric and energy performance. A detailed table (Table 6.2) showing illuminance uniformities and average luminance of Jadavpur University campus roads under this smart lighting scheme is provided below. This smart, upgradable LED streetlight also features some modifications based on prior laboratory experiments. For example, the LED’s CCT was set to 4000 K to optimize reaction times, Small Target Visibility (STV), and general visibility, based on previous experiments [116]. Preliminary findings suggest that warmer CCTs improve object detection in foggy conditions, while cooler CCTs enhance visibility in cold, clear weather [150]. The street LED was also designed to be flicker-free, as flickering can significantly impact human visual and non-visual responses [117]. Additionally, the schedule of lighting conditions (FULL GLOW, PRO, and COUNTER) is forecasted based on traffic density data from campus archives, which is preprogrammed to the luminaire control system to activate the corresponding lighting modes via relay modules. The primary choice for data processing and control in this study is an Arduino UNO microcontroller, selected for its robust performance.

Table 6.2: Illuminance uniformities and average luminance of the simulated scheme

Type of Beam Angle	Measured Illuminance Uniformity	Recommended Illuminance Uniformity	Measured Average Luminance
PRO	0.28 - 0.41	0.3	9 Cd/m2
COUNTER	0.28 - 0.39	0.3	8.7 Cd/m2
FULL GLOW	0.27 - 0.53	0.4	11 Cd/m2

6.4.3 Comparison of the existing and future upgradable smart lighting system

This section provides an in-depth comparison of electrical energy consumption and electricity bill expenses, alongside the calculated energy use and cost estimates. In the current lighting system, all street lights are operational from 5:30 p.m. to 5:30 a.m., a total of 12 hours. In contrast, the lighting plan proposed for future upgrades is divided into two sections: active weekdays and off-weekdays. Active weekdays encompass the five continuous days from Monday to Friday, during which the university is fully open for educational and other activities, while off-weekdays cover Saturday and Sunday, when the university is closed. For the first segment, smart LED lights are scheduled to operate in the ‘FULL GLOW’ mode from 5:30 p.m. to 9:30 p.m. for 4 hours, after which they will switch to ‘PRO’ or ‘COUNTER’ mode, depending on traffic direction, from 9:30 p.m. to 5:30 a.m. for 8 hours. This operation will be managed through a microcontroller. Each luminaire is equipped with a light sensor and real-time clock to automate the LED’s on-and-off cycles based on ambient light, accommodating location-based variations in lighting needs. During the final segment, on off-

weekdays, the lights will operate solely in the 'PRO' or 'COUNTER' modes, depending on traffic density, from 5:30 p.m. to 5:30 a.m. for the entire 12-hour period. To offer further clarity, an additional hypothetical calculation is conducted wherein all existing non-LED street lights are replaced with standard LED lights of equivalent wattage used in the 'FULL GLOW' mode under the BAS system. This calculation serves as a reference for the energy consumption of standard LEDs. Moreover, a comparative analysis is conducted between a PWM-based street lighting system and the BAS-method system, with both systems following the same operational schedule as the smart BAS-enabled system. A concise calculation is presented below:

A. *Calculation for Existing Street Lighting Scheme*:

Total number of street lights in the Jadavpur campus = 136
Total wattage of the street lights measured in the survey = 23,320 W
Existing Lighting scheme = [5:30 p.m. to 5:30 a.m. = 12 h] for 7 days in a week
Total power consumed by the existing street light sources in a year
= {(23,320×7×12) x 52.143}/1000 Kw-hr [one year = 52.143 week]
= 1,02,141.88 Kw-hr
Total generated Electricity bill considering fixed tariff of CESC
= (1,02,141.88×7.22) Rupees
= 7,37,464.374 Rupees

B. *Calculation for Hypothetical Lighting scheme Consisting of Standard LED*:

Total number of standard LED light needed to retrofit the old existing non-LED light sources = 82
Total number of existing LED street lights = 54
Wattage of an individual standard LED light source = 155 W
Hypothetical lighting scheme = [5:30 p.m. to 5:30 a.m. = 12 h] for 7 days in a week
Power consumption of an individual standard LED light source in a year
= (155×12×7×52.143) / 1000 Kw-hr
= 678.902 Kw-hr
Total power consumption by all standard LED light sources.
= (678.902×82) Kw-hr
= 55,669.964 Kw-hr
Total wattage of the existing LED street lights measured in the survey = 4070 W
Total power consumption by all existing LED light sources.
= {(4070×7×12) x 52.143}/1000 Kw-hr [one year = 52.143 week]
=17,826.649 Kw-hr
Total power consumption by all light sources
= (55,669.964+17,826.649) Kw-hr
= 73,496.613 Kw-hr
Total generated electricity bill for all standard LED light sources
= (73,496.613×7.22) Rupees
= 5,30,645.544 Rupees

C. *Calculation for Future Upgradable Smart Street Lighting Scheme*:

Total number of specially designed smart LED street lights = 136
Wattage of an individual LED street light of this kind = 155 W
Developed adaptive street lighting control scheme = [5:30 p.m. to 9:30 p.m. = 4 h in FULL GLOW condition + 9:30 p.m. to 5:30 a.m. = 8 h in PRO or COUNTER condition] for 5 days in a week + [5:30 p.m. to 5:30 a.m. = 12 h in PRO or COUNTER condition] for 2 days in a week
Total power consumption of an individual similar LED over a week
= [{(4×155) + (8×(155/3))} x 5] + [{(12×(155/3))} x 2] watt-hr
= (1033.33×5) + (620×2) watt-hr
= 6406.66 W-hr
≈ 6.407 Kw-hr
Total power consumption of an individual similar light source over a year
= (6.407×52.143) Kw-hr [one year = 52.143 weeks]
= 334.08 Kw-hr
Total power consumption of all similar lights in the future lighting scheme if each and every existing lighting source is retrofitted
= (334.08×136) Kw-hr
= 45,434.88 Kw-hr
Total generated electricity bill for Future Upgradable Smart LED light sources
= (45,434.88×7.22) Rupees
= 3,28,039.834 Rupees

D. *Percentage decrement for Future Scheme*:

Percentage reduction from existing system to BAS method in energy consumption in a year
= {(1,02,141.88–45,434.88) / 1,02,141.88 } x 100%
≈ 55.52%
Percentage reduction in electricity bill for the same in a year ≈ 55.52%
Reduction in CO2 emission for the same
= (1,02,141.88– 45,434.88) x 0.85 Kg
= 48,200.95 Kg
Percentage reduction from hypothetical system to BAS method in energy consumption in a year
= {(73,496.613–45,434.88) / 73,496.613 } x 100%
≈ 38.19%
Percentage reduction in electricity bill for the same in a year ≈ 50.79%
Reduction in CO2 emission for the same
= (73,496.613– 45,434.88) x 0.85 Kg
= 23,852.4731 Kg

E. *Retrofitting Cost and other Calculations*:

Cost of a single smart upgradable street light with driver = 7,500 Rupees
Cost of a single smart controller unit = 263 Rupees

Total cost of the smart system = 7,763 Rupees
Total number of standard LED light needed to retrofit the old existing non-LED light sources = 82
Total number of existing LED street lights = 54
Here, existing street lights only needs smart controller unit (given that it is supported by the LED).
Total cost of all the smart street lights = {(7,763×82) + (263×54)} Rupees
= 6,50,768 Rupees
Approximate Labour charge = (1,507×136) Rupees [Labour charge fixed by Govt.]
= 2,04,952 Rupees [155]
Total cost of retrofitting existing street lights with smart upgradable street lights
= (6,50,768+2,04,952) Rupees
= 8,55,720 Rupees
Time needed to earn back total expenditure by saving electricity bills
= {8,55,720 / (7,37,464.374–3,28,039.834)} years
= 2.09 years
≈ 2 years

F. *Comparative Analysis between BAS method and PWM method*:

Generally used PWM based street lighting control scheme = [5:30 p.m. to 9:30 p.m. = 4 h in full intensity with 100% duty cycle+9:30 p.m. to 5:30 a.m. = 8 h in 40% duty cycle] for 5 days in a week + [5:30 p.m. to 5:30 a.m. = 12 h in 40% duty cycle] for 2 days in a week (Below 40% duty cycle, Illuminance level on street will drop below the recommended value given at IS: 1944–1 and 2 (1970)).
It is found from the study that the energy consumption of a PWM based LED is proportional with the duty cycle applied to it [156]. So, at 40% duty cycle, LED will consume 40% of its rated energy consumption.
Total power consumption of an individual PWM based LED over a week
= [{(4×155) + (8×(40% of 155))} x 5] + [{(12×(40% of 155))} x 2] watt-hr
= [{620+496} x 5]+1488 W-hr
= 7068 W-hr
= 7.068 Kw-hr
Total power consumption of an individual similar PWM enabled light source over a year
= (7.068×52.143) Kw-hr [one year=52.143 weeks]
= 368.55 Kw-hr
Total power consumption of all similar PWM enabled lights in the future lighting scheme if each and every existing lighting source is retrofitted
= (368.55×136) Kw-hr
= 50,122.35 Kw-hr
Total generated electricity bill for PWM enabled Smart LED light sources
= (50,122.35×7.22) Rupees
= 3,61,883.4 Rupees
A detailed graph of Lighting schemes versus electricity bill generated by the lighting schemes per year is given in Fig. 6.14.

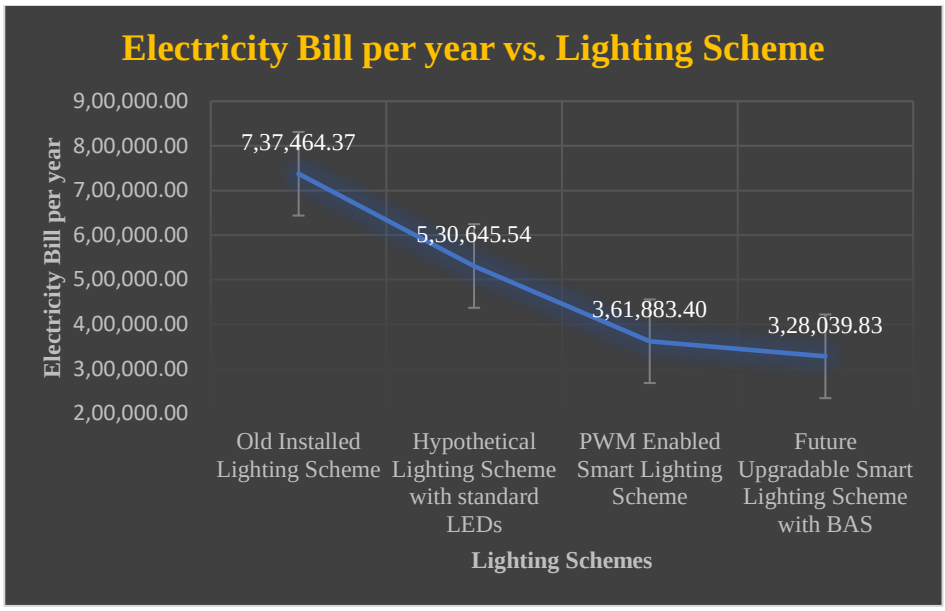

Fig. 6.14: Graph between lighting schemes and electricity bills generated by these schemes

6.4.4 Conclusion

The comparative study above clearly demonstrates that the developed future upgradable smart LED lighting system with Beam Angle Switching (BAS) method will significantly reduce electrical energy consumption and electricity bills, both by 55.52%. It will also reduce CO2 emission by approximately 53.14 ton as formulated by the central electricity authority of ministry of power, Govt. of India. Furthermore, there are also a reduction of 38.19% electrical energy consumption and 26.3-ton CO2 emission from the hypothetical lighting scheme considered for referencing by the BAS method. Moreover, this modern lighting scheme is shown to hold substantial promise for smart city applications. The BAS technique proves more efficient and human-centric than the PWM dimming method, as it achieves lower energy consumption with reduced electricity bills and reduces reaction times for visual or non-visual tasks by eliminating Temporal Light Modulations. This characteristic makes BAS a viable metric for future engineering solutions in smart city infrastructures. However, for optimal effectiveness, it is essential to ensure equal light distribution across the Jadavpur campus to maintain overall illuminance uniformity. If light poles are spaced irregularly, this method may fail, creating alternating shadow and bright zones, resulting in a “Zebra effect.”

6.5 Study on Implementation of PWM Dimming in Beam Angle Switched LED Street Light to Achieve further Energy Efficient Standard Lighting

There are several dimming techniques available, such as constant voltage dimming and PWM (Pulse Width Modulation) dimming. Research has shown that PWM dimming is considered one of the most effective methods in the field of dimming. This technique adjusts the light output of an LED by supplying it with a pulsed DC current with a variable duty cycle. Moreover, the PWM method prevents the LED’s junction temperature from increasing drastically, which contributes to an extended LED lifespan compared to other dimming techniques [25-31]. Additionally, studies

on the BAS method and the effects of lighting parameters on human reaction times reveal that BAS-enabled LED street lights provide extra illuminance on the working plane (in this case, the street), whereas standard LEDs offer higher illuminance than BAS-enabled LEDs. Therefore, the illuminance output needs optimization to meet Indian street lighting standards. Consequently, a study was conducted in the Illumination Engineering Laboratory of the Electrical Engineering department at Jadavpur University to explore the introduction and implementation of PWM dimming in BAS-enabled LED street lights. The major focus of this experimentation is to check whether introduction of PWM dimming in BAS enabled street lights can further reduce the energy consumption of the human centric smart street lights. In each BAS lighting condition, the PWM duty cycle was reduced from 100% to 40% to assess any impact on the quality and illuminance uniformity of the LED street lights. The study concluded that changes in the PWM duty cycle did not significantly affect illuminance uniformity or light quality (CCT, CRI). Furthermore, energy consumption of the LED lights decreased almost linearly with the reduction in duty cycle.

6.5.1 Experimental Setup

This indoor experiment was conducted in a controlled environment at the Illumination Engineering Laboratory of the Electrical Engineering Department at Jadavpur University. The purpose of the experiment was to examine how reducing the duty cycle of the PWM signal supplied to a BAS-enabled street LED affects both the quality of light output and illuminance uniformity at the working plane, as simulated in the laboratory. The quality of light output was evaluated by observing the effect of varying PWM duty cycles on the LED's CCT and CRI. Additionally, overall illuminance uniformity was determined by dividing the minimum illuminance value by the average illuminance value across grid points, ensuring compliance with Indian street lighting standards. The experiment took place in a blacked-out laboratory to minimize light reflection on measuring equipment, allowing for accurate data collection from the LED. A specially designed 55watt IP65 grade LED street light was used, housed in a luminaire casing with a fin-type heat radiator. The LED, equipped with BAS control, featured three lighting states: "FULL GLOW," "PRO," and "COUNTER." In the "FULL GLOW" state, all LED clusters were active, providing maximum light output. The "PRO" state, which reduced light output to about one-third of "FULL GLOW," involved activating a single LED array oriented in the direction of traffic to conserve energy. The "COUNTER" state functioned similarly to "PRO" but directed the light beam against the traffic flow. The LED was mounted on a height-adjustable street light pole fixed at a height of 3.5 meters for this scaled-down setup. Fig. 6.15 (a) illustrates the experimental setup in detail. A PWM control circuit was constructed using a Darlington pair to supply the PWM signal to the LED. An OLED display was connected to monitor duty cycles and analog input, where the duty cycle is adjusted via a 10K potentiometer. The control circuit was built with an Arduino Uno microcontroller, and Fig. 6.15 (b) provides a visual representation of the circuit. Code is given in Annexture 1. The PWM signal’s duty cycle could be adjusted using both coding and potentiometer input. Besides, the frequency of the PWM signal is maintained at a fixed frequency of 7.8 kHz, chosen to prevent temporal light modulation (TLM). Lower frequencies could induce flicker, stroboscopic effects, and phantom array effects, all of which are harmful to LEDs and human health. Sample PWM signal, used in this experiment, is given in Fig. 6.15 (c). The control circuit included three push buttons, allowing users to switch between the BAS lighting modes ("FULL GLOW," "PRO," and "COUNTER"). Following the CIE 140-2000 guidelines [108], a grid of 170 points, arranged in 10 rows and 17 columns, was set up, with

grid point A9 marking the Nadir (maximum illuminance) point. Each grid point was spaced 0.25 m apart, as shown in Fig 6.15 (d). The LED was powered by a Gwinstek programmable DC power supply, controlled via the PWM circuit.

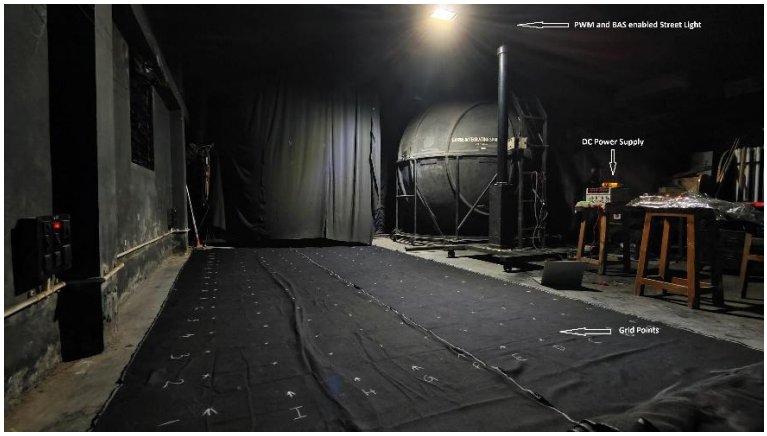

Fig. 6.15 (a): Experimental Setup

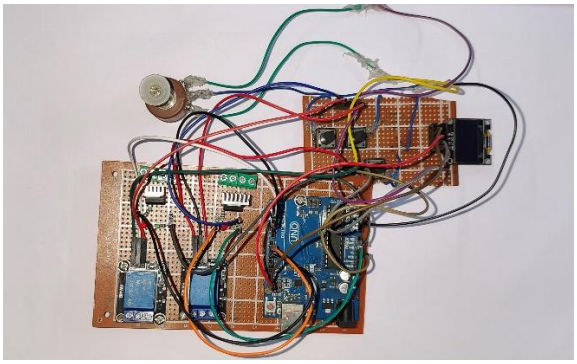

Fig. 6.15 (b): Used Control Circuit

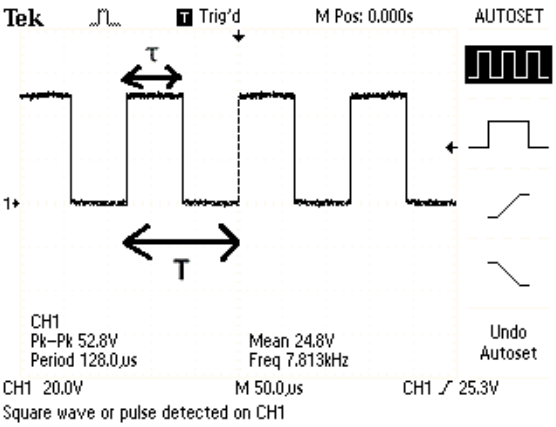

Fig. 6.15 (c): Sample PWM Signal fed in Control Circuit

Fig. 6.15 (d): Grid Points

6.5.2 Experimental Procedure

The experiment begins with the specially designed LED street light mounted on an adjustable pole set to a height of 3.5 meters. Control circuits are connected to the light, and the LED is powered using a programmable DC power supply. The three BAS lighting conditions described earlier are then tested. In each lighting condition, the PWM duty cycle is decreased from 100% to 40% with a decremental step of 5%, while measuring illuminance values on the working plane at each grid point using an illuminance meter (Metravi 1310 Digital Light Meter). The minimum PWM duty cycle of 40% is selected because below this level, the LED fails to provide adequate illuminance on the working plane as per IS 1944-1 and 2 (1970) standards [68]. In addition to illuminance measurements, the LED's energy consumption, CCT, and CRI are recorded at each duty cycle with a DC power supply and a colorimeter (Konika Minolta CL-70F), as shown in Fig. 6.16. The collected data is then systematically organized into tables, and an analysis is performed to reach conclusions.

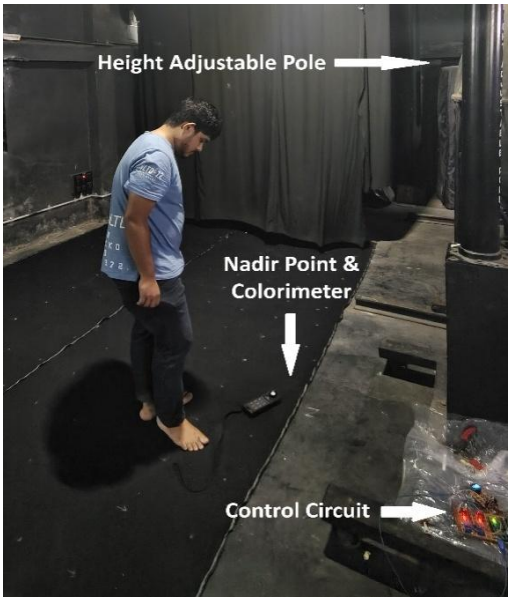

Fig. 6.16: Measurements are Going on

6.5.3 Calculations and Results

In each BAS lighting condition, the PWM signal's duty cycle is varied from 100% down to 40% in steps of 5%. For each set duty cycle, the LED street light is first allowed a 5-minute warm-up period to stabilize its light output before measurements are taken, after which the data is recorded. Using the measured illuminance values, overall illuminance uniformity (U_o) is then calculated with the formula:

$$U_o = {E_{min}}/{E_{avg}}$$

Next, the uniformity values are plotted against the PWM signal's duty cycle for each BAS lighting condition to observe any decline in uniformity as the duty cycle decreases. In addition, measured values of CCT, CRI, illuminance at the nadir point, and power consumption are plotted against the PWM duty cycle to assess if changes in the duty cycle affect these parameters. These graphical representations are provided in Fig. 6.17 (a), (b), (c), (d), (e) respectively. Corresponding data are given in Table 6.3 and Table 6.4. Upon examining the graphs, it is apparent that the duty cycle of the PWM signal does not significantly affect overall illuminance uniformity, although the "PRO" condition shows a slightly lower uniformity. The CCT plots reveal a slight decrease in CCT with decreasing duty cycle across all three BAS lighting conditions, with "PRO" and "COUNTER" showing a marginally steeper decrease than "FULL GLOW." Similarly, the CRI plot indicates a minor decline in CRI as the duty cycle is reduced, with "PRO" and "COUNTER" conditions showing a slightly higher rate of decrease compared to "FULL GLOW." However it can be seen that in both graphs CCT and CRI follows a non-linear but similar type of changes, which is a novel finding in this area. In contrast, both power consumption and illuminance at the nadir point decrease nearly linearly with reductions in the PWM duty cycle for all three BAS lighting conditions.

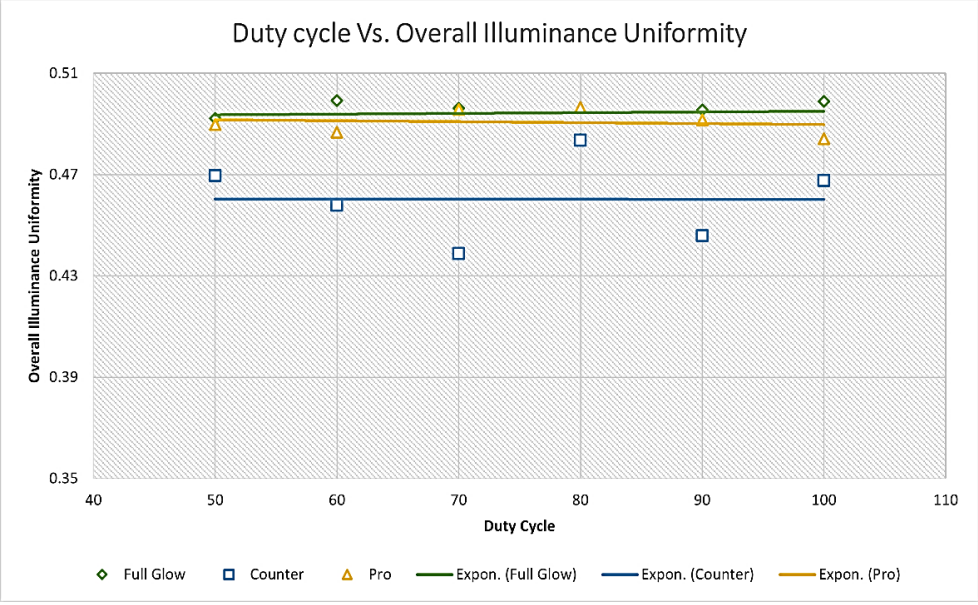

Fig. 6.17 (a): Graphical Representation of Variation of Overall Illuminance Uniformity with Duty Cycle(%)

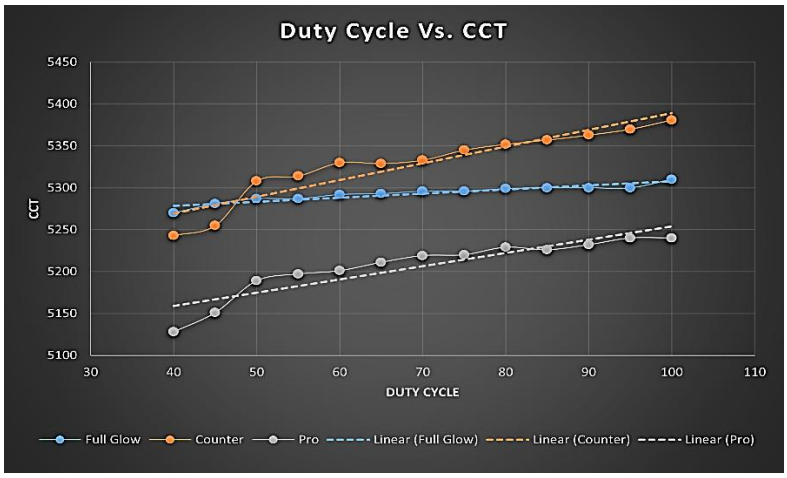

Fig. 6.17 (b): Graphical Representation of Variation of CCT(K) with Duty Cycle(%)

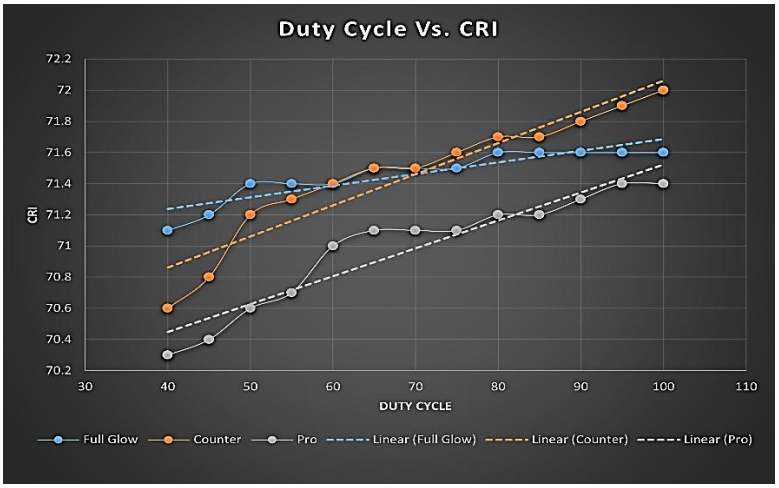

Fig. 6.17 (c): Graphical Representation of Variation of CRI with Duty Cycle(%)

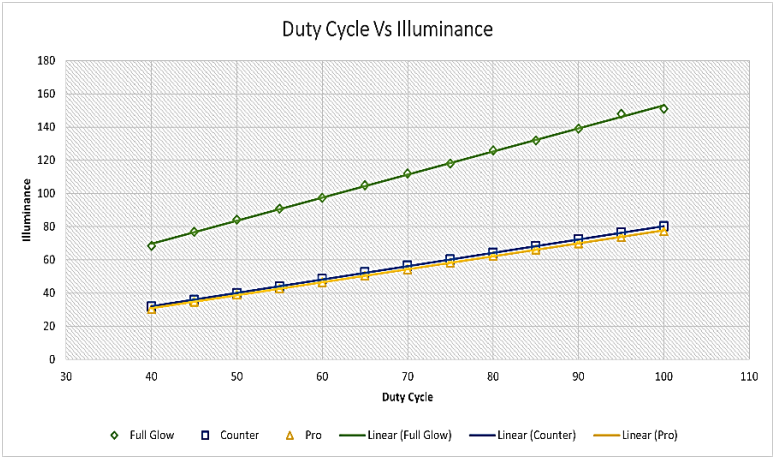

Fig. 6.17 (d): Graphical Representation of Variation of Illuminance(lux) at Nadir point with Duty Cycle(%)

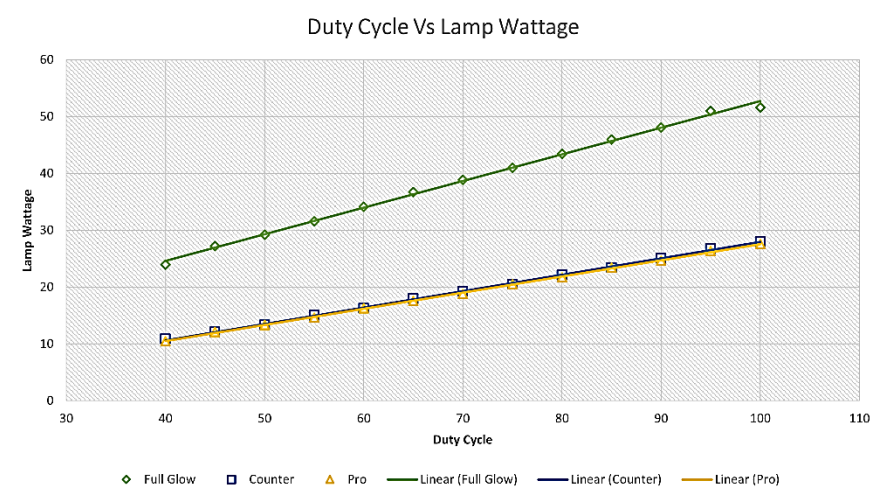

Fig. 6.17 (e): Graphical Representation of Variation of Lamp Wattage with Duty Cycle(%)

Table 6.3: Data Regarding CCT, CRI, Illuminance and wattage of PWM and Bas enabled Street Light

Duty Cycle	CCT(K)			CRI			Illuminance			Wattage		
	Full Glow	Counter	Pro	Full Glow	Counter	Pro	Full Glow	Counter	Pro	Full Glow	Counter	Pro
100	5310	5381	5240	71.6	72	71.4	151	80.2	77.4	51.59	28	27.58
95	5300	5370	5240	71.6	71.9	71.4	148	76.3	73.9	50.99	26.75	26.33
90	5300	5363	5232	71.6	71.8	71.3	139	72.3	70	48.07	25.08	24.66
85	5300	5357	5226	71.6	71.7	71.2	132	68.2	66.3	45.98	23.42	23.41
80	5299	5352	5229	71.6	71.7	71.2	126	64.1	62.4	43.47	22.15	21.73
75	5296	5345	5220	71.5	71.6	71.1	118	60.2	58.4	40.96	20.48	20.48
70	5296	5333	5219	71.5	71.5	71.1	112	56.4	54.3	38.87	19.23	18.81
65	5293	5329	5211	71.5	71.5	71.1	105	52.4	50.4	36.69	17.97	17.55
60	5292	5330	5201	71.4	71.4	71	97.4	48.4	46.7	34.16	16.3	16.3
55	5287	5314	5197	71.4	71.3	70.7	90.8	43.9	42.7	31.56	15.05	14.63
50	5287	5308	5189	71.4	71.2	70.6	84.2	39.9	39	29.23	13.37	13.37
45	5281	5255	5151	71.2	70.8	70.4	76.9	35.9	34.9	27.23	12.12	12.12
40	5270	5243	5128	71.1	70.6	70.3	68.4	31.8	30.4	23.94	10.86	10.45

Table 6.4: Data Regarding Overall Illuminance Uniformity of PWM and Bas enabled Street Light

Duty Cycle	Overall Illuminance Uniformity		
	Full Glow	**Counter**	**Pro**
100	0.4989	0.4677	0.4841
90	0.4956	0.4458	0.4916
80	0.4839	0.4836	0.4965
70	0.4962	0.4388	0.4957
60	0.4993	0.4578	0.4867
50	0.4922	0.4696	0.4898
20	0.4561	0.4392	0.4343

6.5.4 Conclusion

The study clearly indicates that PWM dimming through duty cycle reduction can be effectively implemented alongside the Beam Angle Switching (BAS) method. This combined approach offers a dual benefit in energy savings, one from the BAS method and the other from the PWM dimming application. Furthermore, the results show that adjusting the PWM duty cycle does not significantly alter the lighting characteristics of a BAS-enabled LED street light, as the CCT and CRI values remain relatively stable with changes in duty cycle. Although this experiment was conducted on a scaled-down model, it suggests that a PWM-enabled system could be applied to higher-wattage street lights (e.g., 150 watts) without alteration of the lighting parameters by the PWM dimming observed in this study. The study further confirms that altering the PWM duty cycle does not cause significant color shifts in the LED, as CCT values remain nearly consistent regardless of duty cycle adjustments. Additionally, the integration of PWM dimming with the BAS method is feasible under Indian Lighting Standards, given that overall illuminance uniformity remains unaffected by changes in PWM duty cycle. However, further research is needed to assess how the implementation of PWM dimming within the BAS method may impact road users' decision-making and response to certain stimuli, which falls within the scope of future studies.

Chapter 7: Development of a Low-Cost, High CRI, CCT Tunable BAS Enabled Smart Human Centric LED Street Light Luminaire

7.1 Background

This thesis previously describes the journey of lighting and lighting standards' evolution in introduction chapter. After extensive literature review, this thesis distinguishes the evolution of lighting domain in four steps. They can be roughly categorized as 'energy efficient lighting', 'adaptive or intelligent lighting', 'smart lighting' and the most advanced step 'human centric lighting'. The first type of lighting refers to technologies that reduced the electricity consumption than old lighting systems while maintaining or improving light quality. These solutions reduce energy consumption, lower electricity costs, and minimize environmental impacts by decreasing greenhouse gas emissions. Examples of this type of lighting include LED, CFLs and halogen incandescent bulbs. LEDs are particularly noteworthy, using up to 75% less energy and lasting up to 25 times longer than incandescent bulbs [157]. Similarly, CFLs consume about 70% less energy than incandescent bulbs while providing comparable lighting quality [158]. Adaptive or intelligent lighting refers to advanced lighting systems that adjust in real-time to the environment or operational needs. These systems utilize technologies such as sensors, IoT (Internet of Things), and advanced algorithms to dynamically control light intensity, color, and distribution, enhancing both energy efficiency and user experience. Key features of adaptive lighting include occupancy sensing, where lights turn on or off based on room usage, and daylight harvesting, which adjusts artificial lighting according to natural light levels [159]. Smart lighting refers to advanced lighting systems that integrate digital technology to provide automated, customizable, and energy-efficient illumination. These systems are typically connected to wireless networks, enabling remote control and management through smartphones, voice commands, or integrated platforms like smart home assistants. Smart lighting systems often feature IoT (Internet of Things) connectivity, allowing devices to communicate and adapt dynamically to user preferences, schedules, or environmental changes. For instance, smart lights can adjust brightness based on natural daylight, detect room occupancy to switch on or off, and even change color to suit specific moods or activities [160]. It can be observed that the differences between adaptive or intelligent lighting and smart lighting is quite blur but wireless control and batch control via a

control room (city wide street lighting control) are the advanced feature of smart lighting. Furthermore, the most advanced step till date, human-centric lighting emphasizes a holistic approach to understanding light and illumination as key factors influencing human visual, biological, and behavioral responses. It integrates both the visual and non-visual effects of light on individuals. This concept focuses on lighting solutions that enhance human mood, well-being, and overall health. Often referred to as human factors in illumination, it prioritizes the effect of light on human being's daily lives and physiological balance [44]. Besides, this type of lighting minimizes energy consumption and encompasses all the features of a smart lighting. Research to incorporate this type of lighting schematic in street lighting domain is very little explored. This chapter dedicates all its length to develop a low-cost, high-CRI, smart human centric street lighting solution. It can be divided in three sub-division. The first sub-division describes an experimentation, which optimizes the switching frequency of the PWM (pulse width modulation) dimming to achieve best CCT tunability. The second sub-division talks about the theory and the process of the development of the before-said lighting system. The last sub-division proposes a method and a system to monitor and control the CCT of the system.

7.2 Impact of Different Switching Frequencies of Pulse Width Modulated Signal on Various Lighting Parameters of LEDs

7.2.1 Introductions

Lighting is a fundamental element influencing human well-being, productivity, safety, and security, as well as the industrial and economic growth of India. Historically, traditional light sources like incandescent, metal halide, and fluorescent lamps dominated the Indian market. However, with the advent of advanced power LEDs, these conventional sources are being rapidly replaced for superior energy efficiency, longer lifespan, and better performance of LEDs across parameters such as efficacy, dynamic CCT, CRI, luminance, and illuminance [161]. Recent studies forecast the global market for lighting control systems to grow at a CAGR of 14.2% between 2021 and 2029 [162]. Despite efforts by the Indian government and private sectors to retrofit legacy systems with LEDs, a significant number of older light sources remain in use. Lighting accounts for 18–27% of India's total energy consumption, contributing substantially to greenhouse gas emissions and environmental degradation [137-138,147,162]. A viable solution lies in deploying smart LED systems with advanced lighting controls and dimming techniques to optimize energy use. Smart lighting enables users to automate and regulate various lighting parameters, significantly reducing energy consumption. Common controls include motion sensors, occupancy sensors, and photosensors. Motion and occupancy sensors ensure lights are activated only when spaces are in use, while photosensors adjust lighting based on ambient illumination levels, preventing unnecessary use of outdoor lighting during daylight hours [163]. Various dimming methods, including digital dimming (PWM), analog dimming, and BAS method (beam angle switching), offer enhanced control over lighting [32,156]. Among these, PWM dimming is widely adopted in India due to its ability to modulate LED output by applying a pulsed DC current with a variable duty cycle. This method minimizes heat generation at the LED junction, thereby extending the LED's lifespan [164]. Additionally, PWM dimming significantly improves LED controllability [25,27-28]. To assess

the efficiency of the PWM dimming technique and explore potential enhancements, ongoing research is being conducted. One study revealed that increasing the switching frequency of the applied PWM signal results in a reduced rise in LED junction temperatures for the same duty cycle and current. Conversely, junction temperatures increase proportionally with the duty cycle when frequency and current are kept constant. These findings suggest that higher switching frequencies can effectively prolong the lifespan of LEDs [165]. However, the impact of varying PWM switching frequencies on key lighting parameters, necessary for enabling smart control features in LED systems, remains unexplored. Identifying the optimal frequency range for PWM dimming to achieve system efficiency is still an open question. This research is essential for precisely regulating lighting parameters such as CCT and CRI, which are critical for human-centric lighting applications [166]. Human-centric lighting involves a holistic approach to illumination, addressing both the visual and non-visual effects of light on human behavior, biology, and perception. It prioritizes emotional well-being, health, and overall quality of life, earning the alternative name "human factors in illumination" [11]. Another challenge associated with PWM dimming is the phenomenon of LED color shifts. Studies indicate that color shifts occur with PWM dimming, where changes in the duty cycle alter the CCT. The duty cycle represents the percentage of time the signal remains at a high amplitude within a complete cycle [167]. Understanding and mitigating such effects are critical to ensuring consistent and reliable performance in smart LED lighting systems. A pictorial representation of duty cycle of PWM dimming is given in Fig. 7.1.

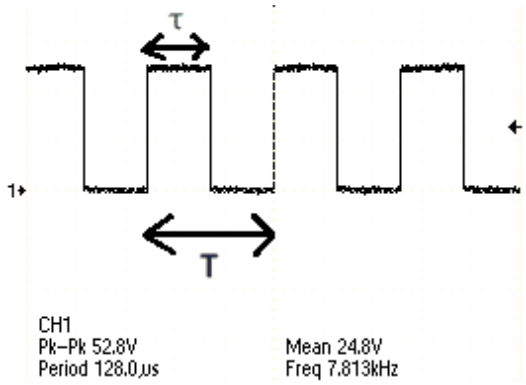

Fig. 7.1: Visual Depiction of Duty Cycle

Where, Duty Cycle or, $D = \frac{\tau}{T}$

Here, D stands for duty cycle, τ stands for the time for which the pulse is high in a cycle, T stands for the time period of the signal.

To investigate the impact of varying switching frequencies on the lighting parameters of PWM-enabled LED lights and to identify the optimal operating frequency range, an experimental setup was developed. The setup was designed within a black box to eliminate ambient light interference. An ESP32 WROOM DA microcontroller module was employed for generating PWM signals at varying frequencies and duty cycles. Adjustments to both frequency and duty cycle were made using two 5k potentiometers. For this experimentation, two SMD bead chip

LEDs with power ratings of 10 watts (TD-LED10W) and 20 watts (TD-LED20W) were used. The selected frequency range for the study was from 100 Hz to 20 kHz, with frequency increments of 1 kHz, except for the first interval, which was 900 Hz. For each switching frequency, the duty cycle was reduced incrementally from 100% to 40% in 10% steps. This range of switching frequencies and duty cycles was chosen to facilitate a basic analysis of the effects of switching frequency on various lighting parameters. Future studies may expand this range and refine frequency intervals to allow for more in-depth exploration. Key lighting parameters such as CCT, CRI, and illuminance were measured using a Konica Minolta CL-70F colorimeter. Previous research has shown that higher switching frequencies in PWM signals enhance LED lifespan, which justified the inclusion of frequencies up to 20 kHz in the study [165]. Results indicated that changes in frequency had minimal effects on CCT and CRI, with standard deviations for these parameters being lowest at higher frequencies near 20 kHz. This finding supports the conclusion that operating at higher switching frequencies, such as 20 kHz, offers optimal performance in terms of lighting stability and efficiency.

7.2.2 Experimental Design and Methodology

This investigation is carried out in a controlled environment within a specially designed black chamber to minimize ambient light interference. The chamber, constructed using wood and perforated steel columns, is located in the Illumination Engineering Section of the Electrical Engineering Department at Jadavpur University, Kolkata. The aim is to analyze the effect of varying PWM switching frequencies on critical lighting parameters such as CCT, CRI, and illuminance of two LEDs, one rated at 10 watts and the other at 20 watts, and to determine the optimal frequency range for dimming operations. The wattage at various dimming stages is also recorded for comparative analysis. The experiment is conducted in a dark environment to eliminate the effects of reflected light on measurement devices, ensuring precise test data from the LEDs. The black chamber has an outer height of 1.6m, a length of 0.9m, and a breadth of 0.7m, with an internal height of 1.5m. It is thermally stable, with the LEDs mounted on a wooden block away from the steel frame. The front of the chamber remains open for ease of measurement but is covered with a thick black jute cloth during measurements to block external light effectively, given in Fig. 7.2 (a). For this study, two high-power, random white-color, 12-volt SMD bead chip LEDs (10 watts - TD-LED10W, and 20 watts - TD-LED20W) are used. Their rated CCT values are 6600K and 8000K, respectively. The LEDs are mounted on aluminum heat sinks for efficient heat dissipation, with thermal paste applied, given in Fig. 7.2 (b). Two identical milky-white hemispherical plastic diffusers are employed to diffuse the light output uniformly. Identical diffusers are used to mitigate any bias in light spectrum alterations due to the diffuser, which is considered negligible for this study [168]. The LEDs are powered by a GWINSTEK DC laboratory-grade power supply, and all photometric measurements are performed using a battery-powered, dark-calibrated Konica Minolta CL70F colorimeter. A PWM signal is generated using a custom-designed microcontroller-based circuit to control LED dimming. The ESP32 WROOM DA microcontroller is chosen for its ability to control switching frequency and duty cycle simultaneously over a wide range. Used code is given in Annexture 1. A separate MOSFET circuit amplifies the PWM signal before it is fed to the LEDs. Two 5k potentiometers are used to manually adjust the switching frequency and duty cycle. Fig. 7.3 provides a detailed graphical representation of the control circuit. The THD (Total Harmonic Distortion) and other electrical parameters such as voltage, current, and

power are kept within the limits specified by Indian Standard IS 16103: Part II: 2012. According to the standard, test parameters must remain stable within ±0.5% during stabilization and ±0.2% during measurement. Harmonic content is limited to 3%. The study begins with the 20-watt LED mounted on a heat sink, with DC power supplied to the system. The duty cycle is initially set to 100%, and the switching frequency is set to 100 Hz using two potentiometers. The nadir point, representing the maximum illuminance on the grid points, drawn on working plane (base of the chamber), is marked. Any slight misalignment of the colorimeter at the nadir point is considered insignificant for the photometric measurements. Subsequently, the duty cycle is decreased incrementally to 40%, in 10% steps, and measurements for CCT, CRI, and illuminance are taken at each step on nadir point. This process is repeated for each switching frequency, which ranges from 100 Hz to 20 kHz in 1 kHz increments, except the first step of 900 Hz, resulting in 21 frequencies. A total of 147 lighting scenes are studied for each LED. After each measurement, the system is turned off for five minutes to allow the LED junction temperature to stabilize, minimizing any potential alterations in photometric parameters due to temperature changes. The cooling interval is determined using a handheld infrared thermometer (HTC MT-4) after preliminary experimental cycles. Once measurements for all 147 lighting scenes are completed for the 20-watt LED, it is replaced with the 10-watt LED, which undergoes the same experimental procedure. Each LED is allowed to stabilize its light output before every stable reading. Data from all 147 lighting scenes for both LEDs are recorded in Excel sheets for statistical analysis. Duty cycles below 40% are not used, as they fail to generate sufficient illuminance on the working plane, as per the recommendations of the Indian Standard IS:1944 Part I&II, 2003.

Fig. 7.2(a): Used Black Chamber

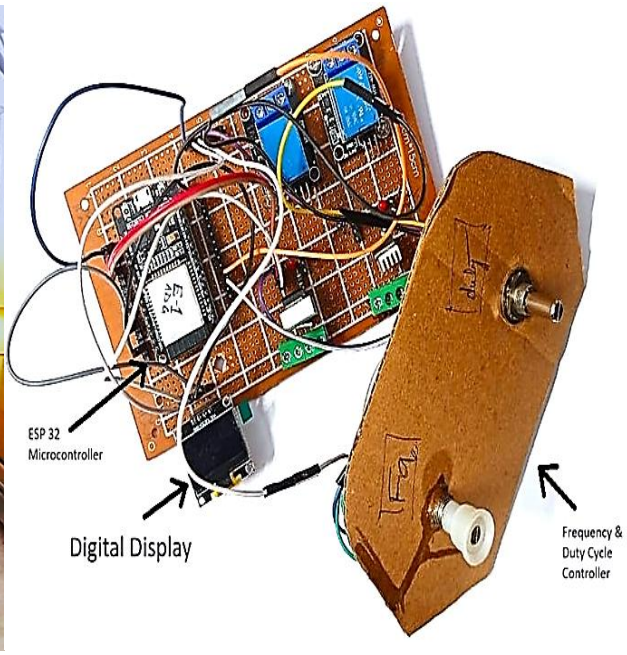

Fig. 7.3: Control Circuit of the System

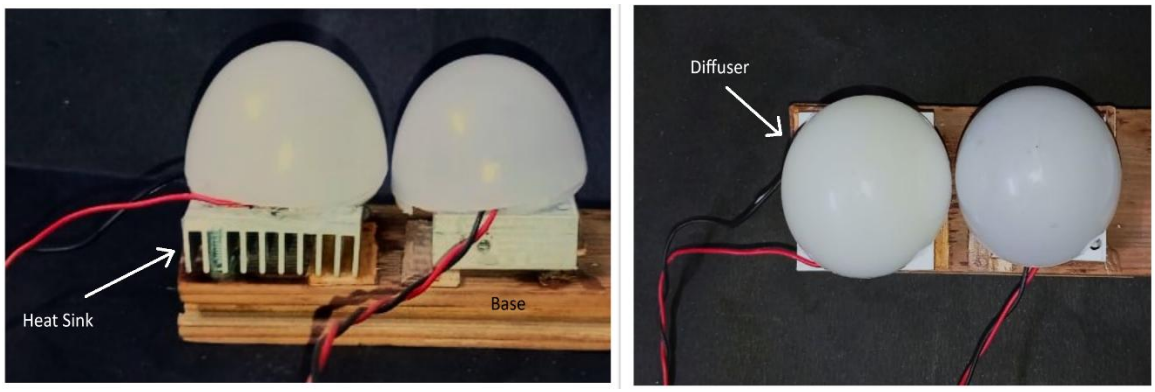

Fig. 7.2(b): Used LEDs with Diffuser and Heat Sink

7.2.3 Calculations and Results

The duty cycle of the Pulse Width Modulated (PWM) signal applied to the cool white LEDs is decreased from 100% to 40%, with a 10% decrement at each unique switching frequency of the PWM signal. The switching frequency is varied from 100 Hz to 20 kHz, with a 1 kHz gap, except for the first gap, which is 900 Hz. The lighting parameters, CCT, CRI, and Illuminance, are recorded for each lighting scene using the previously mentioned colorimeter. After taking the measurements, standard deviations (SD) for CCT and CRI are calculated for all duty cycles associated with each switching frequency of the PWM signal. These SD values are then plotted against the switching frequency, as shown in Fig. 7.4 (a), 7.4 (b), and Fig. 7.5 (a), 7.5 (b), where Fig. 7.4 (a), 7.4 (b) correspond to the 10-watt LED and Fig. 7.5 (a), 7.5 (b) represent the 20-watt LED. In this study, the standard deviations are calculated, using the formula provided, to measure the range of deviation of CCT or CRI values around their mean value for each switching frequency. A lower SD indicates smaller deviation [169].

The formula for the population standard deviation is given as follows:

$$SD = \sqrt[2]{\frac{\sum_{i=1}^{N}(Xi-\mu)^2}{N}}$$

where, SD = Standard deviation of the population; N = Number of observations in population; X_i = i^{th} observation in the population; μ = Mean of the population.

The focus of the study on SD calculation is to analyze how the variation in CCT or CRI occurs for a particular switching frequency due to the change in duty cycle of the applied PWM signal. Furthermore, this analysis helps identify the optimal operational switching frequency, where the deviation or variation is smaller compared to other frequencies. Mathematical linear equations are fitted to the graphs presented in Fig. 7.4 (a), 7.4 (b) and Fig. 7.5 (a), 7.5 (b). Additionally, four other graphs are plotted to show the overall variation of CCT and CRI values against the duty cycle of the PWM signal for each distinct switching frequency. These graphs are depicted in Fig. 7.6 (a), 7.6 (b) for the 10-watt LED, and Fig. 7.7 (a), 7.7 (b) for the 20-

watt LED. Two additional graphs are plotted between recorded illuminance values and duty cycle for each switching frequency, as shown in Fig. 7.8 (a) and 7.8 (b) for the 10-watt and 20-watt LEDs. Furthermore, two more graphs are plotted to show the relationship between CCT values and switching frequency at 100% duty cycle of the PWM signal, illustrating the direct deviation of lighting parameters with respect to switching frequency. These are shown in Fig. 7.9 (a) and 7.9 (b) for the 10-watt and 20-watt LEDs. All the aforementioned curves are plotted for both the 10-watt and 20-watt LEDs.

From the plotted graphs, several observations can be made. As shown in Fig. 7.4 (a), 7.4 (b) and Fig. 7.5 (a), 7.5 (b), it is evident that the SD values of CCT and CRI decrease as the switching frequency increases, with the lowest variation of CCT and CRI occurring at 20 kHz. Moreover, when examining the fitted linear equations derived from the Microsoft Excel plots, it becomes apparent that the slopes of these equations are very small. This suggests that the changes in CCT or CRI values in relation to switching frequency are minimal.

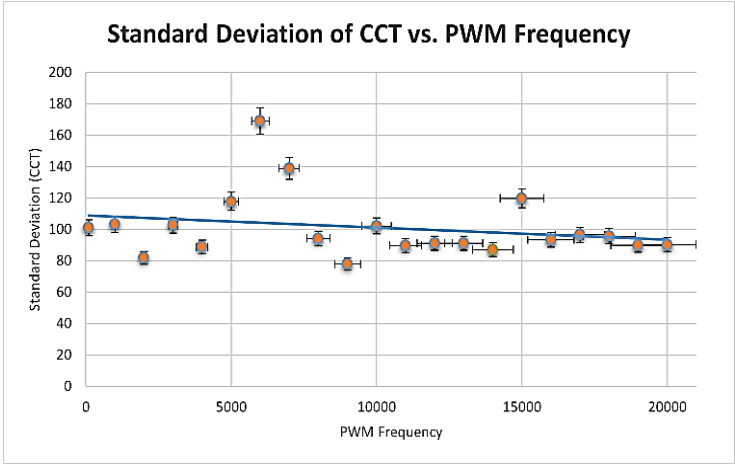

Fig. 7.4(a): SD of CCT vs. Switching Frequency(10W)

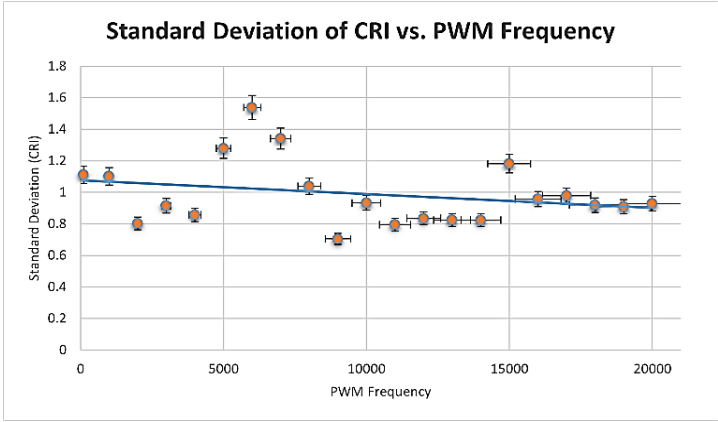

Fig. 7.4(b): SD of CRI vs. Switching Frequency(10W)

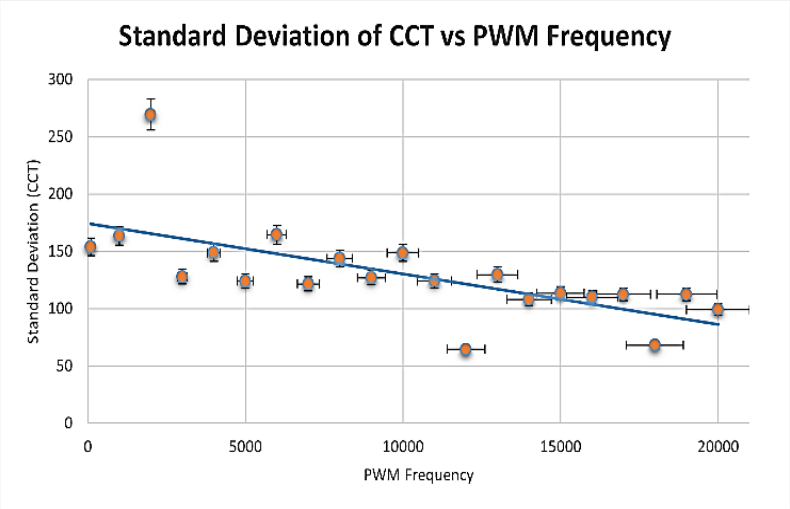

Fig. 7.5(a): SD of CCT vs. Switching Frequency(20W)

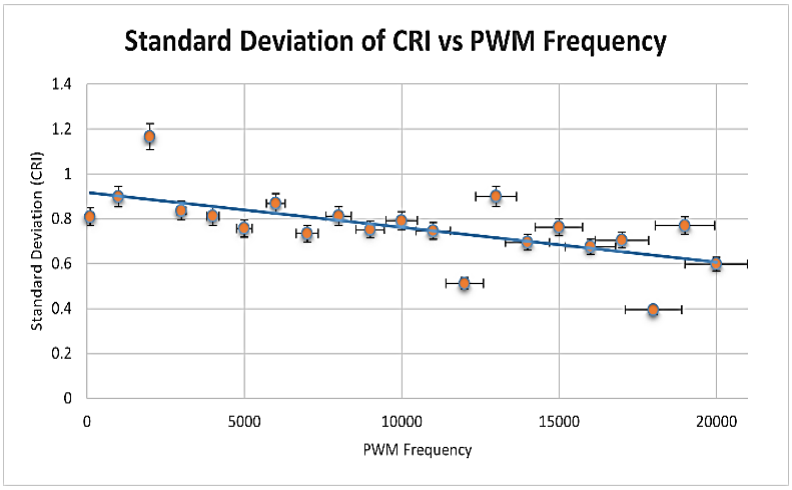

Fig. 7.5(b): SD of CRI vs. Switching Frequency(20W)

The equations derived for these SD calculations are as follows:

$Y_{10} = -0.0008X + 108.74$ ….. Eq.(1) [SD of CCT vs. Switching Frequency, 10 watts]

$Y_{10}^{*} = -9x10^{-06}X + 1.077$ ……. Eq.(2) [SD of CRI vs. Switching Frequency, 10 watts]

Here, 'X' denotes switching frequency and 'Y_{10}' denotes SD of CCT for equation 1 and for equation 2, 'X' denotes switching frequency and 'Y_{10}^{*}' denotes SD of CRI.

$Y_{20} = -0.0044X+174.16$ ……..Eq.(3) [SD of CCT vs. Switching Frequency, 20 watts]

$Y_{20}^{*} = -2x10^{-05}X + 0.9173$ …....Eq.(4) [SD of CRI vs. Switching Frequency, 20 watts]

Here, 'X' denotes switching frequency and 'Y_{20}' denotes SD of CCT for equation 3 and for equation 4, 'X' denotes switching frequency and 'Y_{20}^{*}' denotes SD of CRI.

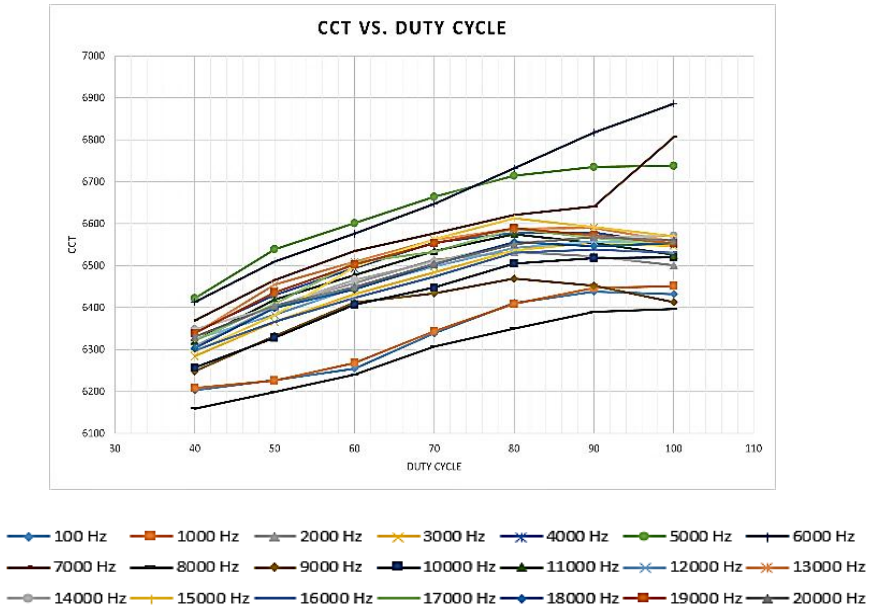

Fig. 7.6(a): CCT vs. Duty Cycle (10W)

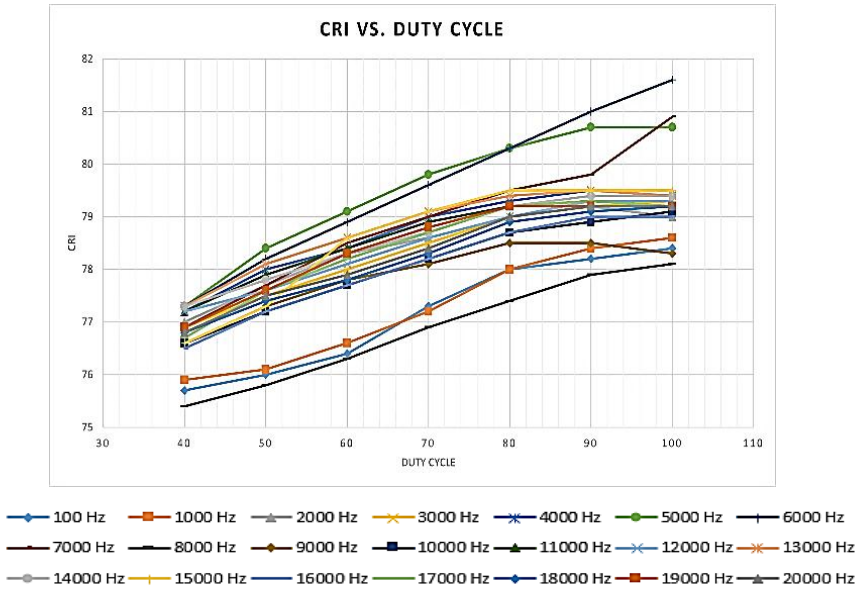

Fig. 7.6(b): CRI vs. Duty Cycle (10W)

These equations indicate that the changes or deviations in CCT or CRI values for the experimental LEDs, in response to the switching frequency of the applied PWM signal, are

minimal, as evidenced by the small slopes of the equations. Additionally, an analysis of the graphs in Fig. 6a, 6b, and Fig. 7a, 7b reveals that the CCT and CRI values vary with changes in the duty cycle of the applied PWM signal, irrespective of the switching frequency. When the duty cycle increases, the CCT and CRI values also rise, indicating that an increase in duty cycle shifts the LED's color toward the cooler CCT range. However, the changes in CCT or CRI due to variations in switching frequency are small, and this change becomes even smaller at higher switching frequencies. Moreover, as shown in Fig. 8a and Fig. 8b, the illuminance values decrease almost linearly as the duty cycle decreases, which is in line with expectations [168]. Finally, the graphs in Fig. 9a and Fig. 9b illustrate that when the duty cycle is fixed at 100%, the CCT and CRI values remain relatively unchanged as the switching frequency of the PWM signal is varied. This is expected because, at 100% duty cycle, the LEDs remain continuously on, and changes in switching frequency do not affect the lighting parameters, as the waveform does not alter.

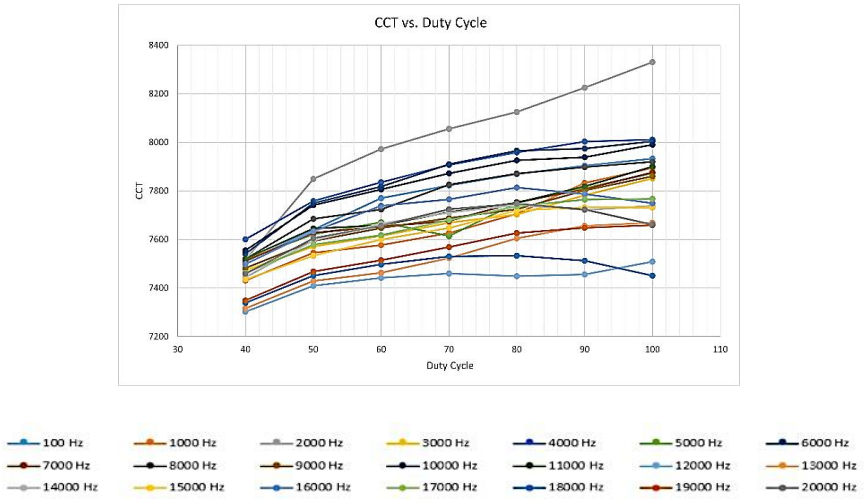

Fig. 7.7(a): CCT vs. Duty Cycle (20W)

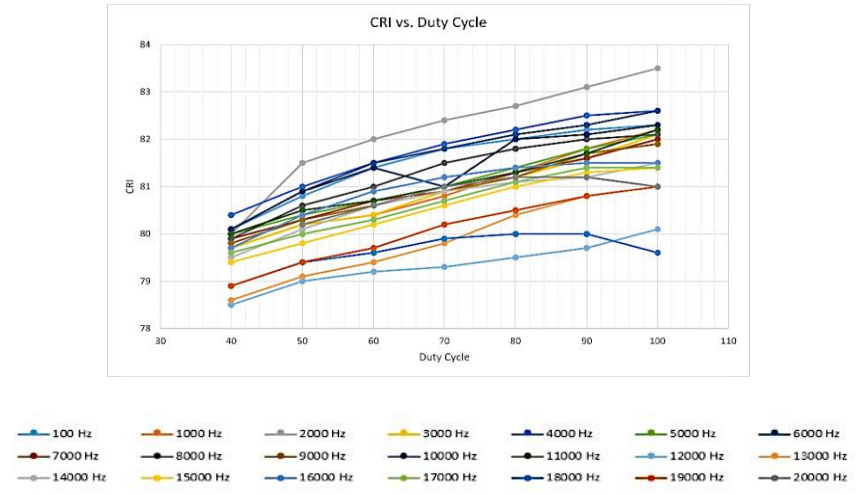

Fig. 7.7(b): CRI vs. Duty Cycle (20W)

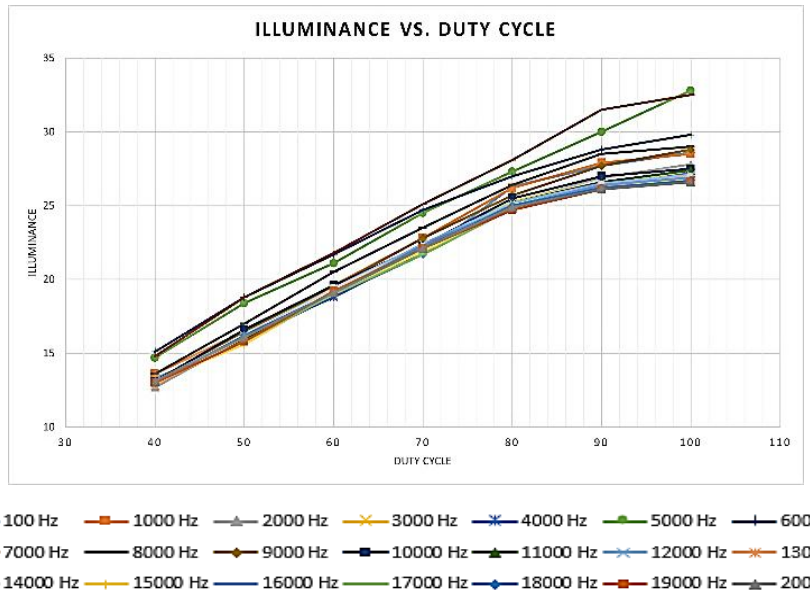

Fig. 7.8(a): Illuminance vs. Duty Cycle (10W)

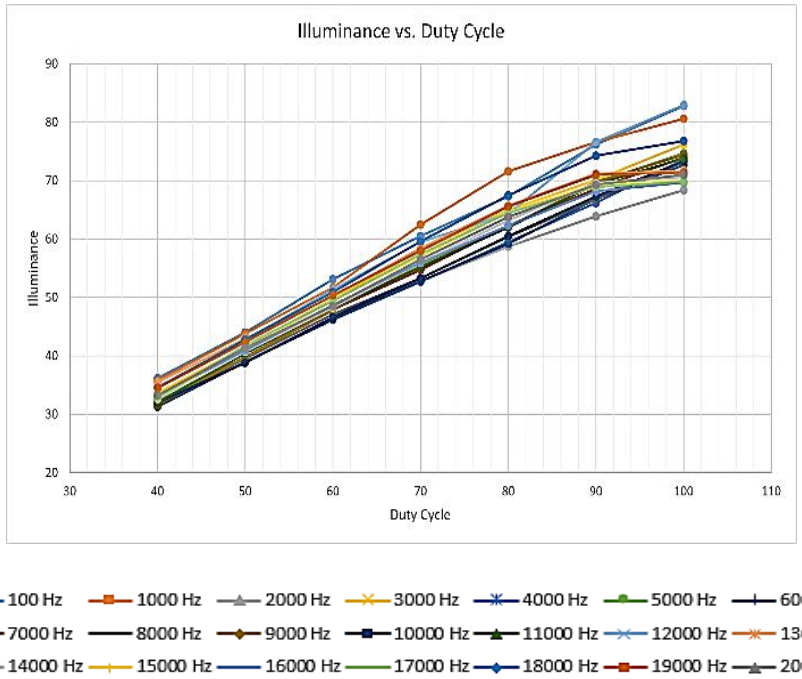

Fig. 7.8(b): Illuminance vs. Duty Cycle (20W)

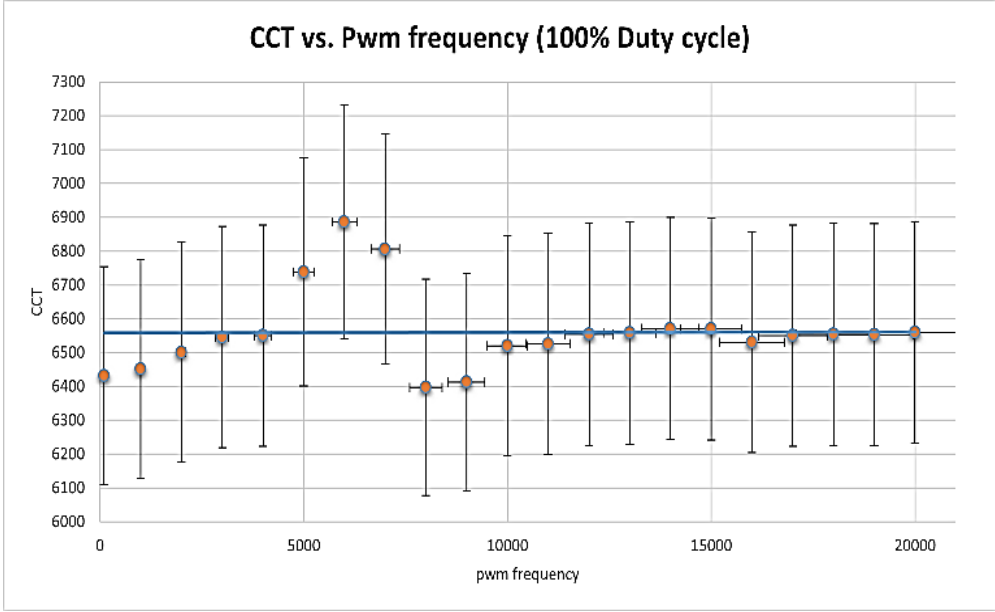

Fig. 7.9(a): CCT vs. Switching Frequency (10W)

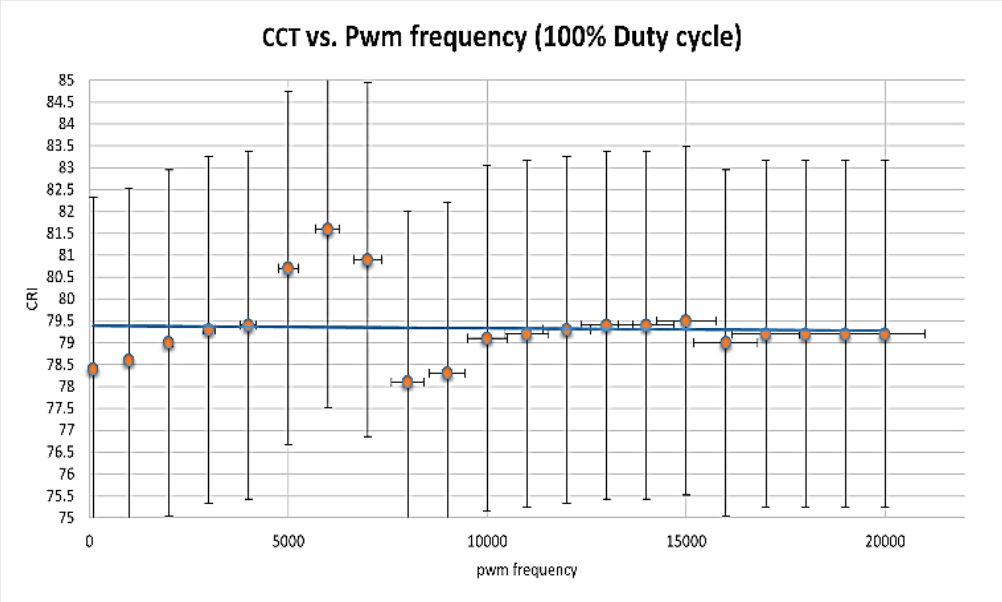

Fig. 7.9(b): CCT vs. Switching Frequency (20W)

7.2.4 Conclusion

This experimentation clearly established that the approach of duty cycle reduction in PWM dimming can be effectively applied to various lighting scenarios, including indoor and outdoor lighting applications such as street lighting. A detailed analysis revealed that while changes in the duty cycle at a fixed PWM signal switching frequency result in slight alterations of CCT

or CRI values, these changes do not impact the overall illumination quality of the LEDs. Additionally, the study highlights that, electrical properties, such as the wattage of LEDs, may influence CCT or CRI values. Further investigations are necessary to understand the previously mentioned effect of wattage in detail. The study also discovered that at higher switching frequencies, the variations in CCT or CRI values around their means, as measured by standard deviations, are significantly reduced. Based on this finding, the study recommends using a high PWM switching frequency, such as 20 kHz, a conclusion supported by the equations presented within this paper. However, since this experimentation was conducted in a controlled laboratory setting, additional experimentations are needed to evaluate the behavior of lighting parameters under real-world conditions. Furthermore, it is essential to conduct additional experiments involving a wider variety of LED modules with different wattage ranges to achieve broader generalizations. It is well established in existing literature that an increase in the junction temperature of LEDs can significantly impact lighting parameters. In this study, however, the increase in junction temperature had negligible effects on the measured values, due to the implementation of a 5-minute cooling interval between consecutive measurements, which effectively minimized residual heat in the LEDs. Nonetheless, further research is warranted to explore this aspect more thoroughly. To enhance the scope of this study, future investigations could expand the range of switching frequencies tested and reduce the gaps between consecutive switching frequencies and duty cycle levels for more granular analysis. These expansions fall within the broader scope of future research on this subject. Lastly, the insights and recommendations from this study provide a solid foundation for designing smart LED control systems and can be utilized in future applications to optimize LED performance.

7.3 Development of a Low-Cost, High CRI, BAS Enabled Smart Human Centric Street Lighting Luminaire

7.3.1 Introduction

Most streets in India still rely on outdated lighting schemes and guidelines. Over 27 million street luminaires, primarily metal halide (MH) lamps, sodium vapor lamps (SVL), and compact fluorescent lamps (CFL), illuminate the country. However, many remain switched on during daylight hours or in low-traffic conditions at night, resulting in significant energy waste. This highlights the need for better roadway lighting designs, especially on highways, to enhance safety and reduce accidents caused by poor visibility. In contrast, India's Street Lighting National Program (SLNP) has successfully replaced a percentage of traditional street lights with energy-efficient LED luminaires nationwide [1]. LEDs consume less electricity, have a longer lifespan, lower energy costs, and a smaller carbon footprint compared to traditional lighting options [9]. This transition has started to reduce the country’s overall power consumption. Furthermore, SPD (spectral power distribution) of a particular LED luminaire can be controlled precisely via color mixing technology, where SPD of light is the key physical property influencing color vision. It defines the power of light at each wavelength within the visible spectrum, typically ranging from 400 to 700 nm. Measurements of SPD in real-world scenarios are typically taken at specific, individual wavelengths rather than continuously across the entire spectrum [170]. The concept of SPD is applicable to both reflective scenarios, where light bounces off an object, and transmissive scenarios, where light passes through materials like glass or translucent plastics [171]. Besides, color mixing is a technique where

colors of two, three or more colored LEDs are mixed by adding their wavelengths together. It follows Grassmann's law of additive color [172]. The drive current of each LED must be independently adjusted to achieve the desired color when using multiple LEDs together. These adjustments are constrained by the maximum current specified by the manufacturer for each LED. The resulting color gamut is defined by the linear combinations of the color coordinates of the individual LEDs as represented in the CIE x-y color space [173]. Recent advancements have ushered lighting design into a new era, introducing the concept of human-centric lighting. This approach views light as a mediator of both visual and non-visual effects, addressing human mood, well-being, and health. It integrates visual, biological, and behavioral responses, emphasizing light's role in regulating the biological clock. Morning light resets the sleep-wake cycle by stimulating the suprachiasmatic nucleus (SCN), which governs circadian rhythms. Human-centric lighting, combined with daylighting and smart LED systems, is poised to shape the future of lighting technology [11]. Light directly and indirectly influences brain function, and optimizing various aspects of lighting design can support desired brain activity. In road lighting design, it is crucial to prioritize object detection, recognition, and decision-making for drivers and pedestrians [174]. That is why it is important to incorporate human centric aspects in street lighting in Indian context. Besides, the demand for high-CRI lighting systems with tunable CCT has made LEDs highly popular. High-CRI lighting is essential in settings where accurate color or object identification and critical task performance are crucial, such as the textile industry, streets at night, food processing industry, and shopping malls [175-176]. Researchers worldwide are working to improve the photometric and colorimetric properties of LEDs and control of those properties, such as CRI, efficacy, variable CCT, and dimming control. Typically, white LED light for general applications is created by applying a $YAG:Ce^{3+}$ yellow phosphor coating on *InGaN* blue LED chips [177]. These LEDs achieve a CRI of 80–85 and high efficacy of 100–200 lm/W [178]. However, their spectrum shows gaps in the red and cyan regions [35]. Efforts to address this include replacing yellow phosphor with alternatives such as red phosphor ($Na_{0.7}Li_{0.15}K_{0.15}La_{0.6}Eu_{0.4}MgWO_6$) [179], far-red emitting phosphor ($SrMgAl_{10}O_{17}:Cr^{3+}$) [181], cyan phosphor ($Na_{0.5}K_{0.5}Li_3SiO_4:Eu^{2+}$) [179], and various phosphor combinations [177,180,182-183]. These methods can raise CRI up to 95 but reduce efficacy to 60–80 lm/W while maintaining constant CCT. Another approach involves using color mixing based on Grassmann's law of additive color [172]. Variable white light sources have been produced by mixing red-green-blue (RGB) [184-186] or red-green-blue-amber (RGBA) [187-188] LEDs, achieving CRI values between 80 and 90. However, these systems suffer from chromaticity shifts due to dimming and temperature changes. Phosphor-coated LEDs exhibit less chromaticity shift compared to color mixing of monochromatic light sources under similar dimming conditions [189]. Systems using cool white-blue and cool white-red mixing can achieve a wide tunable CCT range (2500 K–12500 K) and a CRI near 90, with CCTs above and below 6500 K being generated by before-mentioned respective combinations [190]. However, the deviation from the Planckian locus increases, raising the 'D_{uv}' value. Simulations using red-green-blue-cyan-amber-white (RGB-CAW), RGB-amber, and RGB-white LEDs have achieved a tunable CCT range of 3200 K–7500 K and a maximum CRI of 97 for RGB-CAW [191]. However, such systems are costly and complex, requiring six LED colors. Five-component color mixing methods have achieved CRI values above 90, but their electronic control is highly challenging, limiting practical application [192]. From the above discussion it can be clearly stated that, if all these features are incorporated in conjunction with human centric aspects in street lighting design than it will be very much beneficial for Indian

road lighting scenario. In this context, a street light luminaire is designed in Illumination Engineering section of Electrical Engineering department of Jadavpur University to mitigate all these issues. This prototype used warm white-blue-green LED combination for color mixing, thereby achieving a CCT range starting at 3500K and ending at 8500K, using Grassmann's law of additive color and three-point color mixing. First, the metal core printed circuit board (MCPCB) is designed to mount the mentioned three types of LEDs. After that a control circuit is designed to enable the three-point color mixing, using ESP32 microcontroller, MOSFET drivers and MOSFETs, which will be fitted with the luminaire. Another circuit board, controlled by ESP32, is developed for wireless controlling, via ESP_NOW protocol, of the CCT of the luminaire. Another feature is added with this system, where the CCT of each LED array of implemented three arrays can be controlled individually. Besides, beam angle switching (BAS) method and dimming are also incorporated in the system. This system is designed keeping the previous studies on human centric lighting of this thesis in mind. After development of the system some rudimentary validation of the system is also done in the laboratory. From that, it can be clearly stated that the working of the system is quite satisfactory and features to incorporate smartness is also working properly. It yields high CRI values for all set CCT values, such as 85 for 8000K CCT.

7.3.2 Choosing criterion for LEDs of Street Light Luminaire

This paper proposes a high-CRI, tunable-CCT lighting system by mixing phosphor-coated warm white LEDs (CCT - 3159K) with blue and green LED light sources. The approach fills spectral gaps in the green-cyan (490–540 nm) and red (650–700 nm) regions to improve color rendition while controlling CCT. It can be easily observed that increasing spectral energy in shorter wavelengths (450–540 nm) raises CCT, while higher long-wavelength energy lowers it. By adding green light (peak 516 nm, FWHM 40 nm) and blue light (peak 456 nm, FWHM 30 nm), CCT and color rendition are enhanced, where FWHM (full width at half maximum) is a statistical term that describes the breadth of a curve at half its highest value. Adjusting the blue-green blending ratio achieves a tunable CCT range, ensuring chromaticity coordinates align with the Planckian locus to minimize D_{uv}. The system's luminous efficacy depends on the used individual light sources' efficacy. Furthermore, green light is particularly effective in mesopic photometric systems, which operate at light levels between photopic (bright, cone-dominated vision) and scotopic (dim, rod-dominated vision) conditions. In the mesopic range, both rods and cones contribute to vision, with spectral sensitivity shifting toward shorter wavelengths than photopic condition [193-194]. In mesopic conditions, where both rods and cones contribute to vision, the human eye's sensitivity peaks at 507 nm for rods and 555 nm for cones. Since green light falls within this range, it is particularly effective in enhancing visibility under such lighting conditions. This makes green light beneficial for enhancing visual acuity and contrast perception under mesopic conditions, improving object recognition and safety in low-light environments, where contrast perception is the ability to distinguish differences in brightness or color between two objects or between an object and its background. However, its effectiveness also depends on factors such as the light spectrum, intensity, and the specific application context [195-196]. Besides, incorporating green light in street lighting can potentially reduce energy consumption when applied strategically in mesopic conditions. This is because the human eye is more sensitive to green light under these lighting levels, allowing lower light intensities to achieve comparable visibility. By designing lighting systems

that leverage this mesopic sensitivity, it's possible to maintain visual performance while using less power [194,197]. Indicative figure is given in Fig. 7.10 (b). SPD of the used light sources (WW-G-B LEDs) and the developed light source at 5388K are given in Fig. 7.10 (a) for a quick pictorial comparison. Besides, chromaticity co-ordinates, CCT values and illuminance values of these specific LEDs at full intensity are given in Table 7.1.

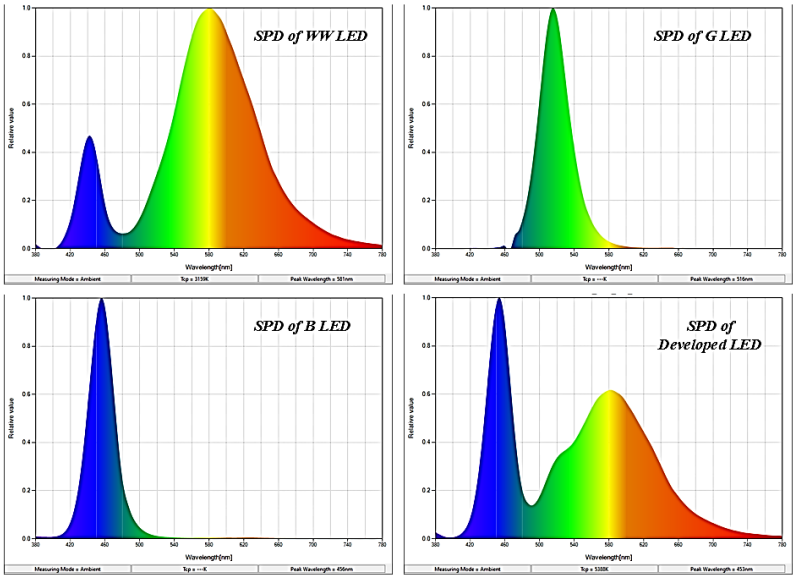

Fig. 7.10(a): Spectral power distribution of the used light sources (WW-G-B LEDs) and the developed light source at 5388K

Table 7.1: Photometric Parameters of the Selected LEDs

LED	X	Y	LUX	CCT
BLUE (B)	0.1498	0.0428	116	N/A
GREEN (G)	0.1457	0.6785	174	N/A
WARM WHITE (WW)	0.4318	0.4128	972	3159

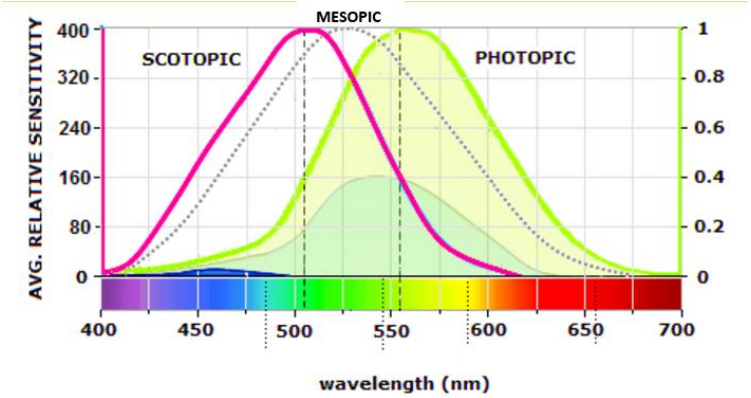

Fig. 7.10(b): Human Sensitivity for Scotopic, Mesopic and Photopic Conditions

7.3.3 Mathematical Basis of the CCT Control

The basis, on which the system works or the CCTs are tuned, is three-point color mixing, following Grassmann's law of additive color. In three-component color mixing, three light sources are combined in specific ratios to create the desired CCT with illuminance. Consider light sources $A(x_a, y_a)$, $B(x_b, y_b)$, and $C(x_c, y_c)$ used for mixing, as depicted in Fig. 7.11. The target CCT point, $T\ (x_t, y_t)$, is located on the CIE 1931 chromaticity diagram. In Fig. 7.11, the extended line from A through T intersects the line connecting B and C at point $M(x_m, y_m)$. The color mixing process involves two stages. First, point $M(x_m, y_m)$ is determined by blending sources B and C. The calculation of M depends on the chromaticity coordinates of the desired CCT point $T(x_t, y_t)$. In the second stage, point $M(x_m, y_m)$ is mixed with source A in the appropriate ratio to attain the final target CCT point $T(x_t, y_t)$ and the required illuminance (E_r).

7.3.3.1 Calculation of $T\ (x_t, y_t)$ and $M(x_m, y_m)$

The chromaticity co-ordinate of $T\ (x_t, y_t)$ can be calculated from the Eqs. (1)–(4) [198,199] for a required CCT (T_c).

For $2222K \leq T_c \leq 4000K$

$$x_t = -0.2661239 \frac{10^9}{{T_c}^3} - 0.2343580 \frac{10^6}{{T_c}^2} + 0.8776956 \frac{10^3}{{T_c}^1} + 0.179910 \quad (1)$$

$$y_t = -0.9549476\ {x_t}^3 - 1.37418593\ {x_t}^2 + 2.09137015 x_t - 0.16748867 \quad (2)$$

For $4000K < T_c \leq 25000K$

$$x_t = -3.0258469\ \frac{10^9}{{T_c}^3} + 2.1070379 \frac{10^6}{{T_c}^2} + 0.2226347 \frac{10^3}{{T_c}^1} + 0.240390 \quad (3)$$

$$y_t = 3.0817580\ {x_t}^3 - 5.87338670\ {x_t}^2 + 3.75112997 x_t - 0.37001483 \quad (4)$$

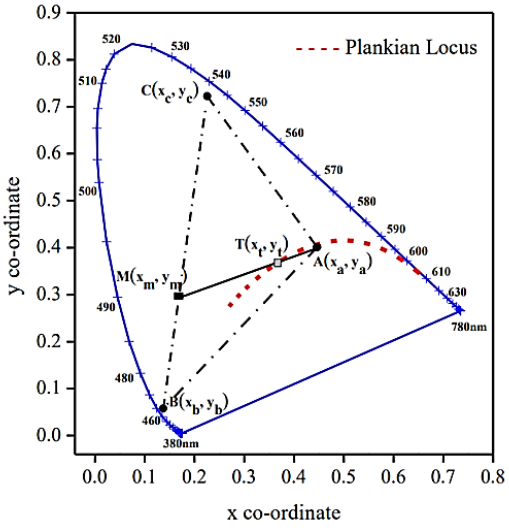

Fig. 7.11: The CIE 1931 Chromaticity Diagram illustrates the chromaticity coordinates of three LED sources, along with the blending lines between them and the Planckian locus

By taking closer look at the Fig. 11, it can be said that the AT line's slope is equal to the AM line's slope, as these two straight lines are same straight-line. Therefore, another equation (Equ (5)) can be derived,

$$y_m = \frac{(y_t - y_a)}{(x_t - x_a)}(x_m - x_a) + y_a \qquad (5)$$

Again, from the figure it can be said that the straight-line MB's slope is equal to the straight-line CB's slope, as they are same straight line. Hence, Equ (6) is derived.

$$y_m = \frac{(y_c - y_b)}{(x_c - x_b)}(x_m - x_b) + y_b \qquad (6)$$

It can be clearly stated that the point *M* will be any arbitrary point on straight line CB and the values of co-ordinates of point $M(x_m, y_m)$ totally determined by the target CCT value or point $T(x_t, y_t)$. Depending upon those values, blending ratio of source *B* and source *C* will change with point $M(x_m, y_m)$. So, the value of x_m can be determined (Equ (7)) from Equs (5) and (6) and can be written as

$$x_m = \frac{\{(y_t - y_a)(x_c - x_b)x_a - (y_c - y_b)(x_t - x_a)x_b + (y_b - y_a)(x_t - x_a)(x_c - x_b)\}}{\{(y_t - y_a)(x_c - x_b) - (y_c - y_b)(x_t - x_a)\}} \qquad (7)$$

The value of y_m can be easily calculated by substituting the value of x_m into equation (5) or (6).

7.3.3.2 Calculation of Illuminance of Source *B* and *C* to achieve point $M(x_m, y_m)$

Grassmann's law of additive color mixing states that the resulting color from combining multiple-colored lights can be mathematically represented as a linear combination of the color stimuli of the individual lights. The perceived color is influenced by the relative intensities and spectral compositions of the combined light sources [200-202]. The point $M(x_m, y_m)$ is located on the line connecting the source points B and C. According to Grassmann's law of color mixing, the chromaticity coordinates of a blended color can be determined as a linear weighted sum of the chromaticity coordinates of the two light sources being mixed. Therefore, Equ (8) can be derived

$$x_m = x_b W_{c1} + x_c W_{c2} \quad and \quad y_m = y_b W_{c1} + y_c W_{c2} \qquad (8)$$

Where, weighted coefficient W_{c1} and W_{c2} are given by Equ (9)

$$W_{c1} = \frac{\frac{L_b}{y_b}}{(\frac{L_b}{y_b} + \frac{L_c}{y_c})} \text{ and } W_{c2} = \frac{\frac{L_c}{y_c}}{(\frac{L_b}{y_b} + \frac{L_c}{y_c})} \qquad (9)$$

L_b and L_c are the luminance values of light source *B* and *C*. Besides, Grassmann's law also stated that (Equ (10))

$$W_{c1} + W_{c2} = 1 \qquad (10)$$

Let, the maximum illuminance of source *B* and *C* is E_{bM} and E_{cM} respectively. Then it can be said that the photometric parameter luminance *L* is equivalent to illuminance *E*, if the distance between source and working plane and the surrounding's reflectance is fixed and the medium's transmittance is constant. Let, the duty cycle applied to the source *B* is D_b and to the source *C* is D_c to achieve the point *M*. Then the instantaneous illuminance of source *B* and *C* can be given by Equ (11).

$$E_b = E_{bM}D_b \approx L_b \text{ and } E_c = E_{cM}D_c \approx L_c \qquad (11)$$

Substituting (11) in (9), Equ (12) can be formulated

$$W_{c1} = \frac{\frac{E_{bM}D_b}{y_b}}{(\frac{E_{bM}D_b}{y_b}+\frac{E_{cM}D_c}{y_c})} \text{ and } W_{c2} = \frac{\frac{E_{cM}D_c}{y_c}}{(\frac{E_{bM}D_b}{y_b}+\frac{E_{cM}D_c}{y_c})} \qquad (12)$$

Let, ratio of two weighted co-efficient, $r(W_{c2}, W_{c1}) = \frac{W_{c2}}{W_{c1}}$ (13)

From (11) and (12) it is found that, $r(W_{c2}, W_{c1}) = \frac{E_{cM}D_c y_b}{E_{bM}D_b y_c}$ (14)

Peak illuminance ratio of source *C* and *B* is $r(E_{cM}, E_{bM}) = \frac{E_{cM}}{E_{bM}}$ (15)

Duty cycle ratio applied to source *C* and *B* is $r(D_c, D_b) = \frac{D_c}{D_b}$ (16)

y co-ordinate ratio of source *C* and *B* is $r(y_c, y_b) = \frac{y_c}{y_b}$ (17)

Substituting (15)-(17) in (14), we get, $r(W_{c2}, W_{c1}) = \frac{r(E_{cM},E_{bM})r(D_c,D_b)}{r(y_c,y_b)}$ (18)

Then, applied duty cycle ratio of source *C* and *B* is,

$$r(D_c, D_b) = \frac{r(W_{c2},W_{c1})r(y_c,y_b)}{r(E_{cM},E_{bM})} \qquad (19)$$

From Equs (8), (10) and (13) value of $r(W_{c2}, W_{c1})$ can be found,

$$r(W_{c2}, W_{c1}) = \frac{(x_b - x_m)}{(x_m - x_c)} \qquad (20)$$

Let, maximum value of illuminance of point $M(x_m, y_m)$ is E_{mM}. It can be calculated by the linear summation of instantaneous illuminance values of source *B* and *C*, when their maximum illuminance values are constant. Then it can be said in Equ (21) that,

$$E_{mM} = E_b + E_c \quad \text{or, } E_{mM} = E_{bM}D_b + E_{cM}D_c \tag{21}$$

From Fig. 11, it can also be said in Equs (22) and (23) that,

$$\frac{(E_{mM}-E_{bM})}{(E_{cM}-E_{bM})} = \frac{d_{bm}}{d_{bc}} \tag{22}$$

$$or, E_{mM} = E_{bM} + \frac{d_{bm}(E_{cM}-E_{bM})}{d_{bc}} \tag{23}$$

Where, d_{bm} and d_{bc} are the linear distances between point *B* and point *M* and point *B* and point *C* respectively. Then,

$$d_{bm} = \sqrt{\{(x_b - x_m)^2 + (y_b - y_m)^2\}} \tag{24}$$

$$d_{bc} = \sqrt{\{(x_b - x_c)^2 + (y_b - y_c)^2\}} \tag{25}$$

Equ (21) can be written as,

$$D_b = \frac{E_{mM}}{E_{bM}+E_{cM}\frac{D_c}{D_b}} \tag{26}$$

$$\text{Or, } D_b = \frac{E_{mM}}{E_{bM}(1+\frac{E_{cM}D_c}{E_{bM}D_b})} \tag{27}$$

From Equs (15), (16) and (27), it can be found that,

$$D_b = \frac{E_{mM}}{E_{bM}(1+r(E_{cM},E_{bM})r(D_c,D_b))} \quad \text{and} \quad D_c = D_b\, r(D_c, D_b) \tag{28}$$

With the help of Equs (19), (20) and (28) the values of D_b and D_c can be realized.

7.3.3.3 Calculation of Duty Cycle applied to Source *A*, *B* and *C* to achieve Point $T(x_t, y_t)$ with Required Illuminance

To generate the required CCT with point $T(x_t, y_t)$, proper mixture of illuminance of source *A* and illuminance of point $M(x_m, y_m)$ is needed. Let, maximum values of illuminances of source *A* are E_{am} and of point $M(x_m, y_m)$ is E_{mM}. Then,

$$E_{mM} = E_{bM}D_b + E_{cM}D_c \tag{21}$$

To attain the required CCT with point *T*, let the duty cycle applied to the source *A* is Da and to the point *M* is Dm. Then instantaneous illuminance value of source *A* and point *M* for the required CCT with point *T* is given by,

$$E_{aT} = E_{aM}D_a \quad and \quad E_m = E_{mM}D_m \qquad (29)$$

So, the instantaneous illuminance values of source *B* and *C* are given with help of Equs (21) and (29). They are,

$$E_{bT} = E_{bM}D_bD_m \quad and \quad E_{cT} = E_{cM}D_cD_m \qquad (30)$$

Similarly, like the previous calculations, the applied duty cycle ratio of source *A* and point *M* is given by Equ (31),

$$r(D_a, D_m) = \frac{r(W_{c4},W_{c3})r(y_a,y_m)}{r(E_{aM},E_{mM})} \qquad (31)$$

Where, Duty cycle ratio applied to source *A* and point *M* is $r(D_a, D_m) = \frac{D_a}{D_m}$ (32)

Peak illuminance ratio of source *A* and point *M* is $r(E_{aM}, E_{mM}) = \frac{E_{aM}}{E_{mM}}$ (33)

y co-ordinate ratio of source *A* and point *M* is $r(y_a, y_m) = \frac{y_a}{y_m}$ (34)

Weighted co-efficient ratio of source *A* and point *M* for color mixing is

$$r(W_{c4}, W_{c3}) = \frac{(x_a - x_t)}{(x_t - x_m)} \qquad (35)$$

Where, W_{c3} and W_{c4} are weighted co-efficient of light source *A* and point *M* according to Grassmann's law of additive color.

At the target CCT point $T(x_t, y_t)$, the required illuminance E_r is the sum of the illuminance contributions from source *A* and point *M*.

(**Note:** The target illuminance of the system must not exceed the maximum illuminance of source *A* when it is operating at full intensity, because here source *A* is the preliminary source of higher luminous efficacy with whom two sources (*B* and *C*) are blended.)

$$E_r = E_{aT} + E_m \qquad (36)$$

$$\text{Or, } E_r = E_{aM}D_a + E_{mM}D_m \qquad (37)$$

Similarly, like the previous calculations, from Equs (37), (32) and (33), the values of D_m and D_a can be calculated.

$$D_m = \frac{E_r}{E_{mM}(1+r(E_{aM},E_{mM})r(D_a,D_m))} \quad \text{and} \quad D_a = D_m\, r(D_a, D_m) \qquad (38)$$

With the help of Equs (31), (35) and (38) the values of D_m and D_a can be realized.

Finally, to achieve the target CCT with point $T(x_t, y_t)$ and target illuminance value E_r , illuminance contributions of the individual LED source are given by,

Illuminance of Source *A*, $E_{aT} = E_{aM}D_a$ **(39)**

Illuminance of Source *B*, $E_{bT} = E_{bM}D_bD_m$ **(40)**

Illuminance of Source *C*, $E_{cT} = E_{cM}D_cD_m$ **(41)**

Duty cycle requirements of individual given LEDs, to get the target CCT with point $T(x_t, y_t)$ and target illuminance value E_r, are given below,

Required duty cycle of light source *A*, $D_a = D_m\, r(D_a, D_m)$ **(42)**

Required duty cycle of light source *B*, $D_bD_m = \frac{E_{mM}D_m}{E_{bM}(1+r(E_{cM},E_{bM})r(D_c,D_b))}$ **(43)**

Required duty cycle of light source *C*, $D_cD_m = D_b\, r(D_c, D_b)\, D_m$ **(44)**

7.3.4 Hardware Implementation: Development of the MCPCB of Street Light Luminaire and Control Circuits

The developed street light luminaire has three novel parts. One is the MCPCB, where the LEDs are mounted, another is the control circuit for implementation of the three-point color mixing, dimming and BAS method. Last but not the least, is the wireless controller for CCT tunability.

7.3.4.1 MCPCB of the Luminaire

MCPCB stands for Metal Core Printed Circuit Board, a type of printed circuit board (PCB) featuring a metal core layer designed to manage heat effectively. This metal core directs heat away from critical components on the board to less sensitive areas, ensuring the board's optimal performance and extended lifespan. Typically, the metal core is made of aluminum or copper and is positioned between an insulating dielectric material and copper trace circuitry. In multilayer MCPCBs, the layers are symmetrically arranged on either side of the metal core. MCPCBs are commonly utilized in applications requiring efficient heat dissipation, such as LED lighting systems, automotive electronics, and renewable energy technologies. In this system a single layered, 6" x 8.5", MCPCB is used and the actual image is given in Fig. 7.12. The design of the luminaire is done in such a way that, it contains three symmetrical individual arrays of LEDs. In a single array, three types of colored LEDs are used to incorporate three-point color mixing and they are warm-white, blue and green. All three types of LEDs are of COB type and of 3 watts except the green one, which is of 1 watt. In a single LED array, there are three distinct columns of LEDs. The central column is composed of green LEDs, while the other two columns feature warm-white and blue LEDs arranged in a zigzag pattern. The system used low powered green LEDs to decrease the excessive green tint in the light output. An individual luminaire needs around 170 watts for working, which is measured in laboratory. This MCPCBs are then mounted on the metallic luminaire using heat sink paste, where the metallic luminaire has fins on the back side of it for proper heat dissipation.

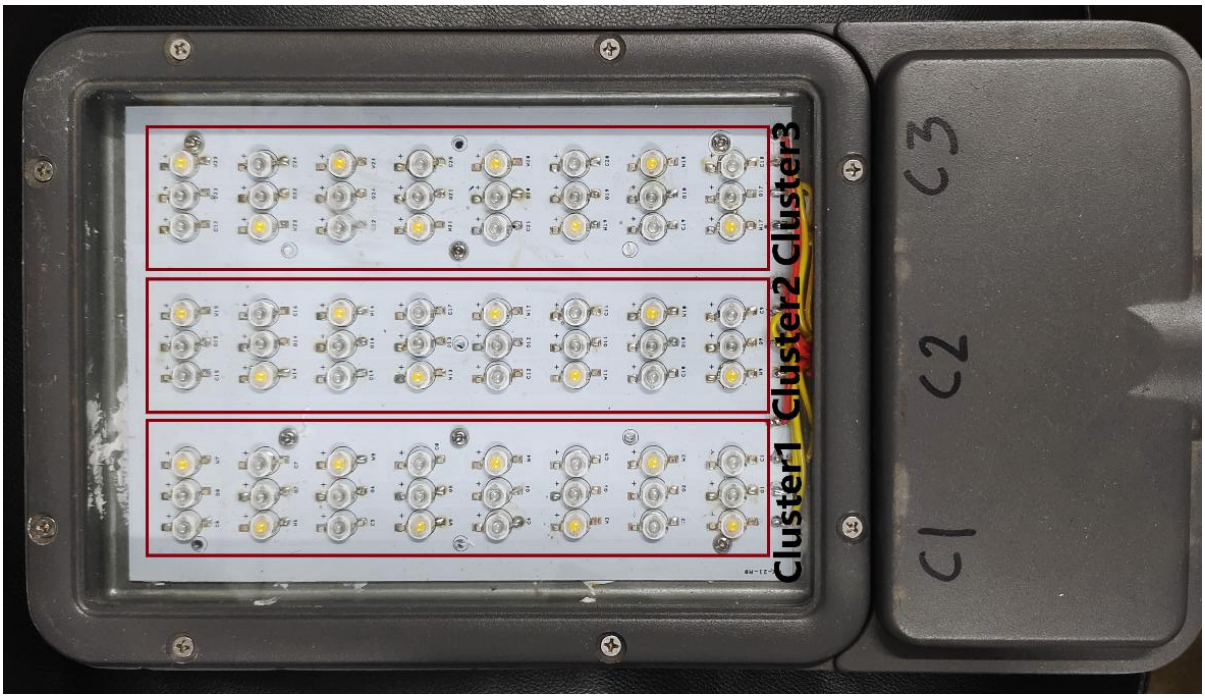

Fig. 7.12: MCPCB of Developed Street Light Luminaire

7.3.4.2 Control Circuit adjacent to Street Light for CCT Tunability and BAS Method Implementation

The system consists two major control circuits. This circuit is attached with luminaire and mounted on the top of the street light pole. The core of the system is an ESP32 WROOM-DA microcontroller board, which controls all the three individual LED arrays by injecting proper calculated duty cycle via PWM (pulse width modulated) signals. The circuit is designed in such a way that CCTs of all these three individual arrays can controlled individually, which means, one can set three CCTs for three LED arrays separately. The circuit has nine IR2110PBF MOSFET drivers for nine P55NF06 MOSFETs, employed for nine columns (3 arrays x 3 columns) of LEDs on the luminaire. The luminaire and the circuit, both are powered by a Meanwell SMPS (switched-mode power supply) named as LRS-200-36, which has DC output voltage of 36 volts and current of 5.9 Amps maximum. This circuit uses buck converter to reduce the DC voltage level from 36 volts to 12 volts and then it is fed to the MOSFET drivers. ESP32 microcontroller board of the circuit pulls the power (required 5 volts) from a L7805 voltage regulator and the regulator gets its input from the buck converter. Three blue 5 mm indicator LEDs are also incorporated in the circuit for showing proper operations of three LED arrays. CCT inputs for three LED arrays are given to the circuit by another wireless control circuit via ESPNOW protocol. Here, in this circuit, the microcontroller sets up nine PWM channel to provide nine different PWM signal to the nine before-mentioned MOSFET drivers. Circuit diagram and the actual image of the circuit is given in Fig. 7.13 (a) and (b).

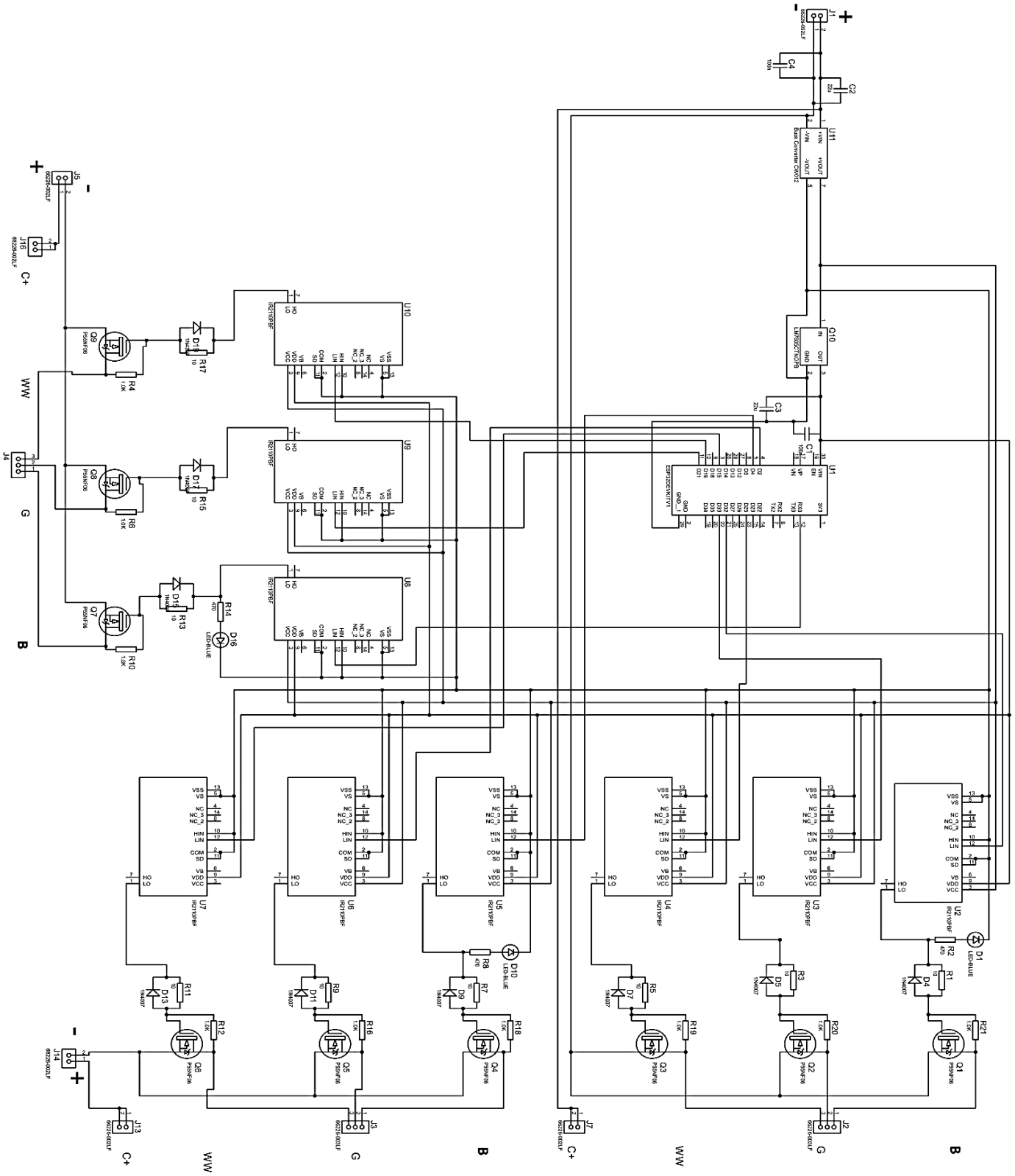

Fig. 7.13(a): Circuit Diagram of Control Circuit adjacent to Street Light

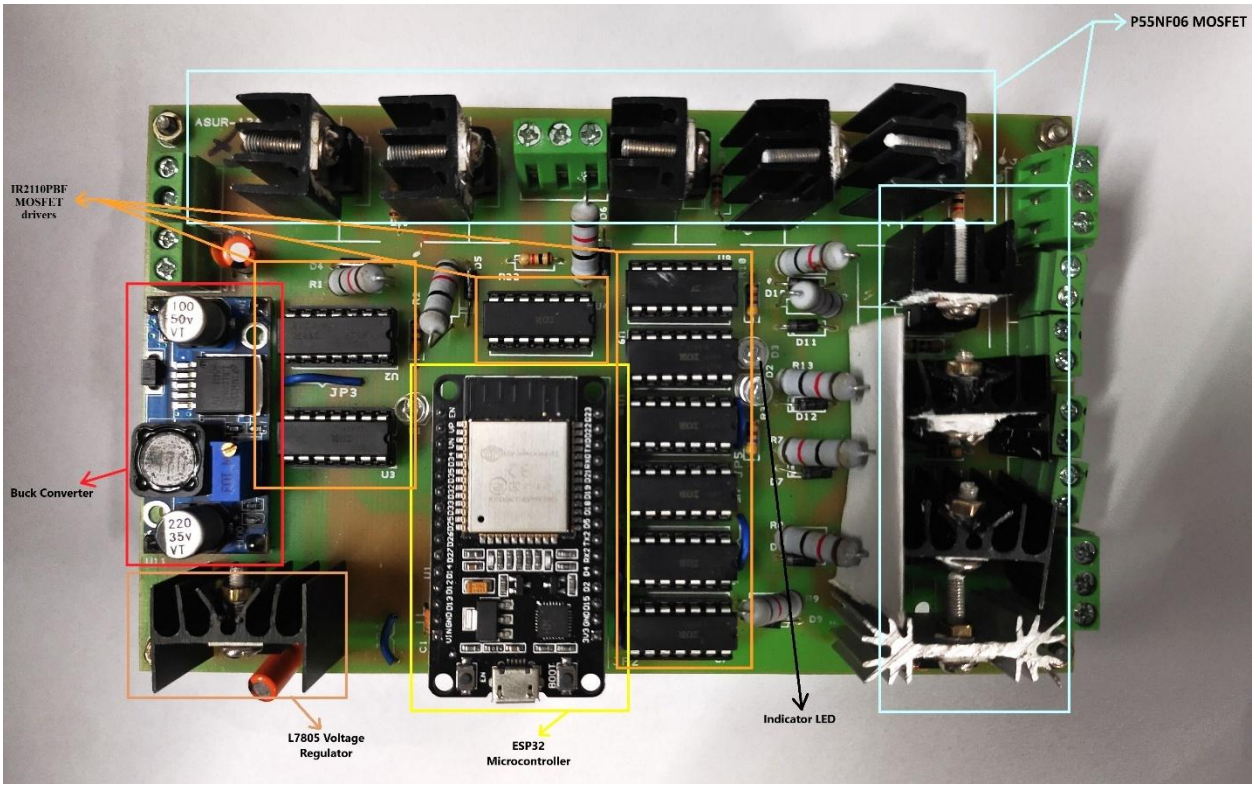

Fig. 7.13(b): Actual Control Circuit adjacent to Street Light

From the circuit diagram, given in Fig. 7.13 (a), the positioning of each component can be clearly seen. Six PBT2 connectors and three PBT3 connectors are used to connect the luminaire and power supply with the circuit. Here PBT stands for Polybutylene Terephthalate, an insulating material. In Fig. 7.13 (a), B stands for blue LED column's negative terminal, G stands for green LED column's negative terminal and WW stands for warm-white LED column's negative terminal. Besides, C+ stands for all three positive terminals of the three LED arrays. Furthermore, other three PBT2 terminals are used to connect the DC supply from SMPS with their positive and negative terminals respectively. Moreover 1 kΩ resistors are connected between the gate and drain of each MOSFET to protect the MOSFET.

7.3.4.3 Hand Held Wireless Control Circuit for Manual Control

Another control circuit is made to control the CCT tunability and BAS method, which will be held in human hand for controlling the street light from distance. This circuit also comes with an ESP32 WROOM DA microcontroller module, whose main task is to gather the reading of three potentiometers, incorporated in the very circuit. The rating of the potentiometers is 10k, which is beneficial for smooth CCT changing. The circuit draws its power from a L7805 voltage regulator, which in turn draws the power from 12 volts 2 Amps DC barrel jack power adapter. It also features a push button, which is used to change or toggle the BAS modes (Full Glow, Pro and Counter) and an OLED 128 x 68 screen to display the set CCT values and the current BAS mode of the street light luminaire. Circuit diagram and the actual image of the circuit is given in Fig. 7.14 (a) and (b).

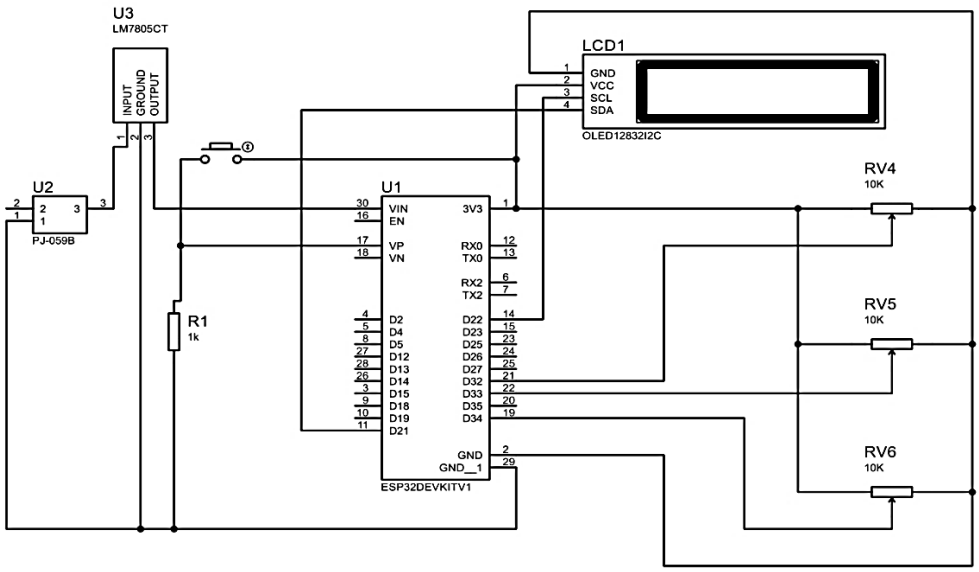

Fig. 7.14(a): Circuit Diagram of Hand-Held Wireless Control Circuit

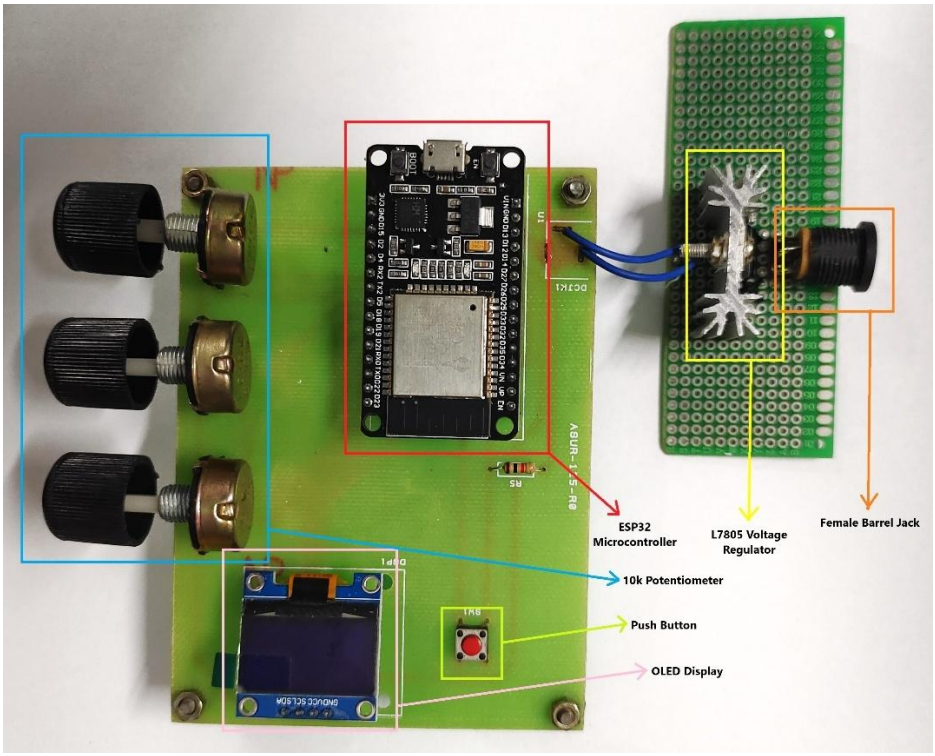

Fig. 7.14(b): Actual Hand-Held Wireless Control Circuit

In the circuit diagram, given in Fig. 7.14 (a), all the components are clearly seen and understandable. A barrel jack female connector (U2) is used to power the circuit via a L7805 voltage regulator, as discussed earlier. The push button, the OLED display and three 10 k potentiometers are also clearly visible in this diagram.

7.3.5 Software Implementation

In this system two control circuits are used, one is mounted with street light luminaire on the light pole and another is used for manual control of the CCT, which is should be held by human hand. Both the circuits used a 32-bit ESP32 microcontroller board to generate desired PWM signals with specific duty cycles. In the circuit adjacent to the street light luminaire, ESP32 establishes nine PWM channel to generate nine PWM signals for nine LED columns incorporated in three LED arrays. Hand held wireless controller circuit sends values from three potentiometers to the previous circuit using ESPNOW protocol. It also shows set CCT values on an OLED display and gives provision of a push button, which is used to toggle the BAS modes in the street lights. Arduino IDE is used to code these two microcontrollers. Mathematical formulations, showed in section 7.3.3, are incorporated to the microcontroller connected on the circuit adjacent to the street light luminaire via coding. Fig. 7.15 (a) and (b), show the flowchart of these two circuits, where step by step workflow of these two circuits are shown.

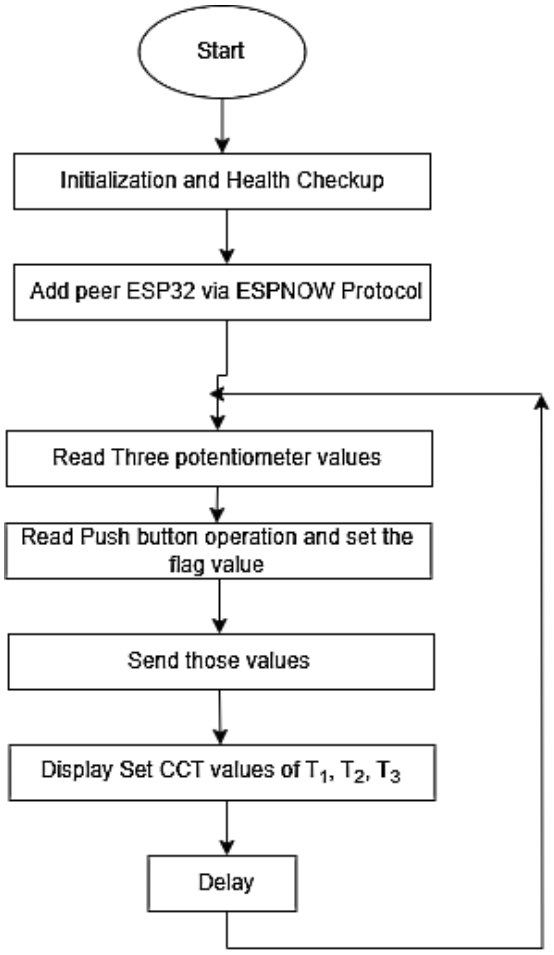

Fig. 7.15(a): Flow Chart of Hand-Held Wireless Control Circuit

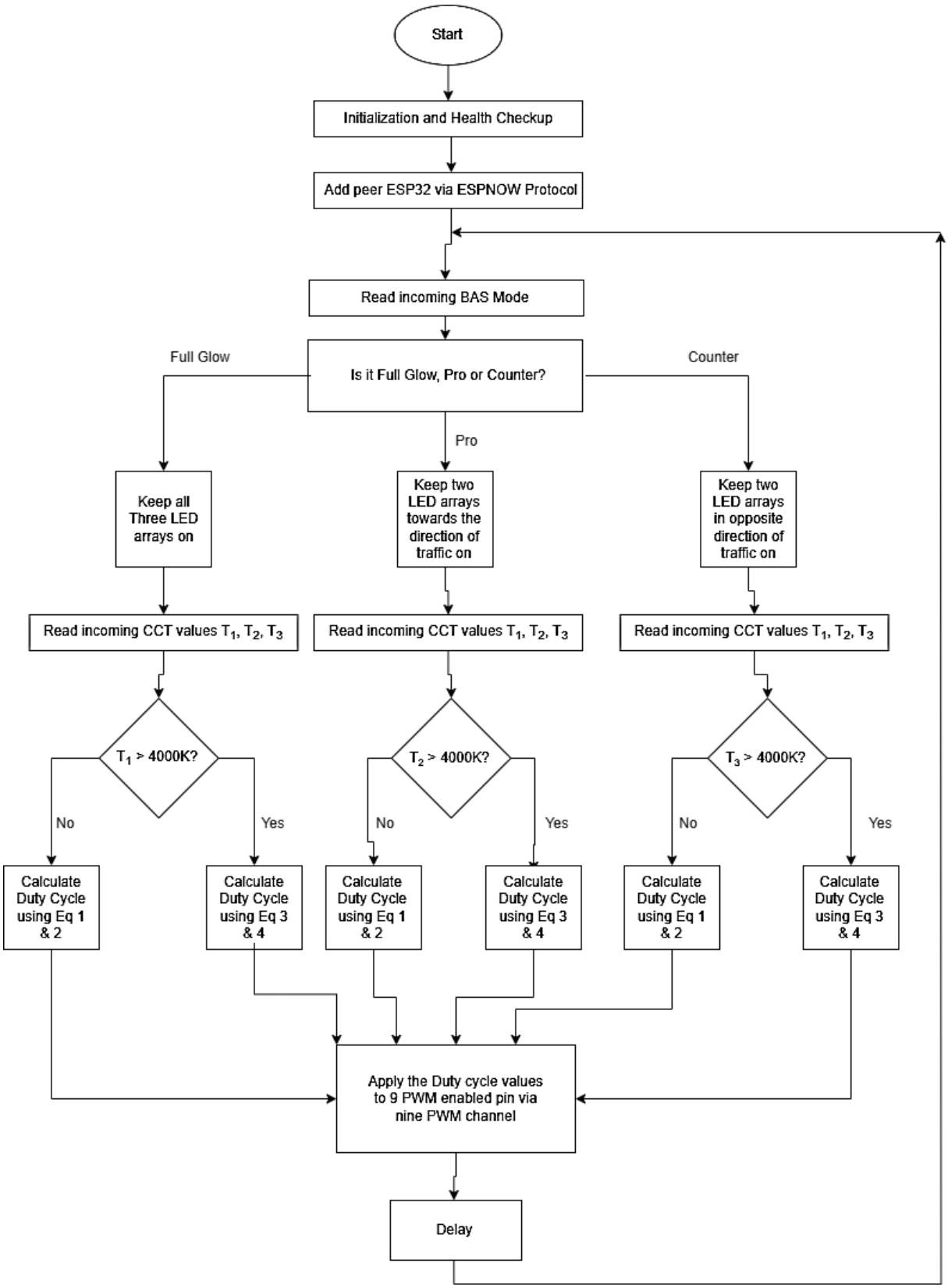

Fig. 7.15(b): Flow Chart of Control Circuit adjacent to Street Light Luminaire

Fig. 7.16 provides a pictorial representation of the total developed system. In the figure, it can be found that a set of nine current limiting resistors are connected to safeguard the operation of individual LED columns. The values of these resistors are 3.3Ω (2 watt), 1Ω (2 watt) and 10Ω (2 watt) for warm-white, green and blue LEDs respectively. Besides, the used codes for these two control circuits are given in Annexture 1.

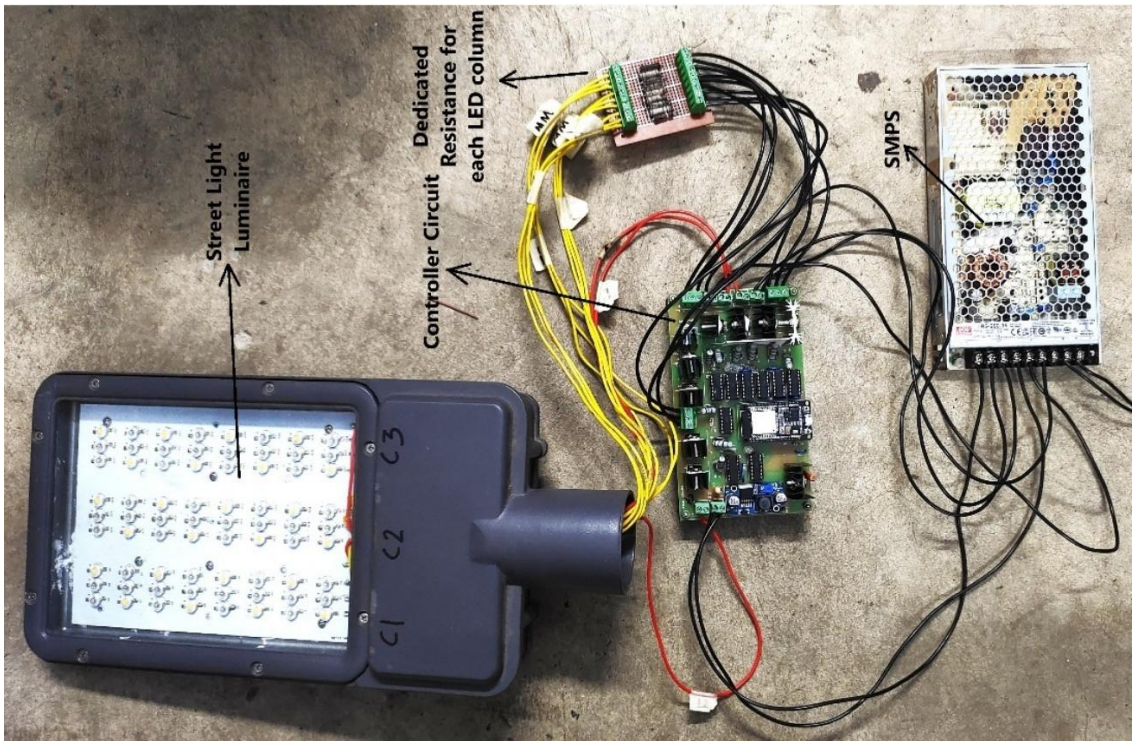

Fig. 7.16: Total Developed Street Light Luminaire with Control and Power Circuit

7.3.6 Discussion

After development of the street light luminaire, it is mounted on a height adjustable pole, with a set height of 3.5 meters, in the laboratory of Illumination engineering section of Electrical Engineering department of Jadavpur University. As previously mentioned, the lab is painted with pitch dark black paint to prevent any reflection of light and incoming stray light, which can mess up the photometric measurements. Illuminance, CCT and CRI values are measured at nadir point for random 10 set CCT values using the before-mentioned three potentiometers incorporated in hand held wireless control circuit. It is seen that the illuminance values are more or less centered at 178.2 lux. Measured CCT values are plotted against set CCT values and it is found that the graph is nearly linear with a slope of value 1, given in Fig. 7.17 (a). This means that the error in generating the given CCT values are very low. Another graph is plotted between the measured CCT values and CRI values in Fig. 7.17 (b). It is also found from that graph that CRI values increase with increment in CCT values, which is quite explainable from the measured SPDs of these 10 measured CCT points, which is given in Fig. 7.17 (c). As CCT increases, the relative spectral powers of higher wavelengths decrease, which creates proper or near equivalent blend of spectrum with nearly equal relative spectral power. Values of set CCT, Measured CCT and CRI are given in Table 7.2.

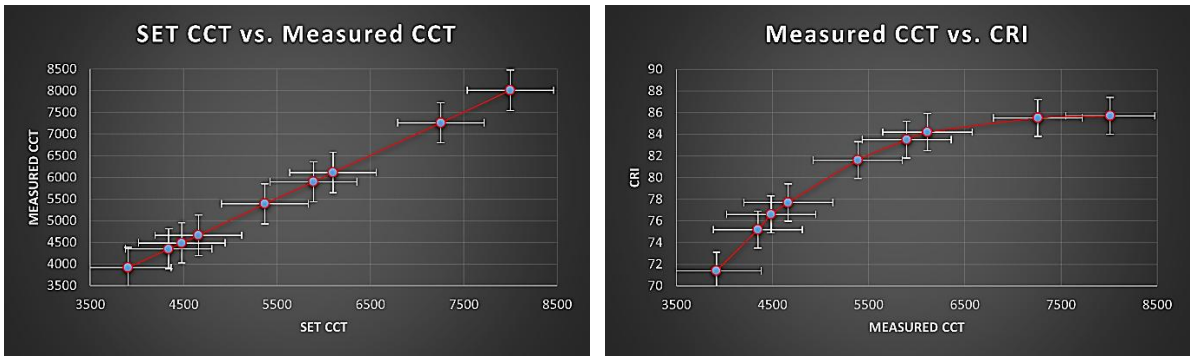

Fig. 7.17(a) & (b): SET CCT vs. Measured CCT and Measured CCT vs. CRI

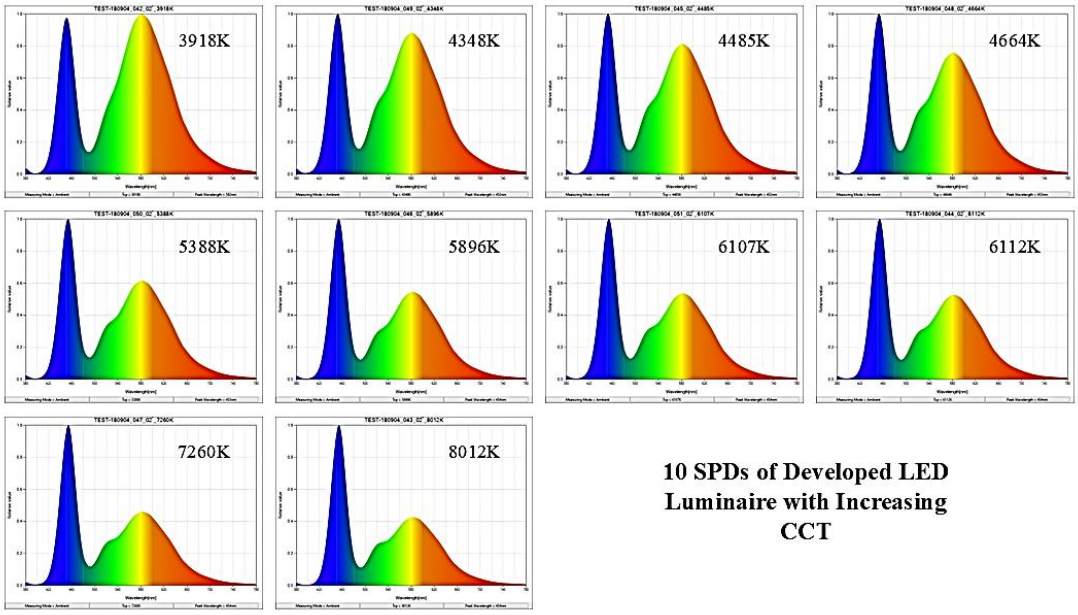

Fig. 7.17(c): SPDs of Developed LED Luminaire with Increasing Measured CCT

Table 7.2: Values of 10 Set CCTs, Measured CCTs and CRIs

SET CCT	Measured CCT	CRI
3904	3918	71.4
4340	4348	75.2
4480	4485	76.6
4660	4664	77.7
5370	5388	81.6
5890	5896	83.5
6100	6112	84.2
7255	7260	85.5
8000	8012	85.7

7.3.7 Conclusion

This article presents a cost-effective, high-color-rendering W-G-B LED-based lighting system capable of producing a wide range of CCTs. A detailed mathematical formulation for the system design is provided, along with its hardware implementation and experimental validation. The system successfully achieves a broad CCT range from 3500K to 8500K. Current market solutions for high-CRI, tunable color temperature light sources typically necessitate at least four light-emitting chips for color mixing, leading to increased manufacturing costs and system complexity. In contrast, this system uses three-chip color mixing to deliver optimal color rendition across the entire CCT range, significantly reducing overall system cost while maintaining high performance. Furthermore, addition of green light, in street light luminaire, is highly effective in mesopic conditions, where both rods and cones contribute to vision, with peak sensitivities at 507 nm and 555 nm, respectively. This enhances visibility, visual acuity, and contrast perception in low-light settings, improving safety. Additionally, green light can reduce energy consumption in street lighting by leveraging the eye's sensitivity under mesopic conditions, allowing lower light intensities to achieve similar visibility.

7.4 Development of A Low-Cost Novel CCT Meter using Machine Learning Regression Techniques to Monitor the Real-time CCTs of the Developed Street Light Luminaire

7.4.1 Introduction

Machine learning in Illumination Engineering provides a wide array of advantages, ranging from enhanced design optimization, lighting management, advanced adaptive control, and energy efficiency to Human-Centric Lighting (HCL). Among the key properties, Correlated Color Temperature (CCT) plays a critical role in designing human-centric lighting schemes. Research indicates that implementing dynamic CCT-based lighting systems in office environments, which mimic natural daylight patterns, significantly boosts worker productivity and regulates hormonal balance, thereby benefiting human health. These findings also underscore the importance of adopting dynamic CCT-enabled street lighting systems [203]. This brings forth significant challenges in optimizing design strategies, control systems, and especially cost-effective methods for measuring human-centric parameters like CCT and Color Rendering Index (CRI) in street lighting systems. Machine learning approaches, including supervised and unsupervised learning, can address these challenges by automating tasks such as CCT and CRI measurements, optimizing lighting system designs, and performing predictive maintenance. This study focuses on machine learning-based methods for CCT measurement. In prior research, an intelligent lighting solution was developed using 200 RGB (Red, Green, Blue) values to predict CCT using a TCS34725 color sensor compliant with the CIE 1931 RGB color space. Gaussian process regression was applied, but only three regression techniques were tested without specifying kernel types, limiting reproducibility [204]. Another study used a deep learning network trained on 191 RGB images, employing a Convolutional Neural

Network (CNN) to create a regression model. The methodology involved transforming RGB values into the CIE 1931 XYZ color space, converting them to chromaticity coordinates (x, y), and estimating CCT using McCamy's and Hernandez's models [205]. A similar approach utilized a deep convolutional attention-based Recurrent Neural Network (RNN) [206]. Other studies have used RGB-to-XYZ transformations and chromaticity coordinates to determine Circadian Stimulus (CS) or estimate CCT with McCamy's model [92,207-210]. The literature reveals that the process of directly transforming CIE 1931 RGB values into CCT for specific luminaires is complex and often incomplete. Recognizing this gap, a low-cost device with a user-friendly interface was developed at the Illumination Engineering Section, Electrical Engineering Department, Jadavpur University. This device simplifies CCT prediction by measuring RGB values from light sources and utilizing an appropriate machine learning regression model. The device comprises an ESP32-WROOM-DA microcontroller, a low-cost TCS3200 programmable color light-to-frequency converter, and an OLED 128x32 display for data visualization [211-212]. A detailed description is provided in experimental setup and procedure section, with a visual representation in Fig. 18. An extensive dataset of RGB values, along with corresponding CCT and illuminance measurements, was obtained using the device and a CL-200A chromameter by Konica Minolta under controlled conditions with two CCT-adjustable smart Halonix LED bulbs. Six machine learning regression models were tested, with the Gaussian Process Regression (GPR) model employing a Matérn kernel ($\upsilon = 1.5$) emerging as the most accurate. This model achieved an R^2 of 0.9721 and a RMSE of 155.058, where 'υ' represents a smoothness parameter balancing flexibility and regularity. The models were evaluated using stratified K-fold cross-validation to ensure generalization and accuracy. Furthermore, this study contributed the following points with novelty towards the development of a CCT meter–

1. A regression-based device offering superior CCT prediction accuracy compared to traditional mathematical models.

2. A low-cost alternative (approx. ₹1000) to high-end modular chromameters priced around ₹500,000.

3. Successful implementation of the GPR model for RGB-to-CCT conversion.

4. A methodology to integrate the device into dynamic CCT-enabled streetlights for maintaining constant CCT values. Furthermore, the developed system is an open-loop system. This device can make it closed loop.

The results of this study provide a significant step toward developing efficient, cost-effective tools for human-centric lighting solutions.

7.4.2 Background

The background of this particular work can be divided into two distinctive parts. One is the machine learning based approach and the other is existing approach.

7.4.2.1 Machine Learning Based Approach

Machine learning proves to be an invaluable tool for accurately evaluating lighting parameters like Correlated Color Temperature (CCT) from RGB values by analyzing large datasets and identifying correlations between RGB inputs compliant with the CIE 1931 RGB color space and their corresponding CCT outputs. Its foundation lies in data-driven algorithms that enhance the precision and reliability of CCT measurements across various lighting applications. In this study, six regression models [213-215] were employed to analyze the measured data. These models are summarized below:

A. Gaussian Process Regression (GPR)

GPR is a non-parametric Bayesian method suitable for modeling complex, non-linear relationships in data. It uses kernel functions to define the similarity between data points and provides predictions along with uncertainty estimates. While GPR is highly flexible and can incorporate prior knowledge, its computational cost scales cubically with the size of the dataset, making it less feasible for large datasets. This study utilized three kernel functions for GPR:

1. Matern Kernel ($\upsilon = 1.5$)
2. Matern Kernel ($\upsilon = 2.5$)
3. RBF (Radial Basis Function) Kernel

B. Support Vector Machine Regression (SVR)

SVR is a supervised learning method leveraging Support Vector Machines for regression tasks. It identifies the optimal fit line (or hyperplane) by maximizing the margin within an allowable error tolerance. This approach effectively captures patterns in data, demonstrating robustness against outliers. However, SVR can be computationally demanding and requires careful tuning of hyperparameters and kernel functions. This study employed the following kernel functions for SVR:

1. Linear Kernel
2. 2nd Order Polynomial Kernel
3. RBF (Radial Basis Function) Kernel

C. Other Regression Techniques

The study also incorporated four additional regression models, each offering distinct advantages:

1. **Random Forest Regression**: This ensemble learning method combines multiple decision trees to improve prediction accuracy and handle large datasets effectively. However, it requires meticulous hyperparameter optimization.

2. **Gradient Boosting Regression**: By sequentially building trees that correct errors from previous iterations, this method enhances accuracy but carries the risk of overfitting.

3. **K-Nearest Neighbors (KNN) Regression**: This approach predicts values based on the nearest *k* data points, offering simplicity but often proving computationally intensive, especially for large datasets.

4. **Linear Regression**: A straightforward technique that builds relationships between variables using linear equations, suitable for simpler datasets.

These diverse regression models were utilized to explore the relationship between RGB values and CCT, emphasizing the strengths and limitations of each method.

7.4.2.2 Existing Approach

In this study, the independent parameters or observed values are the R (Red), G (Green), and B (Blue) components, which comply with the CIE 1931 RGB color space. This color space was introduced by the CIE in 1931 to correlate visible light wavelengths with the colors perceived by the human eye, assigning a numerical representation to every color within the spectrum. For enhanced mathematical convenience, the CIE 1931 RGB color space is often transformed into the CIE 1931 XYZ color space, which remains widely used. The translation from RGB to XYZ values is achieved by multiplying the RGB values by a specific transformation matrix. The CIE 1931 color matching system quantifies colors numerically, enabling their accurate reproduction across various media such as print and digital displays. This system standardizes the specification of measured colors without emphasizing how humans perceive them, ensuring that colors measured in one environment can be reliably replicated in another, maintaining consistency across platforms [216]. From the derived X, Y, Z values, chromaticity coordinates (x, y) can be calculated. These coordinates can then be used in McCamy's equation to estimate Correlated Color Temperature (CCT). However, this approach involves complex and error-prone calculations. McCamy's equation is as follows:

$$T = -437n^3 + 3601n^2 - 6861\,n + 5524.31 \qquad (45)$$

Where, $n = \frac{(x - 0.3320)}{(y - 0.1858)}$, (x, y) is the chromaticity co-ordinate and T is CCT of the LED [67].

In this experiment, the cumbersome process of calculating CCT using McCamy's equation is bypassed by employing machine learning (ML) regression models with the RGB data obtained from the developed device. For comparison, the RGB data was also processed through the traditional McCamy-based methodology to evaluate its accuracy against the ML regression techniques.

7.4.3 Experimental Setup and Procedure

7.4.3.1 Experimental Environment

This experiment was conducted in a controlled environment within a specially designed black chamber constructed from wood and pierced steel columns. The aim was to develop a novel, low-cost CCT meter by applying Machine Learning (ML) Regression models to the measured data. The black, non-reflective environment was crucial to terminate the effect of stray and reflected light on the color sensor of the developed device, ensuring accurate measurements from the CCT-adjustable LED light source. The black chamber used in this study has external dimensions of 1.6 meters in height, 0.9 meters in length, and 0.7 meters in width, with an internal height of 1.5 meters. To ensure thermal stability, the LEDs were mounted on a wooden block, positioned away from the steel frame. The front portion of the chamber was left open to facilitate measurements, but during data collection, a thick black jute cloth was used to cover the opening, effectively blocking external light and ensuring measurement accuracy. A detailed illustration of the chamber is provided in Fig. 7.19. Two high-power 10-watt Bluetooth-enabled, CCT-adjustable LED light sources were used in this experiment. One of these light sources was randomly mounted on the chamber ceiling for the first half of measurements and the other LED is used at the same location for the second half. It is done to cancel out any LED specific bias to the experimental results. They are equipped with a milky-white hemispherical diffuser. To determine the Nadir point, the point of maximum illuminance on the working plane, a grid was drawn on the chamber's bottom surface. Once the Nadir point was identified and marked, four equidistant points were marked around it, each at a distance of 15 cm. Measurements were taken at the Nadir point as well as at these four surrounding points. The LED light sources were controlled via a mobile application provided by the manufacturer. This application featured a dashboard allowing adjustments to the CCT values during the experiment, facilitating precise control of the lighting conditions.

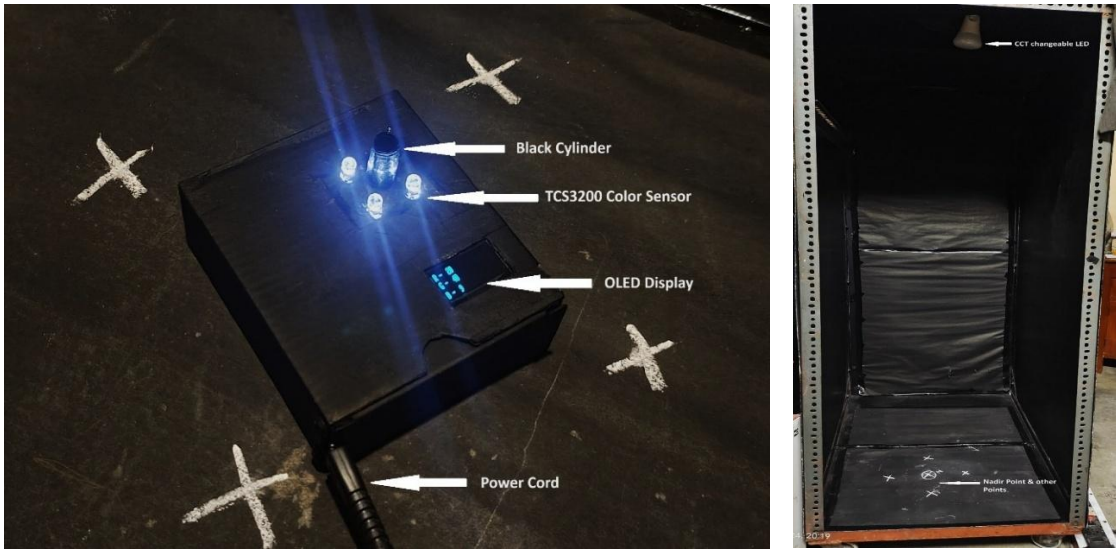

Fig. 7.18 & 7.19: Developed Device to Measure CCT and Experimental Chamber

7.4.3.2 Developed Measuring Device

The measuring device is employed to capture CIE 1931-compliant RGB values for each CCT setting configured by the user through a mobile application. This device is constructed

using a small cardboard box, with a TCS3200 color sensor (manufactured by TAOS) and a 128x32 OLED display mounted on its upper surface. This color sensor is first calibrated and then used in the developed device. Calibration code is given in Annexture 1. The device is powered and controlled by an ESP32-WROOM-DA microcontroller module. The color sensor detects the RGB values and sends them to the microcontroller, which then displays the readings on the OLED screen. The microcontroller is powered by a 5V 2A DC power adapter. To ensure stability in the readings and mitigate undue fluctuations, the microcontroller calculates the average of 100 consecutive RGB measurements and presents this averaged value on the OLED display. Both the inner and outer surfaces of the device are coated with pitch-black paint to prevent any stray or reflected light from reaching the color sensor. For additional protection against unwanted light interference, a small hollow cylinder, with a length of 3", made of black paper is placed over the sensor. This ensures that the sensor receives only direct light from the CCT-adjustable light source. A detailed depiction of the device is provided in Fig. 7.18, while a flowchart outlining the algorithm, written in Arduino IDE, used in the measuring device is presented in Fig. 7.20.

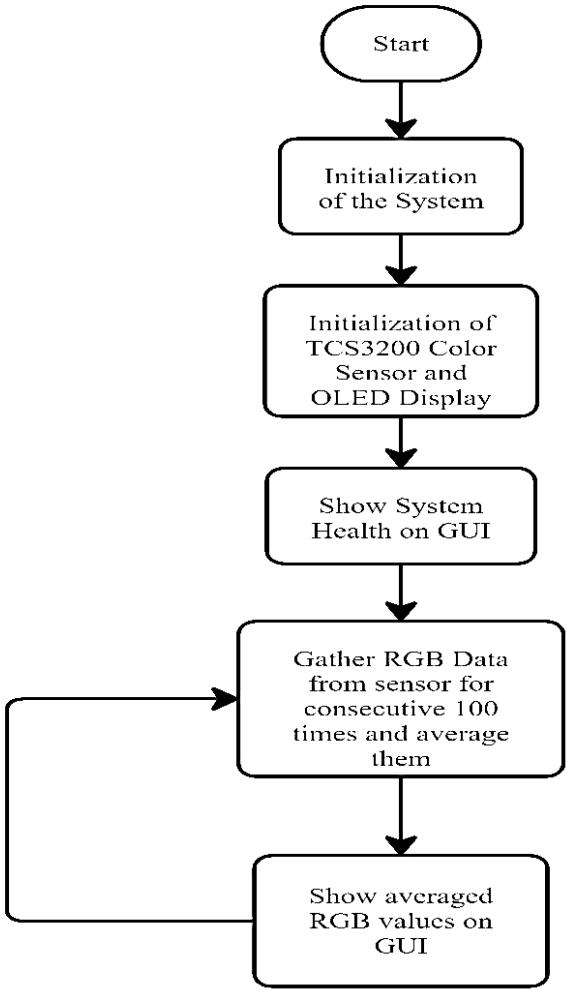

Fig. 7.20: Flow Chart of the Used Code

7.4.3.3 Experimental Procedure

Once the experimental setup is properly established, measurements are conducted at the Nadir point and the four previously mentioned surrounding points. For each CCT setting, five measurements are taken at these points to eliminate any potential position bias in the readings. Using the mobile application dashboard, a random CCT value is first set, and this value is precisely measured at the five points using a Konica Minolta CL200A. In addition, the illuminance values at these points are also measured with the same device. Subsequently, the RGB values are recorded using the developed device. All collected data, CCT, illuminance, and RGB values, are meticulously documented. The measured CCT values range from 2652K to 5522K. In total, 500 sets of CCT, RGB, and illuminance values were recorded during this study. These datasets were systematically entered into an Excel sheet for further analysis.

7.4.3.4 Performance Assessment Metrics

To compare all these over the measured data, some error terms are used and they are R2, MSE and RMSE. The R2 error is a measure of how much of the variance in the variable that is dependent is predicted from the independent variables. It indicates how closely the model's predictions match observed data. R2 error is given by Equ 46.

$$R2\ Error = 1 - \frac{\sum_{i=1}^{n}\left(y_i - \hat{y}_i\right)^2}{\sum_{i=1}^{n}\left(y_i - \bar{y}_i\right)^2} \tag{46}$$

Where, 'y_i' is the measured values of the dependent variable, '$\hat{y}_i$' is predicted values of dependent variable using model, '$\bar{y}_i$' is mean of 'y_i' and observation number is 'n'. The MSE calculates the mean of the squared errors, indicating the disparities between expected and actual values. It represents the mean squared deviation between the actual and projected values. MSE is given by Equ 47.

$$MSE = \frac{\sum_{i=1}^{n}\left(y_i - \hat{y}_i\right)^2}{n} \tag{47}$$

Where, 'y_i' is the measured or observed values of the dependent variable, '$\hat{y}_i$' is predicted values of dependent variable using the model and n is the number of observations. The RMSE is the square root of the MSE. It offers an estimate of the mean value of the error that was made. It has identical units as the measured and anticipated values, which makes it easier to understand in the larger picture of the data. RMSE is given by Equ 48.

$$RMSE = \sqrt{MSE} \tag{48}$$

7.4.4 Results and Analysis

In this study, 500 sets of CCT, RGB, and illuminance values were measured using a chromameter and the developed device within the previously described experimental setup. The CCT values were randomly selected to mitigate any bias caused by the junction temperature rise of the LEDs used. After recording the data, the RGB values were

normalized by dividing each value by 255. This step was performed because each RGB channel uses 8 bits to store a color, resulting in a range of values from 0 to 255. Following normalization, each RGB value is scaled to a range of 0 to 1. This normalization process produced 500 feature vectors, each consisting of three parameters (scaled R, G, B values), alongside 500 target values (CCTs). The normalized RGB values were then input into the previously described regression algorithms to determine the best-performing model based on error metrics. 80% of the dataset was used for training, while the remaining 20% was reserved for testing. All training and testing procedures were carried out using MATLAB software. The performance metrics of the regression algorithms used for CCT estimation are presented in Table 7.3. For each model, graphs showing the relationship between predicted CCT values and actual CCT values were plotted, as depicted in Fig. 7.21. From the metrics in Table 7.3, it is evident that Gaussian Process Regression (GPR) with a Matern kernel ($\nu = 1.5$) outperforms the other models for CCT prediction. The R^2 score and RMSE for this model are 0.9721 and 155.058, respectively. To compare these results with the Mccamy's empirical model, the RGB values were converted to CIE 1931-compliant XYZ values, then to chromaticity coordinates (x, y). Using Mccamy's equation, CCT values were predicted, and the R^2 score and RMSE were calculated. The results showed an R^2 score of 0.9129 and an RMSE of 159.371. From this comparison, it is clear that the GPR model with a Matern kernel ($\nu = 1.5$) significantly outperforms Mccamy's model for predicting CCT from RGB sensor data. Additionally, Table 7.3 ranks the performance of all regression models and Mccamy's model from best to least suited. It can be observed that the GPR model consistently outperforms all other regression techniques in predicting CCT values from RGB inputs.

Table 7.3: Performance Assessment Metrics of ten Machine Learning Regression (MLR) Algorithms

Regression Model Name	R2 Error (Test Data)	MSE (Test Data)	RMSE (Test Data)	Cross Validated MSE	Cross Validated RMSE
GPR: Kernel - Matern ($\upsilon = 1.5$)	**0.9721**	**24042.9984**	**155.058**	**52934.9909**	**230.0761**
GPR: Kernel - Matern ($\upsilon = 2.5$)	0.9621	30328.1002	174.1496	52912.775	230.0278
SVR: Kernel - Gaussian	0.9568	34304.1964	185.2139	69138.414	262.9418
GPR: Kernel - RBF	0.9473	40770.7648	201.9177	54970.4225	234.4577
Random Forest	0.9372	48674.6997	220.6234	79497.6404	281.9533
SVR: Kernel - 2nd Order Polynomial	0.9264	66186.9695	257.2683	114178.2169	312.3934
Maccamy's Model	**0.9129**	**25399.1156**	**159.371**	**58590.5746**	**242.0549**
Gradient Boost	0.9049	73575.2094	271.2475	110013.0026	331.6821

SVR: Kernel - Linear	0.8952	93805.8366	306.2774	144239.2603	379.7884
KNN	0.8504	117709.09	343.0876	165347.4556	406.6293
Linear Regression Model	0.772	130321	361	169998.7143	412.309

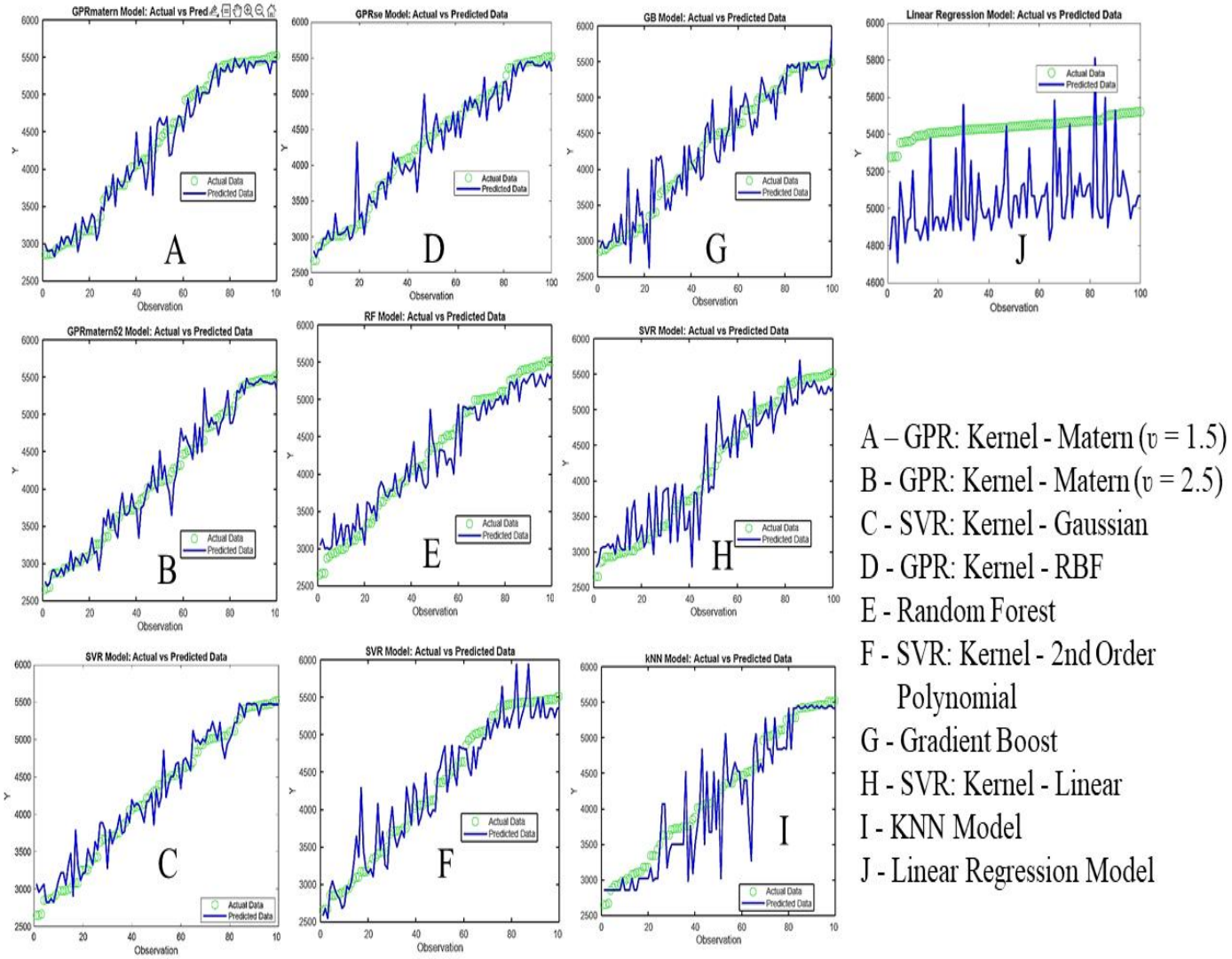

Fig. 7.21: Predicted CCT values vs. Actual CCT values for 10 Regression Models

7.4.5 Conclusions

This experimentation introduces an innovative device and machine learning (ML)-based methodology, designed to measure the dynamic Correlated Color Temperature (CCT) of luminaires, offering a low-cost yet effective alternative to conventional chromameters, which are significantly more expensive. The developed device, combined with advanced

ML techniques, demonstrates the potential for accurate and efficient CCT measurement without reliance on high-cost equipment. The findings highlight that a cost-effective approach can yield results comparable to those obtained using sophisticated devices like chromameters, making the technology more accessible for a broader range of applications. Among the various ML regression models applied in this study, Gaussian Process Regression (GPR) with a Matern kernel ($\nu = 1.5$) emerged as the best-performing algorithm. However, despite its exceptional accuracy, implementing GPR on microcontrollers such as the ESP32 presents considerable challenges. The ESP32's limited computational power and memory capacity restrict its ability to execute GPR, especially with a kernel as computationally demanding as the Matern kernel. These limitations necessitate the use of more advanced AI-enabled hardware for real-time applications. To address these computational constraints, alternative solutions such as the NVIDIA Jetson Nano**,** Google Coral Edge TPU**,** and AI-accelerator-enabled Raspberry Pi were identified as viable platforms for deploying GPR models. Additionally, cloud-based computation offers another pathway to overcome the limitations of microcontroller-based processing. While these solutions provide significant computational advantages, they may introduce additional costs or dependency on external infrastructure, highlighting the trade-offs between cost, performance, and feasibility. Future research aims to optimize GPR algorithms for efficient deployment on constrained platforms like the ESP32, focusing on reducing the computational and memory requirements without compromising accuracy [217-218]. Furthermore, the study underscores the importance of identifying improved color sensors with enhanced sensitivity and precision. Collecting a more extensive and diverse dataset of RGB values is also a priority, as it will enable the training of more robust ML models, ensuring better generalization across various lighting conditions and environments. The development and refinement of such technologies promise to bridge the gap between affordability and high performance, making advanced lighting control accessible to a wider audience.

Chapter 8: Conclusion and Future Scopes

8.1 Conclusion

In the modern era, "smartness" has become an indispensable feature across all systems used in daily life, whether they are electrical, electronic, mechanical, or belong to any other domain. The integration of smart capabilities, the addition of new functionalities, automation, predictive maintenance, and condition monitoring have unlocked vast avenues for research and innovation. Researchers continuously push the boundaries of exploration, and as advancements progress, the definitions and expectations of these domains evolve when incorporated into systems. Over time, there has been a concentrated effort to prioritize human-centric approaches within these fields to reduce human workloads, enhance efficiency, and minimize errors in task execution. Moreover, pressing global challenges such as climate change, overconsumption of fossil fuels, and rising carbon emissions have introduced a critical focus on reducing energy consumption in electrical and electronic systems. This has led to numerous ongoing studies and explorations worldwide. Nations are striving to integrate these innovative features into public infrastructure to achieve dual objectives: optimizing energy usage and embedding human-centric designs. Among such infrastructures, street lighting plays a pivotal role in promoting a country's economic, social, and cultural development while ensuring safety and security through smooth vehicular movement on roads. This doctoral thesis conducts an in-depth examination of human-centric street lighting, with a particular focus on understanding the complex interplay between lighting characteristics and human visual and cognitive responses. By merging laboratory-based experimental data with theoretical insights, it proposes a cost-effective, high-CRI, CCT-tunable smart street lighting system tailored to the Indian context. Additionally, this research investigates energy reduction strategies, including PWM (Pulse Width Modulation) dimming and BAS (Beam Angle Switching) methods, while validating the BAS approach through case studies and real-time CCT monitoring for the proposed system. The thesis can be broadly categorized into two primary components. The first explores the correlation between lighting parameters, such as CCT (Correlated Color Temperature), and human-centric factors like reaction times for object detection, Small Target Visibility (STV), and Visibility Level (VL). This section also integrates findings from EEG (Electroencephalogram) studies, GSR (Galvanic Skin Response) data, and behavioral analyses to establish these relationships. The second component is devoted to the development of a low-cost, high-CRI, CCT-tunable, wirelessly controlled, BAS-enabled street lighting luminaire.

This part examines the synergy between PWM dimming and BAS techniques, validates the BAS method using a lumen maintenance device, includes a case study conducted on university roads, evaluates the impact of PWM dimming switching frequency on lighting parameters such as CCT, and proposes a real-time CCT monitoring and feedback mechanism for the developed street lighting system.

The thesis is systematically divided into eight comprehensive chapters. The first chapter primarily serves as an introduction, providing a detailed overview of the research. It sets the stage by elaborating on the background and context of the study, outlining its significance, and emphasizing the originality of the work. Chapter 2 lays the foundation for human-centric lighting in the arena of street lighting design. It provides an in-depth understanding and definition of human-centric lighting, discussing its benefits, limitations, and experimental implementation in street lighting systems. Chapter 3 introduces the laboratory-developed instruments essential for this research. It details the design, purpose, and functionality of devices like active shutter glasses, a reaction time measuring device, and a galvanic skin response (GSR) measuring device. Chapter 4 examines the visual and non-visual impacts of various LED lighting parameters on object detection. The first section focuses on experiments involving variations in the CCT of main (on-axis) and peripheral (off-axis) light sources. The latter section explores the effects of varying flickering frequencies and temporal light modulations in peripheral sources. Chapter 5 presents a novel investigation into the impacts of CCT variations on human brain activity, cognitive load, and temporal processing. This chapter introduces the use of EEG and GSR to measure mental and physical responses, offering deeper insights into human cognition under different lighting conditions. Chapter 6 explores energy reduction strategies for LED street lighting. It highlights two innovative dimming techniques, PWM (Pulse Width Modulation) dimming and the BAS (Beam Angle Switching) method, and evaluates their combined effects on performance and energy efficiency. Chapter 7 describes the development of a smart, CCT-tunable, human-centric street lighting luminaire. It integrates findings from prior experiments, leveraging three-point color mixing theory to create a cost-effective, efficient, and human-centered design. The chapter also covers the luminaire's developmental process and implementation. Chapter 8 concludes the thesis by summarizing the key findings and proposing future research directions, emphasizing the potential for further innovation in human-centric lighting systems.

The significant contributions and achievements of this research are detailed below.

8.1.1 Advancements in Understanding Correlated Color Temperature (CCT) Effects

The research systematically analyzed the influence of CCT on visual and behavioral responses under varied lighting conditions. Higher CCT levels were found to significantly enhance both eye adaptation and sensitivity, leading to improved small target visibility (STV). The reduction in average reaction times for object detection with increased CCT demonstrates the crucial role of lighting in enhancing road safety. These findings are pivotal for designing street lighting systems that cater to the cognitive demands of road users, particularly drivers.

Moreover, the interaction between main and peripheral light sources revealed critical insights into lighting scene optimization. It was established that, in the absence of peripheral glare or flickering, the optimal CCT for observer well-being and object recognition lies around 4000K.

However, when peripheral sources are present, this optimum shifts to higher CCTs, such as 5000K. These nuanced understandings ensure lighting designs can be tailored to diverse urban and rural settings, balancing visual performance with user comfort.

8.1.2 Peripheral Flickering: A Double-Edged Sword

Peripheral flickering was identified as a critical factor influencing reaction times and object detection capabilities. While it introduces annoyance and acts as a source of peripheral glare, the research highlights the potential for optimizing flickering frequencies to mitigate its adverse effects. By calibrating flickering frequencies to around 3 Hz for ambient light sources at 3000K and 6000K and approximately 5 Hz at 4500K, lighting designs can minimize the impact of flicker on driver reaction times. This innovative approach ensures that flickering can be managed without compromising lighting efficiency or safety.

8.1.3 Validation of Beam Angle Switching (BAS) Method

The BAS method represents a groundbreaking advancement in road lighting technology. This technique allows for dynamic adjustment of light distribution based on traffic density, significantly reducing energy consumption during low-traffic periods. The experimental validation of BAS on motorized roads demonstrated its effectiveness in enhancing object detection while maintaining acceptable longitudinal uniformity. This scalable and adaptable methodology provides a practical solution for integrating energy-efficient lighting into smart city frameworks.

Additionally, the BAS technique proved compatible with existing PWM dimming systems, creating a dual-layer optimization strategy. By combining BAS with PWM dimming, road lighting systems achieve up to 55.52% energy savings while maintaining consistent lighting quality. This dual strategy reduces carbon emissions, with the BAS method alone cutting approximately 53.14 tons of CO2 emissions annually, making it a critical tool for sustainable urban development.

8.1.4 Development of Advanced Devices for Lighting Assessment

To facilitate in-depth analysis of human-centric lighting, this research developed two key devices: the Reaction Time Measuring Compact Device (RTMCD) with special active shutter glass and the Galvanic Skin Response (GSR) device. A more robust device, named Reaction Time Measuring Device v2.0, was later developed by merging the functionalities of previous devices. The control circuit of active shutter glass was eliminated, and its control was integrated into the Arduino Uno microcontroller for improved efficiency. These tools provided precise measurements of visual, behavioral, and physiological responses to varying lighting conditions. The integration of EEG-based assessments further enriched the experimental framework, offering insights into the neural correlates of object recognition and cognitive load.

8.1.5 Development of a low-cost, high-CRI, CCT-tunable, wirelessly controlled, BAS-enabled street lighting luminaire

The novel development of a cost-effective WW-G-B LED lighting system capable of producing a wide range of CCTs (3500K–8500K), with comparatively high CRIs, underscores this research's practical contributions. By reducing system costs and complexity while maintaining high performance, this innovation bridges the gap between laboratory research and real-world applications.

8.1.6 Integration of Human-Centric Design in Road Lighting Standards

Recognizing the outdated nature of existing Indian road lighting standards, this research provides actionable recommendations for integrating human-centric approaches into policy frameworks. The findings advocate for a paradigm shift in road lighting design, emphasizing user behavioral patterns and cognitive responses. Further collaboration with BIS divisions, particularly ETD49 and ETD23, will ensure that these recommendations are aligned with national and international standards.

8.1.7 Environmental and Socioeconomic Impacts

The environmental benefits of this research are profound. The BAS method and other energy-efficient techniques demonstrated substantial reductions in electricity consumption and carbon footprints. By optimizing lighting designs, this research contributes to achieving global sustainability goals, reducing energy costs, and enhancing urban resilience.

8.1.8 Holistic Contribution to Illumination Engineering

Beyond specific findings, this research enriches the broader domain of illumination engineering by introducing methodologies that balance technological innovation with human-centric considerations. The use of EEG and GSR as metrics for evaluating lighting systems represents a novel approach that transcends traditional illuminance-based assessments. This integrated perspective ensures that lighting designs not only meet technical standards but also enhance human well-being.

8.2 Future Scope

Throughout the course of this thesis, several areas were identified where improvements could be made to the existing systems. The types and techniques of the experimentations and developed prototype of the street light luminaire serve as proof of concept and has been successfully validated. While this thesis provides a robust foundation for human-centric road lighting, several avenues for future exploration emerge from the findings. These directions aim to expand the applicability and impact of the research, addressing both theoretical and practical challenges.

8.2.1 Real-World Validation of Laboratory Findings

The controlled experimental setup used in this research offers valuable insights, but field studies on real-world roads are essential to validate these findings. Future research should examine how diverse road types of India and traffic conditions, weather, and ambient lighting influence driver behavior and lighting performance. Longitudinal studies can also assess the long-term impacts of optimized lighting designs on safety and energy consumption.

8.2.2 Advanced Brain-Machine Interface Studies

The integration of EEG-based assessments provides a powerful tool for understanding cognitive and neural responses to lighting. Exploring the temporal dynamics of brain activity under varying lighting conditions will significantly enhance our knowledge of the impact of lighting on human cognitive performance. Such studies can inform the development of lighting systems tailored to specific tasks, such as driving, walking, or cycling. Classification of these recorded EEG data, using machine learning methods, can also give valuable insights on the effect of lighting parameters on human work efficiency and object recognition.

8.2.3 Smart Lighting for Urban Infrastructure

The BAS technique's potential for smart city integration warrants further exploration. Future work should focus on developing adaptive lighting systems that dynamically respond to real-time data, such as traffic density, pedestrian presence, and environmental conditions. Furthermore, studies on batch controlling of these street light luminaires are also necessary. Integrating IoT technologies and machine learning algorithms will enhance the functionality and scalability of these systems.

8.2.4 Device Enhancement and Automation

The RTMD and GSR devices developed in this research have proven effective in controlled experiments, but further refinements are needed for broader application. Enhancing these devices with real-time analytics, predictive capabilities, and user-friendly interfaces will increase their utility. Additionally, automating data collection and analysis will streamline the research process and facilitate large-scale studies.

8.2.5 Spectrum and Wavelength Optimization

The role of specific wavelengths, such as green light in mesopic conditions, remains an area of interest. Future research should investigate how different spectral compositions influence visual acuity, contrast perception, and energy efficiency. This knowledge can inform the design of lighting systems that maximize visibility while minimizing energy consumption.

8.2.6 Further Development of the low-cost, high-CRI, CCT-tunable, wirelessly controlled, BAS-enabled street lighting luminaire

The system can be enhanced by incorporating modern high-power LEDs and optimizing their placement. Additionally, the SMPS (Switched Mode Power Supply) can be eliminated and integrated with the nearby control circuit mounted on the streetlight pole. Further research, using the developed system on real road scenario, is needed to explore the visual and non-visual impacts of varying lighting parameters on human-centric factors such as reaction time for object detection, Small Target Visibility (STV), and Visibility Level (VL).

8.2.7 Behavioral and Psychological Studies

Understanding the long-term psychological and behavioral impacts of lighting on road users is critical for developing truly human-centric systems. Future studies should examine factors

such as stress, fatigue, and decision-making under various lighting conditions. This research will provide a holistic perspective on the interplay between lighting design and human behavior.

8.2.8 Standardization and Policy Development

Collaborating with national and international standardization bodies to update road lighting standards remains a priority. Future work should focus on creating guidelines that reflect the latest research findings, ensuring that lighting designs meet the diverse needs of urban and rural communities.

8.2.9 Exploring New Frontiers in Illumination Engineering

This research opens several new frontiers in illumination engineering, from advanced LED technologies to innovative dimming techniques. Future studies should explore the scalability of these innovations across different domains, such as industrial lighting, architectural lighting, and emergency lighting.

8.2.10 Sustainability and Environmental Impact

Building on the demonstrated environmental benefits of the BAS method, future research should explore additional strategies for reducing the ecological specifically the carbon footprint of lighting systems. This includes investigating renewable energy sources, optimizing material usage, and developing recycling protocols for lighting components.

By addressing these future scopes, this research paves the way for transformative advancements in human-centric lighting, ensuring that the next generation of lighting systems is safer, smarter, and more sustainable.

References

1. Ministry of Power, Govt. of India. (n.d.). *SLNP - DASHBOARD*. Retrieved November 29, 2024, from https://slnp.eeslindia.org/
2. Sarkar, A., Singh, S. K., Jain, N., & Dwidedi, V. (2015). India - Energy-efficient street lighting : implementation and financing solutions. *The World Bank*, Report No: AUS7490. http://documents.banquemondiale.org/curated/fr/444081468282557427/India-Energy-efficient-street-lighting-implementation-and-financing-solutions.
3. Johnson, A. K., Phadke, A., & De La Rue Du Can, S. (2014). Energy Savings Potential for Street Lighting in India. *ERNEST ORLANDO LAWRENCE BERKELEY NATIONAL LABORATORY,* Contract No. DE-AC02-05CH11231. https://eaei.lbl.gov/sites/all/files/lbnl6576e.pdf
4. Peden, M., Richard, S., Sleet, D., Mohan, D., Hyder, A.A., Jarawan, E., Mathers, C. World Report on Road Traffic Injury Prevention // World Health Organization, 2004.
5. Transport Research Wing. Ministry of Road Transport and Highways / Govt. of India. Road Accidents in India, 2019.
6. Vincent, D. S., P. Pitchipoo, and S. Rajakarunakaran. "Elimination of blind Spots for heavy transport vehicles by driver seat design." In *Int Conf Adv Manuf Auto, Kalasalingam University, India*. 2013.
7. A History of Street Lighting in the Old and New Towns of Edinburgh World Heritage Site. Khrystyna Shakhmatova, Krzysztof Jan Chuchra, Steve Francey, original research by Andrew Kerr, February, 2012.
8. Fotios, S., Gibbons, R. Road lighting research for drivers and pedestrians: The basis of luminance and illuminance recommendations // Lighting Res. Technol., 2018, Vol. 50, pp. 154–186.
9. Ikechi Risi, V.B. Omubo-Pepple, M. A. Alabraba. Comparative Study of Light Emitting Diode (LED), Compact Fluorescent (CF) and Incandescent Lamps. Journal of Scientific and Engineering Research, 2018, 5(11):197-203.ISSN: 2394-2630.
10. Commission International de L'E´ clairage. Recommended System for Visual Performance Based Mesopic Photometry. CIE191:2010. Vienna: CIE, 2010.
11. Rea, M.S., Figueiro, M.G., Bullough, J.D. Circadian photobiology: an emerging framework for lighting practice and research // Lighting Res. Technol., 2002, Vol. 34, # 3, pp. 177–190.
12. Houser, K.W., Boyce, P.R., Zeitzer, J.M., Herf, M. Human centric lighting: Myth, magic or metaphor? // Lighting Res. Technol., 2020, # 0, pp. 1–22.
13. Boyce, P. R. (2008). Lighting for driving: roads, vehicles, signs, and signals. http://ci.nii.ac.jp/ncid/BB14353804.
14. Plainis, S., Murray, I. J., & Charman, W. N. (2005). The role of retinal adaptation in night driving. Optometry and Vision Science, 82(8), 682–688. https://doi.org/10.1097/01.opx.0000175559.77853.45.
15. Helms, R. N., & Belcher, M. C. (1992). Lighting for energy-efficient luminous environments. Choice Reviews Online, 29(08), 29–4541. https://doi.org/10.5860/choice.29-4541.
16. IEC (1987) International Lighting Vocabulary. CIE Publication 17.4.-IEC Publication 50(845).
17. Wout Van Bommel , "Road Lighting Fundamentals, Technology and Applications." Springer Publication.2015.

18. Can Cengiz, Visual Performance Under Mesopic Conditions: Towards Determination of Adaptation Luminance, DOCTORAL DISSERTATIONS 163/2015 , Aalto University publication series.
19. Akashi, Y. and Rea, M. (2002) Peripheral detection while driving under a mesopic light level. J. Illum. Eng. Soc. 31, 85–94.
20. Y. Akashi, M. S. Rea, and J. D. Bullough, “Driver decision making in response to peripheral moving targets under mesopic light levels,” Light. Res. Technol., vol. 39, no. 1, pp. 53–67, 2007.
21. T.A. Salthouse, Reaction Time. 2007 Elsevier Inc. All rights reserved, in: This Article Is Reproduced from the Previous Edition, vol. 2, Elsevier Inc, 1996, pp. 377–380.
22. H. Steffan, Accident Investigation – Determination of Cause. Encyclopaedia of Forensic Sciences, Second ed.,, Elsevier Ltd, 2013, pp. 405–413.
23. W. Ing. Adrian, Visibility of targets: model for calculations, Light. Res. Technol. 21 (1989) 181–188.
24. ANSI/IESNA RP-8–00. American National Standard Practice for Roadway Lighting, 2000.
25. Ismail Kıyak. “A Study on the Working Performance of Dimming Methods for Single- and Multichip Power LEDs”. International Journal of Photoenergy. Volume 2012, Article ID 513768, 8 pages. doi:10.1155/2012/513768.
26. W.A. Rodrigues, L.M.F. Morais, P.F. Donoso-Garcia, P.C. Cortizo, S.I. Seleme JR. “Comparative Analysis of Power Leds Dimming Methods”. Power Electronics Conference (COBEP), 2011 Brazilian. IEEE. DOI: 10.1109/COBEP.2011.6085232.
27. Huang-Jen Chiu, Yu-Kang Lo, Yu-Liang Lin and Gwan-Chi Jane. “A Cost-Effective PWM Dimming Method for LED Lighting Applications”. International Journal of Circuit Theory and Applications. Int. J. Circ. Theor. Appl. 2013. Wiley Online Library. DOI: 10.1002/cta.1940.
28. XDP™ Digital Power. “Dimming Control using a PWM Signal”. White Paper, Revision 1.0. Infineon.
29. Swapnil Mahadeokar, Mhalsakant Sardeshmukh. “Energy Efficient PWM Dimmable Smart Digital LED Driver”. Dr. D. Y. Patil Institute of Engineering and Technology, Pune, India 30 Oct - 01 Nov, 2015. 2015 International Conference on Energy Systems and Applications (ICESA 2015). IEEE.
30. D A Filatov, P V Terentyev, A A Sokolova and I S Devyatkin. “Comparative analysis of the energy efficiency of dimmable LED lamps with different types of luminous flux control”. IOP Conf. Series: Earth and Environmental Science. ESDCA-II-2022. IOP Publishing. doi:10.1088/1755-1315/1045/1/012146.
31. Safaa Alaa Eldeen Hamza, Dr. Amin Babiker A/Nabi Mustafa. “The use of Pulse Width Modulation “PWM” Technique in LED Lighting Systems”. International Journal of Science and Research (IJSR). Volume 3 Issue 11, November 2014. Paper ID: OCT141161.
32. Chakraborty, Suddhasatwa, Aiswarya Dev Goswami, and Saswati Mazumdar. "Beam controlled lighting design: An approach towards optimization of road lighting design." Optik 261 (2022): 169165.
33. Hebart, Martin N., Charles Y. Zheng, Francisco Pereira, and Chris I. Baker. "Revealing the multidimensional mental representations of natural objects underlying human similarity judgements." Nature human behaviour 4, no. 11 (2020): 1173-1185.
34. Fotios, S., H. Qasem, C. Cheal, and J. Uttley. "A pilot study of road lighting, cycle lighting and obstacle detection." Lighting Research & Technology 49, no. 5 (2017): 586-602.

35. He, Y., Rea, M., Bierman, A., Bullough, J. Evaluating light source efficacy under mesopic conditions using reaction times // Journal of the Illuminating Engineering Society, 1997, Vol. 26, pp. 125–138.
36. Buyukkinaci, B., Onaygil, S., Guler, O., Yurtseven, M.B. Determining minimum visibility levels in different road lighting scenarios // Lighting Research and Technology, 2017, Vol. 0, pp. 1–12.
37. Rajput K.Y., Khatav G., Pujari M., Yadav P. Intelligent street lighting system using GSM // International Journal of Engineering Science Invention, ISSN (Online): 2319 – 6734, ISSN (Print): 2319 – 6726, March, 2013.
38. Akash R.B., Holabasappa K., Kiran Kumar D.M., Mardi K., Nandini B.M. Street Light Monitoring And Controlling system // International Journal of Modern Trends in Engineering and Research, ISSN (Online): 2349 – 9745, ISSN (Print): 2393 – 8161, April, 2015.
39. Joseph J. F., Durand D. A., Gowtham V. Smart Street Light Unit (SSLU) with Embedded System // International Journal of Modern Communication Technologies & Research (IJMCTR), ISSN: 2321-0850, July 2018.
40. Reyes, Carmina E., Janine Lizbeth C. Rugayan, Carl Jason, G. Rullan, Carlos M. Oppus, and Gregory L. Tangonan. "A study on ocular and facial muscle artifacts in EEG signals for BCI applications." In TENCON 2012 IEEE Region 10 Conference, pp. 1-6. IEEE, 2012.
41. Rubagotti, Matteo, Inara Tusseyeva, Sara Baltabayeva, Danna Summers, and Anara Sandygulova. "Perceived safety in physical human–robot interaction—A survey." Robotics and Autonomous Systems 151 (2022): 104047.
42. Berson, D. M., Dunn, F. A., & Takao, M. (2002). Phototransduction by retinal ganglion cells that set the circadian clock. Science, 295(5557), 1070–1073. https://doi.org/10.1126/science.1067262
43. Hattar, S., Liao, H., Takao, M., Berson, D. M., & Yau, K. (2002). Melanopsin-Containing retinal ganglion cells: architecture, projections, and intrinsic photosensitivity. Science, 295(5557), 1065–1070. https://doi.org/10.1126/science.1069609.
44. Boyce, P. R. (2023). HUMAN FACTORS IN LIGHTING.
45. Dijk, D., & Czeisler, C. (1995). Contribution of the circadian pacemaker and the sleep homeostat to sleep propensity, sleep structure, electroencephalographic slow waves, and sleep spindle activity in humans. Journal of Neuroscience, 15(5), 3526–3538. https://doi.org/10.1523/jneurosci.15-05-03526.1995.
46. Campbell, S. K., Kolobe, T. H., Osten, E. T., Lenke, M., & Girolami, G. L. (1995). Construct validity of the test of infant motor performance. Physical Therapy, 75(7), 585–596. https://doi.org/10.1093/ptj/75.7.585.
47. Scheer, F. a. J. L., & Buijs, R. M. (1999). Light affects morning salivary cortisol in humans. The Journal of Clinical Endocrinology & Metabolism, 84(9), 3395–3398. https://doi.org/10.1210/jcem.84.9.6102.
48. Ruge, H., Stoet, G., & Naumann, E. (2006). Attentional set mixing: Effects on target selection and selective response activation. Psychophysiology, 43(4), 413–421. https://doi.org/10.1111/j.1469-8986.2006.00419.x.
49. Kaida, D., Motoyoshi, H., Tashiro, E., Nojima, T., Hagiwara, M., Ishigami, K., Watanabe, H., Kitahara, T., Yoshida, T., Nakajima, H., Tani, T., Horinouchi, S., & Yoshida, M. (2007). Spliceostatin A targets SF3b and inhibits both splicing and nuclear retention of pre-mRNA. Nature Chemical Biology, 3(9), 576–583. https://doi.org/10.1038/nchembio.2007.18.

50. International Association of Lighting Designers (IALD), LightingEurope. Joint position paper on Human Centric Lighting. February, 2017.
51. W. J. M. Van Bommel, J. B. De Boer, Road Lighting. Eindhoven, Philips Technical Library,1980.
52. CIE Technical report CIE 191:2010, Recommended System for Mesopic Photometry Based on Visual Performance.
53. Lingard, R. and Rea, M. (2002) Off-axis detection at mesopic light levels in a driving context. J. Illum. Eng. Soc. 31, 33–39.
54. Inoue, Y. (2018). Our action in the new century of IEIJ to realize the human centric lighting of new era. Journal of Science and Technology in Lighting, 41(0), 7–8. https://doi.org/10.2150/jstl.ieij17a000007.
55. Gooley JJ, Ho Mien I, St Hilaire MA, Yeo SC, Chua EC, van Reen E, Hanley CJ, Hull JT, Czeisler CA, Lockley SW. Melanopsin and rod-cone photoreceptors play different roles in mediating pupillary light responses during exposure to continuous light in humans. Journal of Neuroscience 2012; 32: 14242–14253.
56. Spitschan M, Jain S, Brainard DH, Aguirre GK. Opponent melanopsin and S-cone signals in the human pupillary light response. PNAS 2014; 111: 15568–15572.
57. Lewy AJ, Wehr TA, Goodwin FK, Newsome DA, Markey SP. Light suppresses melatonin secretion in humans. Science 1980; 210: 1267–1269.
58. Zeitzer JM, Dijk DJ, Kronauer RE, Brown EN, Czeisler CA. Sensitivity of the human circadian pacemaker to nocturnal light: melatonin phase resetting and suppression. Journal of Physiology 2000; 526: 695–702.
59. Cajochen C, Zeitzer JM, Czeisler CA, Dijk DJ. Dose-response relationship for light intensity and ocular and electroencephalographic correlates of human alertness. Behavioural Brain Research 2000; 115: 75–83.
60. Lockley SW, Evans EE, Scheer FAJL, Brainard GC, Czeisler CA, Aeschbach D. Short-wavelength sensitivity for the direct effects of light on alertness, vigilance, and the waking elecgroencephalogram in humans. Sleep Physiology 2006; 29: 161–168.
61. Cajochen C, Munch M, Kobialka S, Krauchi K, Steiner R, Oelhafen P, Orgul S, WirzJustice A. High sensitivity of human melatonin, alertness, thermoregulation, and heart rate to short wavelength light. Journal of Clinical Endocrinology and Metabolism 2005; 90: 1311–1316.
62. Prayag AS, Jost S, Avouac P, Dumortier D, Gronfier C. Dynamics of non-visual responses in humans: as fast as lightning? Frontiers in Neuroscience 2019: 13.
63. Czeisler CA, Kronauer RE, Allan JS, Duffy JF, Jewett ME, Brown EN, Ronda JM. Bright light induction of strong (type 0) resetting of the human circadian pacemaker. Science 1989; 244: 1328–1333.
64. Vi, S. (2017). Threshold exposure duration for recognition of test objects in Pre-School and school children. Advances in Ophthalmology & Visual System, 7(7). https://doi.org/10.15406/aovs.2017.07.00252.
65. Iadarola, Grazia, Valeria Bruschi, Stefania Cecchi, Nefeli Aikaterini Dourou, and Susanna Spinsante. "Low-cost monitoring for stimulus detection in skin conductance." Acta IMEKO 12, no. 3 (2023): 1-6.

66. P. Pitchipoo, R. Sivaprakasam. Analysis of Prime Reasons for Night Time Accidents in Public Transport Corporations. Proceedings of International Conference on Advances in Industrial Engineering Applications (ICAIEA2014) January 6–8, 2014.
67. Bureau Of Indian Standard IS:1944 (Part I &II) – 1970. Code of Practice for Lighting of Public Thoroughfares (First Revision), 3rd March, 1970.
68. CIE Pub. No. 115. Lighting of Roads for Motor and Pedestrian Traffic. 1995.
69. CIE Pub. No. 12.2. Recommendations for the Lighting of Roads for Motorized Traffic. 1997.
70. C. Shooner, K.T. Mullen, Enhanced luminance sensitivity on color and luminance pedestals: threshold measurements and a model of parvocellular luminance processing, J. Vis. 20 (6) (2020) 1–14, 12.
71. Peden, M. M., & Puvanachandra, P. (2019). Looking back on 10 years of global road safety. International Health, 11(5), 327–330. https://doi.org/10.1093/inthealth/ihz042.
72. R. Elvik, A meta-analysis of evaluations of public lighting as accident countermeasure, Transp. Res. Rec. 1485 (1995) 112–123.
73. L. Djokic, A. Cabarkapa, A. Djuretic, Drivers' Impressions Under High-pressure Sodium and Street Lighting, Light. Res. Technol. 0 (2017) 1–13.
74. Rockwell T.H., Hungerford J.C., Balasubramanian K.N. Evaluation of illumination designs for accident reduction at night-time - accident highway sites. Proceedings of American Association for Automotive Medicine. 1976.
75. P.C. Box, Freeway accidents and illumination, Highw. Res. Rec. 416 (1972) 10–20.
76. P.C. Box, Major accident reduction by illumination, Transp. Res. Rec. 1247 (1989) 32–38.
77. F.R. Beyer, K. Ker, Street lighting for preventing road traffic injuries, Cochrane Database Syst. Rev. Issue 1 (2009). Art. No.: CD004728.
78. Haycock, B.C., Campos, J.L., Koenraad, N., Potter, M., Advani, S.K. Creating Headlight Glare in a Driving Simulator. Transportation Research Part F: Traffic Psychology and Behavior. 61, 93–106. ISSN 1369–8478. 2019.
79. P.T. Stone, Fluorescent lighting and health, Light. Res. Technol. 24 (2) (1992) 55–61.
80. E. Ja´ en, E. Colombo, C. Kirschbaum, A simple visual task to assess flicker effects on visual performance, Light. Res. Technol. 4 (43) (2011) 457–471.
81. J.A. Veitch, S.L. McColl, Modulation of fluorescent light: flicker rate and light source effects on visual performance and visual comfort, Light. Res Technol. 27 (4) (1995) 243–256.
82. IEEE 2015. IEEE Std 1789–2015 IEEE Recommended Practices for Modulating Current in High-Brightness LEDs for Mitigating Health Risks to Viewers.
83. L.M. Debney, Visual stimuli as migraine trigger factors, J. Light Vis. Environ. 34 (2) (1984) 94–100.
84. NEMA, 2015. SSL 7A-2015. Phase-Cut Dimming for Solid State Lighting: Basic Compatibility. Virginia: NEMA.
85. Commision Internationale de l′Eclairage (CIE), Visual aspects of time-modulated lighting systems – definitions and measurement models, CIE Publ. TN 006 (2016) 2016.
86. Commision Internationale de l′Eclairage (CIE), 2004. Guide for the Lighting of Road Tunnels and Underpasses, vol. 88 CIE Publications, Vienna, Austria.
87. Lange H. De, Eye's response at flicker fusion to square-wave modulation of a test field surrounded by a large steady field of equal mean luminance, J. Opt. Soc. Am. 51 (4) (1961) 415–421.
88. D. Juri, Kropotov. Psychometrics and Neuropsychological Assessments. Functional Neuromarkers for Psychiatry, Elsevier Ltd,, 2016.

89. CIE Pub. No. 15.2. Colorimetry (2nd Edition)(E), 1986.
90. Emil Wolf. 1961. Progress in Optics. North Holland Pub. Co.
91. T.M. Goodman, Color Design: Theories and Applications. A volume in Woodhead Publishing Series in Textiles, second ed., Elsevier, 2017.
92. C.S. McCamy. Correlated Color Temperature as an Explicit Function of Chromaticity Coordinates. 1992 by John Wiley & Sons, Inc.
93. Eastman, A.A. and McNelis, J.F. (1963) An evaluation of sodium, mercury and filament lighting for roadways, *Illum. Eng.*, 58, 28–34.
94. de Boer, J.B. (1974) Modern light sources for highways, *J. Illum. Eng. Soc.*, 3, 142–152.
95. Buck, J.A., McGowan, T.K. and McNelis, J.F. (1975) Roadway visibility as a function of light source color, *J. Illum. Eng. Soc.*, 5, 20–25.
96. Veitch, J. A., & Miller, N. J. (2024). Effects of Temporal Light Modulation on Individuals Sensitive to Pattern Glare. *LEUKOS*, 20(3), 310–346. https://doi.org/10.1080/15502724.2023.2299210.
97. Commission Internationale de l'Eclairage (CIE). Final report CIE stakeholder workshop for temporal light modulation standards for lighting systems. CIE TN 008:2017. Vienna, Austria: CIE, 2017. Retrieved 2 September 2020, from http://files.cie.co.at/943_CIE_TN_ 008-2017.pdf.
98. Commission Internationale de l'Eclairage (CIE). 2020. ILV: international lighting vocabulary. 2nd ed. Vienna (Austria): CIE. No. CIE S 017/E:2020.
99. Boyce, P. R., Veitch, J. A., Newsham, G. R., Jones, C. C., Heerwagen, J., Myer, M., & Hunter, C. M. (2006). Lighting quality and office work: two field simulation experiments. Lighting Research & Technology, 38(3), 191–223. https://doi.org/10.1191/1365782806lrt161oa.
100. Nakajima Y, Sakaguchi Y. 2015. Transient twinkle perception is induced by sequential presentation of stimuli that flicker at frequencies above the critical fusion frequency. Atten Percept Psychophys. 77(8):2711–2727.
101. Berman SM, Greenhouse DS, Bailey IL, Clear RD, Raasch TW. 1991. Human electroretinogram responses to video displays, fluorescent lighting, and other high frequency sources. Optometry Vision Sci. 68(8):645–662.
102. Commission Internationale de l'Eclairage (CIE). 2022. Visual aspects of time-modulated lighting systems. Vienna (Austria): CIE. No. CIE 249:2022.
103. Brown E, Foulsham T, Lee C-S. 2020. Research note: visibility of temporal light artefact from flicker at 11 kHz. Light Res Technol. 52(3):371–376.
104. Poplawski ME, Miller NJ. 2011. Exploring flicker in solid-state lighting: what you might find, and how to deal with it. Illuminating Engineering Society of North America Annual Conference; Oct. Austin (TX).
105. Wilkins AJ. 1986. Intermittent illumination from visual display units and fluorescent lighting affects movement of the eyes across text. Hum Factors. 28(1):75–81.
106. Veitch JA, Newsham GR. 1998. Lighting quality and energy-efficiency effects on task performance, mood, health, satisfaction and comfort. J Illum Eng Soc. 27(1):107–129.
107. E.R. Hansen, J.S. Larsen, Reflection factors for pedestrian's clothing, Light. Res. Technol. 11 (3) (1979) 154–157.
108. CIE Pub. No. 140, Road Lighting Calculations, 2000.
109. Adrian Ing. W, Glare in street lighting, Light. Res. Technol. 30 (1965). Issue 2_IEStrans.
110. M.S. Janoff, Towards Development of a Visibility Model for Roadway Lighting Design. Winter, Journal of the Illuminating Engineering Society, 1993.

111. Aulhorn E. Graefe's Archiv fur Ophthalmologie. 167,1, 4, 1964.
112. A. Remole, Brightness enhancement versus darkness enhancement at a border, Vis. Res. 17 (1977) 1095–1100.
113. O. Guler, S. Onaygil, Evaluation of visibility level formula in road lighting with field measurements, Istanb. Tech. Univ. (1) (2002).
114. Zheng, C. Y., Pereira, F., Baker, C. I., & Hebart, M. N. (2019). Revealing interpretable object representations from human behavior. ICLR 2019.
115. Uttley, J., Fotios, S., & Cheal, C. (2017). Effect of illuminance and spectrum on peripheral obstacle detection by pedestrians. Lighting Research & Technology, 49(2), 211-227.
116. Goswami, Aiswarya Dev, Jyotipriya Roy, Atanu Naskar, and Suddhasatwa Chakraborty. "A laboratory based study on the effect of CCT change of LED light sources on reaction time and visibility level for object recognition." Optik 264 (2022): 169353.
117. Goswami, Aiswarya Dev, Suddhasatwa Chakraborty, Budhaditya Ghosh, Jyotipriya Roy, and Atanu Naskar. "A laboratory based study on the effect of peripheral flickering LED sources on reaction time of drivers for object recognition." Optik 273 (2023): 170428.
118. Biswas, Rakesh, Suddhasatwa Chakraborty, and Pratik Nath. "Laboratory based EEG study to investigate the influence of light sources on brain processing for detection of object designed with metal halide and high-pressure sodium lamp." Journal of Science and Technology in Lighting 41 (2018): 30-39.
119. Chakraborty, Suddhasatwa, Debtanu Ray, and Ishan Palit. "An EEG based comparative study on driver's performance under the influence of metal halide and high pressure sodium lighting." Optik 245 (2021): 167676.
120. Pan, Zelei, Haiyan Wang, Jinchun Wu, and Quan Chen. "Non-visual effects of CCT on drivers, evidence from EEG." Intelligent Human Systems Integration 69, no. 1 (2023).
121. Arai, Tamio, Ryu Kato, and Marina Fujita. "Assessment of operator stress induced by robot collaboration in assembly." CIRP annals 59, no. 1 (2010): 5-8.
122. Can, Yekta Said, Bert Arnrich, and Cem Ersoy. "Stress detection in daily life scenarios using smart phones and wearable sensors: A survey." Journal of biomedical informatics 92 (2019): 103139.
123. Bifet, Albert, and Ricard Gavalda. "Learning from time-changing data with adaptive windowing." In Proceedings of the 2007 SIAM international conference on data mining, pp. 443-448. Society for Industrial and Applied Mathematics, 2007.
124. Setz, Cornelia, Bert Arnrich, Johannes Schumm, Roberto La Marca, Gerhard Tröster, and Ulrike Ehlert. "Discriminating stress from cognitive load using a wearable EDA device." IEEE Transactions on information technology in biomedicine 14, no. 2 (2009): 410-417.
125. Klem, G. H., Luders, H., Jasper, H. H., & Elger, C. (1999). The ten-twenty electrode system of the International Federation. The International Federation of Clinical Neurophysiology. PubMed, 52, 3–6. https://pubmed.ncbi.nlm.nih.gov/10590970.

126. Likert, Rensis. "A technique for the measurement of attitudes." Archives of psychology (1932).
127. Boucsein, W. (2011). Electrodermal Activity. In Springer eBooks. https://doi.org/10.1007/978-1-4614-1126-0.
128. Delorme, Arnaud, and Scott Makeig. "EEGLAB: an open source toolbox for analysis of single-trial EEG dynamics including independent component analysis." Journal of neuroscience methods 134, no. 1 (2004): 9-21.

129. Makeig, Scott, Marissa Westerfield, T-P. Jung, Sonia Enghoff, Jeanne Townsend, Eric Courchesne, and Terrence J. Sejnowski. "Dynamic brain sources of visual evoked responses." Science 295, no. 5555 (2002): 690-694.
130. P. Campisi and D. La Rocca, ―Brain waves for automatic biometric-based user recognition,‖ IEEE Trans. Inf. Forens. Security, vol. 9, no. 5, pp. 782–800, May 2014.
131. International Energy Agency (IEA). (2006) Light's Labour's Lost: Policies for Energy Efficient Lighting, Paris, France: IEA.
132. Ożadowicz, A., & Grela, J. (2016). Energy saving in the street lighting control system—a new approach based on the EN-15232 standard. Energy Efficiency, 10(3), 563–576. https://doi.org/10.1007/s12053-016-9476-1.
133. Kostic, M., & Djokic, L. (2009). Recommendations for energy efficient and visually acceptable street lighting. Energy, 34(10), 1565–1572. https://doi.org/10.1016/j.energy.2009.06.056.
134. Lutron. (2016). Lutron dimming LEDs via PWM and CCR. In www.lutron.com/help (Application Note #360, Revision C, Customer Assistance — 1.844.LUTRON1).
135. Jang, J.W., Choi, S.Y., Son, J.K. Degradation model of LED based on accelerated life test // In 18th IEEE International Symposium on the Physical and Failure Analysis of Integrated Circuits (IPFA), IEEE, 2011, pp. 1–4.
136. Energy Efficient Street Lighting: Guidelines / The European PPP Expertise Centre (EPEC), 2010.
137. Lighting the cities / European Commission, 2013.
138. Mohamed, S. Smart Street lighting control and monitoring system for electrical power saving by using VANET // International Journal of Communications, Network and System Sciences, 2013, # 6, pp. 351–360.
139. Literature Summary of Lifetime Testing of Light Emitting Diodes and LED Products / Lighting Research Centre, Rensselaer Polytechnic Institute, June 4th, 2021.
140. Understanding power LED lifetime analysis: How intuitive graphical data sets help lighting designers accurately predict power LED reliability in different operating environments / Technology White Paper, PHILIPS, LUMILEDS.
141. LED Luminaire Lifetime: Recommendations for Testing and Reporting / Solid-State Lighting Product Quality Initiative, Next Generation Lighting Industry Alliance, LED Systems Reliability Consortium, Third Edition, September, 2014.
142. Self-Ballasted LED Lamps for General Lighting Services; Part 2 Performance Requirements (First Revision), IS 16102 (Part 2), 2017.
143. IES Approved Method: Measuring Luminous Flux and Colour Maintenance of LED Packages, Arrays and Modules / The Solid-state Lighting Sub-Committee, ANSI/IES LM-80–15.
144. Projecting Long Term Lumen Maintenance of LED Light Sources, IESNA, IES TM-21–11.
145. Zhang, J., Zhu, M., Hao, C., Tang, J., Yang, Q. Reliability analysis of high-power LED streetlight // In 2012 9th International Conference on Fuzzy Systems and Knowledge Discovery, IEEE, 2012, pp. 2755–2758.
146. Chen, Q., Chen, Q., Luo, X. Fast estimation of LED's accelerated lifetime by online test method // In 2014 IEEE 64th Electronic Components and Technology Conference (ECTC), IEEE, 2014, pp. 1992–1995.
147. Q. Li-jun, S. Zi-zheng, J. Feng, Intelligent streetlight energy saving system based on LonWorks power line communication technology, 4th International Conference on Electric Utility Deregulation and Restructuring and Power Technologies (DRPT), IEEE, pp 663–667, (2011).

148. Y.K. Cheng, K.W.E. Cheng, General Study for using LED to replace traditional lighting devices, 2nd International Conference on Power Electronics Systems and Applications, (2006).
149. B. Das, S. Bardhan, T. Maity, S. Mazumdar, Variable CCT constant illuminance white LED light communication system with dimming feature, Results in Optics 1 (2020) 100013, https://doi.org/10.1016/j.rio.2020.100013 , (2020).
150. W. Park, M. Jin, Y. Kim, K. Kim, S. Lee, Investigating the effect of road lighting color temperature on road visibility in night foggy conditions. Appl. Ergon. 106, 103899 (2023).
151. T. Eichhorn, Analog PWM Dimming in White-LED Drivers, Application Report, SNVA768– December (Texas Instruments, 2016).
152. I.E. Society, ANSI/IES LM-73-18, ISBN-13: 978-0-87995-199-0, (2018).
153. I.E. Society, ANSI/IES TM-21 Calculator Beta, (2018).
154. Lutron, Control of LEDs, Application Note #138, Technical White Paper, May, Customer Service/Quotes: 1.888.LUTRON1, (2014).
155. Public Works Department, Government of West Bengal, Schedule of Rates for Electrical Works, April, (2014).
156. A. Goswami, J. Dev, Roy, and Suddhasatwa Chakraborty, Study on Implementation of PWM Dimming in Beam Angle Switched LED Street Light to Achieve Energy Efficient Standard Lighting. In 2023 IEEE 3rd Applied Signal Processing Conference (ASPCON), pp. 33–37. IEEE, (2023).
157. U.S. Department of Energy. (2021). Energy-efficient lighting: Overview. https://www.energy.gov
158. Energy Saving Trust. (2022). Benefits of energy-efficient lighting. https://energysavingtrust.org.uk
159. Illuminating Engineering Society. (2021). Smart and adaptive lighting systems overview. https://www.ies.org
160. Illuminating Engineering Society. (2022). Overview of smart lighting systems. https://www.ies.org
161. Jang, Je Wook, Seung Yoon Choi, and Joong Kon Son. "Degradation model of LED based on accelerated life test." In 18th IEEE International Symposium on the Physical and Failure Analysis of Integrated Circuits (IPFA), pp. 1-4. IEEE, 2011.
162. Posted by: Editor, Lighting India. (2022, June 12). Posted by: Editor, Lighting India. https://www.lightingindia.in/controlling-energy-consumption-in-lighting/
163. Ciabattoni, Lucio, Alessandro Freddi, Gianluca Ippoliti, Maurizio Marcantonio, Davide Marchei, Andrea Monteriu, and Matteo Pirro. "A smart lighting system for industrial and domestic use." In 2013 IEEE international conference on mechatronics (ICM), pp. 126- 131. IEEE, 2013.
164. Ho, Kun-Che, Shun-Chung Wang, and Yi-Hua Liu. "Dimming Techniques focusing on the improvement in luminous efficiency for high-brightness LEDs." Electronics 10, no. 17 (2021): 2163.
165. Yang, Nick GM, Brian YR Shieh, Trio FY Zeng, and SW Ricky Lee. "Analysis of pulse driven LED junction temperature and its reliability." In 2018 15th China International Forum on Solid State Lighting: International Forum on Wide Bandgap Semiconductors China (SSLChina: IFWS), pp. 1-3. IEEE, 2018.
166. Goswami, Aiswarya Dev, and Suddhasatwa Chakraborty. "Road Lighting Standards' Evolution and Future Development of Smart Street Lighting Based Upon Users' Performance In View of Human Centric Lighting: A Review." Light & Engineering 31, no. 5, 2024.

167. Dyble, Marc, Nadarajah Narendran, Andrew Bierman, and Terence Klein. "Impact of dimming white LEDs: chromaticity shifts due to different dimming methods." In Fifth international conference on solid state lighting, vol. 5941, pp. 291-299. SPIE, 2005.
168. Lu, Guangjun, W. D. Van Driel, Xuejun Fan, M. Yazdan Mehr, Jiajie Fan, Cheng Qian, K. M. B. Jansen, and G. Q. Zhang. "Colour shift and mechanism investigation on the PMMA diffuser used in LED-based luminaires." Optical Materials 54 (2016): 282-287.
169. Whitley E, Ball J. Statistics review 1: presenting and summarising data. Crit Care. 2002 Feb;6(1):66-71.
170. D.H. Brainard, Color Vision Theory, Editor(s): Neil J. Smelser, Paul B. Baltes, International Encyclopedia of the Social & Behavioral Sciences, Pergamon, 2001, Pages 2256-2263, ISBN 9780080430768, https://doi.org/10.1016/B0-08-043076-7/00666-5.
171. Chuang, YC. (2015). Spectral Power Distribution. In: Luo, R. (eds) Encyclopedia of Color Science and Technology. Springer, Berlin, Heidelberg. https://doi.org/10.1007/978-3-642-27851-8_352-1.
172. J.B. Murdoch, Illumination Engineering—From Edison's Lamp to Laser, 1st ed., Macmillan, New York, NY, USA, 1985, p. 541.
173. Ries, H., Leike, I., & Muschaweck, J. A. (2003). Mixing colored LED sources. Proceedings of SPIE, the International Society for Optical Engineering/Proceedings of SPIE, 5186, 27. https://doi.org/10.1117/12.509669.
174. Fotios, S., Cheal, C. Obstacle detection: A pilot study investigating the effects of lamp type, illuminance and age // Light. Res. Technol., 2009, Vol. 41, # 4, pp. 321–342.
175. Bahar Barati, Elvin Karana, D. Sekulovski, Sylvia Pont, Retail lighting and textiles: designing a lighting probe set, Light. Res. Technol. 49 (2015), https://doi.org/10.1177/1477153515602953.
176. Ferenc Szabo, ´ Renata Gazdag-Keri, Janos Schanda, P.´ eter Csuti, Alexander Wilm, Elmar Baur, A study of preferred colour rendering of light sources: shop lighting, Light. Res. Technol. 48 (2015), https://doi.org/10.1177/1477153515573042.
177. Ange Wang, Jiangnan Dai, Hao Wang, Yun Mou, Zhang yi, Liu Jiaxin, Zhihua Zheng, Yang Peng, Changqing Chen, White light-emitting diodes with ultrahigh color rendering index by red/green phosphor layer configuration structure, IEEE Trans. Electron Devices (2019) 1–6, https://doi.org/10.1109/TED.2019.2949054.
178. Yang Peng, Yun Mou, Qinglei Sun, Hao Cheng, Mingxiang Chen, Xiaobing Luo, Facile fabrication of heat-conducting phosphor-in-glass with dual-sapphire plates for laser-driven white lighting, J. Alloys Compd. 790 (2019), https://doi.org/10.1016/j.jallcom.2019.03.220.
179. Ming Zhao, Hongxu Liao, Maxim Molokeev, Yayun Zhou, Qinyuan Zhang, Quanlin Liu, Xia Zhiguo, Emerging ultra-narrow-band cyan-emitting phosphor for white LEDs with enhanced color rendition, Light Sci. Appl. 8 (2019) 38, https://doi.org/10.1038/s41377-019-0148-8.
180. Bing Han, Beibei Liu, Yazhou Dai, Jie Zhang, Hengzhen Shi, Alkali metal ion substitution induced luminescence enhancement of NaLaMgWO6:Eu3+ red phosphor for white light-emitting diodes, Ceram. Int. 45 (2018), https://doi.org/10.1016/j.ceramint.2018.10.256.
181. Ya-jie Han, Lei Shi, Han Liu, Zhi-wei Zhang, A novel far red-emitting phosphor SrMgAl10O17: Cr3+ for warm w-LEDs, Optik 195 (2019) 162014, https://doi.org/10.1016/j.ijleo.2018.11.166. ISSN 0030-4026.

182. P. Ge, Z. Zhou, J. Zhang, Hong Wang, Stacked phosphor coating technology for white LEDs with high colour temperature and high colour rendering index, Light. Res. Technol. 51 (2017), https://doi.org/10.1177/1477153517727579 , 147715351772757.
183. Xing Yang, Jiachao Chen, Chufen Chai, Songsheng Zheng, Chao Chen, Near ultraviolet excited white light emitting diode (WLED) based on the blue LiCaPO4: Eu2+ phosphor, Optik 198 (2019) 163238, https://doi.org/10.1016/j.ijleo.2019.163238. ISSN 0030-4026.
184. Sau Ng, K.H. Loo, Y. Lai, Chi. Tse, Color control system for RGB LED with application to light sources suffering from prolonged aging, IEEE Trans. Ind. Electron. 61 (2014) 1788–1798, https://doi.org/10.1109/TIE.2013.2267696.
185. Fu-Cheng Wang, Chun-Wen Tang, Bin-Juine Huang, Multivariable robust control for a red–green–blue LED lighting system, IEEE Trans. Power Electron. 25 (2010) 417–428, https://doi.org/10.1109/TPEL.2009.2026476.
186. Fuzheng Zhang, Peak wavelength selection of chips for three-chip LED light sources with high color fidelity, Optik 224 (2020) 165725, https://doi.org/10.1016/j.ijleo.2020.165725. ISSN 0030-4026.
187. Xiaoqing Zhan, Wenguan Wang, Henry Chung, A novel color control method for multicolor LED systems to achieve high color rendering indexes, IEEE Trans. Power Electron. (2017), https://doi.org/10.1109/TPEL.2017.2785307 , 1-1.
188. Dang Rui, Nan Wang, Gang Liu, Huijiao Tan, Four component, white LED with good colour quality and minimum damage to traditional Chinese paintings, Light. Res. Technol. 51 (7) (2018) 1077–1091, https://doi.org/10.1177/1477153518819039.
189. Yoshihiro Ohno "Color rendering and luminous efficacy of white LED spectra", Proc. SPIE 5530, Fourth International Conference on Solid State Lighting, (20 October 2004); https://doi.org/10.1117/12.565757.
190. Rajib Malik, Kalyankumar Ray, Saswati Mazumdar, A low-cost, wide-range, CCT-tunable, variable-illuminance LED lighting system, Leukos (2019) 1–20, https://doi.org/10.1080/15502724.2018.1541747.
191. L. Lohaus, E. Leicht, S. Dietrich, R. Wunderlich, S. Heinen, Advanced color control for multicolor LED illumination systems with parametric optimization, November, in: IECON 2013-39th Annual Conference of the IEEE Industrial Electronics Society, IEEE, 2013, pp. 3305–3310.
192. Jingxin Nie, Qi Wang, Weimin Dang, Wentian Dong, Shuzhe Zhou, Xin yu, Guoyi Zhang, Bo Shen, Zhizhong Chen, Fei Jiao, Chengcheng Li, Jinglin Zhan, Yifan Chen, Yiyong Chen, Xiangning Kang, Yongzhi Wang, Tunable LED lighting with five channels of RGCWW for high circadian and visual performances, IEEE Photonics J. (2019), https://doi.org/10.1109/JPHOT.2019.2950834, 1-1.
193. Rea, M. S., & Bullough, J. D. (2007). Application of visual performance metrics to nighttime driving and street lighting. Lighting Research & Technology.
194. Goodman, T. (2009). Mesopic vision and public lighting: A review of visual performance under mesopic conditions. Lighting Journal.
195. He, Y., & Rea, M. S. (2010). The mesopic optimization of outdoor lighting for pedestrians. Building and Environment.

196. Fotios, S., & Gibbons, R. (2005). Road lighting and driving: A review of visual and psychological needs. Lighting Research & Technology.
197. Rea, M. S., Bullough, J. D., & Akashi, Y. (2004). Driving visibility and mesopic lighting. Lighting Research & Technology.
198. Kim, Chang Yeong (2002). Color temperature conversion system and method using the same US 7024034 B2.
199. Pradip Maiti, Biswanath Roy, Development of dynamic light controller for variable CCT white LED light source, Leukos 11 (2015) 1–14, https://doi.org/10.1080/15502724.2015.1011784.
200. Hunt, R. W. G., & Pointer, M. R. (2011). *Measuring Colour* (4th ed.). John Wiley & Sons.
201. Fairchild, M. D. (2013). Color Appearance Models (3rd ed.). Wiley-IS&T Series in Imaging Science and Technology.
202. Wyszecki, G., & Stiles, W. S. (2000). Color Science: Concepts and Methods, Quantitative Data and Formulae (2nd ed.). Wiley.
203. Das, Basudeb, and Saswati Mazumdar. "Low cost, high color rendition, CCT variable lighting system based on WGB LED." Optik 231 (2021): 166321.
204. Ghosh, Arijit, Parthasarathi Satvaya, Palash Kumar Kundu, and Gautam Sarkar. "Calibration of RGB sensor for estimation of realtime correlated color temperature using machine learning regression techniques." Optik 258 (2022): 168954.
205. Catalbas, Mehmet Cem, and Matej Bernard Kobav. "Measurement of correlated color temperature from RGB images by deep regression model." Measurement 195 (2022): 111053.
206. Mane, S. S., & Santra, A. K. (2023). Deep Convolutional Attention based Bidirectional Recurrent Neural Network for Measuring Correlated Colour Temperature from RGB images. International Journal on Recent and Innovation Trends in Computing and Communication, 11(8s), 256–270. https://doi.org/10.17762/ijritcc.v11i8s.7205 .
207. Trinh, V. Q., Babilon, S., Myland, P., & Khanh, T. Q. (2022). Processing RGB color sensors for measuring the circadian stimulus of artificial and daylight light sources. Applied Sciences, 12(3), 1132. https://doi.org/10.3390/app12031132 .
208. IEC 61966-2-1:1999/AMD1:2003. Amendment 1 – Multimedia systems and equipment - Colour measurement and management – Part 2-1: Colour management - Default RGB colour space – sRGB.
209. Valencia, Juan-Sebastián Botero, Francisco-Eugenio López Giraldo, and Jesús-Francisco Vargas Bonilla. "Calibration method for Correlated Color Temperature (CCT) measurement using RGB color sensors." In Symposium of Signals, Images and Artificial Vision- 2013: STSIVA-2013, pp. 1-6. IEEE, 2013.
210. Tatu, Cosmin. "Correlated color temperature determination for led modules using a digital color sensor." UPB Sci. Bull. Ser. A Appl. Math. Phys 75, no. 1 (2013): 225-232.
211. TCS3200, TCS3210 Datasheet. Programmable Color Light-ToFrequency Converter. Taos099 – July 2009.
212. Smith, Joe. "Calculating color temperature and illuminance using the TAOS TCS3414CS digital color sensor." Designer's Notebook (2009): 1-7.
213. Vapnik, V. (2013). The nature of statistical learning theory. Springer Science & Business Media.

214. Williams, Christopher, and Carl Rasmussen. "Gaussian processes for regression." Advances in neural information processing systems 8 (1995).
215. Zemel, Richard, and Toniann Pitassi. "A gradient-based boosting algorithm for regression problems." Advances in neural information processing systems 13 (2000).
216. CIE 015:2018 Colorimetry, 4th Edition. (2018). CIE. https://doi.org/10.25039/tr.015.2018
217. Yi, Hualing, Qingyu Xiong, Qinghong Zou, Rui Xu, Kai Wang, and Min Gao. "A novel random forest and its application on classification of air quality." In 2019 8th International Congress on Advanced Applied Informatics (IIAI-AAI), pp. 35-38. IEEE, 2019.
218. https://github.com/TronixLab/ArduinoMicroML

Annexture 1

This part of the thesis describes all the Arduino IDE written and other codes, used in each system incorporated in this thesis.

A. Code of RTMCD

```
#include <LiquidCrystal.h>
LiquidCrystal lcd(12, 11, 5, 4, 3, 2);
double i = 0;
double a = millis();
double c;
int d = 0;
void stpwatch();
void pause();
void setup() {
  lcd.begin(16, 4);
  lcd.clear();
  Serial.begin(9600);
  pinMode(8, INPUT);
  digitalWrite(8, LOW);
  pinMode(7, INPUT);
  digitalWrite(7, LOW);
}
void (*resetFunc)(void) = 0;
void loop() {
  lcd.clear();
  lcd.print("Press Start");
  delay(100);
  Serial.println("press start");
  if (digitalRead(8) == HIGH) {
    if (digitalRead(8) == HIGH && d == 1) {
      resetFunc();
    }
    stpwatch();
    pause();
    [88]
  }
}
void stpwatch() {
  Serial.println("8 = high");
  lcd.clear();
  a = millis();
  Serial.println(a);
  while (digitalRead(7) == LOW) {
```

```
    Serial.println(" d ");
    c = millis();
    i = (c - a) / 1000;
    lcd.print(i);
    lcd.setCursor(7, 0);
    lcd.print("Sec");
    lcd.setCursor(0, 0);
    Serial.println(c);
    Serial.println(a);
    Serial.println(i);
    Serial.println("......");
    delay(10);
  }
}
void pause() {
  if (digitalRead(7) == LOW)
    Serial.println("7 = high");
  while (digitalRead(8) == LOW) {
    Serial.println(" e ");
    lcd.setCursor(4, 2);
    lcd.print(i);
    lcd.setCursor(10, 2);
    lcd.print(" Sec");
    lcd.setCursor(11, 0);
    lcd.print("");
    lcd.setCursor(0, 0);
    delay(10);
    d = 1;
  }
}
```

B. Code of RTMD v2.0

```
#include <Wire.h>
#include <Adafruit_GFX.h>
#include <Adafruit_SSD1306.h>

#define SCREEN_WIDTH 128
#define SCREEN_HEIGHT 32
#define SCREEN_ADDRESS 0x3C

#define BUTTON_START 2  // Pin for the start button
#define BUTTON_STOP 3   // Pin for the stop button
#define glass 4
```

```
12
13 Adafruit_SSD1306 display(SCREEN_WIDTH, SCREEN_HEIGHT, &Wire, -1);
14
15 volatile bool timerRunning = false;
16 volatile bool ilglass = false;
17 volatile unsigned long startTime = 0;
18 double currentTime = 0;
19 int i = 1;
20
21 void startButtonISR(void) {
22   if (!timerRunning) {
23     timerRunning = true;
24     startTime = millis();
25     ilglass = true;
26   }
27 }
28
29 void stopButtonISR(void) {
30   if (timerRunning) {
31     timerRunning = false;
32     i = 0;
33   }
34 }
35
36 void setup() {
37   pinMode(BUTTON_START, INPUT_PULLUP);
38   pinMode(BUTTON_STOP, INPUT_PULLUP);
39   pinMode(glass, OUTPUT);
40
41   digitalWrite(glass, HIGH);
42
43   attachInterrupt(digitalPinToInterrupt(BUTTON_START), startButtonISR,
   FALLING);
44   attachInterrupt(digitalPinToInterrupt(BUTTON_STOP), stopButtonISR,
   FALLING);
45
46   display.begin(SSD1306_SWITCHCAPVCC, SCREEN_ADDRESS);
47   if (!display.begin(SSD1306_SWITCHCAPVCC, SCREEN_ADDRESS)) {
48     Serial.println(F("SSD1306 allocation failed"));
49     for (;;)
50       ;
51   }
52 }
53
54 void loop() {
```

```
  if (!timerRunning && i == 1) {
    display.setTextSize(2);
    display.setTextColor(WHITE);
    display.setCursor(0, 0);
    display.print("RTMCD v2.0");
    display.display();
  }
  if (timerRunning) {
    currentTime = millis() - startTime;
    double reactionTime = currentTime / 1000;
    display.clearDisplay();
    display.setTextSize(2);
    display.setTextColor(SSD1306_WHITE);
    display.setCursor(0, 8);
    display.print("T-");
    display.print(reactionTime);  // Display time in seconds
    display.print(" s");
    display.display();

    // Print timer details in the Serial Monitor
    Serial.print("Elapsed Time: ");
    Serial.print(reactionTime);  // Print time in seconds
    Serial.println(" s");
  }
  if (currentTime > 700) {
    ilglass = false;
    digitalWrite(glass, HIGH);
  }
  if (ilglass) {
    digitalWrite(glass, LOW);
  }
}
```

C. JAVA Code to calculate the VL and STV values

```
import java.math.*;
import java.util.Scanner;
public
class Atanu {
public
  static void main(String[] args) {
    float dist, height, lt, lb1, lb2, target_size, lb, lla, la, F,
      L, B, C, AA, AL, AZ, DL1, DL2, DL3, DL4, FA, TGB, FCP, RT, TA, M,
VL, RWVL;
```

```
9       F = 0;
10      L = 0;
11      FCP = 0;
12      Scanner sc = new Scanner(System.in);
13      System.out.println("Enter LT");
14      lt = sc.nextFloat();
15      System.out.println("enter target size");
16      target_size = sc.nextFloat();
17      System.out.println("enter distance");
18      dist = sc.nextFloat();
19      float temp = (float)Math.atan(target_size / dist);
20      System.out.println(temp);
21      float A = (float)(Math.atan(target_size / dist) * 60 * 180 / 3.14);
22      System.out.println("A = " + A);
23      System.out.println("enter lb1");
24      lb1 = sc.nextFloat();
25      System.out.println("enter lb2");
26      lb2 = sc.nextFloat();
27      lb = (lb1 + lb2) / 2;
28      System.out.println("lb = " + lb);
29      lla = (float)Math.log10(lb);
30      System.out.println("lla = " + lla);
31      la = lb;
32      System.out.println("Enter reaction time RT");
33      RT = sc.nextFloat();
34      System.out.println("Enter age");
35      TA = sc.nextFloat();
36      if (la >= 0.6) {
37        F = (float)
38              Math.pow(Math.log10(4.2841 * Math.pow(la, 0.1556)) + (0.1684 *
    Math.pow(la, 0.5867)), 2);
39        L = (float)
40              Math.pow(0.05946 * Math.pow(la, 0.466), 2);
41      } else if (la > 0.00418 && la < 0.6) {
42        F = (float)Math.pow(10, 2 * (0.0866 * Math.pow(lla, 2) + (0.3372 *
    lla) - 0.072));
43        L = (float)Math.pow(10, 2 * (0.319 * lla - 1.256));
44      } else if (la < 0.00418) {
45        F = (float)Math.pow(10, (0.346 * lla + 0.056));
46        L = (float)Math.pow(10, 0.0454 * Math.pow(lla, 2) + (1.055 * lla) -
    1.782);
47      }
48      System.out.println("F = " + F);
49      System.out.println("L = " + L);
50      B = (float)(Math.log10(A) + 0.523);
```

```
51      C = lla + 6;
52      AA = (float)(0.360 - ((0.0972 * Math.pow(B, 2)) / (Math.pow(B, 2) -
    (2.513 * B) + 2.789)));
53      AL = (float)(0.355 - (0.1217 * (Math.pow(C, 2)) / (Math.pow(C, 2) -
    (10.40 * C) + 52.28)));
54      AZ = (float)Math.pow((Math.pow(AA, 2) + Math.pow(AL, 2)) / 2.1, 0.5);
55      DL1 = (float)(2.6 * Math.pow((Math.pow(F, 0.5) / A) + Math.pow(L,
    0.5), 2));
56      System.out.println("B = " + B);
57      System.out.println("C = " + C);
58      System.out.println("AA = " + AA);
59      System.out.println("AL = " + AL);
60      System.out.println("AZ = " + AZ);
61      System.out.println("DL1 = " + DL1);
62      DL2 = DL1 * ((AZ + RT) / RT);
63      System.out.println("DL2 = " + DL2);
64      if (TA < 64) {
65        FA = (float)((Math.pow(TA - 19, 2) / 2160) + 0.99);
66      } else {
67        FA = (float)((Math.pow(TA - 56.5, 2) / 116.3) + 1.43);
68      }
69      System.out.println("FA = " + FA);
70      DL3 = DL2 * FA;
71      System.out.println("DL3 = " + DL3);
72      TGB = (float)(-0.6 * Math.pow(la, -0.1488));
73      System.out.println("TGB = " + TGB);
74      if (lla > -2.4 && lla < -1) {
75        M = (float)Math.pow(10, -Math.pow(10, -(0.075 * Math.pow(lla + 1,
    2)) + 0.0245));
76        FCP = (float)(1 - ((M * Math.pow(A, TGB)) / (2.4 * DL1 * (AZ + 2) /
    2)));
77      } else if (lla >= -1) {
78        M = (float)Math.pow(10, -Math.pow(10, -(0.125 * Math.pow(lla + 1,
    2)) + 0.0245));
79        FCP = (float)(1 - ((M * Math.pow(A, TGB)) / (2.4 * DL1 * (AZ + 2) /
    2)));
80      } else if (lla <= -2.4) {
81        FCP = 0.5F;
82      }
83      System.out.println("FCP = " + FCP);
84      if (lt < lb) {
85        DL4 = DL3 * FCP;
86      }
87      else DL4 = DL3;
88      System.out.println("DL4 = " + DL4);
```

```
    VL = (lt - lb) / DL4;
    RWVL = (float)Math.pow(10, -0.1 * VL);
    System.out.println("vl value is " + VL);
    System.out.println("rwvl value is " + RWVL);
  }
}
```

D. Code for Flickering Peripheral Light Sources

```
void setup() {
  pinMode(13, OUTPUT);
  pinMode(12, OUTPUT);
  Serial.begin(9600);
  delay(100);
}
void loop() {
  Serial.println("LED is now Blinking");
  digitalWrite(13, HIGH);
  digitalWrite(12, HIGH);  // turn the LED on by making the voltage HIGH
  delay(50);
  //delay(62.5);
  //delay(100);
  //delay(166.67);
  digitalWrite(13, LOW);
  digitalWrite(12, LOW);  // turn the LED off by making the voltage LOW
  delay(50);
  //delay(62.5);
  //delay(100);
  //delay(166.67);
}  //10Hz = 50ms, 8Hz = 62.5 ms, 5Hz = 100ms, 3hz = 166.67ms
```

E. Code for GSR Device

```
#include <SPI.h>
#include <SD.h>
#include "RTClib.h"

RTC_DS3231 rtc;

#define PIN_SPI_CS 4
File myFile;

const int GSRPIN = A0;
int sensorValue = 0;
```

```
int gsr_average = 0;
int human_resistance = 0;
long sum = 0;

const int LED = 5;
int k = 0;

void setup() {
  Serial.begin(9600);

  pinMode(LED, OUTPUT);

  Serial.println("SD card is starting");
  SD.begin(PIN_SPI_CS);
  if (!SD.begin(PIN_SPI_CS)) {
    Serial.println(F("SD CARD FAILED, OR NOT PRESENT!"));
    while (1)
      ;  // stop the program
  }
  Serial.println(F("SD CARD INITIALIZED."));

  Serial.println("RTC is starting");
  if (!rtc.begin()) {
    Serial.println("Couldn't find RTC");
    while (1)
      ;
  }
  Serial.println(F("RTC INITIALIZED."));

  //rtc.adjust(DateTime(2024, 01, 9, 18, 37, 45));

  delay(1000);
  myFile = SD.open("gsr.txt", FILE_WRITE);
  if (myFile) {
    Serial.println(F("Demarkation is done"));
    myFile.println("-------------------------------------");
    myFile.close();
  }
}

void loop() {
  GSR();
  RTC();
  SDcard();
}
```

```
57
58 void SDcard() {
59   myFile = SD.open("gsr.txt", FILE_WRITE);
60
61   if (myFile) {
62     Serial.println(F("Writing log to SD Card"));
63
64     DateTime now = rtc.now();
65     myFile.print(now.year(), DEC);
66     myFile.print('-');
67     myFile.print(now.month(), DEC);
68     myFile.print('-');
69     myFile.print(now.day(), DEC);
70     myFile.print(' ');
71     myFile.print(now.hour(), DEC);
72     myFile.print(':');
73     myFile.print(now.minute(), DEC);
74     myFile.print(':');
75     myFile.print(now.second(), DEC);
76
77     myFile.print("  --  ");
78     myFile.print("gsr_average = ");
79     myFile.print(gsr_average);
80     digitalWrite(LED, HIGH);
81     myFile.println(", ");  // delimiter between data
82     myFile.close();
83
84   } else {
85     Serial.print(F("SD Card: error on opening file "));
86     Serial.println("gsr.txt");
87   }
88 }
89
90 void RTC() {
91   DateTime now = rtc.now();
92   Serial.print(now.year(), DEC);
93   Serial.print('-');
94   Serial.print(now.month(), DEC);
95   Serial.print('-');
96   Serial.print(now.day(), DEC);
97   Serial.print(' ');
98   Serial.print(now.hour(), DEC);
99   Serial.print(':');
100  Serial.print(now.minute(), DEC);
101  Serial.print(':');
```

```
  Serial.print(now.second(), DEC);
  Serial.print("  --  ");
  Serial.print("gsr_average =");
  Serial.println(gsr_average);
}

void GSR() {
  for (int i = 0; i < 10; i++)  //Average of 10 sensor data represents one final value.
  {
    sensorValue = analogRead(GSRPIN);
    sum = sum + sensorValue;
    //Serial.println(sum);
    delay(5);
  }
  gsr_average = sum / 10;
  delay(500);
  sum = 0;
}
```

F. MATLAB Code for Feature Extraction from ERP Plots

```
erp_signal_table = readtable("D:\PhD\CCT vs EEG fq paper\DATA\EEG\EDF\Only P6\ERP ICA.csv");
erp_signal = erp_signal_table{:, 2};
time = erp_signal_table{:, 1};
erp_data = [time, erp_signal];

plot(time, erp_signal);
title('ERP Signal');
xlabel('Time (s)');
ylabel('Amplitude (μV)');

baseline_end_time = 0;
baseline_end_index = find(time == baseline_end_time);

% Calculate peak amplitude and latency after stimulus onset
[peak_amplitude, relative_peak_index] = max(abs(erp_signal(baseline_end_index:end)));
peak_index = baseline_end_index + relative_peak_index - 1; % Get the correct index in the original signal
peak_latency = time(peak_index);

window_start_index = 104;
```

```
auc = trapz(time(window_start_index:end), erp_signal(window_start_index:end)); % If over a specific window, adjust 'time' and 'erp_signal' accordingly

onset_latency = 0;

baseline_value = mean(erp_signal(1:baseline_end_index)); % Assuming baseline_end_index is known
rise_time = peak_latency - onset_latency;

half_peak_value = 0.5 * peak_amplitude;
half_peak_indices = find(abs(erp_signal(baseline_end_index:end)) >= half_peak_value);
half_peak_width = time(half_peak_indices(end)) - time(half_peak_indices(1));

slope = (peak_amplitude - baseline_value) / (peak_latency - onset_latency);

[pks, locs] = findpeaks(erp_signal(baseline_end_index:end));
if length(locs) > 1
    inter_peak_interval = time(locs(2)) - time(locs(1));
else
    inter_peak_interval = NaN; % Not enough peaks to calculate
end

pre_stimulus_end_index = baseline_end_index - 1;
post_stimulus_start_index = baseline_end_index + 1;
pre_stimulus_baseline = mean(erp_signal(1:pre_stimulus_end_index)); % Define pre_stimulus_end_index
post_stimulus_baseline = mean(erp_signal(post_stimulus_start_index:end)); % Define post_stimulus_start_index
baseline_shift = post_stimulus_baseline - pre_stimulus_baseline;

window_start_index = 104;
mean_amplitude = mean(erp_signal(window_start_index:end)); % Define window indices

% Define feature names
feature_names = {'Peak Amplitude', 'Peak Latency (samples)', 'AUC', 'Onset Latency (samples)', 'Rise Time (samples)', 'Half-Peak Width (samples)', 'Slope', 'Inter-Peak Interval (samples)', 'Baseline Shift', 'Mean Amplitude'};

% Define corresponding feature values
```

```
feature_values = [peak_amplitude, peak_latency, auc, ...
                  onset_latency, rise_time, ...
                  half_peak_width, slope, ...
                  inter_peak_interval, baseline_shift, ...
                  mean_amplitude];

% Combine feature names and values into a table
features_table = table(feature_names', feature_values', 'VariableNames', {'Feature Name', 'Value'});

% Write the table to a CSV file
writetable(features_table, 'D:\PhD\CCT vs EEG fq paper\DATA\EEG\EDF\Only P6\erp_features.csv');
```

G. MATLAB Code for Feature Extraction from Relative Log Power Spectral Plot

```
% Load the log power vs. frequency data from a CSV file
data = readtable("D:\PhD\CCT vs EEG fq paper\DATA\EEG\EDF\Only P6\Log Power vs fq ICA.csv"); % Adjust the path accordingly
frequency = data{:, 1};  % Assuming frequency is in the first column
log_power = data{:, 2};  % Assuming log power is in the second column

% Initialize a table to store feature names and values
feature_names = {};
feature_values = [];

% 1. Peak Frequency (Dominant Frequency)
[peak_power, peak_index] = max(log_power);
peak_frequency = frequency(peak_index);
feature_names{end+1} = 'Peak Frequency (Hz)';
feature_values(end+1) = peak_frequency;

% 2. Peak Power
feature_names{end+1} = 'Peak Power (dB)';
feature_values(end+1) = peak_power;

% Define frequency bands
delta_band = [0.5 4];
theta_band = [4 8];
alpha_band = [8 13];
beta_band = [13 30];
gamma_band = [30 49];

% Function to calculate band power
```

```
calculate_band_power = @(band) trapz(frequency(frequency >= band(1) & frequency <= band(2)), ...
                                     log_power(frequency >= band(1) & frequency <= band(2)));

% 3. Band Power for each EEG frequency band
delta_power = calculate_band_power(delta_band);
theta_power = calculate_band_power(theta_band);
alpha_power = calculate_band_power(alpha_band);
beta_power = calculate_band_power(beta_band);
gamma_power = calculate_band_power(gamma_band);

feature_names{end+1} = 'Delta Band Power (dB)';
feature_values(end+1) = delta_power;

feature_names{end+1} = 'Theta Band Power (dB)';
feature_values(end+1) = theta_power;

feature_names{end+1} = 'Alpha Band Power (dB)';
feature_values(end+1) = alpha_power;

feature_names{end+1} = 'Beta Band Power (dB)';
feature_values(end+1) = beta_power;

feature_names{end+1} = 'Gamma Band Power (dB)';
feature_values(end+1) = gamma_power;

% 4. Relative Band Power
total_power = trapz(frequency, log_power);

relative_delta_power = delta_power / total_power;
relative_theta_power = theta_power / total_power;
relative_alpha_power = alpha_power / total_power;
relative_beta_power = beta_power / total_power;
relative_gamma_power = gamma_power / total_power;

feature_names{end+1} = 'Relative Delta Power';
feature_values(end+1) = relative_delta_power;

feature_names{end+1} = 'Relative Theta Power';
feature_values(end+1) = relative_theta_power;

feature_names{end+1} = 'Relative Alpha Power';
feature_values(end+1) = relative_alpha_power;

```

```
feature_names{end+1} = 'Relative Beta Power';
feature_values(end+1) = relative_beta_power;

feature_names{end+1} = 'Relative Gamma Power';
feature_values(end+1) = relative_gamma_power;

% 5. Bandwidth of Peak
half_peak_power = peak_power / 2;
half_power_indices = find(log_power >= half_peak_power);

bandwidth_of_peak = frequency(half_power_indices(end)) -
   frequency(half_power_indices(1));
feature_names{end+1} = 'Bandwidth of Peak (Hz)';
feature_values(end+1) = bandwidth_of_peak;

% 6. Spectral Centroid
spectral_centroid = sum(frequency .* log_power) / sum(log_power);
feature_names{end+1} = 'Spectral Centroid (Hz)';
feature_values(end+1) = spectral_centroid;

% 7. Spectral Entropy
normalized_power = log_power / sum(log_power);
spectral_entropy = -sum(normalized_power .* log(normalized_power + eps));
   % +eps to avoid log(0)
feature_names{end+1} = 'Spectral Entropy';
feature_values(end+1) = spectral_entropy;

% 8. Low-Frequency / High-Frequency Power Ratio
low_frequency_power = calculate_band_power([0.5 8]); % Delta + Theta
high_frequency_power = calculate_band_power([30 49]); % Gamma

lf_hf_ratio = low_frequency_power / high_frequency_power;
feature_names{end+1} = 'LF/HF Power Ratio';
feature_values(end+1) = lf_hf_ratio;

% 9. Mean Power
mean_power = mean(log_power);
feature_names{end+1} = 'Mean Power (dB)';
feature_values(end+1) = mean_power;

% Combine feature names and values into a table
features_table = table(feature_names', feature_values', 'VariableNames',
   {'Feature Name', 'Value'});

% Write the features table to a CSV file
```

```
writetable(features_table, 'D:\PhD\CCT vs EEG fq paper\DATA\EEG\EDF\Only P6\Features_fq.csv'); % Adjust the path accordingly

disp('Features extracted and saved successfully.');
```

H. Code for MS Device

```
#include <SPI.h>
#include <LoRa.h>
#include <Wire.h>
#include <BH1750.h>
int relay = 6;
int i = 0;
float lux = 0;
float lux1 = 0;
float avg_lux = 0;
float actual_avg_lux = 0;
String msg = "";
BH1750 lightMeter;
//int counter = 0;
void setup() {
  Serial.begin(9600);
  Serial.println("LoRa Sender is working");
  if (!LoRa.begin(433E6)) {
    Serial.println("Starting LoRa is failed!");
    while (1)
      ;
  }
  pinMode(6, OUTPUT);
  Wire.begin();

  lightMeter.begin();
  Serial.println(F("BH1750 Test"));
}

void loop() {
  digitalWrite(relay, LOW);
  Serial.println("LED is ON");
  for (i = 0; i < 19; i++) {
    delay(10000);
    lux = lightMeter.readLightLevel();
    lux1 = (lux1 + lux);
  }
  avg_lux = lux1 / 18;
```

```
  lux1 = 0;

  actual_avg_lux = ((0.000000645577 * (pow(avg_lux, 3))) - (0.000338559 *
(pow(avg_lux, 2))) + (0.128392 * avg_lux) + 0.244231);

  Serial.print("Light:  ");
  Serial.print(actual_avg_lux);
  Serial.println(" lx");
  digitalWrite(relay, HIGH);
  Serial.println("LED is OFF");
  delay(120000);

  msg = "Illuminance is " + (String)actual_avg_lux + "lux";

  Serial.print("Sending message ");
  Serial.println();
  Serial.println(msg);

  LoRa.beginPacket();
  LoRa.print(msg);
  LoRa.endPacket();
  msg = "";
}
```

I. Code for UISD Device

```
#include <SPI.h>
#include <LoRa.h>

#include <SD.h>
#include <RTClib.h>

#define PIN_SPI_CS_1 10
#define PIN_SPI_CS_2 6
#define FILE_NAME "log.txt"

RTC_DS3231 rtc;

File myFile;

String str="";

void setup()
{
```

```
  pinMode(PIN_SPI_CS_1, OUTPUT);
  pinMode(PIN_SPI_CS_2, OUTPUT);
  Serial.begin(9600);

  if (!rtc.begin()) {
    Serial.println(F("Couldn't find RTC"));
    while (1);
  }
  Serial.println(F("Real Time Clock Initialized"));

  //Setup for date
  if (rtc.lostPower()) {
    Serial.println("RTC lost power, lets set the time!");
    rtc.adjust(DateTime(F(__DATE__), F(__TIME__)));
  }

  rtc.adjust(DateTime(2022, 12, 8, 14, 19, 20));

  digitalWrite(PIN_SPI_CS_1, HIGH);
  digitalWrite(PIN_SPI_CS_2, LOW);
  if (!SD.begin(PIN_SPI_CS_2)) {
    Serial.println(F("SD CARD FAILED, OR NOT PRESENT!"));
    while (1); // don't do anything more:
  }

  Serial.println(F("SD CARD INITIALIZED."));
  Serial.println(F("--------------------"));

  digitalWrite(PIN_SPI_CS_1, LOW);
  digitalWrite(PIN_SPI_CS_2, HIGH);
  Serial.println("LoRa Receiver started");

  if (!LoRa.begin(433E6))
  {
    Serial.println("Starting LoRa failed!");
    while (1);
  }
  Serial.println("LoRa Receiver is working");
}

void loop()
{
  digitalWrite(PIN_SPI_CS_1, LOW);
  digitalWrite(PIN_SPI_CS_2, HIGH);
  int packetSize = LoRa.parsePacket();
```

```
64   delay(10);
65   if (packetSize!=0)
66   {
67     Serial.println("Received value of illuminance '");
68     Serial.println(packetSize);
69     while (LoRa.available())
70     {
71       str=str+((char)LoRa.read());
72     }
73     Serial.print(str);
74     Serial.print("' with RSSI ");
75     Serial.println(LoRa.packetRssi());
76
77 // open file for writing
78   digitalWrite(PIN_SPI_CS_1, HIGH);
79   digitalWrite(PIN_SPI_CS_2, LOW);
80
81   myFile = SD.open(FILE_NAME, FILE_WRITE);
82
83   if (myFile) {
84     Serial.println(F("Writing log to SD Card"));
85
86     // write timestamp
87     DateTime now = rtc.now();
88     myFile.print(now.year(), DEC);
89     myFile.print('-');
90     myFile.print(now.month(), DEC);
91     myFile.print('-');
92     myFile.print(now.day(), DEC);
93     myFile.print(' ');
94     myFile.print(now.hour(), DEC);
95     myFile.print(':');
96     myFile.print(now.minute(), DEC);
97     myFile.print(':');
98     myFile.print(now.second(), DEC);
99
100    myFile.print("  "); // delimiter between timestamp and data
101
102    // write data
103    myFile.print("Received Data = ");
104    myFile.print(str);
105    myFile.println(", "); // delimiter between data
106
107    myFile.write("\n"); // new line
108
```

```
    myFile.close();
  } else {
    Serial.print(F("SD Card: error on opening file "));
    Serial.println(FILE_NAME);
  }
  str="";
  delay(2000); // delay 2 seconds
  }
}
```

J. Code for PWM dimming in BAS Enabled Street Light

```
#include <SPI.h>
#include <Wire.h>
#include <Adafruit_GFX.h>
#include <Adafruit_SSD1306.h>
#define SCREEN_WIDTH 128  // OLED display width, in pixels
#define SCREEN_HEIGHT 32  // OLED display height, in pixels
#define OLED_RESET -1  // Reset pin # (or -1 if sharing Arduino reset pin)
#define SCREEN_ADDRESS 0x3C
//< See datasheet for Address; 0x3D for 128x64, 0x3C for 128x32>
Adafruit_SSD1306 display(SCREEN_WIDTH, SCREEN_HEIGHT, &Wire, OLED_RESET);

int sensorValue = 0;
int PWMVAL = 0;
int duty1 = 0;

const int led1 = 9;
const int led2 = 10;
const int analogpin = 2;
int duty = 0;

unsigned long ONCycle;   //oncycle  variable
unsigned long OFFCycle;  // offcycle variable got microsecond
float T;
int F;

const int PRO = 8;
const int PROin = 9;
const int COUNTER = 10;
const int COUNTERin = 11;
const int FullGlowin = 12;

```

```
int i = 0;
int j = 0;
int k = 0;

void setup() {

Serial.begin(9600);
display.begin(SSD1306_SWITCHCAPVCC, 0x3C);
display.clearDisplay();
if (!display.begin(SSD1306_SWITCHCAPVCC, SCREEN_ADDRESS)) {
Serial.println(F("SSD1306 allocation failed"));
for (;;)
;  // Don't proceed, loop forever
}
pinMode(PRO, OUTPUT);
pinMode(COUNTER, OUTPUT);
pinMode(PROin, INPUT);
pinMode(COUNTERin, INPUT);
pinMode(FullGlowin, INPUT);
pinMode(led1, OUTPUT);
pinMode(led2, OUTPUT);
pinMode(PulseIN, INPUT);

display.setTextSize(1);
display.setTextColor(WHITE);
display.setCursor(0, 0);
display.println("BAS and PWM");
display.setTextSize(1);
display.setTextColor(WHITE);
display.setCursor(0, 10);
display.println("Control Panel");
display.display();

delay(3000);
}

void loop() {
flag();
Mode();
setPWM();
Oled();
}

void Oled() {
```

```
76 display.setTextSize(1);
77 display.setTextColor(WHITE);
78 display.setCursor(0, 0);
79 display.println("POT Value -> ");
80 display.setCursor(80, 0);
81 display.println(sensorValue);
82 display.setTextSize(1);
83 display.setCursor(0, 12);
84 display.println("Brightness -> ");
85 display.setCursor(85, 12);
86 display.println(duty1);
87 display.setCursor(105, 12);
88 display.println(" %");
89 display.setTextSize(1);
90 display.setTextColor(WHITE);
91 display.setCursor(0, 24);
92 display.println("Duty Cy. -> ");
93 display.setCursor(80, 24);
94 display.println(duty);
95 display.setCursor(102, 24);
96 display.println(" %");
97 display.display();
98 display.clearDisplay();
99 }
100
101void setPWM() {
102
103sensorValue = analogRead(analogpin);
104Serial.println(sensorValue);
105delay(10);
106PWMVAL = (sensorValue) / 4;
107analogWrite(led1, PWMVAL);
108analogWrite(led2, PWMVAL);
109duty1 = (100 * PWMVAL) / 255;
110Serial.println(duty1);
111Serial.println(PWMVAL);
112ONCycle = pulseIn(led1, HIGH);
113OFFCycle = pulseIn(led1, LOW);
114Serial.println(ONCycle);
115Serial.println(OFFCycle);
116T = ONCycle + OFFCycle;
117duty = (ONCycle / T) * 100;
118F = 1000000 / T;
119Serial.println(duty);
120}
```

```
121
122void Mode() {
123while (i == 1) {
124digitalWrite(PRO, HIGH);
125digitalWrite(COUNTER, LOW);
126if (digitalRead(COUNTERin) == HIGH || digitalRead(FullGlowin) == HIGH)
127break;
128}
129while (j == 1) {
130digitalWrite(PRO, LOW);
131digitalWrite(COUNTER, HIGH);
132if (digitalRead(PROin) == HIGH || digitalRead(FullGlowin) == HIGH)
133break;
134}
135while (k == 1) {
136digitalWrite(PRO, HIGH);
137digitalWrite(COUNTER, HIGH);
138if (digitalRead(PROin) == HIGH || digitalRead(COUNTERin) == HIGH)
139break;
140}
141while (i == 0 && j == 0 && k == 0) {
142digitalWrite(PRO, HIGH);
143digitalWrite(COUNTER, HIGH);
144if (digitalRead(PROin) == HIGH || digitalRead(COUNTERin) == HIGH ||
   digitalRead(FullGlowin) == HIGH)
145break;
146}
147}
148
149void flag() {
150if (digitalRead(PROin) == HIGH) {
151i = 1;
152} else if (digitalRead(COUNTERin) == HIGH) {
153j = 1;
154} else if (digitalRead(FullGlowin) == HIGH) {
155k = 1;
156} else {
157i = 0;
158j = 0;
159k = 0;
160}
161}
```

K. Code for Tunable Switching Frequency and Duty Cycle Enabled PWM Generating System

```
#include <Arduino.h>
#include <SPI.h>
#include <Wire.h>
#include <Adafruit_GFX.h>
#include <Adafruit_SSD1306.h>

#define SCREEN_WIDTH 128  // OLED display width, in pixels
#define SCREEN_HEIGHT 32  // OLED display height, in pixels

#define OLED_RESET -1        // Reset pin # (or -1 if sharing Arduino reset pin)
#define SCREEN_ADDRESS 0x3C  ///< See datasheet for Address; 0x3D for 128x64, 0x3C for 128x32>
Adafruit_SSD1306 display(SCREEN_WIDTH, SCREEN_HEIGHT, &Wire, OLED_RESET);

const int potFrequencyPin = 34;  // Analog input pin for frequency control
const int potDutyCyclePin = 35;  // Analog input pin for duty cycle control
const int ledPin = 2;            // PWM output pin

int potFrequencyValue = 0;  // Variable to store frequency value
int potDutyCycleValue = 0;  // Variable to store duty cycle value
int frequency = 0;
float dutyCycle = 0;
float brightness = 0;

void setup() {
  pinMode(ledPin, OUTPUT);
  Serial.begin(9600);
  display.begin(SSD1306_SWITCHCAPVCC, 0x3C);
  display.clearDisplay();
  if (!display.begin(SSD1306_SWITCHCAPVCC, SCREEN_ADDRESS)) {
    Serial.println(F("SSD1306 allocation failed"));
    for (;;)
      ;  // Don't proceed, loop forever
  }

  // Set the PWM frequency to an initial value
  int initialFrequency = 1000;        // Initial PWM frequency in Hz
  ledcSetup(0, initialFrequency, 8);  // Channel 0, 8-bit resolution
  ledcAttachPin(ledPin, 0);           // Attach PWM channel to the LED pin

```

```
  display.setTextSize(1);
  display.setTextColor(WHITE);
  display.setCursor(0, 0);
  display.println("Variable");
  display.setTextSize(1);
  display.setTextColor(WHITE);
  display.setCursor(0, 10);
  display.println("Fq & Duty");
  display.display();
  delay(3000);
}

void loop() {
  // Read potentiometer values for frequency and duty cycle
  potFrequencyValue = analogRead(potFrequencyPin);
  potDutyCycleValue = analogRead(potDutyCyclePin);
  Serial.print("potFrequencyValue -- ");
  Serial.println(potFrequencyValue);
  Serial.print("potDutyCycleValue -- ");
  Serial.println(potDutyCycleValue);

  // Map potentiometer values to desired range
  frequency = map(potFrequencyValue, 0, 4095, 1000, 30000);  // Frequency range: 1000-30000 Hz
  dutyCycle = map(potDutyCycleValue, 0, 1023, 0, 255);       // Duty cycle range: 0-255 (8-bit)
  brightness = (dutyCycle / 1023) * 100;

  // Update PWM frequency and duty cycle
  ledcWriteTone(0, frequency);  // Set the PWM frequency
  Serial.print(frequency);
  Serial.println("  Hz");
  ledcWrite(0, dutyCycle);  // Set the PWM duty cycle
  Serial.println(dutyCycle);
  Serial.print(brightness);
  Serial.println("  %");

  delay(500);  // Optional delay for smoother adjustments
  Oled();
}

void Oled() {

  display.setTextSize(1);
  display.setTextColor(WHITE);
```

```
  display.setCursor(0, 0);
  display.println("Frequency -> ");
  display.setCursor(80, 0);
  display.println(frequency);
  display.setCursor(114, 0);
  display.println("Hz");
  display.setTextSize(1);
  display.setCursor(0, 12);
  display.println("Brightness -> ");
  display.setCursor(85, 12);
  display.println(brightness);
  display.setCursor(105, 12);
  display.println(" %");
  display.setTextSize(1);
  display.setTextColor(WHITE);
  display.setCursor(0, 24);
  display.println("Duty Cy. -> ");
  display.setCursor(80, 24);
  display.println(dutyCycle);
  display.setCursor(102, 24);
  display.println(" %");
  display.display();
  display.clearDisplay();
}
```

L. Code for Adjacent Control Circuit of the Developed Low-cost, High CRI, BAS enabled CCT Tunable Humna Centric Smart Street Lighting Luminaire

```
#include <esp_now.h>
#include <WiFi.h>
#include <math.h>

const int PWM_CHANNEL1 = 0;  // ESP32 has 16 channels which can generate
16 independent waveforms
const int PWM_CHANNEL2 = 1;
const int PWM_CHANNEL3 = 2;
const int PWM_CHANNEL4 = 3;
const int PWM_CHANNEL5 = 4;
const int PWM_CHANNEL6 = 5;
const int PWM_CHANNEL7 = 6;
const int PWM_CHANNEL8 = 7;
const int PWM_CHANNEL9 = 8;

const int PWM_FREQ = 5000;     // code uses 5,000Hz
```

```
16 const int PWM_RESOLUTION = 8;  // code uses resolution of 5,000Hz
17
18 // The max duty cycle value based on PWM resolution (will be 255 if
   resolution is 8 bits)
19 const int MAX_DUTY_CYCLE = (int)(pow(2, PWM_RESOLUTION) - 1);
20 const int C1_CW = 32;
21 const int C1_G = 33;
22 const int C1_WW = 25;
23
24 const int C2_CW = 4;
25 const int C2_G = 2;
26 const int C2_WW = 15;
27
28 const int C3_CW = 3;
29 const int C3_G = 21;
30 const int C3_WW = 19;
31
32 const int DELAY_MS = 500;  // delay between fade increments
33
34 // REPLACE WITH THE MAC Address of your receiver
35 uint8_t broadcastAddress[] = { 0xB0, 0xA7, 0x32, 0x14, 0x61, 0x18 };
36
37 // Define variables to store whether duty cycle is properly given
38 int D11 = 0;
39 int D12 = 0;
40 int D13 = 0;
41 int D21 = 0;
42 int D22 = 0;
43 int D23 = 0;
44 int D31 = 0;
45 int D32 = 0;
46 int D33 = 0;
47
48 int varifier1 = 0;
49 int varifier2 = 0;
50 int varifier3 = 0;
51
52 int CCT1 = 0;
53 int CCT2 = 0;
54 int CCT3 = 0;
55
56 double Xt = 0;
57 double Yt = 0;
58
59 double Xa = 0.4318;
```

```
60 double Ya = 0.402243;
61 double Xb = 0.1498;
62 double Yb = 0.0428;
63 double Xc = 0.1457;
64 double Yc = 0.6785;
65 double Xm = 0;
66 double Ym = 0;
67
68 double EaM = 972;
69 double EbM = 116;
70 double EcM = 174;
71 double EmM = 0;
72 double Er = 300;
73
74 double Lbm = 0;
75 double Lbc = 0;
76
77 double r1 = 0;
78 double r2 = 0;
79 double r3 = 0;
80 double r4 = 0;
81
82 double Db = 0;
83 double Dc = 0;
84 double Da = 0;
85 double DbT = 0;
86 double DcT = 0;
87 double Dm = 0;
88
89 // Define variables to store incoming readings
90 int incomingAnalog1 = 0;
91 int incomingAnalog2 = 0;
92 int incomingAnalog3 = 0;
93 int incomingBAS = 0;
94
95 // Variable to store if sending data was successful
96 String success;
97
98 //Structure example to send data
99 //Must match the receiver structure
100typedef struct struct_message {
101   int analog1;
102   int analog2;
103   int analog3;
104   int BAS;
```

```
} struct_message;

// Create a struct_message called dutycyclereading to send whether PWM is working or not
struct_message DutyCycleReading;

// Create a struct_message to hold incoming pot readings
struct_message incomingReading;

esp_now_peer_info_t peerInfo;

// Callback when data is sent
void OnDataSent(const uint8_t *mac_addr, esp_now_send_status_t status) {
  Serial.print("\r\nLast Packet Send Status:\t");
  Serial.println(status == ESP_NOW_SEND_SUCCESS ? "Delivery Success" : "Delivery Fail");
  if (status == 0) {
    success = "Delivery Success :)";
  } else {
    success = "Delivery Fail :(";
  }
}

// Callback when data is received
void OnDataRecv(const uint8_t *mac, const uint8_t *incomingData, int len) {
  memcpy(&incomingReading, incomingData, sizeof(incomingReading));
  Serial.print("Bytes received: ");
  Serial.println(len);
  incomingAnalog1 = incomingReading.analog1;
  incomingAnalog2 = incomingReading.analog2;
  incomingAnalog3 = incomingReading.analog3;
  incomingBAS = incomingReading.BAS;
}

void setup() {
  // Init Serial Monitor
  Serial.begin(115200);

  // Set device as a Wi-Fi Station
  WiFi.mode(WIFI_STA);

  pinMode(C1_CW, OUTPUT);
  pinMode(C1_G, OUTPUT);
  pinMode(C1_WW, OUTPUT);
```

```
147  pinMode(C2_CW, OUTPUT);
148  pinMode(C2_G, OUTPUT);
149  pinMode(C2_WW, OUTPUT);
150  pinMode(C3_CW, OUTPUT);
151  pinMode(C3_G, OUTPUT);
152  pinMode(C3_WW, OUTPUT);
153
154  // Sets up a channel (0-15), a PWM duty cycle frequency, and a PWM
   resolution (1 - 16 bits)
155  ledcSetup(PWM_CHANNEL1, PWM_FREQ, PWM_RESOLUTION);
156  ledcSetup(PWM_CHANNEL2, PWM_FREQ, PWM_RESOLUTION);
157  ledcSetup(PWM_CHANNEL3, PWM_FREQ, PWM_RESOLUTION);
158  ledcSetup(PWM_CHANNEL4, PWM_FREQ, PWM_RESOLUTION);
159  ledcSetup(PWM_CHANNEL5, PWM_FREQ, PWM_RESOLUTION);
160  ledcSetup(PWM_CHANNEL6, PWM_FREQ, PWM_RESOLUTION);
161  ledcSetup(PWM_CHANNEL7, PWM_FREQ, PWM_RESOLUTION);
162  ledcSetup(PWM_CHANNEL8, PWM_FREQ, PWM_RESOLUTION);
163  ledcSetup(PWM_CHANNEL9, PWM_FREQ, PWM_RESOLUTION);
164  ledcAttachPin(C1_CW, PWM_CHANNEL1);
165  ledcAttachPin(C1_G, PWM_CHANNEL2);
166  ledcAttachPin(C1_WW, PWM_CHANNEL3);
167  ledcAttachPin(C2_CW, PWM_CHANNEL4);
168  ledcAttachPin(C2_G, PWM_CHANNEL5);
169  ledcAttachPin(C2_WW, PWM_CHANNEL6);
170  ledcAttachPin(C3_CW, PWM_CHANNEL7);
171  ledcAttachPin(C3_G, PWM_CHANNEL8);
172  ledcAttachPin(C3_WW, PWM_CHANNEL9);
173
174  // Init ESP-NOW
175  if (esp_now_init() != ESP_OK) {
176    Serial.println("Error initializing ESP-NOW");
177    return;
178  }
179
180  // Once ESPNow is successfully Init, we will register for Send CB to
181  // get the status of Trasnmitted packet
182  esp_now_register_send_cb(OnDataSent);
183
184  // Register peer
185  memcpy(peerInfo.peer_addr, broadcastAddress, 6);
186  peerInfo.channel = 0;
187  peerInfo.encrypt = false;
188
189  // Add peer
190  if (esp_now_add_peer(&peerInfo) != ESP_OK) {
```

```
191    Serial.println("Failed to add peer");
192    return;
193  }
194  // Register for a callback function that will be called when data is
   received
195  esp_now_register_recv_cb(OnDataRecv);
196}
197
198void loop() {
199
200  Serial.println(incomingAnalog1);
201  Serial.println(incomingAnalog2);
202  Serial.println(incomingAnalog3);
203
204  CCT1 = incomingAnalog1;
205  CCT2 = incomingAnalog2;
206  CCT3 = incomingAnalog3;
207
208  CCT1 = map(CCT1, 0, 4095, 3076, 9000);
209  CCT2 = map(CCT2, 0, 4095, 3076, 9000);
210  CCT3 = map(CCT3, 0, 4095, 3076, 9000);
211
212  Serial.println(CCT1);
213  Serial.println(CCT2);
214  Serial.println(CCT3);
215
216  if (incomingBAS == 1) {
217    fullglow();
218    Serial.println("Fullglow");
219  } else if (incomingBAS == 2) {
220    pro();
221    Serial.println("Pro");
222    varifier3 = 0;
223  } else if (incomingBAS == 3) {
224    counter();
225    Serial.println("Counter");
226    varifier1 = 0;
227  }
228
229  // Set values to send
230  DutyCycleReading.analog1 = varifier1;
231  DutyCycleReading.analog2 = varifier2;
232  DutyCycleReading.analog3 = varifier3;
233
234  // Send message via ESP-NOW
```

```
235  esp_err_t result = esp_now_send(broadcastAddress, (uint8_t
   *)&DutyCycleReading, sizeof(DutyCycleReading));
236
237  if (result == ESP_OK) {
238    Serial.println("Sent with success");
239  } else {
240    Serial.println("Error sending the data");
241  }
242  //Display();
243  delay(DELAY_MS);
244}
245
246void Display() {
247  // Display Readings in Serial Monitor
248}
249
250float colormixing(int CCT) {
251  if (2222 <= CCT && CCT <= 4000) {
252    Xt = ((-0.2661239 * (pow(10, 9) / pow(CCT, 3))) + (-0.2343580 *
   (pow(10, 6) / pow(CCT, 2))) + (0.8776956 * (pow(10, 3) / CCT)) +
   0.179910);
253    if (Xt <= 0.50338) {
254      Yt = ((-0.9549476 * (pow(Xt, 3))) + (-1.37418593 * (pow(Xt, 2))) +
   (2.09137015 * (Xt)) + (-0.1674886));
255    } else {
256      Yt = ((-1.1063814 * (pow(Xt, 3))) + (-1.34811020 * (pow(Xt, 2))) +
   (2.18555832 * (Xt)) + (-0.20219683));
257    }
258  } else if (4001 <= CCT && CCT <= 25000) {
259    Xt = ((-3.0258469 * (pow(10, 9) / pow(CCT, 3))) + (2.1070379 *
   (pow(10, 6) / pow(CCT, 2))) + (0.2226347 * (pow(10, 3) / CCT)) +
   0.240390);
260    if (Xt <= 0.38405) {
261      Yt = ((3.0817580 * (pow(Xt, 3)) + (-5.87338670 * (pow(Xt, 2))) +
   (3.75112997 * (Xt)) + (-0.37001483)));
262    } else {
263      Yt = ((-1.1063814 * (pow(Xt, 3))) + (-1.34811020 * (pow(Xt, 2))) +
   (2.18555832 * (Xt)) + (-0.20219683));
264    }
265  }
266
267  Serial.println("Xt and Yt are calculated....");
268  Serial.println(Xt, 4);
269  Serial.println(Yt, 4);
270
```

```
271  // Check for division by zero
272  double denominator = ((Yt - Ya) * (Xc - Xb)) - ((Yc - Yb) * (Xt - Xa));
273  if (fabs(denominator) < 1e-6) {  // Small threshold to avoid division by
   zero
274    Serial.println("Error: Division by zero in Xm calculation");
275    return -1;
276  }
277
278  Xm = ((((Yt - Ya) * (Xc - Xb) * Xa) - ((Yc - Yb) * (Xt - Xa) * Xb) +
   ((Yb - Ya) * (Xt - Xa) * (Xc - Xb))) / denominator);
279  Ym = ((((Yc - Yb) / (Xc - Xb)) * (Xm - Xb)) + Yb);
280
281  Serial.println("Xm and Ym are calculated....");
282  Serial.println(Xm, 4);
283  Serial.println(Ym, 4);
284
285  // Blending ratios for sources B and C
286  if (fabs(Xm - Xc) < 1e-6) {  // Check for division by zero
287    Serial.println("Error: Division by zero in r1 calculation");
288    return -1;
289  }
290
291  r1 = ((Xb - Xm) / (Xm - Xc));
292  r2 = (r1 * (Yc / Yb) * (EbM / EcM));
293
294  // Ensure r1 and r2 are normalized
295  double Wc1 = 1 / (1 + r1);
296  double Wc2 = 1 - Wc1;
297
298  Lbm = sqrt((sq(Xb - Xm)) + (sq(Yb - Ym)));
299  Lbc = sqrt((sq(Xb - Xc)) + (sq(Yb - Yc)));
300  EmM = (EbM + ((Lbm / Lbc) * (EcM - EbM)));
301
302  Serial.println("EmM is calculated....");
303  Serial.println(Wc1, 4);
304  Serial.println(Wc2, 4);
305  Serial.println(Lbm, 4);
306  Serial.println(Lbc, 4);
307  Serial.println(EmM, 4);
308
309  Db = ((EmM / EbM) * (1 / (1 + ((EcM / EbM) * (r2)))));
310  Dc = (Db) * (r2);
311
312  // Enforce valid duty cycle ranges
313  Db = constrain(Db, 0, 1);
```

```
  Dc = constrain(Dc, 0, 1);

  // Ratios for source A
  r3 = ((Xa - Xt) / (Xt - Xm));
  r4 = ((r3 * (Ya / Ym)) / (EaM / EmM));

  // Check and normalize r3, r4
  if (fabs(1 + r4) < 1e-6) {
    Serial.println("Error: Division by zero in Dm calculation");
    return -1;
  }

  Dm = ((Er / EmM) * (1 / (1 + ((EaM / EmM) * (r4)))));
  Da = (Dm) * (r4);

  // Ensure duty cycles are within range
  Da = constrain(Da, 0, 1);
  DbT = (Db) * (Dm);
  DcT = (Dc) * (Dm);

  DbT = constrain(DbT, 0, 1);
  DcT = constrain(DcT, 0, 1);

  Serial.println("Da, Db and Dc are calculated....");
  Serial.println(Da, 4);
  Serial.println(Db, 4);
  Serial.println(Dc, 4);
  Serial.println(Dm, 4);

  Serial.println("DbT and DcT are calculated....");
  Serial.println(DbT, 4);
  Serial.println(DcT, 4);

  return Da;  // Return the first valid duty cycle (or extend for
   multiple)
  return DbT;
  return DcT;
}

void fullglow() {
  cluster1();
  cluster2();
  cluster3();
}

```

```
358void pro() {
359  cluster1();
360  cluster2();
361  ledcWrite(PWM_CHANNEL7, 0);
362  ledcWrite(PWM_CHANNEL8, 0);
363  ledcWrite(PWM_CHANNEL9, 0);
364}
365
366void counter() {
367  cluster2();
368  cluster3();
369  ledcWrite(PWM_CHANNEL1, 0);
370  ledcWrite(PWM_CHANNEL2, 0);
371  ledcWrite(PWM_CHANNEL3, 0);
372}
373
374void cluster1() {
375  colormixing(CCT1);
376  D11 = (Da * 100);
377  D12 = (DbT * 100);
378  D13 = (DcT * 100);
379
380  Serial.print("Duty Cycle for cluster1-  D11- ");
381  Serial.print(D11);
382  Serial.print("%");
383  Serial.print(" D12- ");
384  Serial.print(D12);
385  Serial.print("%");
386  Serial.print(" D13- ");
387  Serial.print(D13);
388  Serial.println("%");
389
390  D11 = map(D11, 0, 100, 0, MAX_DUTY_CYCLE);
391  D12 = map(D12, 0, 100, 0, MAX_DUTY_CYCLE);
392  D13 = map(D13, 0, 100, 0, MAX_DUTY_CYCLE);
393
394  ledcWrite(PWM_CHANNEL1, D11);
395  ledcWrite(PWM_CHANNEL2, D12);
396  ledcWrite(PWM_CHANNEL3, D13);
397  varifier1 = 1;
398}
399
400void cluster2() {
401  colormixing(CCT2);
402  D21 = (Da * 100);
```

```
403  D22 = (DbT * 100);
404  D23 = (DcT * 100);
405
406  Serial.print("Duty Cycle for cluster2-  D21- ");
407  Serial.print(D21);
408  Serial.print("%");
409  Serial.print(" D22- ");
410  Serial.print(D22);
411  Serial.print("%");
412  Serial.print(" D23- ");
413  Serial.print(D23);
414  Serial.println("%");
415
416  D21 = map(D21, 0, 100, 0, MAX_DUTY_CYCLE);
417  D22 = map(D22, 0, 100, 0, MAX_DUTY_CYCLE);
418  D23 = map(D23, 0, 100, 0, MAX_DUTY_CYCLE);
419
420  ledcWrite(PWM_CHANNEL4, D21);
421  ledcWrite(PWM_CHANNEL5, D22);
422  ledcWrite(PWM_CHANNEL6, D23);
423  varifier2 = 1;
424}
425
426void cluster3() {
427  colormixing(CCT3);
428  D31 = (Da * 100);
429  D32 = (DbT * 100);
430  D33 = (DcT * 100);
431
432  Serial.print("Duty Cycle for cluster3-  D31- ");
433  Serial.print(D31);
434  Serial.print("%");
435  Serial.print(" D32- ");
436  Serial.print(D32);
437  Serial.print("%");
438  Serial.print(" D33- ");
439  Serial.print(D33);
440  Serial.println("%");
441
442  D31 = map(D31, 0, 100, 0, MAX_DUTY_CYCLE);
443  D32 = map(D32, 0, 100, 0, MAX_DUTY_CYCLE);
444  D33 = map(D33, 0, 100, 0, MAX_DUTY_CYCLE);
445  ledcWrite(PWM_CHANNEL7, D31);
446  ledcWrite(PWM_CHANNEL8, D32);
447  ledcWrite(PWM_CHANNEL9, D33);
```

```
448  varifier3 = 1;
449}
```

M. Code for Wireless Handheld Control Circuit used for the Developed Low-cost, High CRI, BAS enabled CCT Tunable Human Centric Smart Street Lighting Luminaire

```
1  #include <esp_now.h>
2  #include <WiFi.h>
3
4  #include <Wire.h>
5  #include <SPI.h>
6
7  #include <Adafruit_GFX.h>
8  #include <Adafruit_SSD1306.h>
9
10 #include <math.h>
11
12 #define SCREEN_WIDTH 128     // OLED display width, in pixels
13 #define SCREEN_HEIGHT 32     // OLED display height, in pixels
14 #define OLED_RESET -1        // Reset pin # (or -1 if sharing Arduino
   reset pin)
15 #define SCREEN_ADDRESS 0x3C  ///< See datasheet for Address; 0x3D for
   128x64, 0x3C for 128x32>
16
17 // Declaration for an SSD1306 display connected to I2C (SDA, SCL pins)
18 Adafruit_SSD1306 display(SCREEN_WIDTH, SCREEN_HEIGHT, &Wire, OLED_RESET);
19
20 // REPLACE WITH THE MAC Address of your receiver
21 uint8_t broadcastAddress[] = { 0xB0, 0xA7, 0x32, 0x13, 0xC4, 0xB4 };
22
23 // Define variables to store pot readings to be sent
24 int analogValue1;
25 int analogValue2;
26 int analogValue3;
27
28 int i = LOW;
29 int j = LOW;
30 int k = LOW;
31 int l = 0;
32
33 #define button_pin 36
34
35 // Define variables to store incoming readings
36 int incomingvarifier1 = 0;
```

```
int incomingvarifier2 = 0;
int incomingvarifier3 = 0;

// Variable to store if sending data was successful
String success;

//Structure example to send data
//Must match the receiver structure
typedef struct struct_message {
  int analog1;
  int analog2;
  int analog3;
  int BAS;
} struct_message;

// Create a struct_message called BME280Readings to hold sensor readings
struct_message potReading;

// Create a struct_message to hold incoming sensor readings
struct_message incomingReading;

esp_now_peer_info_t peerInfo;

// Callback when data is sent
void OnDataSent(const uint8_t *mac_addr, esp_now_send_status_t status) {
  Serial.print("\r\nLast Packet Send Status:\t");
  Serial.println(status == ESP_NOW_SEND_SUCCESS ? "Delivery Success" :
"Delivery Fail");
  if (status == 0) {
    success = "Delivery Success :)";
  } else {
    success = "Delivery Fail :(";
  }
}

// Callback when data is received
void OnDataRecv(const uint8_t *mac, const uint8_t *incomingData, int len)
{
  if (len >= sizeof(incomingReading)) {
    memcpy(&incomingReading, incomingData, sizeof(incomingReading));
    Serial.print("Bytes received: ");
    Serial.println(len);
    incomingvarifier1 = incomingReading.analog1;
    incomingvarifier2 = incomingReading.analog2;
    incomingvarifier3 = incomingReading.analog3;
```

```
  } else {
    Serial.println("Received data size mismatch");
  }
}

void setup() {
  // Init Serial Monitor
  Serial.begin(115200);
  display.begin(SSD1306_SWITCHCAPVCC, SCREEN_ADDRESS);
  display.clearDisplay();

  //set the resolution to 12 bits (0-4095)
  analogReadResolution(12);
  pinMode(34, INPUT);
  pinMode(33, INPUT);
  pinMode(32, INPUT);
  pinMode(button_pin, INPUT);

  // Init OLED display
  if (!display.begin(SSD1306_SWITCHCAPVCC, SCREEN_ADDRESS)) {
    Serial.println(F("SSD1306 allocation failed"));
    for (;;)
      ;
  }

  display.setTextSize(1);
  display.setTextColor(WHITE);
  display.setCursor(0, 0);
  display.println("PWM controller");

  // Set device as a Wi-Fi Station
  WiFi.mode(WIFI_STA);

  // Init ESP-NOW
  if (esp_now_init() != ESP_OK) {
    Serial.println("Error initializing ESP-NOW");
    return;
  }

  // Once ESPNow is successfully Init, we will register for Send CB to
  // get the status of Trasnmitted packet
  esp_now_register_send_cb(OnDataSent);

  // Register peer
  memcpy(peerInfo.peer_addr, broadcastAddress, 6);
```

```
  peerInfo.channel = 0;
  peerInfo.encrypt = false;

  // Add peer
  if (esp_now_add_peer(&peerInfo) != ESP_OK) {
    Serial.println("Failed to add peer");
    return;
  }
  // Register for a callback function that will be called when data is
   received
  esp_now_register_recv_cb(OnDataRecv);
}

void loop() {
  // Beam Angle Switching Enabling
  i = digitalRead(button_pin);

  if (i == LOW && j == LOW && k == LOW) {  // FUll glow
    l = 1;
  } else if (i == HIGH && j == LOW && k == LOW) {  // Pro or Counter
    l = 2;
    i = !i;
    j = !j;
  } else if (i == HIGH && j == HIGH && k == LOW) {  // Pro or Counter
    l = 3;
    i = !i;
    j = !j;
    k = !k;
  } else if (i == HIGH && j == LOW && k == HIGH) {  // Full glow
    i = !i;
    k = !k;
  }

  Serial.print("BAS:  ");
  Serial.println(l);

  analogValue1 = analogRead(34);
  analogValue2 = analogRead(33);
  analogValue3 = analogRead(32);
  Serial.println(analogRead(34));
  Serial.println(analogRead(33));
  Serial.println(analogRead(32));

  // Set values to send
  potReading.analog1 = analogValue1;
```

```
169   potReading.analog2 = analogValue2;
170   potReading.analog3 = analogValue3;
171   potReading.BAS = 1;
172
173   // Send message via ESP-NOW
174   esp_err_t result = esp_now_send(broadcastAddress, (uint8_t
    *)&potReading, sizeof(potReading));
175
176   if (result == ESP_OK) {
177     Serial.println("Sent with success");
178   } else {
179     Serial.println("Error sending the data");
180   }
181   updateDisplay();
182   delay(100);
183}
184
185void updateDisplay() {
186   // Display Readings on OLED Display
187   display.clearDisplay();
188   display.setTextSize(1);
189   display.setTextColor(WHITE);
190   display.setCursor(0, 0);
191   if (incomingvarifier1 == 1 && incomingvarifier2 == 1 &&
    incomingvarifier3 == 1) {
192     display.print("BAS - Full glow");
193   } else if (incomingvarifier1 == 0 && incomingvarifier2 == 1 &&
    incomingvarifier3 == 1) {
194     display.print("BAS - Counter");
195   } else if (incomingvarifier1 == 1 && incomingvarifier2 == 1 &&
    incomingvarifier3 == 0) {
196     display.print("BAS - Counter");
197   }
198   delay(250);
199   display.clearDisplay();
200   //display.cp437(true);
201   display.setCursor(0, 0);
202   display.print("Analog val1- ");
203   display.setCursor(40, 0);
204   display.print(analogValue1);
205   display.setCursor(0, 12);
206   display.print("Analog val2- ");
207   display.setCursor(40, 12);
208   display.print(analogValue2);
209   display.setCursor(0, 24);
```

```
  display.print("Analog val3- ");
  display.setCursor(40, 24);
  display.print(analogValue3);

  // Display Readings in Serial Monitor
  if (incomingvarifier1 == 1 && incomingvarifier2 == 1 &&
incomingvarifier3 == 1) {
    Serial.println("BAS - Full glow");
  } else if (incomingvarifier1 == 0 && incomingvarifier2 == 1 &&
incomingvarifier3 == 1) {
    Serial.println("BAS - Counter");
  } else if (incomingvarifier1 == 1 && incomingvarifier2 == 1 &&
incomingvarifier3 == 0) {
    Serial.println("BAS - Counter");
  }
  Serial.print("Analog val1- ");
  Serial.println(analogValue1);
  Serial.print("Analog val2- ");
  Serial.println(analogValue2);
  Serial.print("Analog val3- ");
  Serial.println(analogValue3);
  Serial.println(success);
}

```

N. Code for Registering R-G-B values of a Particular CCT using the Developed Novel CCT Meter using ML Regression Technique

```
#include <SPI.h>
#include <Wire.h>
#include <Adafruit_GFX.h>
#include <Adafruit_SSD1306.h>

#define SCREEN_WIDTH 128  // OLED display width, in pixels
#define SCREEN_HEIGHT 32  // OLED display height, in pixels

#define OLED_RESET -1        // Reset pin # (or -1 if sharing Arduino
reset pin)
#define SCREEN_ADDRESS 0x3C  ///< See datasheet for Address; 0x3D for
128x64, 0x3C for 128x32>
Adafruit_SSD1306 display(SCREEN_WIDTH, SCREEN_HEIGHT, &Wire, OLED_RESET);

#define S2 32        /*Define S2 Pin Number of ESP32*/
#define S3 33        /*Define S3 Pin Number of ESP32*/
```

```
#define sensorOut 25 /*Define Sensor Output Pin Number of ESP32*/
#define S1 18
#define S0 19
#define OE 5

/*Enter the Minimum and Maximum Values which getting from Calibration
  Code*/
int R_Min = 8;   /*Red minimum value*/
int R_Max = 96;  /*Red maximum value*/
int G_Min = 9;   /*Green minimum value*/
int G_Max = 101; /*Green maximum value*/
int B_Min = 2;   /*Blue minimum value*/
int B_Max = 28;  /*Blue maximum value*/

/*Define int variables*/
int Red = 0;
int Red_inst = 0;
int Green = 0;
int Green_inst = 0;
int Blue = 0;
int Blue_inst = 0;
int i = 0;

int redValue = 0;
int greenValue = 0;
int blueValue = 0;
int Frequency = 0;

void setup() {
  pinMode(S2, OUTPUT);       /*Define S2 Pin as a OUTPUT*/
  pinMode(S3, OUTPUT);       /*Define S3 Pin as a OUTPUT*/
  pinMode(sensorOut, INPUT); /*Define Sensor Output Pin as a INPUT*/
  pinMode(S1, OUTPUT);
  pinMode(S0, OUTPUT);
  pinMode(OE, OUTPUT);
  digitalWrite(S1, LOW);
  digitalWrite(S0, HIGH);
  digitalWrite(OE, HIGH);
  Serial.begin(115200); /*Set the baudrate to 115200*/
  display.begin(SSD1306_SWITCHCAPVCC, 0x3C);
  display.clearDisplay();
  if (!display.begin(SSD1306_SWITCHCAPVCC, SCREEN_ADDRESS)) {
    Serial.println(F("SSD1306 allocation failed"));
    for (;;)
      ;  // Don't proceed, loop forever
```

```
59    }
60
61    display.setTextSize(1);
62    display.setTextColor(WHITE);
63    display.setCursor(0, 0);
64    display.println("RGB Data");
65    display.setTextSize(1);
66    display.setTextColor(WHITE);
67    display.setCursor(0, 10);
68    display.println("Logger");
69    display.display();
70    delay(3000); /*Wait for 3000mS*/
71  }
72
73  void loop() {
74    for (i; i <= 100; i++) {
75      Red_inst = getRed();
76      Red = (Red + Red_inst);
77      Serial.println(Red_inst);
78      delay(15);
79    }
80    Red = Red / 100;
81    Serial.println(Red);
82    redValue = map(Red, R_Min, R_Max, 255, 0); /*Map the Red Color Value*/
83    i = 0;
84
85    for (i; i <= 100; i++) {
86      Green_inst = getGreen();
87      Green = (Green + Green_inst);
88      Serial.println(Green_inst);
89      delay(15);
90    }
91    Green = Green / 100;
92    Serial.println(Green);
93    greenValue = map(Green, G_Min, G_Max, 255, 0); /*Map the Green Color
    Value*/
94    i = 0;
95
96    for (i; i <= 100; i++) {
97      Blue_inst = getBlue();
98      Blue = (Blue + Blue_inst);
99      Serial.println(Blue_inst);
100     delay(15);
101   }
102   Blue = Blue / 100;
```

```
103  Serial.println(Blue);
104  blueValue = map(Blue, B_Min, B_Max, 255, 0); /*Map the Blue Color
   Value*/
105  i = 0;
106
107  Serial.print("Red = ");
108  Serial.print(redValue); /*Print Red Color Value on Serial Monitor*/
109  Serial.print("    ");
110  Serial.print("Green = ");
111  Serial.print(greenValue); /*Print Green Color Value on Serial Monitor*/
112  Serial.print("    ");
113  Serial.print("Blue = ");
114  Serial.println(blueValue); /*Print Blue Color Value on Serial Monitor*/
115  Oled();
116  //delay(1000);              /*wait a second*/
117}
118
119int getRed() {
120  digitalWrite(S2, LOW);
121  digitalWrite(S3, LOW);
122  Frequency = pulseIn(sensorOut, LOW); /*Get the Red Color Frequency*/
123  return Frequency;
124}
125
126int getGreen() {
127  digitalWrite(S2, HIGH);
128  digitalWrite(S3, HIGH);
129  Frequency = pulseIn(sensorOut, LOW); /*Get the Green Color Frequency*/
130  return Frequency;
131}
132
133int getBlue() {
134  digitalWrite(S2, LOW);
135  digitalWrite(S3, HIGH);
136  Frequency = pulseIn(sensorOut, LOW); /*Get the Blue Color Frequency*/
137  return Frequency;
138}
139
140void Oled() {
141  display.setTextSize(1);
142  display.setTextColor(WHITE);
143  display.setCursor(0, 0);
144  display.println("R - ");
145  display.setCursor(30, 0);
146  display.println(redValue);
```

```
147   display.setTextSize(1);
148   display.setCursor(0, 12);
149   display.println("G - ");
150   display.setCursor(30, 12);
151   display.println(greenValue);
152   display.setTextSize(1);
153   display.setTextColor(WHITE);
154   display.setCursor(0, 24);
155   display.println("B - ");
156   display.setCursor(30, 24);
157   display.println(blueValue);
158   display.display();
159   display.clearDisplay();
160 }
```

O. Code of Calibration of RGB Sensor used in Developed Novel CCT Meter

```
1   #define S2 32        /*Define S2 Pin Number of ESP32*/
2   #define S3 33        /*Define S3 Pin Number of ESP32*/
3   #define sensorOut 25 /*Define Sensor Output Pin Number of ESP32*/
4   #define S1 18
5   #define S0 19
6   #define OE 5
7
8   /*Define int variables*/
9   int Red = 0;
10  int Green = 0;
11  int Blue = 0;
12  int Frequency = 0;
13
14  void setup() {
15    pinMode(S2, OUTPUT);       /*Define S2 Pin as a OUTPUT*/
16    pinMode(S3, OUTPUT);       /*Define S3 Pin as a OUTPUT*/
17    pinMode(sensorOut, INPUT); /*Define Sensor Output Pin as a INPUT*/
18    pinMode(S1, OUTPUT);
19    pinMode(S0, OUTPUT);
20    pinMode(OE, OUTPUT);
21    digitalWrite(S1, LOW);
22    digitalWrite(S0, HIGH);
23    digitalWrite(OE, HIGH);
24    Serial.begin(115200); /*Set the baudrate to 115200*/
25    Serial.print("This is TCS3200 Calibration Code");
26  }
27
```

```
28 void loop() {
29   Red = getRed();
30   delay(200); /*wait a 200mS*/
31   Green = getGreen();
32   delay(200); /*wait a 200mS*/
33   Blue = getBlue();
34   delay(200); /*wait a 200mS*/
35   Serial.print("Red Freq = ");
36   Serial.print(Red); /*Print Red Color Value on Serial Monitor*/
37   Serial.print("   ");
38   Serial.print("Green Freq = ");
39   Serial.print(Green); /*Print Green Color Value on Serial Monitor*/
40   Serial.print("   ");
41   Serial.print("Blue Freq = ");
42   Serial.println(Blue); /*Print Blue Color Value on Serial Monitor*/
43 }
44
45 int getRed() {
46   digitalWrite(S2, LOW);
47   digitalWrite(S3, LOW);
48   Frequency = pulseIn(sensorOut, LOW); /*Get the Red Color Frequency*/
49   return Frequency;
50 }
51
52 int getGreen() {
53   digitalWrite(S2, HIGH);
54   digitalWrite(S3, HIGH);
55   Frequency = pulseIn(sensorOut, LOW); /*Get the Green Color Frequency*/
56   return Frequency;
57 }
58
59 int getBlue() {
60   digitalWrite(S2, LOW);
61   digitalWrite(S3, HIGH);
62   Frequency = pulseIn(sensorOut, LOW); /*Get the Blue Color Frequency*/
63   return Frequency;
64 }
```

Annexture 2

This part of the thesis describes the steps of calculation of small target visibility or STV, mentioned in Chapter 4.

Small Target Visibility (STV) represents the average visibility of targets across a roadway area for a specific traffic direction. It is calculated by averaging the Visibility Level (VL) values at multiple grid points. VL quantifies the visibility of a target at a specific location for a particular observer and direction, representing the amount exceeding the visibility threshold. VL is a unitless ratio. To determine STV for a given grid and traffic direction, VL and Relative Weighted VL (RWVL) must be calculated for each grid point using the following steps.

Step 1 To initiate the calculation, the target's position within the grid, the observer's location (15 meters away), and the viewing direction are established. The observer is modeled as an adult (20 years old) with normal vision and a fixation time of 0.7 seconds. The target is a flat, 8cm x 8cm square positioned perpendicularly to the road surface and the observer's horizontal line of sight. The target exhibits Lambertian reflectance with a value of 0.37.

Target luminance (L_t) is computed for the target's center point. Background luminance (L_{b1}) is determined at the pavement point adjacent to the target's base, while background luminance (L_{b2}) is calculated at a point beyond the target along the observer's line of sight through the target's top center. Both L_{b1} and L_{b2} are calculated as if the observer's viewpoint were slightly elevated (one degree) above the road surface. In this document, the target's background luminance (L_b) is determined as the average of L_{b1} and L_{b2}:

$$L_b = (L_{b1} + L_{b2}) / 2 \quad (1)$$

The values L_t and L_b are then used, together with constants for the target size, observer age, and fixation time, to calculate visibility level (VL).

Step 2 is about the calculation of the adaptation luminance (L_a), the Log_{10} of L_a (LL_a), and the visual angle (A) in minutes subtended by the target:

$$L_a = L_b + L_v \quad (2)$$

(Since we have done this experiment in a controlled environment so there is no veiling luminance L_V)

$$LL_a = Log_{10}(L_a) \quad (3)$$

$$A = \tan^{-1} (\text{Target size} / \text{Distance observer to target}) * 60 \quad (4)$$

For a standard target size of 0.08 meters and an observer distance of 15 meters, the value of "A" is 18.33 minutes.

Step 3 The determination of visual system sensitivity involves assessing how it changes with varying adaptation luminance levels. This process utilizes one of three specific equations, depending on the value of L_a:

If, L_a = > 0.6

$$\text{then, } F = [\text{Log}_{10}(4.2841 * L_a^{0.1556}) + (0.1684 * L_a^{0.5867})]^2$$

$$\text{and } L = (0.05946 * L_a^{0.466})^2 \quad (5)$$

If, 0.00418 < L_a < 0.6

$$\text{then, } F = 10^{\{2*[(0.0866*LL_a{}^2)+(1.055*LL_a)-0.072]\}}$$

$$\text{and } L = 10^{[2*(0.319*LL_a-1.256)]} \quad (6)$$

If, La < 0.00418

$$\text{then, } F = 10^{[2*(0.346*LL_a+0.056)]}$$

$$\text{and } L = 10^{[(0.0454*LL_a{}^2)+(0.3372*LL_a)-1.782]} \quad (7)$$

Step 4 is to determine the intermediate functions using the following equations:

$$B = \text{Log}_{10}(A) + 0.523 \quad (8)$$

$$C = LL_a + 6 \quad (9)$$

$$AA = 0.360 - \{(0.0972 * B^2)/[B^2 - (2.513 * B) + 2.789]\} \quad (10)$$

$$AL = 0.355 - \{0.1217 * [C^2/(C^2 - (10.40 * C) + 52.28)]\} \quad (11)$$

$$AZ = \sqrt{\frac{AA^2+AL^2}{2.1}} \quad (12)$$

$$DL_1 = 2.6*[\frac{\sqrt{F}}{A} + \sqrt{L}]^2 \quad (13)$$

Step 5 The calculation process involves determining the value of M using one of three equations, contingent upon the value of LL_a. Subsequently, the negative contrast adjustment factor (FCP) is calculated. It's important to note that the accuracy of FCP diminishes when LL_a falls below -2.4, corresponding to an adaptation luminance (L_a) of less than 0.00418 cd/m². In practical scenarios involving negative contrast, such low levels of adaptation are typically not encountered:

If, -2.4 < LL_a < -1

$$\text{then, } M = 10^{-10^{-\{[0.075*(LL_a+1)^2]+0.0245\}}} \quad (14)$$

If, LL_a > = -1

$$\text{then, } M = 10^{-10^{-\{[0.125*(LL_a+1)^2]+0.0245\}}} \quad (15)$$

If, $LL_a <= -2.4$

then, FCP = 0.5 (TGB and FCP need not be calculated) (16)

Otherwise,

$$TGB = -0.6(L_a)^{-0.1488} \quad (17)$$

$$FCP = 1 - \left[\frac{(M)(A)^{TGB}}{2.4(DL_1)^{\frac{(AZ+2)}{2}}}\right] \quad (18)$$

Step 6 is about calculation involves determining an age-based adjustment factor (FA) for the observer's age (TA), which is 60 years in this document. This factor is then used to adjust the value of DL accordingly:

$$DL_2 = DL_1 * [(AZ + T)/T] \quad (19)$$

Step 7 is calculation of the adjustment factor (FA) based on the observer's age (TA), which is 60 years in this document. This factor is then applied to adjust the value of DL:

If, age is <= 64

$$\text{then, } FA = [(TA - 19)^2/2160] + 0.99 \quad (20)$$

If age is over 64

$$\text{then, } FA = [(TA - 56.5)^2/116.3] + 1.43 \quad (21)$$

$$DL_3 = DL_2 * FA \quad (22)$$

Step 8 is the calculation involves determining an adjustment factor if the target's luminance is lower than the background luminance (negative contrast):

If L_t is less than L_b

$$\text{then, } DL_4 = DL_3 * FCP \quad (23)$$

$$\text{otherwise, } DL_4 = DL_3 \quad (24)$$

Step 9 is to calculate VL:

$$VL = (L_t - L_b)/DL_4 \quad (25)$$

Step 10 is determination of the relative weighted visibility level RWVL.

Across a roadway, Visibility Level (VL) values can be both positive and negative.

[1] A magnitude below 1.0 (positive or negative) signifies that the target is below the visibility threshold for a standard observer with a 0.7-second fixation time. Higher VL values indicate easier or faster target detectability. However, a direct comparison between VL values is not straightforward. For instance, a VL of 9.5 at one point and 0.5 at another is not equivalent to two

points with an average VL of 5. To address this, Relative Weighted VL is employed. This method down weights the influence of extremely high VL values in the calculation of the summary metric, Small Target Visibility (STV). Here, ABS(X) denote the absolute value of 'X'.

$$\text{RWVL} = 10^{[-0.1*ABS(VL)]} \qquad (26)$$

the Final Steps After all *RWVL* values are calculated for all grid points, calculate the Average *RWVL*:

$$\text{ARWVL} = (\text{Sum of all RWVL})/\ (\text{Number of points in the grid}) \qquad (27)$$

Finally, calculate the Weighted Average *VL*, also known as Small Target Visibility or *STV*:

$$\text{STV} = \text{Weighted Average VL} = -10 * \text{Log}_{10}(\text{ARWVL}) \qquad (28)$$

Aishwarya Dev Goswami
29/1/2025